Multidimensional Vibrational Spectroscopy of Hydrogen-Bonded Systems in the Liquid Phase: Coupling Mechanisms and Structural Dynamics

D i s s e r t a t i o n

zur Erlangung des akademischen Grades

d o c t o r r e r u m n a t u r a l i u m

(Dr. rer. nat.)

im Fach Physik

eingereicht an der

Mathematisch-Naturwissenschaftlichen Fakultät I

der Humboldt-Universität zu Berlin

von

Diplom-Physiker Nils Huse
geboren am 26. September 1972 in Hamburg

Präsident der Humboldt-Universität zu Berlin
in Vertretung Prof. Dr. H. J. Prömel

Dekan der Mathematisch-Naturwissenschaftlichen Fakultät I
Prof. Th. J. Buckhout, PhD

Gutachterinnen und Gutachter: 1. Prof. Dr. T. Elsässer
2. Prof. Dr. B. Röder
3. Prof. Dr. D. Stehlik

Tag der mündlichen Prüfung: 17. Februar 2006

Zusammenfassung

Wasserstoffbrücken stellen, verglichen mit ionischen oder kovalenten Bindungen, schwache Wechselwirkungen dar, dennoch haben sie großen Einfluß auf die Struktur und das dynamische Verhalten molekularer Systeme. Sie sind von fundamentaler Bedeutung in der Natur und spielen unter anderem eine Schlüsselrolle im Genom aller lebenden Organismen, in der Struktur und Funktion von Eiweißen und in den besonderen Eigenschaften des Wassers. Die Forschung an wasserstoffverbrückten Systemen hat ihre Ursprünge im neunzehnten Jahrhundert, und das Wasserstoffbrückenkonzept entwickelte sich zu Beginn des zwanzigsten Jahrhunderts. Seitdem ist die Infrarotspektroskopie eine der wesentlichen wissenschaftlichen Methoden zur Untersuchung dieser Wechselwirkung.

Die Motivation dieser Arbeit ist das tiefere Verständnis intermolekularer Wasserstoffbrücken in Flüssigkeiten und molekularen Komplexen in flüssiger Umgebung. Berühmte Wissenschaftler wie Wilhelm Conrad Röntgen, Walther Nernst, Anders Jonas Ångström und Linus Pauling haben wasserstoffverbrückte Systeme untersucht, unter anderem Essigsäuredimere und Wasser. Diese Systeme bilden O–H$\cdots$O-Brücken aus, in denen die OH-Streckschwingung eine sehr empfindliche Sonde struktureller Dynamik und zugrunde liegender Kopplungen zwischen den molekularen Bestandteilen darstellt. Essigsäuredimere in apolaren Lösungsmitteln bilden mittelstarke Wasserstoffbrücken und haben eine wohldefinierte Geometrie. Im Gegensatz dazu werden Wassermoleküle von schwachen Wasserstoffbrücken zusammengehalten und bilden ein schnell fluktuierendes Netzwerk mit einer Vielzahl an Wasserstoffbrückenlängen und -winkeln.

Mit dem Aufkommen gepulster Lasertechnologie ist es möglich geworden, molekulare Prozesse in Echtzeit zu verfolgen und letztendlich ultraschnelle Zeitauflösung zu erreichen, die es erlaubt, Kernbewegungen zu verfolgen. Zeitaufgelöste Infrarotspektroskopie ist wegen ihrer chemischen Spezifität und auf kleine Molekülbereiche beschränkten Information zu einer wichtigen experimentellen Methode geworden. Die Entwicklung optischer Analoga der mehrdimensionalen Kernmagnetresonanzspektroskopie hat sich als besonders geeignet in der ultraschnellen Infrarotspektroskopie erwiesen. Ein Teil dieser Dissertation wurde der Verbesserung dieser Techniken gewidmet und das erste passiv-phasenstarre Experiment zur kohärenten mehrdimensionalen Infrarotspektroskopie gebaut.

Essigsäure bildet symmetrische Dimere in apolaren Flüssigkeiten und dient als Modellsystem gekoppelter intermolekularer Wasserstoffbrücken. Eine auf experimentellen Ergebnissen basierende quantenmechanische Beschreibung dieses Systems fehlte bisher, aber ihre Entwicklung würde wesentlich zum Verständnis ähnlicher jedoch komplexerer Systeme beitragen wie z.B. DNS-Basenpaare. Die OH-Streckschwingung in Essigsäure-Dimeren zeigt eine sehr komplexe Absorptionsbande, deren Ursprung seit mehr als einem halben Jahrhundert diskutiert wird. Drei Kopplungsmechanismen werden für dieses absorptive

Verhalten verantwortlich gemacht: (i) exzitonische Davidov-Kopplung zwischen entarteten OH-Streckmoden, (ii) anharmonische Kopplung zwischen den OH-Streckmoden und niederfrequenten Wasserstoffbrückenmoden und (iii) Fermi-Resonanzen zwischen dem ersten angeregten Zustand der OH-Streckmoden und Kombinations- und Obertönen anderer intramolekularer Schwingungsmoden.

Die experimentellen Ergebnisse ultraschneller Pump-Tast- und Photonenecho-Schwingungsspektroskopie wurden mit quantenchemischen Rechnungen kombiniert, um die verschiedenen Beiträge zur diskutierten Linienform aufzugliedern. Die Davidov-Kopplung zwischen den OH-Streckmoden erweist sich als gering und ihre Stärke wird mit weniger als 10cm^{-1} abgeschätzt. Starke anharmonische Kopplungen mit kubischen Kraftkonstanten, die größer als 150cm^{-1} sind, existieren zwischen den OH-Streckmoden und der niederfrequenten Dimerstreck- und der ebenen Dimerbiegemode. Letztere haben Eigenfrequenzen von 145cm^{-1} und 165cm^{-1}. Deutlich unterdämpfte kohärente Kernbewegungen der Monomere, d.h. Wellenpakete in Wasserstoffbrückenmoden, können durch Anregung der OH-Streckmoden sogar in flüssiger Phase erzeugt werden. Diese Kohärenzen haben ein Dephasierungszeit von 0.7ps. Kohärente Polarisationen der OH-Streckmode zerfallen mit einer Dephasierungszeit von 200fs und zeigen ausgeprägte Schwebungen aufgrund von Quanteninterferenzen, die durch gleichzeitige Anregung von Kohärenzen in Wasserstoffbrückenmoden verursacht werden. Fermi-Resonanzen zwischen dem ersten angeregten Zustand der OH-Streckmoden und Kombinations- und Obertönen der OH-Biegeschwingung, den Streckmoden der CO-Gruppe und der Methyltorsionsmode beruhen auf gleichstarker anharmonischer Kopplung mit kubischen Kraftkonstanten von 150cm^{-1}. Schnellere Dephasierung dieser Übergänge verschleiert ihre Natur im Zeitraum, während sich die langsamer dephasierenden Wellenpakete der Dimermoden auf längeren Zeitskalen offenbaren. Jedoch werden die linearen und kohärenten zweidimensionalen Spektren durch Fermi-Resonanzen dominiert. Lebensdauermessungen der OH-Streck- und der OH-Biegemode ergeben Werte von 200fs bzw. 250fs. Ein dominanter Zerfallskanal der OH-Streckmoden scheint nicht zu existieren. Zusammenfassend wurde das erste umfassende, auf experimentellen Ergebnissen basierende quantenmechanische Modell entwickelt, das Essigsäuredimere in der Gasphase und in apolaren Lösungsmitteln mit hoher Güte beschreibt und Jahrzehnte alte Fragen beantwortet.

Eine der Schlüsselfragen der Wasserforschung berührt die Struktur dieses schnell fluktuierenden Wasserstoffbrückennetzwerkes und sein dynamisches Verhalten. Charakteristische Zeitskalen dieser Dynamik umfassen einen weiten Bereich. Äquivalent dazu zeigt die spektrale Dichte des Wassers viele ausgeprägte Merkmale im Bereich einiger Gigahertz bis zu Frequenzen harter Röntgenstrahlung. Wasserstoffverbrückung zwischen Wassermolekülen ist hauptverantwortlich für dieses Verhalten und viele spektroskopische Experimente im Infrarot sind in den letzten 15 Jahren veröffentlicht worden. Allerdings haben nur wenige Studien reines Wasser (flüssiges H_2O) untersucht, weil die Hauptsonde, die OH-Streckschwingung (ν_{OH}), einen zu hohen Absorptionsquerschnitt hat, um Experimente in Transmission mit Wasserfilmen, die dicker als ein 1μm sind, durchzuführen. Eine neu entwickelte Probenzelle mit vernachlässigbaren Fensterbeiträgen während der Pulsüberlappung, die einen 500nm dicken, stabilen Wasserfilm enthält, ermöglicht Untersuchungen mit Pump-Tast- und Photonenecho-Schwingungsspektroskopie an reinem Wasser mit der zur Zeit höchstmöglichen Zeitauflösung.

Die OH-Streckschwingung wurde mit kohärenter mehrdimensionaler Infrarotspektroskopie untersucht. Am auffälligsten ist die schnelle spektrale Diffusion der ν_{OH}-Mode innerhalb von 50fs. Dies wird durch verhinderte Rotationsschwingungen im Wasserstoffbrückennetzwerk, Librationen genannt, verursacht, die auf das schwingungsangeregte Wassermolekül reagieren. Als Resultat verschwindet die zeitliche Korrelation der Übergangsfrequenz eines angeregten Wassermoleküls innerhalb von 50fs. Mit anderen Worten verliert ein Wassermolekül sein Gedächtnis der Übergangsfrequenz, mit der es angeregt worden ist, innerhalb von 50fs. Ein sehr schneller Zerfall der Polarisationsanisotropie mit einer Zeitkonstante von 80fs nach OH-Streckanregung wird ebenfalls beobachtet. Dies beruht auf resonantem Energietransfer zwischen benachbarten Wassermolekülen. Die Lebensdauer des ersten angeregten Zustandes der OH-Streckmode beträgt 200fs und ist damit kürzer als vermutet worden war aufgrund von Experimenten an isotopisch verdünntem Wasser. Die Thermalisierung des Anregungsvolumens findet innerhalb von nur wenigen Pikosekunden statt. Das bedeutet, daß Temperatursprünge von mehr als 100K innerhalb von nur 2ps möglich sind, was ebenfalls bemerkenswert schnell ist.

Schließlich wurden die OH-Biegeschwingung und die hochfrequenten Librationen mit ultraschneller Pump-Tast-Schwingungsspektroskopie untersucht. Die OH-Biegeschwingung ist die intramolekulare Mode mit der niedrigsten Eigenfrequenz und kann daher nur durch Kopplung an Moden des Wasserstoffbrückennetzwerkes abgeregt werden. Trotz dieser interessanten direkten Kopplung ist wenig bekannt über das dynamische Verhalten dieser Schwingung. Es zeigt sich, daß die Lebensdauer nur 170fs beträgt, und die Librationsantwort schneller als die Zeitauflösung von 70fs ist. Nach Femtosekunden-Anregung dieser Moden verteilt die einsetzende Populationsrelaxation die Überschußenergie auf niederfrequente Moden, und das Anregungsvolumen erreicht sein thermisches Gleichgewicht noch schneller als nach Anregung der OH-Streckschwingung. Die Zeitkonstanten dieser Thermalisierung durch Biege- und Librationsanregung sind 800fs bzw. 430fs.

Ein umfassendes Wassermodell, das die Ergebnisse verschiedener experimenteller Techniken wie z.B. Neutronen- und Röntgenbeugung, Röntgenabsorptionsspektroskopie an Feinstrukturkanten und Schwingungsspektroskopie richtig beschreibt, ist immer noch nicht vorhanden. Es wäre daher wünschenswert, die unterschiedlichen Techniken zu kombinieren, um zeitaufgelöste komplementäre Informationen zu erhalten. Auch sind Wechselwirkungen zwischen Wasser und Eiweißen bzw. DNS hochgradig relevant in vielen biologischen Systemen, und es sind noch viele Frage zu molekularen Kopplungsmechanismen offen, die vielleicht mit zeitaufgelöster Schwingungsspektroskopie beantwortet werden könnten.

Contents

Figures

Tables

1 Hydrogen bonds

> *Unter einer Nebenvalenz wird man dann eine Bindekraft zu verstehen haben, die zwar genügt, um zwei Atomgruppen durch atomare Bindung zu vereinigen, die jedoch nicht befähigt ist, ein Elektron zu ketten. Diese Definitionen lassen sich mit der Ansicht vereinen, dass sich Haupt- und Nebenvalenzen nur durch ihren Energieinhalt unterscheiden und dass die Hauptvalenzen stärkeren Affinitätswirkungen entsprechen als die Nebenvalenzen.*
>
> Alfred Werner, 1902

A hydrogen bond is a simple structural motif that consists of a donor and at least one acceptor atom, X and Y, between which a hydrogen atom is located: X–H$\cdots$Y. The donor forms a covalent bond with the hydrogen atom whereas the interaction between the hydrogen atom and the acceptor is often considerably weaker* [1]. Despite its simplicity, the relevance of hydrogen bonds in nature can hardly be overestimated. It is a unique interaction that is strong enough to create stable genetic code [2] or rigid lever arms which allow a muscle to contract [3]. But it is also weak enough for the rigid double helix that contains the genetic code to open during cell division [4] or a peptide to bend in the initial event of vision [5]. And in combination with the simple tetrahedral charge structure of an H_2O molecule, liquid water displays properties that are vital for life. This thesis contributes to the knowledge that has been gathered about hydrogen-bonded systems by investigating nuclear motions in pure water and in acetic acid dimers dissolved in apolar liquids with femtosecond nonlinear vibrational spectroscopy.

1.1 Introduction

The hydrogen bond concept is often accredited to Latimer and Rodebush [6] but rather engendered over several decades and many scientists have contributed to it. The term *hydrogen bond* was probably introduced by Pauling in the 1920s, a time when considerable dissent existed over the chemical nature of hydrogen bonds [7]. Pauling has attributed the idea of hydrogen bonds to Moore and Winmill [8] although explicit reference to a theory by Werner is made in their publication. Werner's work [9] reveals how close his idea of the *Nebenvalenz*† was to modern conceptions of the hydrogen bond.

*If the hydrogen bond interaction is much weaker than the XH bond, perturbation theory can be used and the resulting expansion terms are identified as electrostatic, covalent, dispersive, etc. This approach is not useful for very strong hydrogen bonds, X—H—Y, where the state of the hydrogen nucleus is described by a single-well potential that is located between the two heavier atoms.

†In his publication, Werner stated that a secondary valence (*Nebenvalenz*) cannot be conceived as a real valence (*Hauptvalenz*) and might as well be termed pseudo valence (*Pseudovalenz*).

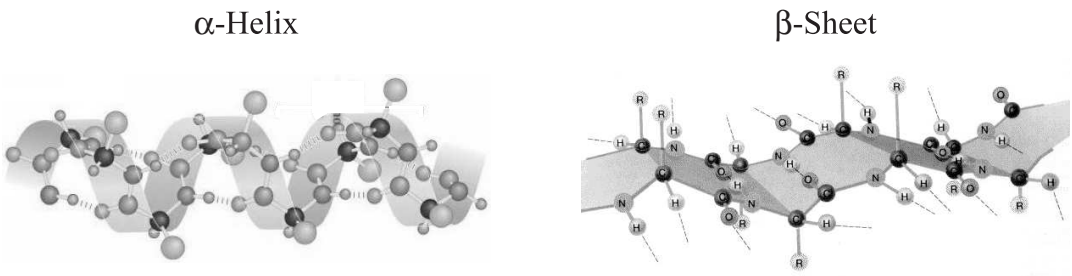

Figure 1.1: Illustration of the two secondary structures in proteins. Oxygen atoms of the carbonyl groups form hydrogen bonds with the N–H groups of other amino acids.

Pfeiffer was among the first to propose intramolecular hydrogen bond formation (innere Komplexsalzbildung) in organic chemistry [10] but an appreciation of how vital hydrogen bonds are to biological systems was yet to come. Pauling ascribed great importance to hydrogen bonds [11] noting that '...it will be found that the significance of the hydrogen bond for physiology is greater than that of any other single structural feature.' It was Pauling, Corey, and Branson who postulated the existence of the α-helix [12], one of the two secondary structures in proteins that result from hydrogen bond formation. The β-sheet was identified later by Blake and coworkers [13]. Both structures are illustrated in Figure 1.1. They are held together by hydrogen bonds between the C=O and the N–H groups of different amino acids and are essential for protein function.

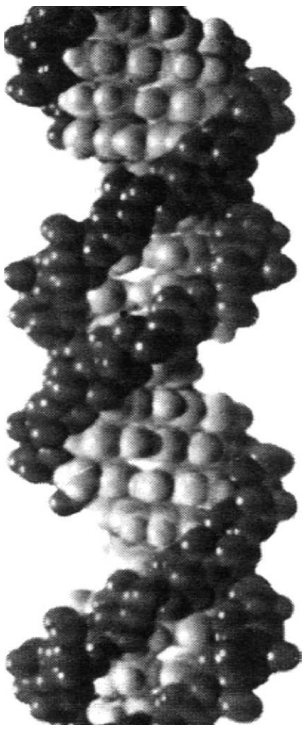

Figure 1.2: Rendered 3D image of B-type DNA.

Another prominent example of hydrogen bonds in biology is the base pairing in deoxyribose nucleic acid (DNA), the sequence that constitutes the genetic code. The double helical structure was predicted by Watson and Crick from data taken by Rosalind Franklin [2]. An electron density isosurface of such data is shown in Figure 1.2. The sugar phosphate backbones (dark colour) of the two DNA strands are held together by hydrogen bonds between the base pairs (light colour). The multitude of such bonds along with stacking interactions and the helical geometry makes DNA and α-helices very rigid structures. Hydrogen bonds are usually found in protein-cofactor and enzyme-ligand interactions where they are broken and reformed in cyclic processes such as binding/unbinding events [14, 15]. Also, an important class of chemical reactions involve intra- and intermolecular proton and hydrogen transfer processes that are mediated by hydrogen bonds [16–18]. Proton transfer occurs continuously in liquid water and is of great physiological importance in intra- and intercellular signalling pathways [19]. This simple type of reaction is closely connected to hydrogen bond reformation but will not be treated in this thesis. Several reviews have been published that cover proton transfer reactions [20–22].

In the effort to understand hydrogen-bonded systems, structural informations were obtained with various techniques which

advanced the knowledge of such systems substantially. In fact, structural information is indispensable but for a comprehensive understanding additional dynamical information is necessary. Charge transfer, energy transfer and relaxation, solvation, structural fluctuations, and collisions are ultrafast processes which determine the behaviour of hydrogen-bonded systems on femtosecond to picosecond timescales. The challenge is to investigate these fast processes and link them to ultrafast structural changes. Diffraction techniques with ultrafast time resolution have started to emerge [23–27] that hold very promising applications. Ultimately, one would hope for an experimental technique that allows to follow structural dynamics on the level of electrons and atomic nuclei from attoseconds onward. At the moment, spectroscopy from the infrared to the ultraviolet is still superior in applicability and is the most widely used tool for the investigation of sub-picosecond dynamics.

1.2 Hydrogen bonds & vibrational spectroscopy

Time-resolved electronic spectroscopy has allowed to follow chemical reaction dynamics in real time, something that seemed impossible before the invention of ultrafast lasers. However, transitions are typically probed that involve electrons which participate in covalent bonds and are thus delocalised over several atoms. The local nature of many molecular vibrations generally allows vibrational spectroscopy to obtain more site-specific information than is accessible with electronic spectroscopy. Intramolecular vibrations of specific functional groups are probed which couple to other parts of the molecule and the environment, e.g. the solvent or a protein surrounding. Furthermore, electronic spectroscopy in liquids has to deal with significant broadening of electronic transitions causing spectral overlap of absorption and fluorescence spectra. Vibrational absorption lines rarely exceed 50cm^{-1} linewidth except for those of hydrogen-bonded groups. One reason is the relation between an oscillator's anharmonicity α (the difference between the fundamental and the first overtone transition) and the dephasing time T_2 of the transition, the inverse of which determines the linewidth [28]:

$$T_2^{-1} \propto \frac{\alpha}{\mu\epsilon^2} \int_0^\infty dt \, \langle F(0)F(t)\rangle. \tag{1.1}$$

F is a fluctuating force that a solvent vibrational mode exerts on the probe oscillator, μ is the reduced mass of the nuclei that constitute the system, and ϵ is the average transition energy. Typical anharmonicities of vibrational oscillators are smaller than 20cm^{-1}. Such values are more than an order of magnitude less than those of electronic oscillators. The exception to the rule are vibrational oscillators that are affected by hydrogen bonds, in particular the XH stretching vibrations [1].

The effect of hydrogen bond formation on the vibrational absorption spectra became evident in the 1930s [30–36] and since then has been exploited in linear and nonlinear infrared spectroscopy to study hydrogen-bonded systems. The most obvious change upon hydrogen bond formation is the red shift of the XH stretching frequency as can be seen from Figure 1.3 in which crystallographic and spectroscopic data of hydrogen-bonded systems in crystalline phase is summarised. The cause for this shift is a softening of

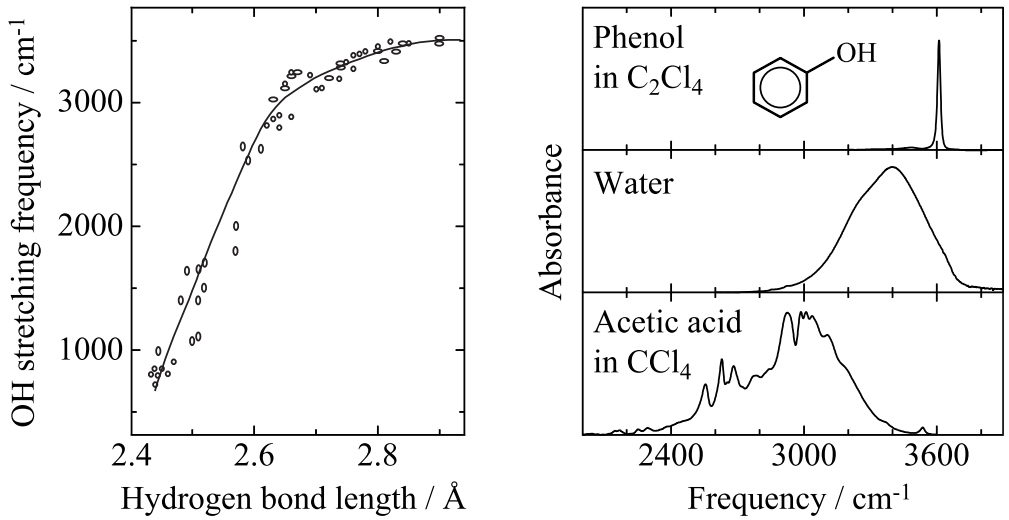

Figure 1.3: Left: OH stretching frequencies in crystals as a function of the hydrogen bond length, redrawn from [29]. Right: Absorption spectra of the OH stretching vibration, ν_{OH}, in different molecules. The OH group of phenol in C_2Cl_4 is a free group. For comparison, the corresponding absorption spectra of hydrogen-bonded systems are plotted below.

the covalent bond, often accompanied by the formation of a double-well potential with increased anharmonicity in each well. The anharmonicity increases with shorter hydrogen bond length r_{XY} which is defined as the distance between the X and the Y nucleus in the X–H$\cdots$Y structure. Since the energy of the hydrogen bond also increases with shorter r_{XY}, the XH stretching frequency is indicative of the strength of the hydrogen bond. It depends monotonously on r_{XY} over a wide range [29, 37–40]. However, the relation is not unambiguous because the XH stretching frequency depends to a lesser extent on the hydrogen bond angle, i.e. the angle in the X–H$\cdots$Y structure [41]. The hydrogen bond in water is considered a weak hydrogen bond whereas the one in acetic acid dimers is of intermediate strength with a hydrogen bond length of 2.68Å‡ [42]. Such moderately strong hydrogen bonds are typically dominated by electrostatic interactions [43, 44]. Theoretical modelling also suggests that deviations from linearity of the hydrogen bond increase the contribution of dispersion forces [45]. For very short hydrogen bond lengths below 2.35Å a potential with a single minimum is formed. In such systems, the eigenfrequency of the proton is in the range of 1000cm^{-1} to 1200cm^{-1} and the bond character is mainly covalent [46].

Apart from the evident red shift of absorption bands, the increased anharmonicity in hydrogen-bonded systems has several consequences [41] which are illustrated in Figure 1.4: (i) Solvent-solute interactions lead to faster dephasing times resulting in spectral broadening. (ii) Hydrogen bond vibrations efficiently couple to the XH stretching vibration, ν_{XH}, resulting in Franck-Condon progressions with one quantum of the ν_{XH} vibration

‡The ν_{OH} band of the acetic acid dimer dissolved in carbon tetrachloride is not significantly shifted to smaller frequencies as compared to the gas phase dimer, indicating a very similar hydrogen bond geometry in gas phase and apolar liquids.

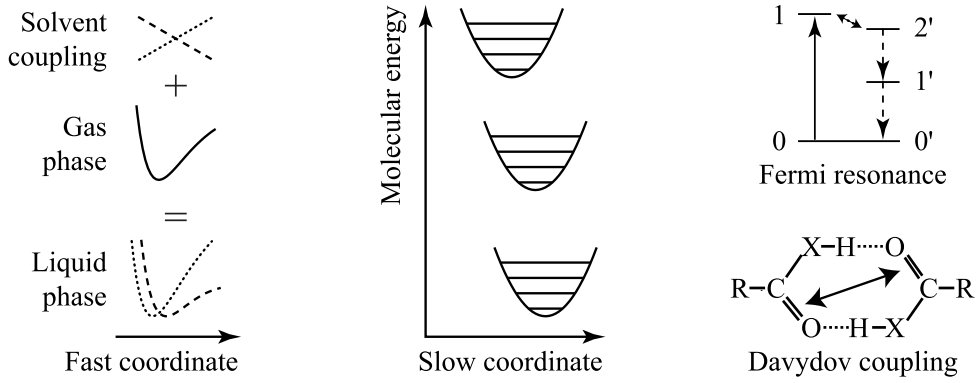

Figure 1.4: Consequences of hydrogen bonding: Line broadening (left), Franck-Condon progressions (centre), Fermi resonances (top right), Davydov coupling (bottom right).

and one or several quanta of the hydrogen bond vibrations. (iii) In systems with weak to intermediately strong hydrogen bonds the levels of the ν_{XH}vibrations are shifted into resonance with combination and overtones of other intramolecular vibrations (Fermi resonances) resulting in new energy relaxation pathways; in strong hydrogen bonds direct resonances between the ν_{XH}vibrations and intramolecular vibrations can have the same effect. (iv) In systems with several hydrogen bonds, (nearly) degenerate oscillators are coupled (Excitonic/Davydov coupling). These phenomena lead to complicated lineshapes [1], the understanding of which poses a scientific challenge in itself.

Linear spectroscopy cannot dissect the different contributions to the lineshapes and underlying intra- and intermolecular coupling mechanism nor can it characterise the system dynamics. Time-resolved nonlinear spectroscopy techniques are required to resolve optical responses on the time scale of nuclear motions. Because vibrational spectroscopy is particularly sensitive to structure, nonlinear vibrational spectroscopy is a powerful tool to study structural dynamics. In this thesis, ultrafast vibrational pump-probe and photon echo spectroscopy are used to investigate pure and isotopically diluted water as well as acetic acid dimers in apolar solvents. These two systems represent limiting cases of hydrogen-bonded systems in the liquid phase. The acetic acid dimer in an apolar solvent is a well-defined planar structure that is held together by two intermolecular hydrogen bonds. Its structural motif resembles the base pairs in B-type DNA. Liquid water is quite the opposite. It constitutes a rapidly fluctuating extended hydrogen-bonded network which has been extensively studied but still remains unknown to a relevant extent.

The thesis will give a brief introduction to theoretical concepts of nonlinear spectroscopy and two types of spectroscopic techniques in chapter 2. A description of the basic laser system and the different frequency conversion schemes follows in chapter 3 which also includes a detailed introduction to the experimental nonlinear spectrometers. Chapter 4 contains an extensive study of the acetic acid dimer. This model system has been widely discussed over many decades and this chapter addresses some fundamental issues about coupling mechanisms in hydrogen-bonded molecules that extend beyond this specific system. Results on pure and isotopically diluted water are presented in chapter 5. It is subdivided into two parts, one of which is the first study of ultrafast structural dynamics

in pure water by means of coherent two-dimensional infrared spectroscopy of the OH stretching vibration. The second part investigates the OH bending vibration and the high-frequency modes of the hydrogen bond network of pure water for the first time with spectrally resolved pump-probe spectroscopy. Both experimental chapters begin with a short historical account and try to give an overview of the many previous publications. Finally, a summary concludes this thesis.

2 Nonlinear spectroscopy

Bietet einerseits die Spektralanalyse [...] ein Mittel von bewunderungswürdiger Einfachheit dar, die kleinsten Spuren gewisser Elemente in irdischen Körpern zu entdecken, so eröffnet sie andererseits der chemischen Forschung ein bisher völlig verschlossenes Gebiet, das weit über die Grenzen der Erde, ja selbst unseres Sonnensystems, hinausreicht.

R. Bunsen und G. Kirchhoff*, 1860

Optical spectroscopy has proved long ago how powerful a tool it is to study matter and its interactions. In particular, linear absorption spectroscopy is a very efficient method but it will not reveal information on the evolution of the system under study. Such information is accessible when multiple interactions between the system and the interrogating light field occur, thereby allowing to follow dynamics in the system. It is the realm of nonlinear spectroscopy. This chapter will introduce basic concepts on which the analysis and conclusions of this work will rest. The chapter is based on Shaul Mukamel's book on nonlinear optical spectroscopy [47], the thesis of Erik Nibbering [48], and a lecture given by Peter Hamm [49].

2.1 Nonlinear polarisation

Electric fields such as laser pulses that interact with matter can induce transient polarisations. According to Maxwell's equations, such polarisations act as a source of propagating electromagnetic fields. The determination of these emitted fields is essentially a measurement of the induced polarisation which can be linked to properties of the quantum mechanical object. A common approach to describe a field-induced polarisation that does not depend linearly on the field intensity is the expansion in powers of the electric field [50]:

$$\begin{aligned} P_i(\omega) &= \chi^{(1)}_{ij}(\omega)E_j(\omega) + \chi^{(2)}_{ijk}(\omega,\omega_1,\omega_2)E_j(\omega_1)E_k(\omega_2) \\ &\qquad + \chi^{(3)}_{ijkl}(\omega,\omega_1,\omega_2,\omega_3)E_j(\omega_1)E_k(\omega_2)E_l(\omega_3) + \dots \\ &= P_i^{(1)}(\omega) + P_i^{(2)}(\omega) + P_i^{(3)}(\omega) + \dots, \end{aligned} \tag{2.1}$$

where P_i and E_i are the polarisation and electric field components, respectively. $\chi^{(n)}$ is the electric susceptibility tensor of order n. Together, they constitute the optical response in

*From the closing remarks of the treatise *Chemische Analyse durch Spektralbeobachtungen.*

the frequency domain. Here and in the following, summation is over all pair-wise indices according to Einstein's summation convention. ω determines the sum or difference of the field frequencies, e.g. $\omega = \omega_1 + \omega_2 - \omega_3$. It should be noted that high enough field intensities will cause the perturbative approach (2.1) to converge only for very high orders and a description in terms of Raby frequencies [51] is favourable. In the perturbative limit, optical phenomena can be grouped according to their field dependence. The nonlinear techniques that have been used in this work induce third-order polarisations and will be described in section 2.3.

Optical response functions

In quantum mechanics, the polarisation P_i is defined as the expectation value of the dipole operator μ_i and for a statistical ensemble such as molecules in solution, the system's state is most conveniently described by the density operator $\rho(t)$. The polarisation in the time-domain is then given by

$$P_i(t) = \langle \mu_i \rho(t) \rangle, \tag{2.2}$$

where $\langle O \rangle$ denotes the expectation value of the operator O. It is equal to the trace of the corresponding matrix representation. Thus, certain properties of the quantum object can be linked to the measured polarisation if $\rho(t)$ is known. The temporal evolution of the density operator is described by the Liouville-Von Neumann equation:

$$\frac{d}{dt}\rho = -\frac{i}{\hbar}\left[H, \rho\right] \tag{2.3}$$

which is the analogue of the Schrödinger equation for a quantum state vector description [52]. H is the Hamilton operator of the system and is generally not fully known. For many purposes, however, it suffices to consider only a subset of the system degrees of freedom.

In the following, the interaction between the electromagnetic field and the quantum system shall be limited to electric dipole interactions. Furthermore, the electromagnetic field is treated classically, i.e. the substitution $\hat{E}_i \rightarrow \langle \hat{E}_i \rangle = E_i(t)$ is made. The Hamiltonian is then given by

$$H(t) = H_0 - \mu_i E_i(t) \tag{2.4}$$

with H_0 as the Hamiltonian of the isolated system. In the simple case of a two-level system, the eigenvectors of the isolated system can be chosen as a complete basis set $\{|\,1\,\rangle, |\,2\,\rangle\}$. In this representation, the Liouville-Von Neumann equation becomes a set of coupled differential equations called the optical Bloch equations which describe the time evolution of the diagonal elements, ρ_{ii} (populations), and the off-diagonal elements, ρ_{ij} (polarisations), of the system:

$$\begin{aligned} \dot{\rho}_{11} &= +i\Omega_R^*\rho_{21} - i\Omega_R\rho_{12}, & \dot{\rho}_{12} &= +i\Omega_R^*(\rho_{22} - \rho_{11}) + i\omega\rho_{12}, \\ \dot{\rho}_{22} &= -i\Omega_R^*\rho_{21} + i\Omega_R\rho_{12}, & \dot{\rho}_{21} &= -i\Omega_R(\rho_{22} - \rho_{11}) - i\omega\rho_{21}, \end{aligned} \tag{2.5}$$

with

$$\begin{aligned} \hbar\omega &= 2H_{0,22} = -2H_{0,11} \\ \hbar\Omega_R &= E_i\mu_{i,12} = E_i\mu_{i,21}^* \,. \end{aligned} \tag{2.6}$$

The transition frequency between states $|\,1\,\rangle$ and $|\,2\,\rangle$ is ω and Ω_R is the so-called Rabi frequency.

If the interaction energy $\mu_i E_i$ is small compared to the transition energies of the isolated system, the relative change of the Hamilton operator's eigenvalues is small. This is true for the systems under study in this thesis. We can thus use perturbation theory to express the density operator in the cumulant expansion that allows linking higher order polarisations in (2.1) to terms in this expansion. For the cumulant expansion to converge, it is useful to transform from the Schrödinger picture to the interaction picture [52] by use of a unitarian time evolution operator:

$$\begin{aligned} U_0(t,t_0) &= \mathrm{e}^{-\frac{i}{\hbar}H_0(t-t_0)}, \\ \mu_i(t) &= U_0(t,t_0)\cdot\mu_i\cdot U_0^\dagger(t,t_0), \\ \rho_I(t) &= U_0^\dagger(t,t_0)\cdot\rho(t)\cdot U_0(t,t_0). \end{aligned} \tag{2.7}$$

In the Schrödinger picture, μ_i is time-independent, in the interaction picture it is not. For simplicity, the dipole operator in the interaction picture is denoted by $\mu_i(t)$.

The Liouville-Von Neumann equation (2.3) can be formally integrated and substituted into itself iteratively to yield the desired series in powers of E_i. In the interaction picture this cumulant expansion takes the form

$$\begin{aligned} \rho_I(t) \;=\; \rho_I(t_0) + \sum_{n=1}^{\infty}\left(-\frac{i}{\hbar}\right)^n \int_{t_0}^{t} d\tau_n \int_{t_0}^{\tau_n} d\tau_{n-1}\ldots\int_{t_0}^{\tau_2} d\tau_1\, E_{i_1}(\tau_1)\ldots E_{i_n}(\tau_n) \\ \times\;\big[\mu_{i_n}(\tau_n),\ldots\big[\mu_{i_1}(\tau_1),\rho(t_0)\big]\ldots\big]\,. \end{aligned} \tag{2.8}$$

The quantum mechanical expectation value is independent of the chosen representation, i.e. $\langle A\rangle = \langle A_I\rangle$, and by use of (2.2) and (2.8) the polarisation of order n is given by

$$\begin{aligned} P_i^{(n)}(t) \;=\; \left(-\frac{i}{\hbar}\right)^n \int_{-\infty}^{t} d\tau_n \int_{-\infty}^{\tau_n} d\tau_{n-1}\ldots\int_{-\infty}^{\tau_2} d\tau_1\, E_{i_1}(\tau_1)\ldots E_{i_n}(\tau_n) \\ \times\;\big\langle\mu_i(t)\,\big[\mu_{i_n}(\tau_n),\ldots\big[\mu_{i_1}(\tau_1),\rho(-\infty)\big]\ldots\big]\big\rangle\,. \end{aligned} \tag{2.9}$$

The unperturbed system does not evolve if subjected to H_0 and hence t_0 was set to $-\infty$ in (2.8). When a coordinate transformation is applied, such that $\tau_1 = 0$, $t_1 = \tau_2 - \tau_1$, $t_2 = \tau_3 - \tau_2, \ldots,$ $t_n = t - \tau_n$, the nonlinear polarisation can be written as a series of n convolutions of the electric fields and the expectation value $S^{(n)}$ of the nested commutators:

$$\begin{aligned} P_i^{(n)}(t) \;=\; \int_{-\infty}^{\infty} dt_n \,\ldots\int_{-\infty}^{\infty} dt_1\, E_{i_1}(t-t_n-\cdots-t_1)\ldots E_{i_n}(t-t_n) \\ \times\; S^{(n)}_{i,i_1,\ldots,i_n}(t_1,\ldots,t_n)\,. \end{aligned} \tag{2.10}$$

$S^{(n)}$ is the optical response function in the time domain. It contains Heaviside functions to obey causality:

$$\begin{aligned} S^{(n)}_{i,i_1,\ldots,i_n}(t_1,\ldots,t_n) \;=\; \left(-\frac{i}{\hbar}\right)^n \Theta(t_1)\ldots\Theta(t_n)\;\big\langle\mu_i(t_1+\cdots+t_n) \\ \times\;\big[\mu_{i_n}(t_1+\cdots+t_{n-1}),\ldots\big[\mu_{i_1}(0),\rho(-\infty)\big]\ldots\big]\big\rangle\,. \end{aligned} \tag{2.11}$$

Feynman diagrams

The optical response function is a sum of 2^{n-1} real† tensors of rank n+1, each of which consists of (n+1)-point dipole correlation functions $\langle \mu_i \mu_{i_n} \dots \mu_{i_1} \rho \rangle$. These tensors along with the possible field interactions represent different quantum paths often called Liouville space pathways (for details see [47]). They can be represented graphically by double-sided Feynman diagrams. There are four possible tensors for $n = 3$ with different combinations of dipole operators on the left and right of the density operator as shown below for a two-level system:

$$\begin{aligned} S^{(3)} &= i\,\hbar^{-3}\,\Theta(t_1)\Theta(t_2)\Theta(t_3)\,\Big[\big(\langle \mu_i \mu_{i_1} \rho \mu_{i_2} \mu_{i_3} \rangle + \langle \mu_i \mu_{i_2} \rho \mu_{i_1} \mu_{i_3} \rangle \\ &\qquad + \langle \mu_i \mu_{i_3} \rho \mu_{i_1} \mu_{i_2} \rangle + \langle \mu_i \mu_{i_3} \mu_{i_2} \mu_{i_1} \rho \rangle - h.c.\big)\Big] \\ &= i\,\hbar^{-3}\,\Theta(t_1)\Theta(t_2)\Theta(t_3)\,\sum_{\alpha=1}^{4}\{R_\alpha - R_\alpha^\dagger\} \end{aligned} \tag{2.12}$$

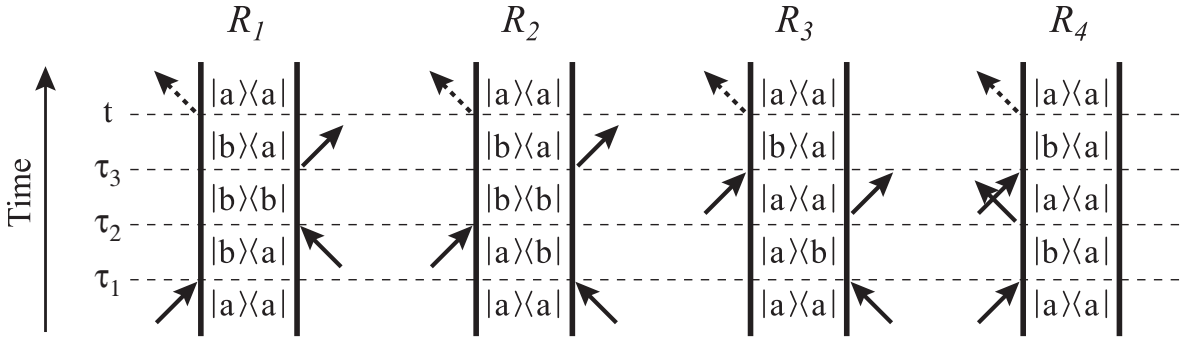

In these diagrams, time is running from bottom to top and vertical lines represent the time evolution of the bra and the ket of the ensemble state. Each arrow represents a complex field interaction and arrows that point toward the diagram mean an increase in the quantum number of the bra or the ket, arrows that point away from the diagram mean the opposite. An arrow to the right represents a complex field interaction with phase $\mathrm{e}^{-i(\omega t + k_i r_i)}$, an arrow to the left represents the complex conjugate. The directions of the arrows in the Feynman diagrams depend on resonance conditions and phase-matching and will be discussed in section 2.3. The overall sign of each diagram is given by $(-1)^p$ with p as the number of arrows on the right. The dashed arrow does not corresponds to a dipole interaction that is part of the nested commutators but represents the dipole operator in (2.2). It is associated with the emitted field whose k-vector and frequency are fixed by the sum of the three preceding field interactions. By convention, the dashed arrow points to the left.

Feynman diagrams are convenient to establish the relevant terms of optical response functions. Once the eigenstates of model Hamiltonians are known, resonance and phase-matching conditions exclude most of the possible field interactions and certain diagrams. In chapter 4 model calculations are presented which make use of this formalism.

†Physical observables such as $P_i^{(n)}$ only have real expectation values. This implies that for each tensor in the optical response function there exists a hermitian conjugate.

The reduced density matrix

Molecules in solution constitute a system with a large number of degrees of freedom, i.e. 10^{23} or more, and it is impossible to know the entire microscopic state. But often, a subset of the molecules' degrees of freedom, $|\, m \,\rangle$, is of interest. The surrounding solvent is treated as a thermal bath with eigenstates $|\, \beta \,\rangle$. The molecular subsystem can be described by a reduced density operator [53] and the elements of the corresponding density matrix are defined by:

$$\sigma_{mn} = \sum_{\beta} \langle\, \beta\, m \,|\, \rho \,|\, \beta\, n \,\rangle. \tag{2.13}$$

The diagonal elements of the reduced density matrix describe the population of the molecular states and the off diagonal ones the coherences between molecular states. The time-dependent interaction with the environment results in a decay of the populations and coherences. The decay of the coherences is usually called phase relaxation or simply dephasing. The loss of coherence is a manifestation of the time-dependent entropy s of the chosen subsystem:

$$\frac{ds}{dt} = kT \frac{d}{dt} \langle \sigma \ln \sigma \rangle \neq 0\,. \tag{2.14}$$

The density operator of the entire system commutes with the total Hamiltonian whereas the reduced density operator σ and any function thereof does not. Therefore, it is not constant in time (see Eq. 2.3) and neither is the reduced system's entropy s. Dephasing is only defined in the context of reduced systems.

2.2 Calculation of optical response functions

To model the response function, a suitable degree of freedom $|\, a \,\rangle$ is chosen, in the following referred to as the probe oscillator. This might be the OH stretching vibration of the acetic acid dimer. Its eigenfrequency shall be a function of the coordinates Q_i of the vibrational degrees of freedom it is coupled to. The latter are assumed to have a much lower eigenfrequency and therefore, the Born-Oppenheimer approximation [54] applies. The unperturbed Hamiltonian can then be written as

$$H_0 = \sum_{a} |\, a \,\rangle H_0^{(a)} \langle\, a \,|\,. \tag{2.15}$$

The operators $H_0^{(a)}$ will be a function of the coordinates Q_i. For a molecule in solution, the solvent modes constitute a fluctuating environment that affect the eigenenergies of an anharmonic oscillator. For two states of the probe oscillator, $|\, a \,\rangle$ and $|\, b \,\rangle$, the effect of this interaction can be described by an energy gap operator $G^{(ab)}$:

$$H_0^{(b)}(t) = H_0^{(a)} + \Delta_{ba} + G^{(ab)}(t), \tag{2.16}$$

where the average energy difference of the two states $\Delta_{ba} = \langle \epsilon_b - \epsilon_a \rangle$ is chosen such that $\langle G^{(ab)} \rho(-\infty) \rangle$ vanishes. For a given transition, $|\, a \,\rangle \rightarrow |\, b \,\rangle$, the dipole operator in the

interaction picture can be expanded to yield:

$$\begin{aligned}\mu_i^{(ab)}(t) &= \mathrm{e}^{\frac{i}{\hbar}H_0^{(a)}t}\mu_i\mathrm{e}^{-\frac{i}{\hbar}H_0^{(b)}t} \\ &= \mathrm{e}^{\frac{i}{\hbar}H_0^{(a)}t}\mu_i\mathrm{e}^{-\frac{i}{\hbar}H_0^{(a)}t}\mathrm{e}^{-\frac{i}{\hbar}\Delta_{ba}t}\,\exp_+\!\left(-\frac{i}{\hbar}\int_0^t d\tau\, G^{(ab)}(\tau)\right) \\ &= \mu_i\mathrm{e}^{-\frac{i}{\hbar}\Delta_{ba}t}\,\exp_+\!\left(-\frac{i}{\hbar}\int_0^t d\tau\, G^{(ab)}(\tau)\right).\end{aligned} \tag{2.17}$$

In the last step of (2.17) use was made of the fact that in the Born-Oppenheimer approximation the dipole operator is constant with respect to the other vibrational degrees of freedom. The expression $\exp_+(\ldots)$ is the positively time ordered exponential.

In the following, the rotating wave approximation will be used, i.e. only resonant transitions are considered because of the weak nonlinear susceptibilities and the strong resonant enhancement of signals in the investigated systems.

The cumulant approximation

In order to provide a link between the energy gap fluctuations of a transition and spectroscopic observables, it is useful to first consider the case of linear polarisation for a single transition. It is described by the two-point dipole correlation function

$$\langle\mu_i(t)\mu_j(0)\rho(-\infty)\rangle = \mu_i\mu_j\,\mathrm{e}^{\frac{i}{\hbar}\Delta t}\Big\langle\exp_+\Big[-\frac{i}{\hbar}\int_0^t d\tau\, G(\tau)\Big]\rho(-\infty)\Big\rangle\,. \tag{2.18}$$

The superscript $^{(ab)}$ that indexes the probe oscillator transition has been omitted for better readability. To approximate the expectation value of the time ordered exponential the following ansatz introduced by Magnus [55] is made:

$$\Big\langle\exp_+\Big[\lambda\int_0^t d\tau\, G(\tau)\Big]\rho(-\infty)\Big\rangle \;\stackrel{!}{\equiv}\; \exp\left[\sum_{n=1}^{\infty}\frac{\lambda^n}{n!}\,g_n(t)\right] \;\stackrel{\lambda=i/\hbar}{\equiv}\; \mathrm{e}^{-g(t)}. \tag{2.19}$$

This cumulant expansion defines the lineshape function $g(t)$ from which the absorption and emission spectra of the corresponding transition can be calculated (Eq. 2.34). Sorting in powers of λ identifies the $g_n(t)$ as time ordered integrals over n-point correlation functions of G. By definition of G, the linear term g_1 vanishes. Terms with $n > 2$ are taken to be zero which is exact for harmonic oscillators and systems with energy fluctuations that follow Gaussian statistics [47]. The cumulant approximation then leads to

$$g(t) = \frac{1}{\hbar^2}\int_0^t d\tau\int_0^\tau d\tau'\big\langle G(\tau')G(0)\rho(-\infty)\big\rangle \equiv \int_0^t d\tau\int_0^\tau d\tau' C(\tau'). \tag{2.20}$$

The two-point correlation of the energy gap operator is usually called the frequency fluctuation correlation function $C(t)$ and is a measure of the system's memory for its previous transition frequencies. It allows for the use of classical stochastic theories [56–58] and will be discussed in the context of the Brownian oscillator. Along the same lines, expressions

for the third-order response and the four tensors in (2.12) are found. They can be expressed by means of the same lineshape function over different time intervals and take the form

$$\begin{aligned}
R_1 &= \mu_{i_1}^{(ab)}\mu_{i_2}^{(ab)}\mu_{i_3}^{(ba)}\mu_{i}^{(ba)}\,\mathrm{e}^{-\frac{i}{\hbar}(\Delta_{ba}t_1+\Delta_{ba}t_3)} \\
&\qquad\times\ \mathrm{e}^{-g(t_1)-g^*(t_2)-g^*(t_3)+g(t_1+t_2)+g^*(t_2+t_3)-g(t_1+t_2+t_3)}, \\
R_2 &= \mu_{i_1}^{(ab)}\mu_{i_2}^{(ab)}\mu_{i_3}^{(ba)}\mu_{i}^{(ba)}\,\mathrm{e}^{+\frac{i}{\hbar}(\Delta_{ba}t_1-\Delta_{ba}t_3)} \\
&\qquad\times\ \mathrm{e}^{-g^*(t_1)+g(t_2)-g^*(t_3)-g^*(t_1+t_2)-g(t_2+t_3)+g^*(t_1+t_2+t_3)}, \\
R_3 &= \mu_{i_1}^{(ab)}\mu_{i_2}^{(ba)}\mu_{i_3}^{(ab)}\mu_{i}^{(ba)}\,\mathrm{e}^{+\frac{i}{\hbar}(\Delta_{ba}t_1-\Delta_{ba}t_3)} \\
&\qquad\times\ \mathrm{e}^{-g^*(t_1)+g^*(t_2)-g(t_3)-g^*(t_1+t_2)-g^*(t_2+t_3)-g^*(t_1+t_2+t_3)}, \\
R_4 &= \mu_{i_1}^{(ab)}\mu_{i_2}^{(ba)}\mu_{i_3}^{(ab)}\mu_{i}^{(ba)}\,\mathrm{e}^{-\frac{i}{\hbar}(\Delta_{ba}t_1+\Delta_{ba}t_3)} \\
&\qquad\times\ \mathrm{e}^{-g(t_1)-g(t_2)-g(t_3)+g(t_1+t_2)+g(t_2+t_3)-g(t_1+t_2+t_3)}.
\end{aligned} \tag{2.21}$$

$\Delta_{xy}/\hbar$ is the Lamor-frequency with which the phase of coherences evolves during the time interval t_i if the system is in state $|\,x\,\rangle\langle\,y\,|$. For $x = y$, Δ_{xy} is zero and has been omitted.

It is indeed remarkable that the second order cumulant approximation allows for the description of all linear and nonlinear spectroscopy since the optical response functions can be calculated from a single lineshape function and linear combinations thereof. However, the model cannot account for radiationless decay nor does it tell more about the nature of the bath modes that the probe oscillator is coupled to.

Coupling of discrete harmonic modes

Nuclear motions that couple to the probe transition can be incorporated in the lineshape function. Such motions are typically the normal modes of molecules but may also be arbitrary solvent modes. Following the pioneering theoretical work of Bratos and several others [59–63], a model Hamiltonian for a fast mode $\vec{q}$, a slow mode $\vec{Q}$, and a bath $\vec{x}_n$ will be used. In this Hamiltonian, the fast mode is coupled to the slow mode which in turn is coupled to the bath:

$$H_0 = \frac{\vec{p}^2}{2m} + \frac{m\omega_q^2(\vec{Q})\vec{q}^2}{2} + \frac{\vec{P}^2}{2M} + \frac{M\Omega^2(\vec{x}_n)\vec{Q}^2}{2} + \sum_n \frac{\vec{p}_n^2}{2m_n} + \frac{m_n\omega_n^2\vec{x}_n^2}{2}\,, \tag{2.22}$$

with the reduced masses m, m_n, and M and the eigenfrequencies ω_0, ω_n, and Ω. In general, the effective eigenfrequencies of the fast mode and the slow mode will depend on $\vec{Q}$ and the $\vec{x}_n$, respectively, regardless of the specific type of interaction between the coupled oscillators:

$$\omega_q(\vec{Q}) = \omega_0 + \frac{d\omega_q}{d\vec{Q}}\vec{Q} + O(\vec{Q}^2) \tag{2.23}$$

$$\Omega(\vec{x}_n) = \Omega_0 + \sum_n \frac{d\Omega}{d\vec{x}_n}\vec{Q} + O(\vec{x}_n^2). \tag{2.24}$$

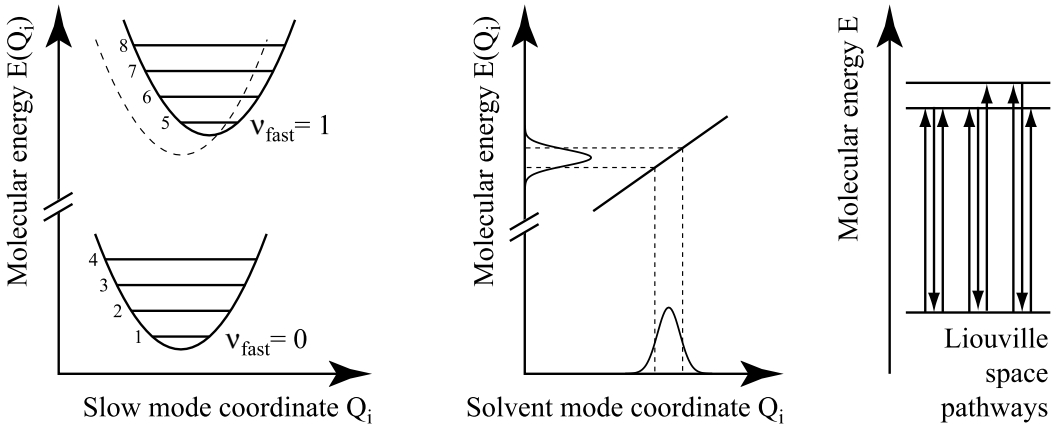

Figure 2.1: Potential energy surfaces for two coupled harmonic oscillators in the Born-Oppenheimer approximation (left), energy gap fluctuations due to linear coupling of the probe oscillator to an overdamped Brownian oscillator (centre), and Liouville space pathways for a three-level system (right).

When approximating to first order, the Hamiltonians $H_0^{(a)}$ of the slow mode are linearly displaced harmonic oscillators as shown on the left of Figure 2.1. For the ground and first excited state of the probe oscillator, they take the form:

$$\begin{aligned} H_0^{(0)} &= \frac{\hbar\Omega}{2}\big[\mathbf{P}^2+\mathbf{Q}^2\big], \\ H_0^{(1)} &= \frac{\hbar\Omega}{2}\big[\mathbf{P}^2+\mathbf{Q}^2\big]+\hbar\omega_q(\mathbf{Q}) \\ &\approx \frac{\hbar\Omega}{2}\big[\mathbf{P}^2+\mathbf{Q}^2+2\mathbf{D}\mathbf{Q}\big]+\hbar\omega_0. \end{aligned} \tag{2.25}$$

Dimensionless momentum, position, and displacement operators have been introduced by rescaling the original operators:

$$\mathbf{P}=\frac{\vec{P}}{\sqrt{M\Omega\hbar}}, \qquad \mathbf{Q}=\sqrt{\frac{M\Omega}{\hbar}}\,\vec{Q}, \qquad \mathbf{D}=\sqrt{\frac{\hbar}{M\Omega}}\,\frac{1}{\Omega}\frac{d\omega_q}{d\vec{Q}}, \qquad F=\frac{\mathbf{D}^2}{2}. \tag{2.26}$$

F is the Huang-Rhys factor which determines the amplitude of the system's lineshape function. The corresponding time correlation function is best determined via its Fourier transform which is called the spectral density. It can be calculated analytically [47]:

$$\begin{aligned} \tilde{C}(\omega) &= iF\left[\frac{\bar{n}_\omega+1}{(\Omega-\omega)(\Omega+\omega)+i\omega\gamma(\omega)}-\frac{\bar{n}_\omega+1}{(\Omega-\omega)(\Omega+\omega)-i\omega\gamma(\omega)}\right]\Omega^3, \\ \gamma(\omega) &= \pi\sum_n \frac{\vec{k}_n^2}{2m_n\omega_n^2}\,\delta(\omega-\omega_n), \qquad \bar{n}_\omega=\left(\mathrm{e}^{\beta\hbar\omega}-1\right)^{-1}, \qquad \beta=1/kT, \end{aligned} \tag{2.27}$$

where T is the absolute temperature and k is the Boltzmann constant. In classical stochastic theory, $\gamma(\omega)$ is the Fourier transform of a non-Markovian friction $\tilde{\gamma}(t)\neq\gamma\delta(t)$

that implies a stochastic driving force of Brownian motion with a finite correlation time [64, 65]. In the Markovian limit, the friction is δ-like and the damping term γ is constant.

By performing contour integration and taking the frictionless limit $\gamma \to 0$ the spectral density of an undamped slow mode can be retrieved: The corresponding lineshape function is calculated from (2.20) by inserting $\int \tilde{C}(\omega)\mathrm{e}^{-i\omega\tau'}$ and permuting the order of integration:

$$\tilde{C}(\omega) = F\Big[(\bar{n}_\omega + 1)\delta(\Omega - \omega) + \bar{n}_\omega\delta(\Omega + \omega)\Big]\Omega^2, \tag{2.28}$$

$$g(t) = F\Big[(\bar{n}_\Omega + 1)(1 - \mathrm{e}^{-i\Omega t}) + \bar{n}_\Omega(1 - \mathrm{e}^{i\Omega t})\Big]. \tag{2.29}$$

The extension to several normal modes is straight forward since the total correlation function is a linear superposition of the individual ones.

Continuous distributions of oscillators

A molecule in solution is usually coupled to a very large number of bath modes. For such systems, it is often possible to represent the bath by a continuous distribution of harmonic oscillators that couple linearly to the probe oscillator [66, 67]. The corresponding Hamiltonian can be written as follows:

$$H_0 = \frac{\vec{p}^2}{2m} + \int_0^\infty d\Omega\varrho(\Omega)\left[\frac{m\omega_q^2(\vec{Q}(\Omega))\vec{q}^2}{2} + \frac{\vec{P}^2(\Omega)}{2M(\Omega)} + \frac{M(\Omega)\Omega^2\vec{Q}^2(\Omega)}{2}\right] \tag{2.30}$$

Interestingly, an infinite number of undamped harmonic oscillators is equivalent to one overdamped Brownian oscillator. The name of the latter stems from the fact that the equation of motion of the high frequency oscillator's nuclear coordinate coincides with the Langevin equation of a Brownian particle in an external force field [64]. If the number of degrees of freedom N is very large, i.e. $N \to \infty$, the central limit theorem implies a Gaussian statistical distribution of the corresponding nuclear coordinates as depicted in the centre of Figure 2.1. The driving force in the quantum Brownian oscillator model is represented by the coupling to the large number of bath modes. To model the lineshape function, (2.27) is recast to a common denominator; the spectral density of the Brownian oscillator yields [47]

$$\begin{aligned}\tilde{C}(\omega) &= 2F\Omega(\bar{n}_\omega + 1)\,\frac{\omega\Omega^2/\gamma}{\omega^2 + (\Omega^2/\gamma - \omega^2/\gamma)^2} \\ &\overset{\gamma\gg\Omega}{=} 2\,\lambda\,(\bar{n}_\omega + 1)\,\frac{\omega\Lambda}{\omega^2 + \Lambda^2}.\end{aligned} \tag{2.31}$$

where the bottom row is the strong coupling approximation with $\lambda = F\Omega$ as the magnitude of the energy gap fluctuations and $\Lambda = \Omega^2/\gamma$ as the inverse correlation time of the bath dynamics. This spectral density is identical to the one in (2.27) that results from the coupling in (2.22). In the Markovian limit, γ is constant and the corresponding correlation and lineshape functions can be calculated analytically [47, 65]. In the high temperature

limit they are:

$$C(t) \overset{\beta\hbar\Lambda\ll 1}{=} \Delta^2 \mathrm{e}^{-\Lambda t} + i\lambda\Lambda \mathrm{e}^{-\Lambda t} \tag{2.32}$$

$$g(t) \overset{\beta\hbar\Lambda\ll 1}{=} \frac{\Delta^2}{\Lambda^2}\left(\mathrm{e}^{-\Lambda t} + \Lambda t - 1\right) - i\frac{\lambda}{\Lambda}\left(\mathrm{e}^{-\Lambda t} - 1\right), \tag{2.33}$$

with $\Delta^2 = 2\lambda/\beta\hbar$. A note should be made on the time dependence of the imaginary part that differs from reference [47]: the time ordered integration in (2.20) allows adding a constant when performing the inner integration. This cancels the extra linear term in t and results in a frequency shift that leads to the symmetric expressions for absorption and emission spectra commonly used:

$$\sigma_a(\omega) = \frac{1}{2\pi}\,\Re\int_{-\infty}^{\infty} dt\, \mathrm{e}^{i(\omega-\omega_q)t - g(t)}, \tag{2.34}$$

$$\sigma_e(\omega) = \frac{1}{2\pi}\,\Re\int_{-\infty}^{\infty} dt\, \mathrm{e}^{i(\omega-\omega_q)t - g^*(t)}. \tag{2.35}$$

The relative frequency shift 2λ of the maxima of σ_a and σ_e is the well-known Stokes shift.

When the imaginary part of (2.33) is neglected, the lineshape model of Kubo [56] is retrieved which interpolates between two important limiting cases: In the slow modulation (static) limit, the correlation time Λ^{-1} of the bath dynamics is long compared to the dephasing process of the probed transition. Line broadening is inhomogeneous and the absorption and emission profiles are Gaussians:

$$\Lambda \ll \Delta \quad \Rightarrow \quad C(t) = \Delta^2 \quad \text{and} \quad g(t) = \frac{1}{2}\Delta^2 t^2. \tag{2.36}$$

In the fast modulation limit, the bath modes modulate the transition frequency so quickly that the radiation field couples to an average transition. Line broadening is homogeneous (motional narrowing) and the absorption and emission profiles are Lorentzians:

$$\Lambda \gg \Delta \quad \Rightarrow \quad C(t) = \delta(t) \quad \text{and} \quad g(t) = \Gamma t - 1 \tag{2.37}$$

with $\Gamma = \lambda/\beta\hbar\Lambda$. When the two limiting cases are combined, the Bloch model is retrieved [68] that features an infinitely short homogeneous and an infinitely long inhomogeneous contribution to the correlation function:

$$C(t) = \frac{\delta(t)}{T_2^*} + \Delta^2 \quad \text{and} \quad g(t) = \frac{t}{T_2^*} + \frac{1}{2}\Delta^2 t^2. \tag{2.38}$$

T_2^* is called the pure dephasing time and Δ the static inhomogeneity.

As already mentioned in chapter 1, vibrational spectroscopy permits linking structural dynamics to transition frequency changes. This means that structural correlations and dynamics can be inferred from the frequency correlation function. The latter can in principle be determined from the decay of the echo peak shift described in the next section.

Advanced lineshape functions

The OH stretching vibration is the main probe of vibrational spectroscopy when hydrogen-bonded systems are studied. This vibration is particularly sensitive to hydrogen bonding and it becomes strongly anharmonic upon formation of an O–H$\cdots$O bond. The Hamiltonian (2.22) is quite a simple model for the fast oscillator to which slow modes couple and several refinements have been suggested [69–71]. The approach by Rösch and Ratner [70] models an ionic hydrogen-bonded system of the form X–H$\cdots$Y$^-$ in a solvent. The phase relaxation of the fast mode is caused by dipole interactions between the XH dipole $\vec{\mu}$ and the fluctuating electric field $\vec{E}_S(t)$ of the solvent with correlation time Λ^{-1}:

$$H_S = \vec{\mu}\cdot\vec{E}_S(t) \quad \text{and} \quad \langle E_S(t)E_S(0)\rangle = E_S^2 \mathrm{e}^{-\Lambda|t|}. \tag{2.39}$$

The ionic vibrations that modulate the hydrogen bond were assumed to be negligibly perturbed by the fluctuating environment, i.e. the ionic coordinate $\vec{Q}$ commutes with H_S. Thus, the lineshape function consists of two terms, one of which is identical to (2.27). The other one reflects the coupling between the XH stretching mode and solvent electric field and is given by

$$g_S(t) = 2\varepsilon^2 \int_0^t d\tau\,(t-\tau)\cos\bigl(2F\sin(\Omega\tau)\bigr)\,\mathrm{e}^{i\omega\tau-\Lambda\tau-2F[2\bar{n}_\Omega+1][1-\cos(\Omega\tau)]} \tag{2.40}$$

with $\varepsilon = \vec{\mu}\cdot\vec{E}_S$. All other symbols are identical to (2.26). Bratos, Witkowski, and Maréchal have all published theoretical work that incorporates Fermi resonances in the lineshape function [62, 72, 73]. Finally, Henri-Rousseau and coworkers considered several partial models for solvent interactions, hydrogen bond modes, and Fermi resonances and combined them to formulate a more general lineshape function [74, 75].

Summing over states

Discrete modes may also be taken into account by summing over all relevant Liouville space pathways of the density of discrete states [76] as pictured on the right of Figure 2.1. It is of advantage when calculating an optical response with no analytic lineshape function available. Typically, molecular dynamics (MD) simulations deliver the eigenstates and transition dipole moments of the molecular system from which theoretical data can be generated and compared to experimental data. The liquid environment that surrounds the molecular system is still treated as a bath and the system-bath coupling is incorporated in the lineshape function.

The vibrational response of the acetic acid dimer in gas phase and apolar solvents has been modelled by this approach with a lineshape function that is linear in time [77, 78]. It is generally not true but a valid assumption for this system because the broadening of the vibrational transitions is predominantly homogeneous (p. 69) and thus described by (2.37). Furthermore, an energetic multi-level structure is assumed instead of a two-level

system. Then, equations 2.21 become

$$\begin{aligned}
R_1 &= \sum_{a,b,c,d} P(a)\,\mu_{i_1}^{(ab)}\mu_{i_2}^{(ac)}\mu_{i_3}^{(cd)}\mu_{i}^{(bd)}\,\mathrm{e}^{-(\frac{i}{\hbar}\Delta_{ba}+f_{ba})t_1}\,\mathrm{e}^{-(\frac{i}{\hbar}\Delta_{bc}+f_{bc})t_2}\,\mathrm{e}^{-(\frac{i}{\hbar}\Delta_{bd}+f_{bd})t_3},\\
R_2 &= \sum_{a,b,c,d} P(a)\,\mu_{i_1}^{(ab)}\mu_{i_2}^{(ac)}\mu_{i_3}^{(bd)}\mu_{i}^{(cd)}\,\mathrm{e}^{-(\frac{i}{\hbar}\Delta_{ab}+f_{ab})t_1}\,\mathrm{e}^{-(\frac{i}{\hbar}\Delta_{cb}+f_{cb})t_2}\,\mathrm{e}^{-(\frac{i}{\hbar}\Delta_{cd}+f_{cd})t_3},\\
R_3 &= \sum_{a,b,c,d} P(a)\,\mu_{i_1}^{(ab)}\mu_{i_2}^{(bc)}\mu_{i_3}^{(ad)}\mu_{i}^{(dc)}\,\mathrm{e}^{-(\frac{i}{\hbar}\Delta_{ab}+f_{ab})t_1}\,\mathrm{e}^{-(\frac{i}{\hbar}\Delta_{ac}+f_{ac})t_2}\,\mathrm{e}^{-(\frac{i}{\hbar}\Delta_{dc}+f_{dc})t_3},\\
R_4 &= \sum_{a,b,c,d} P(a)\,\mu_{i_1}^{(ab)}\mu_{i_2}^{(bc)}\mu_{i_3}^{(cd)}\mu_{i}^{(da)}\,\mathrm{e}^{-(\frac{i}{\hbar}\Delta_{ba}+f_{ba})t_1}\,\mathrm{e}^{-(\frac{i}{\hbar}\Delta_{ca}+f_{ca})t_2}\,\mathrm{e}^{-(\frac{i}{\hbar}\Delta_{da}+f_{da})t_3}.
\end{aligned} \tag{2.41}$$

The coefficients f_{xy} are generally complex and depend on the state $|\,x\,\rangle\langle\,y\,|$ of the system. $P(a)$ is the population probability of state $|\,a\,\rangle\langle\,a\,|$ and for an ensemble in thermal equilibrium the Boltzmann-factor applies:

$$P(a) = \frac{\mathrm{e}^{-\beta E_a}}{\sum_a \mathrm{e}^{-\beta E_a}}\,, \qquad \beta^{-1} = kT. \tag{2.42}$$

The summation can be limited to (i) transitions that lie within the spectral bandwidth of the electric fields, (ii) transitions with significant dipole moments, and (iii) states for which $P(a)$ is of relevant magnitude. A possible counting of states is indicated on the left of Figure 2.1. For normal modes the sum over all states can be reduced to a product of sums each of which runs over the states of a single normal mode, i.e. $\Sigma_{a,b,c,d} = \Pi_j \Sigma_{a_j,b_j,c_j,d_j}$, where the subscript j means that summation is restricted to the state vectors of each normal mode. The matrix elements of the dipole operators $\mu_i^{(ab)}$ in (2.41) may be approximated by the Franck-Condon factors‡ $|\Gamma_i^{(ab)}|^2$ for two states of the slow mode with [79]

$$\Gamma_i^{(ab)}(\mathrm{D}_i) = \mathrm{e}^{-\mathrm{D}_i^2/2}\,\mathrm{D}_i^{a+b}\sqrt{a!b!}\sum_{k=0}^{\mathrm{Min}(a,b)}\frac{(-1)^{\mathrm{Min}(a,b)+k}\,\mathrm{D}_i^{-2k}}{k!(a-k)!(b-k)!}\,. \tag{2.43}$$

Most often resonant enhancement is exploited to induce polarisations. Thus, the rotating wave approximation is used in many cases and summation needs only be over states between which resonant transitions can occur.

2.3 Third-order spectroscopic techniques

In principle, all spectroscopic information is contained in the linear absorption spectrum. But various coupling mechanisms of an oscillator to its surrounding may congest and broaden its absorption line such that it is impossible to dissect the different contributions. Multi-dimensional spectroscopy exploits multiple interactions between matter and light fields that offer many more experimental parameters than linear spectroscopy, e.g.

‡Some authors refer to the Franck-Condon factor as the amplitude of the transition probability.

multiple polarisation and propagation directions, spectral position and bandwidth, and temporal duration and time delays between field interactions. In this thesis acetic acid dimers in carbon tetrachloride as well as pure and isotopically mixed water have been studied with pump-probe and photon echo spectroscopy. The application of these two nonlinear techniques permit to gain further understanding of molecular dynamics, coupling mechanisms and transient structures.

Pump-probe spectroscopy

The pump-probe technique employs a strong pump pulse, E_{pump}, to induce an optical transition in the sample that is monitored by a delayed weak pulse called the probe pulse, E_{probe}. The latter passes through the sample at a slightly different angle to separate it from the pump pulse thereby selecting only certain Liouville space pathways that contribute to the detected signal. The induced transient third-order polarisation, $P^{(3)}$, will generate an electromagnetic field, E_{signal}, that propagates parallel to the probe pulse. The probe pulse and the emitted field are then either directly interfered on a detection device or spectrally dispersed by an optical grating and their spectral components interfered on an array of detection devices as sketched in Figure 2.2.

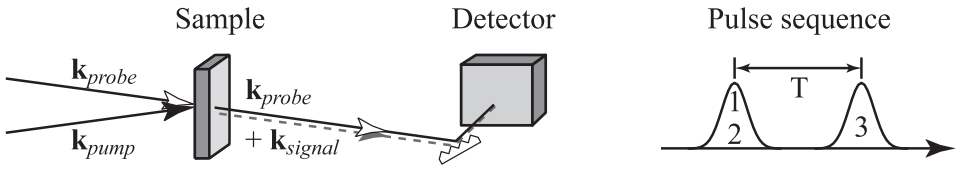

Figure 2.2: Schematic arrangement of **k**-vectors in a pump-probe experiment. The probe pulse acts as a reference field for heterodyne detection of the third-order signal.

The method of detecting a frequency-modulated electromagnetic field by non-linear mixing with a reference field is called heterodyne detection[§]. Variations of the temporal delay T between the two pulses, called the population time, allow to follow the transient transmission changes due to the optically triggered coherent and incoherent processes. When the emitted field is weak compared to the probe pulse, the corresponding transmission change is given by

$$\begin{aligned}\Delta\mathrm{T}(T,\omega) &= \frac{I(T,\omega)-I_0(\omega)}{I_0(\omega)} = \frac{\int_G dt|E_{probe}(\omega)+E_{signal}(T,\omega)|^2}{\int_G dt|E_{probe}(\omega)|^2}-1 \\ &\approx \frac{2\int_G dt\,\Re\{E_{probe}(\omega)E^*_{signal}(T,\omega)\}}{\int_G dt|E_{probe}(\omega)|^2}. \end{aligned} \tag{2.44}$$

I and I_0 are the total transmitted probe pulse intensities with and without excitation (pump pulse unblocked and blocked). $\Re$ denotes the real part of a complex number and

§In spectroscopy, the term *heterodyne* is not always used in the original sense of radio technology where it refers to the reference field's frequency being different from that of the signal. Furthermore, the term *homodyne* erroneously but often refers to spectrally integrated signal detection without a reference field.

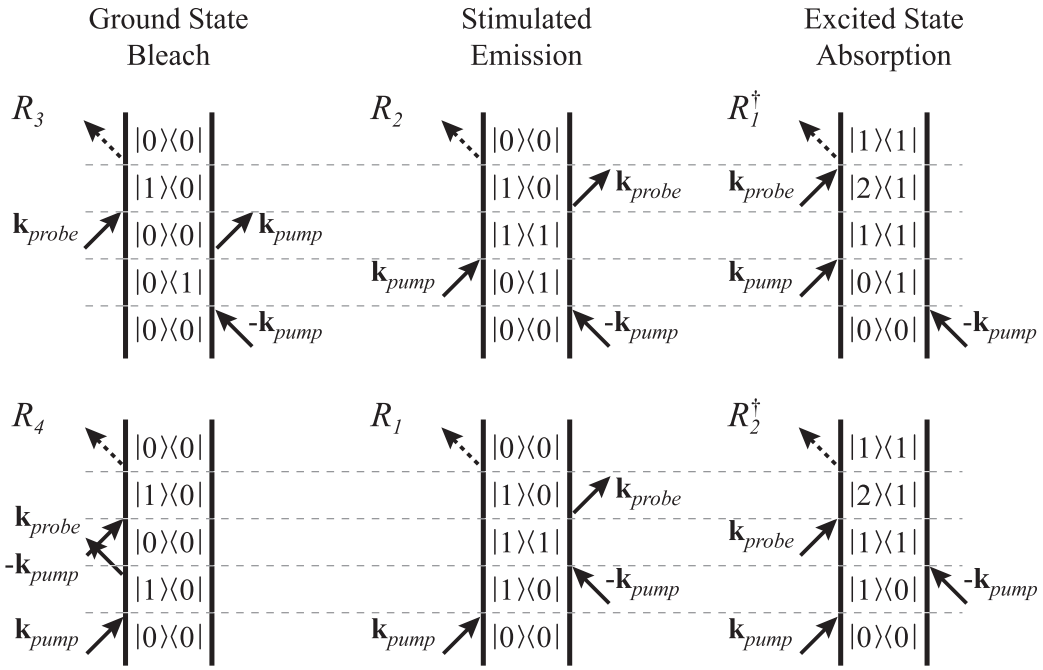

Figure 2.3: The six Feynman diagrams that contribute to the pump-probe signal of a three-level system for temporally separated pulses. Two of each represent ground state bleaching, stimulated emission and excited state absorption, respectively.

G the time gate of the electronic integrators. It comprises the support of E_{probe} and E_s. In the following, the absorbance change $\Delta A = -\log(\Delta \mathrm{T})$ will be used as the measured signal. Note that increased transmission yields a negative absorbance change and decreased transmission yields a positive absorbance change.

The optical interactions that lead to the third-order polarisation can be described by perturbation theory because interaction energies are small [80]. Since the pump and the probe pulse are non-collinear, only Liouville space pathways will contribute to the signal that fulfil the phase-matching condition $\mathbf{k}_{signal} = \mathbf{k}_{probe}$. For a three-level system and a pump pulse that precedes the probe pulse the possible quantum pathways are pictured by the Feynman diagrams in Figure 2.3. They can be identified as bleaching of the probe oscillator's ground state, stimulated emission from and absorption of the first excited state. It is instructive to consider the response function of a homogeneously broadened oscillator with a linewidth Γ:

$$S^{(3)}(\tau=0, T=0, t) = \frac{i}{\hbar^3}\left(4\mu_{01}^4 \mathrm{e}^{-i\omega_{10}t} - 2\mu_{01}^2\mu_{21}^2 \mathrm{e}^{-i\omega_{21}t}\right)\mathrm{e}^{-\Gamma t}, \tag{2.45}$$

with the transition dipole moments μ_{01} and μ_{21} and transition frequencies ω_{01} and ω_{21}. Let the pump and probe pulses be short compared to the lifetime and the dephasing time such that δ-like pulses can be assumed and $P^{(3)} \propto S^{(3)}$. This also justifies setting τ=0. Then, the absorbance change will be of Lorentzian shape:

$$\Delta A(T=0, \omega) \propto -\frac{8\mu_{01}^4}{(\omega_{10}-\omega)^2+\Gamma^2} + \frac{4\mu_{01}^2\mu_{21}^2}{(\omega_{21}-\omega)^2+\Gamma^2}. \tag{2.46}$$

The negative term is the sum of ground state bleaching and stimulated emission and the positive one is the excited state absorption. The latter is typically red-shifted in anharmonic oscillators and vanishes with the decay of the excited state population. It therefore gives direct access to the time constants of energy relaxation. Stimulated emission also decays with the lifetime of the excited state population, yet it cannot be distinguished spectrally from ground state bleaching. The bleach recovery dynamics will involve additional energy relaxation processes such as thermalisation in liquids: the immediate environment of the relaxed oscillator has accepted the absorbed energy. Depending on the coupling to the surroundings the transition energy of the relaxed oscillator has shifted and only regains its original value after thermal equilibrium of the probe volume has been reached.

Pump-probe spectroscopy measures population differences. For harmonic oscillators $\omega_{21} = \omega_{10}$ and $\mu_{12} = \sqrt{2}\mu_{01}$. It implies that ground state bleaching, stimulated emission, and excited state absorption cancel, i.e. $\Delta A(\omega) = 0$. This does not pose a problem in Raman-spectroscopy which is sensitive to individual level populations [81]. Fortunately, most vibrational oscillators are at least slightly anharmonic. This is particularly true for hydrogen-bonded systems [1, 82]. The degree of anharmonicity, $\Delta_{10} - \Delta_{21}$, varies and is most pronounced for stretching vibrations of hydrogen-bonded XH groups.

When the time order is reversed, i.e. $T < 0$, a signal will be generated that rises at the rate of the inverse dephasing time of the transition for $T \to 0$. This signal is the perturbed free induction decay¶ [83, 84]. It is caused by the excitation of a coherent polarisation and can only be observed in spectrally resolved pump-probe measurements, the spectral integral vanishes. More contributions arise during pulse overlap that have been termed 'coherent artifact'. These signals partially stem from quantum pathways in which the $\mathbf{k}_{probe}$-interaction occurs between the two $\mathbf{k}_{pump}$-interactions and from optical Kerr effect induced refractive index changes [50] that shift the probe pulse spectrum. The latter phenomenon is called cross-phase modulation in analogy to the self-phase modulation of light fields in media with large nonlinear coefficients.

The pump-probe technique is a powerful spectroscopic method that is fairly intuitive. It can reveal information on lifetimes, vibrational cooling, anharmonic coupling, spectral diffusion, energy transfer, and rotational dynamics [85]. It can measure vibrational wave packets dynamics that stem from coherent superpositions of quantum states corresponding to coherent intra- and intermolecular nuclear motions. However, it cannot recover the correlation functions previously discussed that provide a deeper insight into line broadening.

Photon echo spectroscopy

This spectroscopy technique owes its name to the analogous spin echo in magnetic resonance spectroscopy: the recurrence of an initial macroscopic polarisation called the photon echo[86]. A real echo only occurs in inhomogeneous ensembles in which a field interaction has created a macroscopic polarisation. The phases of the microscopic polarisations of the ensemble members evolve with different Lamor-frequencies and the macroscopic sum of these polarisations vanishes although each excited oscillator is still in a polarisation state

¶For historic reasons, the term *induction* is used instead of *polarisation* because the analogous phenomena in magnetic resonance spectroscopy were observed earlier than in electronic or vibrational spectroscopy.

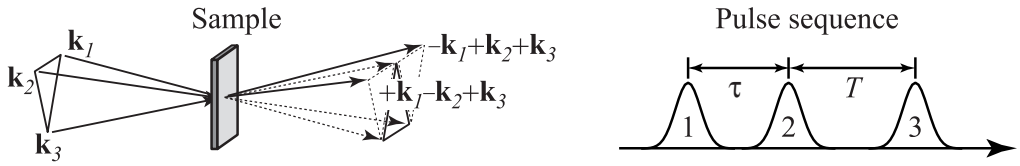

Figure 2.4: Schematic arrangement of the **k**-vectors and the pulse sequence in a three-pulse photon echo experiment. The directions for the real ($\mathbf{k}_3+\Delta\mathbf{k}_{21}$) and the virtual echo ($\mathbf{k}_3-\Delta\mathbf{k}_{21}$) are separated by twice the grating vector $\Delta\mathbf{k}_{21}=\mathbf{k}_2-\mathbf{k}_1$.

with well-defined phase. After a time τ, called the coherence time, a second and third field interaction reverse the time evolution and the macroscopic polarisation recurs after twice the time τ – just like an echo. For homogeneously broadened transitions no echo will occur. Instead, the induced polarisation will decay freely and the process is referred to as the free induction decay as opposed to the perturbed one mentioned above. Nonetheless, the term 'photon echo' will also be used for such cases throughout this thesis. Photon echo spectroscopy with identical pulses is often called degenerate four-wave mixing but the latter term also applies to pump-probe spectroscopy and spectral hole burning experiments with continuous-wave lasers were no echo occurs. Considering the large bandwidth of ultrashort pulses, the ultrafast photon echo spectroscopy is degenerate in the sense that the three pulses are not independently tunable. Furthermore, the investigated systems in this thesis have such broad absorption bands that only one band at a time is covered by the spectral bandwidth of the pulses.

The phase-matching direction in photon-echo experiments is not parallel to any of the incident pulse propagation directions as shown in Figure 2.4. The signal direction can be understood in terms of diffractive optics: the first two interactions create a transient grating with a grating vector that is the difference of their **k**-vectors and the third interaction is a diffraction into the first orders of that grating. The grating is a spatial one for $\tau=0$, similar to holographic gratings, and is a frequency grating for $\tau\neq 0$ with a grating constant of τ^{-1}. A photon echo can be measured with two pulses but usually three pulses are used so that the time interval between the second and the third interaction can also be controlled.

The two signal directions of interest are described by different sets of Feynman diagrams displayed in Figure 2.5. The diagrams $R_1^{\dagger}$, R_2, and R_3 in the top row have Lamor-frequencies of opposite sign in the first time interval τ and last time interval t. As a consequence, an ensemble of oscillators with a distribution of Lamor-frequencies dephases during τ but rephases during t. These diagrams are called the rephasing diagrams and constitute the photon echo. The signal direction of the photon echo is $\mathbf{k}_3+\mathbf{k}_2-\mathbf{k}_1$. The diagrams in the bottom row are non-rephasing and constitute the so-called virtual echo with the signal direction $\mathbf{k}_3-\mathbf{k}_2+\mathbf{k}_1$.

Three experimental time delay scans have to be distinguished. When the first time delay (coherence time τ) is varied and $T=0$, a (two-pulse) photon echo is measured, varying τ with $T\neq 0$ constitutes a three-pulse photon echo. When $\tau=0$ while varying the second time delay (population time T), a transient grating is measured. Next, the photon echo

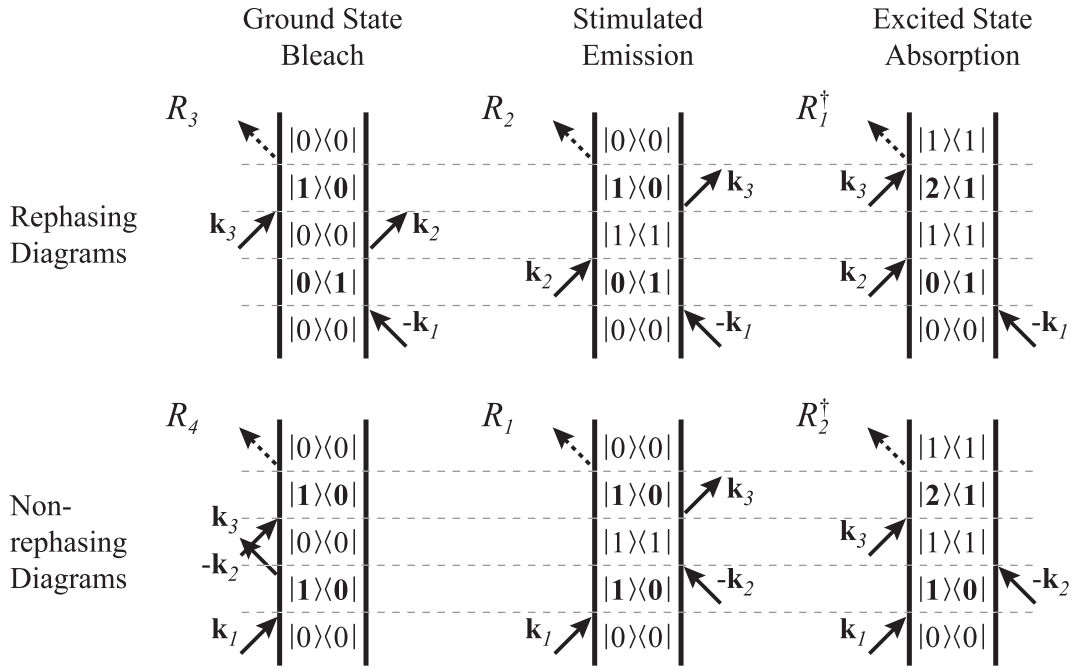

Figure 2.5: The six rephasing and non-rephasing Feynman diagrams of a photon-echo experiment. For the rephasing diagrams the ensemble state in the third time period $|x\rangle\langle y|$ is just the adjoint state of the first time period

signal in the Bloch model (Eq. 2.38) is discussed. The corresponding optical response of an inhomogeneous ensemble of three-level systems can be calculated from (2.21) and (2.38):

$$S^{(3)}(\tau, T=0, t) = \frac{i}{\hbar^3}\left(4\mu_{01}^4 \mathrm{e}^{-i(\omega_{10}(t-\tau)} - 2\mu_{01}^2\mu_{21}^2 \mathrm{e}^{-i(\omega_{21}t-\omega_{10}\tau)}\right) \mathrm{e}^{-\Delta^2(t-\tau)^2/2-\Gamma(t+\tau)}. \quad (2.47)$$

Equation 2.47 reveals some interesting properties of a photon echo. For a given time delay τ the signal is maximal and the phase is zero for $t=\tau$. This is the echo condition. The time-integrated intensity $\int dt|S^{(3)}(\tau,T,t)|^2$ does not have its maximum at $\tau = 0$. This peak shift is a measure of the initial spectral inhomogeneity and its decay is related to spectral diffusion. In Figure 2.6, the modulus squared of the optical response, $|S^{(3)}|^2$, is plotted as a function of t for different values of τ. The emitted signal decays so rapidly that although the peak intensity is largest for $\tau = 0$, the integral is not. The latter is plotted in the same graph (dotted line) as a function of τ. For $\tau = 0$ the polarisations of all excited oscillators have the same phase and similar to diffusive processes this phase distribution will quickly spread during the time period t without any rephasing. For $\tau > 0$, the phase distribution has broadened during the coherence time τ and rephases during t. The temporal shape of the emitted signal is Gaussian with a characteristic width Δ^{-1}. If no coherence decay occurred, the maximum signal would be measured for coherence times τ much larger than Δ^{-1}. Because of the coherence decay, a coherence time τ_{ps} exist where the ensemble coherence is significant but τ is already a substantial fraction of Δ^{-1}. Analytically, the peak shift is a Gaussian error function.

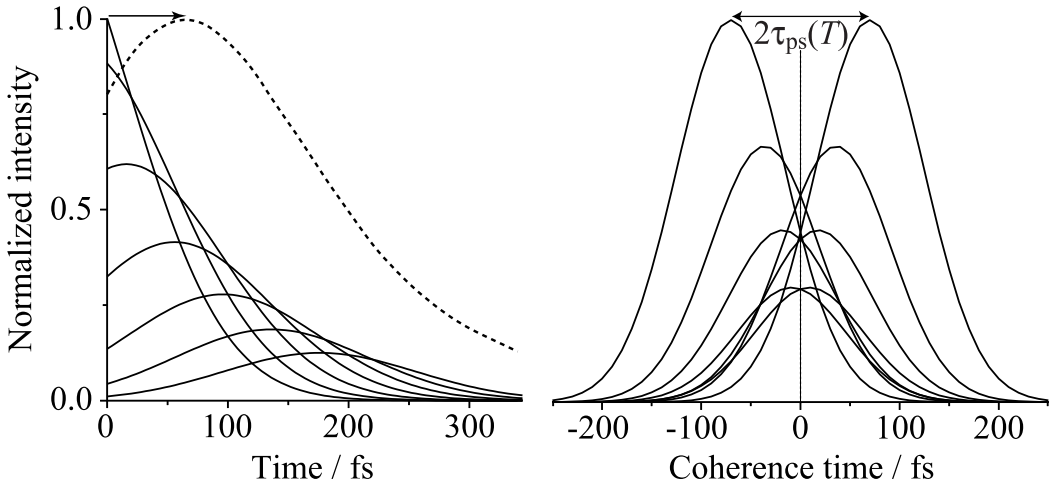

Figure 2.6: On the left, the modulus squared of the response function is plotted as a function of t for six different values of τ (0fs, 40fs, 80fs, 120fs, 160fs, and 200fs) with $\Gamma^{-1} = 200$fs and $\Delta = 57$fs. The dashed line is the time integral of this response as a function of τ. On the right, a peak shift simulation for different population times, 0fs, 40fs, 80fs, and 120fs, with a peak shift decay of 60fs and a transient grating decay of 100fs is shown.

Experimentally, the peak shift is measured for different population times for both, the real and the virtual echo. Although the correlation function is not directly accessible, it was shown that for an inhomogeneously broadened two-level system the correlation function $C(t)$ can be deduced from the peak shift decay [87–90]. During pulse overlap there will also be additional contributions that were already mentioned in the context of pump-probe spectroscopy. These contributions are oftentimes larger than the signal one is interested in. Hence, reliable decay constants can best be extracted for coherence or population times for which the pulses are well separated in time.

When τ is set to zero and T is scanned the experiment is called the transient grating. If this signal is heterodyne-detected, it gives information comparable to pump-probe signals. Otherwise, it will contain the real and the imaginary part of the emitted signal field and will decay with twice the time constant because the signal intensity and not the amplitude is measured. During the population time T a two-level system will either be in the ground or excited state and no phase evolution but population relaxation, energy transfer and spectral diffusion will occur. This is not true for multi-level structures such as the OH stretching vibration of acetic acid dimers (cf. chapter 4).

2D spectra & spectral interferometry

Two-dimensional Fourier transform spectroscopy (2D-FTS) is heterodyne-detected photon echo spectroscopy with Fourier transformation of the coherence and emission time axes, τ and t. The basic principle is identical to linear Fourier transform spectroscopy (FTS) but is extended to two dimensions, ν_1 and ν_3, correlating excitation and emission processes [91]. In the weak excitation regime where the perturbative expansion of the

induced polarisation quickly converges (cf. Eq. 2.1), this technique is the optical analogue of nuclear Overhauser spectroscopy (NOESY) [92, 93] because of the three field interactions the two techniques have in common. For population time $T = 0$ it is often conceived as the analogue of magnetic resonance correlation spectroscopy (COSY) [93, 94] but in the perturbative limit the difference of two versus three field interactions exist.

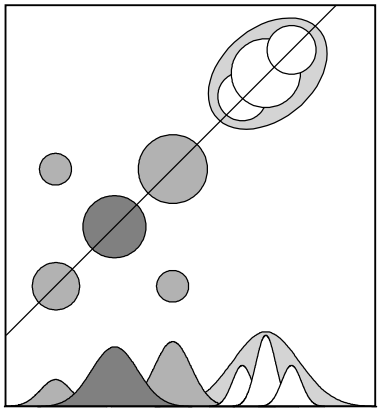

Figure 2.7: Manifestation of coupled oscillators and inhomogeneously broadened lineshapes in 2D spectra.

Interestingly, it could be shown that for a vibrational transition with a long dephasing time compared to the temporal pulse width and under weak excitation conditions, the real part of the complex two-dimensional (2D) spectrum contains the same information as a 2D spectrum of a time-resolved double-resonance spectrum [95]. An illustration of a 2D spectrum is given in Figure 2.7. On the bottom is a linear spectrum which does not tell about coupled oscillators nor inhomogeneous distributions of transition frequencies. In the 2D spectrum above, cross peaks (off-diagonal) reveal the coupling between two oscillators (dark grey). The light grey peak on the right is inhomogeneously broadened. In 2D spectra, the underlying homogeneous lineshapes are circular and line up along the diagonal to form an elliptical inhomogeneous lineshape.

A 2D-FT spectrum is recorded by measuring the electric field emitted by an induced third-order polarisation as a function of coherence time τ and emission time t. The latter is the time after the third interaction. The ν_1-dimension is the Fourier transform of the emitted field along the coherence time axis, the ν_3-dimension is the Fourier transform along the emission time axis. Thus, the emitted field has to be known, i.e. its amplitude and phase (relative to the reference field) have to be measured in the time domain or equivalently, the real and imaginary parts of the complex electric field have to be measured in the spectral domain.

Electric fields can be fully characterised by several methods such as electro-optic sampling [96] or heterodyne detection. The first measures the absolute phase of electric fields whereas the latter only determines the relative phase of the electric field with respect to a reference field. Heterodyne detection can be implemented in the time or the spectral domain, both leading to the same result. The generated third-order signal is spatially overlapped with a strong reference pulse – the local oscillator[‖] – and the two electromagnetic fields are interfered on a detection device. In temporal interferometry, the delay between signal and local oscillator is varied thereby time-gating the signal. In spectral interferometry, the signal and the local oscillator are dispersed by an optical grating and the frequency components are interfered on a array of detection elements. The emitted field is extracted from the spectral interferogram according to the procedure introduced by Lepetit and coworkers [97]. This retrieval of the complex spectral field is illustrated in Figure 2.8. The interferogram is Fourier transformed to a time domain signal which is symmetric about the time origin defined by the local oscillator pulse. Since the time

‖In radios, the received signal is mixed with a reference field that is generated by a local oscillator.

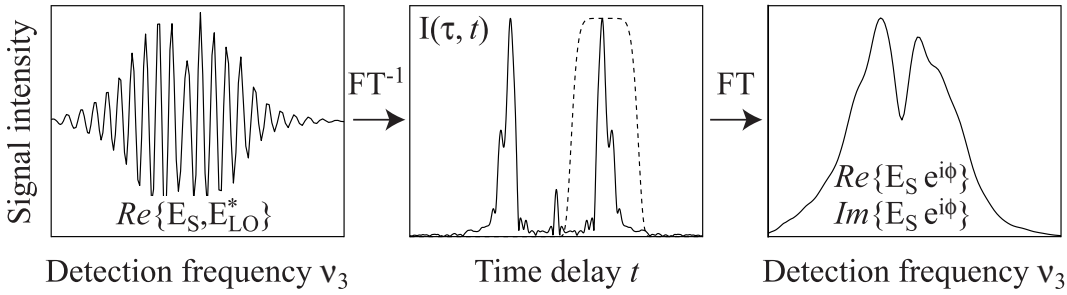

Figure 2.8: Illustration of signal processing in spectral interferometry. The complex electric field E_S can be measured if the reference field E_{LO} is known.

domain signal has to obey causality, the real signal occurs at positive emission times if the local oscillator is advanced. If the local oscillator is retarded, the signal will precede the local oscillator. Therefore, the Fourier transformed signal is multiplied by an appropriate filter function. In Figure 2.8a super-Gaussian filter is applied rather than the Heaviside function $\theta(0)$. Such a filter function suppresses a constant background and fast oscillations that are beyond the spectral resolution of the monochromator. It also avoids introduction of spectral artifacts due to sharp edges around zero time delay. The filtered signal is Fourier transformed back to the spectral domain and divided by the local oscillator field. Two implicit assumptions are made in this procedure: the spectral phase of the local oscillator is linear over its spectral bandwidth, $\varphi_{LO} = 2\pi\nu_3 t$, and the transmission changes can be corrected for by dividing the signal by the square root of the sample transmission. The latter is true if the sample transmission is not below 50% in the spectral range of the excitation pulses.

The exact phase t between the signal field and the local oscillator is not always known to the desired degree of accuracy, e.g. it differs by an equivalent of ±5fs for the pulses used in this thesis. An additional pump-probe spectrum with the same time delay T between the second and third interaction can be used to 'phase' the 2D spectrum after

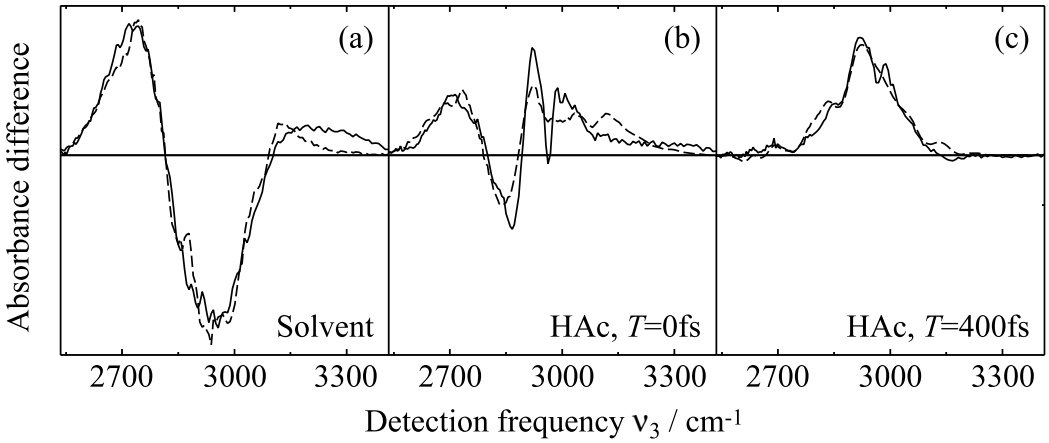

Figure 2.9: Pump-probe spectra (solid) and ν_1-integrated spectra (dashed) for CCl_4 (a) and acetic acid dimers dissolved in CCl_4 at $T = 0$fs (b) and $T = 400$fs (c).

signal processing. The 2D spectrum is integrated along the excitation frequency axis ν_1 and the integrated real part is fit to the pump-probe spectrum by varying the phase angle between the integrated real and imaginary parts. Examples of such fits are shown in Figure 2.9 for 2D spectra of carbon tetrachloride and acetic acid dimers in the region of the OH stretching vibration. The full 2D spectra are displayed and discussed in chapter 4.

3 Experimental

I have often had cause to feel that my hands are cleverer than my head. That is a crude way of characterizing the dialectics of experimentation. When it is going well, it is like a quiet conversation with Nature.

George Wald, 1968

This work investigates the ultrafast dynamics of hydrogen bonded systems in the liquid phase on time scales of less than 100fs. The main probes are molecular vibrations with eigenfrequencies between 1000cm^{-1} and 3800cm^{-1}. Currently, no lasers with sufficiently short output pulses in the required frequency range are available and thus, frequency conversion devices are needed. Furthermore, the optical cross-sections of the corresponding vibrational transitions are weak compared to electronic transitions and require pulse energies of several microjoule. This demands amplified lasers and optical parametric amplifiers.

A few important developments in laser technology should be mentioned that eventually led to unprecedented optical investigations of nature. Stimulated emission is the basic principle of the laser and was formulated when Einstein introduced the idea of quantised radiation [98]. Microwave amplification by stimulated emission of radiation was successfully demonstrated in 1954 and brought about the acronym *maser* [99]. A few years later, the first lasers were constructed [100, 101] originally termed optical masers. Shortly after, the first nanosecond laser was built and pushed the limit of optical time resolution below microseconds [102]. Until the early 1980s, laser pulses of picosecond [103, 104] and femtosecond [105, 106] time duration followed. It took another two decades to produce attosecond pulses in the soft x-ray region [107]. Such pulses are based on the invention of chirped pulse amplification (CPA) and lasers based on Titanium-doped sapphire crystals (Ti^{3+}:Al_2O_3). Chirped pulse amplifiers provide high pulse intensities of several mJ [108], Ti:sapphire crystals display among other favourable features an enormous gain bandwidth [109, 110] and have become the current basis for most pulsed laser systems in the ultrafast (sub-picosecond) time domain. Along with powerful Ti:sapphire laser systems, widely tunable and very stable optical parametric amplifiers (OPAs) have been developed that reach frequencies from the ultraviolet (UV) to the infrared (IR) at high pulse energies [111–114].

3.1 The laser system

The laser system consists of a commercial Ti:Sapphire-based entity and a homebuilt OPA as shown schematically in Figure 3.1. The Ti:Sapphire oscillator (Spectra Physics

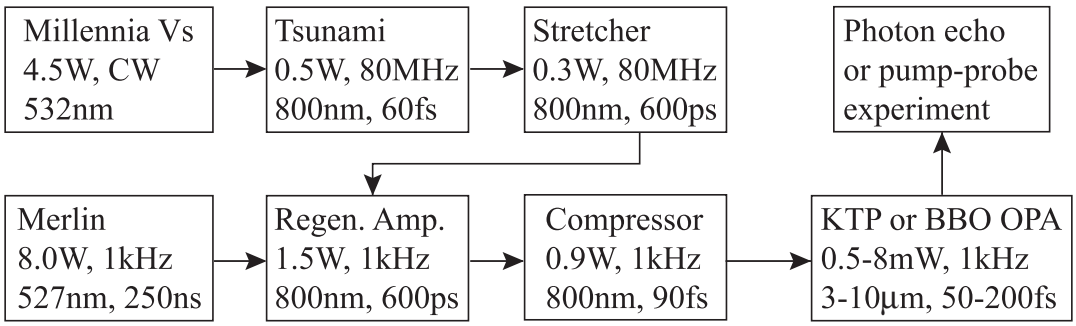

Figure 3.1: Flow diagram of the nonlinear infrared experiment consisting of a commercial Ti:sapphire laser system, a homebuilt OPA, and a nonlinear experimental setup.

Tsunami) is pumped at 532 nm by an intra-cavity doubled Nd^{3+}:YVO_4 laser (Spectra Physics Millenia) and passively mode-locked due to Kerr-lensing [115, 116]. The oscillator emits 60fs pulses centred at 800nm with a pulse energy of about 6nJ. After passing an optical diode (Faraday isolator) the oscillator pulses are stretched by a factor of 10^4 before entering the Pockel cell-switched cavity to avoid peak intensities on the optical elements that exceed their damage threshold. In the second cavity, another Ti:Sapphire crystal is pumped with 8W of 527nm light by an intra-cavity doubled Q-switched Nd^{3+}:YLF laser (spectra Physics Merlin) that operates at 1kHz with 250ns pulses. The oscillator pulses entering the regenerative amplifier are then amplified to 1.5mJ in about 25 passes before they are coupled out by a second Pockel cell and compressed to 90fs with 1mJ pulse energy. The intensity of the resulting pulse train fluctuates by less than 2%.

Optical frequency conversion

A wide frequency tuning range is required when investigations of ultrafast dynamics shall comprise the majority of intramolecular transitions. Nowadays, Ti:Sapphire based laser systems in combination with frequency conversion devices are typically used. In this work, two similar optical parametric amplifiers (OPAs) were used to convert the 800nm light into pulses in the wavelength range of 3 to 10μm. This conversion is achieved by difference frequency generation (DFG) in birefringent crystals with large second order nonlinear susceptibilities [117]. A strong pump wave $(\mathbf{k}_1, \omega_1)$ and a collinear weak seed wave $(\mathbf{k}_2, \omega_2)$ generate a third light wave $(\mathbf{k}_3, \omega_3)$ at their difference frequency. Simultaneously, the wave at the lower frequency ω_2 is amplified to fulfil energy and momentum conservation:

$$\omega_1 = \omega_2 + \omega_3, \tag{3.1}$$

$$\mathbf{k}_1 = \mathbf{k}_2 + \mathbf{k}_3. \tag{3.2}$$

Equation 3.2 describes the phase-matching condition, where identical phases of the three light fields are involved such that constructive interference between the pump wave and the converted waves occurs during propagation through the nonlinear crystal. The light wave at frequency ω_1 is called the fundamental whereas ω_2 and ω_3 are termed signal and idler, respectively. Phase-matching is achieved by exploiting the birefringence of the crystal.

In birefringent crystals, at least one optic crystal axis can be defined such that this axis and the **k**-vector of the incident light span the principal plane. For light polarised perpendicular to the crystal axis (ordinary polarisation), the refractive index is constant with respect to the **k**-vector direction. This is not true for light polarised parallel to the optical crystal axis (extraordinary polarisation). For biaxial crystals, the refractive index dependence on polarisation and **k**-vector direction is more complicated. For details, the reader is referred to reference [117]. Phase-matching is optimal for certain polarisation directions of the three light waves, e.g. group velocity mismatch between light pulses usually favours a certain polarisation configuration over another: in type-I phase-matching, the signal and the idler wave have the same polarisation direction which is perpendicular to the one of the fundamental wave. In type-II phase-matching, the signal wave is polarised perpendicular to the idler and the fundamental wave [117]. Rotation of the crystal normal to the principal plane matches the refractive index for the extraordinary waves to constructively interfere with the ordinary waves over the crystal length according to (3.2):

$$\frac{n_1}{\lambda_1} = \frac{n_2}{\lambda_2} + \frac{n_3}{\lambda_3}. \tag{3.3}$$

Three nonlinear crystals were employed in this work*: For highest pulse energies, a crystal made of $KTiOPO_4$ (KTP) was used to generate idler pulses with wavelengths between 2.9 and 3.5μm (the signal being extraordinarily polarised). For widest tunability, a β-barium borate (BBO) crystal was used for signal and idler generation (the polarisations being ordinary and extraordinary, respectively) followed by difference frequency generation from the BBO-signal and -idler pulses in a Ag_2GaS crystal (type-I phase-matching) resulting in mid-infrared pulse tunable from 3 to 10μm.

Mid-infrared light sources

The basic design of the optical parametric amplifier is shown in Figure 3.2 [113]. From the incoming 800nm pulse (300μJ) 1% are split off, polarisation-rotated by 90° and focused with a lens (f=100mm) into a 1mm sapphire plate to generate super continuum radiation (white light) [118]. The white light contains the near-infrared (NIR) frequencies of the signal and serves as a seed pulse that is re-focused by a second lens (f =50mm) into the first 4mm nonlinear crystal (KTP or BBO).

After passing a manual delay stage, another 10% of the 800nm pulse are split off and focused (f = 500mm) into the first crystal. This first pump pulse is collinearly overlapped in space and time with the white light to amplify the seeding signal pulse. The amplified signal and newly generated idler pulses are separated from the fundamental with the help of a dichroic mirror. Thereafter, the signal is reflected by a polarising beam splitter (transmitting the idler) and is re-colimated with a sperical mirror (R = -500mm). The latter is placed on a manual translation stage to overlap the signal with the remaining fundamental pulse in time. The second pump pulse is adjusted in beam diameter with a 4:1 telescope to match the signal beam diameter and is then overlapped with the signal.

*KTP - positive biaxial, point group mm2, $\theta = 27°$, $\phi = 0°$. BBO - negative uniaxial, point group 3m, $\theta = 30°$, $\phi = 0°$. Ag_2GaS: negative uniaxial, point group $\bar{4}2m$, $\theta = 37°$, $\phi = 45°$.

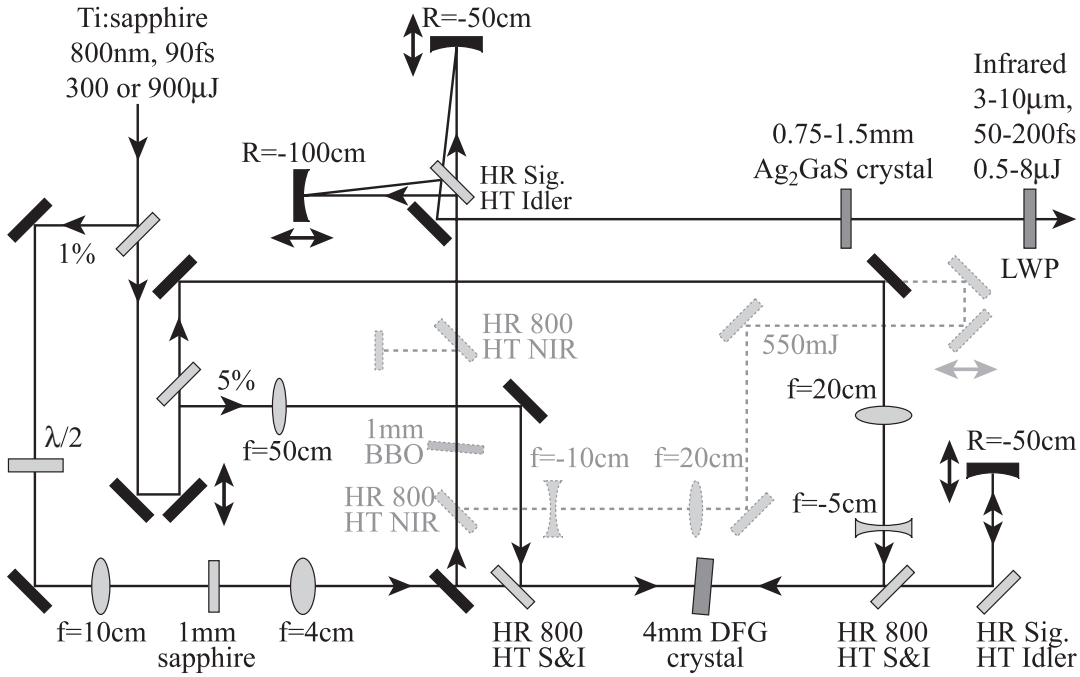

Figure 3.2: Design of the optical parametric amplifier. The KTP-OPA uses the idler of the optical parametric generation in the BBO crystal. The dashed optical path is used when more power from the BBO-OPA is needed. HR/HT: high reflection/transmission, S&I: signal & idler.

After the second pass through the nonlinear crystal, about 60μJ of combined signal and idler power are generated and separated from the 800nm pulse with a dichroic mirror.

In the case of the KTP-OPA the signal is blocked by an appropriate long wave pass filter (LWP) that transmits the idler which has a pulse length of about 120fs at 3μm with 8μJ pulse energy at less than 1% (rms) noise level. The noise of the Ti:sapphire amplifier is typically two times larger. The frequency range of this OPA is limited by the onset of a broad absorption band at 4μm in KTP shown in Figure 3.3.

For larger tunability and shorter pulses an OPA with two DFG processes is used at the expense of pulse energy. A BBO crystal replaces the KTP crystal and is set to generate a signal beam between 1.2 and 1.6μm. The corresponding idler beam ranges between 2.4 and 1.6 μm. These two pulses are mixed in a Ag_2GaS crystal yielding mid-infrared pulses between 3 and 10μm. Pulses are typically 100fs at 3μm with 2μJ pulse energy. However, the actual bandwidth is sufficient for sub-70fs pulses. For the newly designed passively phase-locked four-wave-mixing experiment, a second 1mm thick BBO crystal is used in a third amplification stage with a 500μJ pump pulse to generate more than 200μJ of combined signal and idler power. Difference frequency generation yields pulses of up to 9μJ energy that are as short as 50fs at 3μm when chirp-compensated. The latter is achieved by inserting CaF_2 to compensate for linear chirp of germanium-based optical elements [119] and fine-tuning of the OPA delays to maximise the spectrally integrated third-order signal from a 1mm thick CaF_2 window. Full pulse characterisation is done by frequency-resolved optical gating (FROG) [120] as described in section 3.5. The pulse

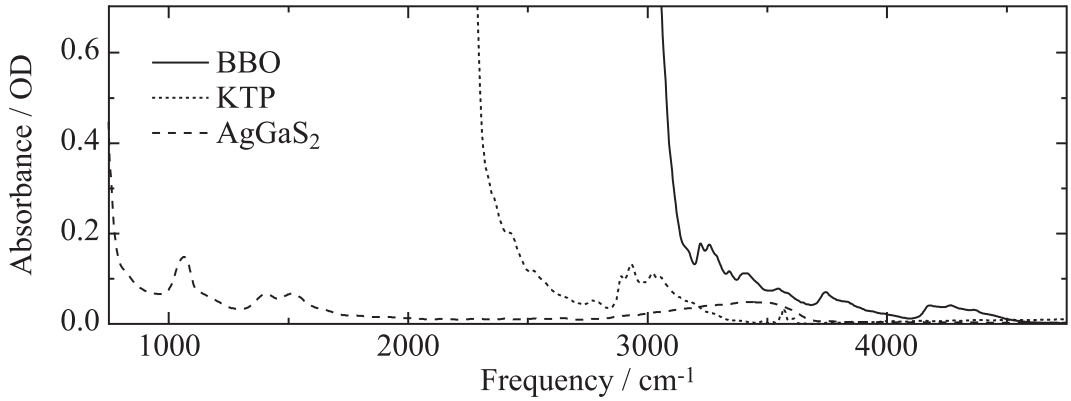

Figure 3.3: Long-wavelength absorption edges of KTP (4mm), BBO (1mm), and $AgGaS_2$ (0.75mm), limiting the maximum idler wavelength in difference frequency generation.

stability of the BBO-OPA is extraordinarily high with a noise level of better than 0.2% (rms) in the center of the infrared pulse spectrum which is about an order of magnitude less than the noise level of the Ti:saphire laser [121].

3.2 Pump-probe spectroscopy

The pump-probe experiments were performed with the setup shown in Figure 3.4. The infrared pulse emerging from the OPA passes through a barium fluoride (BaF_2) wedge and an optical chopper that is synchronised to the Q-switch of the CPA pump laser. The chopper runs at half the repetition rate of the CPA and blocks every second pump pulse so that alternately sample transmission with and without pump pulse excitation is recorded. After passing an optical delay line, the pump pulse is focused into the sample with a 30° off-axis parabolic mirror where its 300μm focus is spatially overlapped with the focus of the probe pulse.

The reflected pulses from the front and the back surface of the BaF_2 wedge have about 4% of the pump pulse energy and are used as probe and reference pulse, respectively. The reference pulse is needed to eliminate signal fluctuations due to sample variations in sample cells and intensity fluctuations of the probe pulse. After reflection from the wedge, the two pulses are focused by a spherical mirror and re-collimated by a second one. This 2:3-reflection telescope serves as a beam expander to have a probe beam focus that is about half the size of the pump beam focus to ensure probing of a fairly homogeneous pump volume. The probe and the reference pulse are focused by the parabolic mirror into the sample with the reference focus sufficiently displaced from the probe focus but still close enough to monitor sample variations in time that also affect the pump-probe focal region.

The three pulses emerging from the sample are collimated by a second 30° off-axis parabolic mirror. The pump beam is blocked and the remaining two pulses are focused into the entrance slit of a monochromator. The monochromator optics image each spectral component of the focus into a plane where two arrays of 16 infrared sensitive mercury

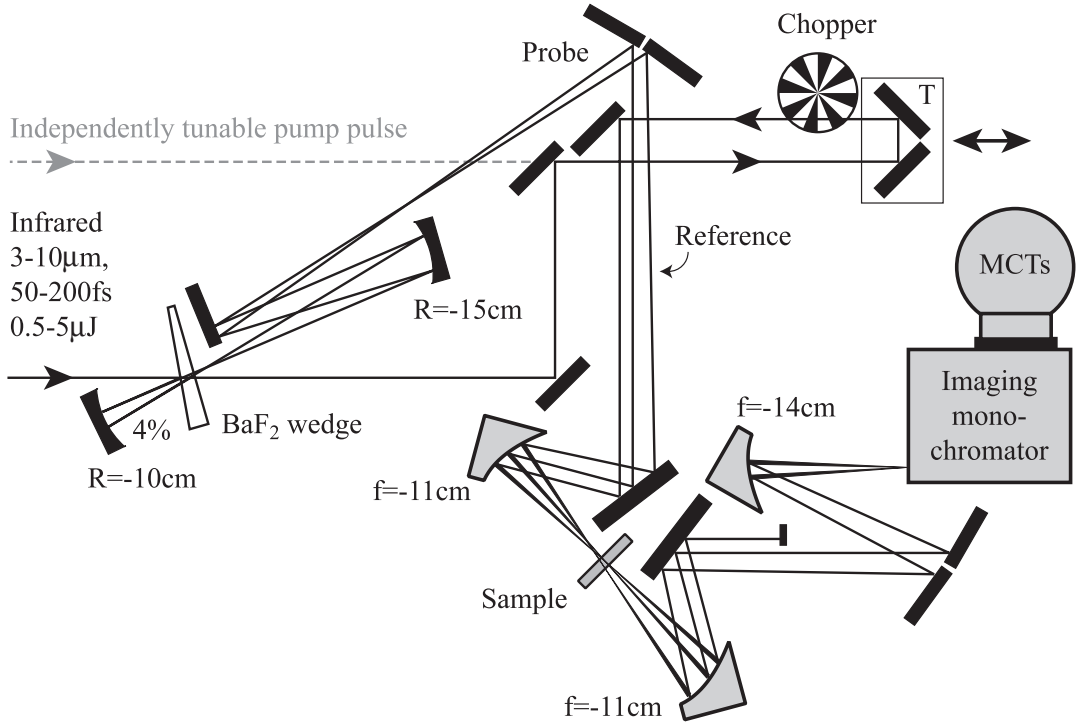

Figure 3.4: Schematic of the pump-probe setup. The generated third-order signal propagates collinear to the probe pulse. Note that the reference pulse is not parallel to the pump/probe pulse to avoid passage through the excited sample volume.

cadmium telluride detector elements (MCTs) record the spectral intensities. The MCTs act as photo-resistors and absorption of infrared photons changes the bias current in each of the detector elements. The transient current change is integrated by gated electronics that are synchronised to the CPA pulses and the resulting voltage at the integrator output is fed into a fast AD-converter for multi-channel single shot data acquisition. When the intensities of the two reference pulses, $I_0^{(R)}$ (pump pulse blocked) and $I^{(R)}$ (pump pulse not blocked), are taken into account, the transient absorbance change is given by:

$$\Delta A(T,\omega) = -\log\left(\frac{I(T,\omega)}{I_0(\omega)} \cdot \frac{I_0^{(R)}(\omega)}{I^{(R)}(\omega)}\right). \tag{3.4}$$

The underlying transmission change $\Delta T = I/I_0$ has already been defined in (2.44). The spectral normalisation allows for the detection of relative absorbance changes as small as 10^{-5}.

Ultrafast spectroscopy requires dispersion control because of the large bandwidth of the short pulses. In order to keep pulse shapes invariant during propagation, mainly reflective optics are employed except for the BaF_2 wedge and the long wave pass filter that is based on sapphire or germanium. For the same reason, care has to be take when the pulse spectra overlap with water vapour or carbon dioxide absorption lines that are shown in Figure 3.5. The experimental setup is enclosed in a box that can be purged with nitrogen

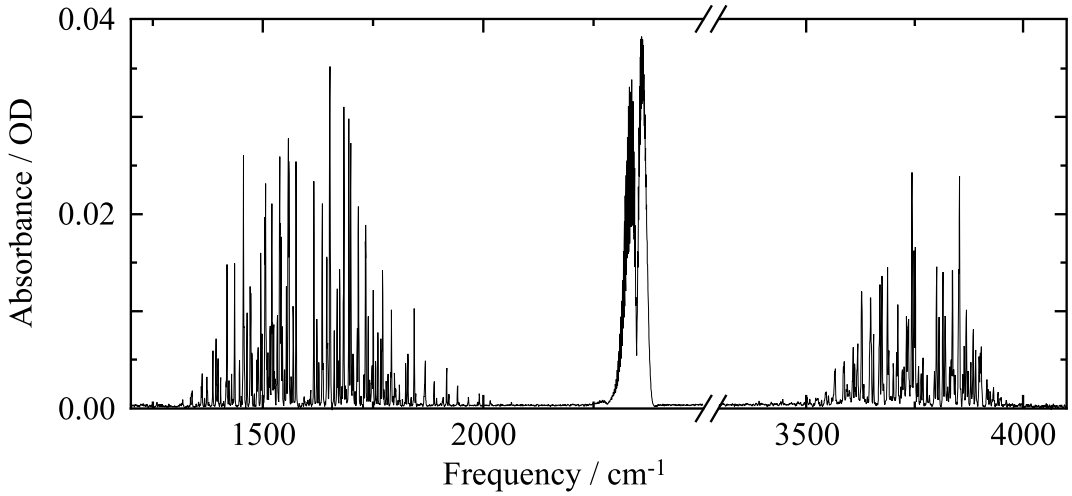

Figure 3.5: Absorbance of ambient air at room temperature with about 25% relative humidity in the frequency range relevant to this work. The R- and P-branch of the bending and the symmetric/antisymmetric stretching rovibrators of water vapor are centred around 1600cm^{-1} and 3800cm^{-1}, respectively. The corresponding stretching vibrations of CO_2 exist at 2400cm^{-1}.

to have sufficient pulse energy at the sample and little dispersion and re-shaping of the spectral components during pulse propagation.

Two-colour pump-probe experiments, with pump and probe pulses independently tunable, were also performed which required a slight modification of the experimental setup. The optical path for an independently tunable pump pulse is plotted as a grey dashed line in Figure 3.4. Furthermore, the polarisation of the pump pulse could be changed by use of an 90° optical lift or a zero-order half-wave plate to measure spectrally resolved polarisation anisotropy decays [85].

3.3 Photon echo spectroscopy

The three-pulse photon echo setup is depicted in Figure 3.6. Two beam splitters divide the incoming infrared pulse into three equal replicas, two of which pass over motorised delay stages to give full control over the pulse sequence. To reduce group velocity dispersion mainly reflective gold optics were chosen similar to the pump-probe setup described above. The beam splitters are based on CaF_2 substrates that show only little dispersion in the selected wavelength range. The three pulses are focused into the sample with 30° off-axis parabolic mirrors. The angles between the propagating directions of the pulses are kept small at about 2° to have a parallel components of the three k-vectors along the optic axis. It is these components that generate a frequency grating in the sample with grating vector $\Delta\mathbf{k}_{21} = \mathbf{k}_2 - \mathbf{k}_1$. The third pulse is scattered off this grating in the direction of the first grating orders $\mathbf{k}_3 \pm \Delta\mathbf{k}_{21}$.

The emerging pulses of interest are drawn as lines in Figure 3.6. They are collimated by a second parabolic mirror, pulses $\mathbf{k}_1$ and $\mathbf{k}_2$ are blocked by an appropriate mask whereas

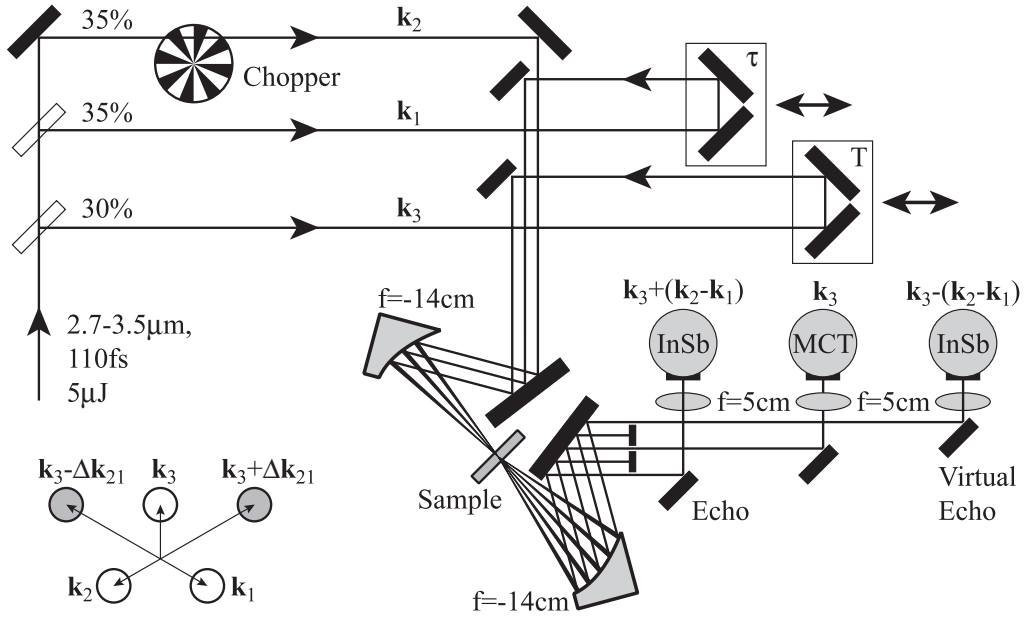

Figure 3.6: Three-pulse photon echo experiment. In the lower left the k-vector projections onto the focal plane behind the sample are shown. The grating vector is defined as $\Delta\mathbf{k}_{21} = \mathbf{k}_2 - \mathbf{k}_1$.

pulse $\mathbf{k}_3$ is focused by a CaF_2 lens onto a MCT detector element (0.5x0.5mm^2) for pump-probe measurements. The two signals, termed echo and virtual echo, are focused onto indium antimonide (InSb) detector elements (0.25x0.25mm^2) that are an order of magnitude more sensitive at 3 microns than the MCT detector. The array of circles in the lower left of the schematic setup shows the beam arrangement after collimation by the parabolic mirror†. For illustration purposes the actual beam arrangement has been rotated clockwise by 60°. In the setup $\mathbf{k}_1$ and $\mathbf{k}_3$ have the same height because they have to propagate parallel to the delay stages whereas $\mathbf{k}_2$'s lateral position can easily be moved without changing its orientation.

In principle, four-wave mixing is a background-free technique. However, scattered light from imperfect interfaces has to be suppressed by spatial filtering. In addition, an optical chopper alternately blocks the beam that contributes the least to scatter allowing to subtract most of the background similarly to the subtraction of the probe pulse in pump-probe experiments. The chopper is also used to find the spatial overlap of pulses: when a thin piece of Germanium is placed at the sample position, pulse $\mathbf{k}_3$ serves as the probe pulse monitored by the MCT detector and $\mathbf{k}_1$ or $\mathbf{k}_2$ acts as the pump pulse. The pump pulse creates long-lived free charge carriers that cause a strong absorbance change that can easily be detected. A two-photon absorption spike during temporal overlap of the pulses is a measure of pulse width and zero delay. Alignment of the optics is facilitated by using a small 1mW red diode laser that takes the same path over reflective optics as do the infrared pulses at fivefold wavelength.

†In front of the parabolic mirror the position of the three pulses is the (point-)mirror image with respect to the optic axis.

3.4 Two-dimensional spectroscopy

Correlated spectroscopy (COSY) was the first and simplest experimental techniques in multidimensional nuclear magnetic resonance (NMR) spectroscopy to measure structure-related nuclear spin coupling by correlation of nuclear spin coherences [93, 94, 122]. Many powerful techniques of higher dimensionality engendered and with the advent of powerful ultrafast light sources optical analogues in electronic and vibrational spectroscopy were experimentally realised [123]. The heterodyne-detected photon echo is used to record two-dimensional (2D) spectra but independent of whether temporal or spectral interferometry is used for detection, the signal depends on the relative phase between third-order signal and local oscillator. Therefore, phase stability during data acquisition is of utmost importance for reliable data. Sufficient phase stability is crucial [124, 125] but currently does not seems to be implemented in many experimental setups. Two newly developed passively phase-locked visible 2D spectrometers [126, 127] are based on an elegant idea of M. Cowan [128]. Actively phase-stabilised spectrometers are certainly attractive and have also been developed [125, 129]. To stabilise the phase of the interferometric setup actively, a continuous-wave (cw) laser beam of short enough wavelength is sent over the same optics as the signal generating pulses and the interference signal of each pair of cw-beams is used as an optical ruler and feed-back signal to stabilise the optical path length. This type of phase-stabilisation has the advantage of less pulse energy losses because only three pulse replicas of equal intensity are generated instead of four. But active phase-stabilisation is technically much more demanding and the inherent pointing stability of the passively phase-locked setup is also absent.

A passively phase-locked heterodyne-detected photon echo spectrometer for the mid-infrared frequency range was developed as part of this thesis in collaboration with the Miller group of the University of Toronto to measure 2D spectra. The setup is shown in Figure 3.7 and is the first of its kind featuring passive phase-locking in vibrational photon echo spectroscopy. The infrared pulse is first split by an ordinary beam splitter into two identical replicas, one of which passes an optical delay stage that defines the waiting time T (section 2.3). Then, both pulses are focused by a 90° off-axis parabolic mirror onto a diffractive optic (DO), i.e. a reflective optical grating, and the diffracted pulses are collimated by an identical parabolic mirror. A mask allows the four first-order pulses to pass while blocking all other diffraction orders. Spatially, the four pulses are situated at the four corners of a square as shown at the bottom of Figure 3.7. Three of the pulses generate a four-wave mixing signal. The fourth pulse termed the local oscillator‡ (LO) is used to measure the emitted electric field of the third-order polarisation in the time or frequency domain as already described in detail in section 2.3. A half-wave plate for each pulse is placed behind the mask to have control over the linear polarisation directions. The two beams that originate from the pulse reflected at the beam splitter pass an extra 4mm of CaF_2 to compensate for the passage through the beam splitter substrate. To compensate for the neutral density filter that attenuates the local oscillator, 1mm of anti-reflection coated germanium is placed in the path of the three signal-generating pulses. Finally,

‡The term stems from radio technology where a truly local oscillator in the receiver is tuned to the carrier frequency of a radio signal for demodulation, e.g. difference frequency generation.

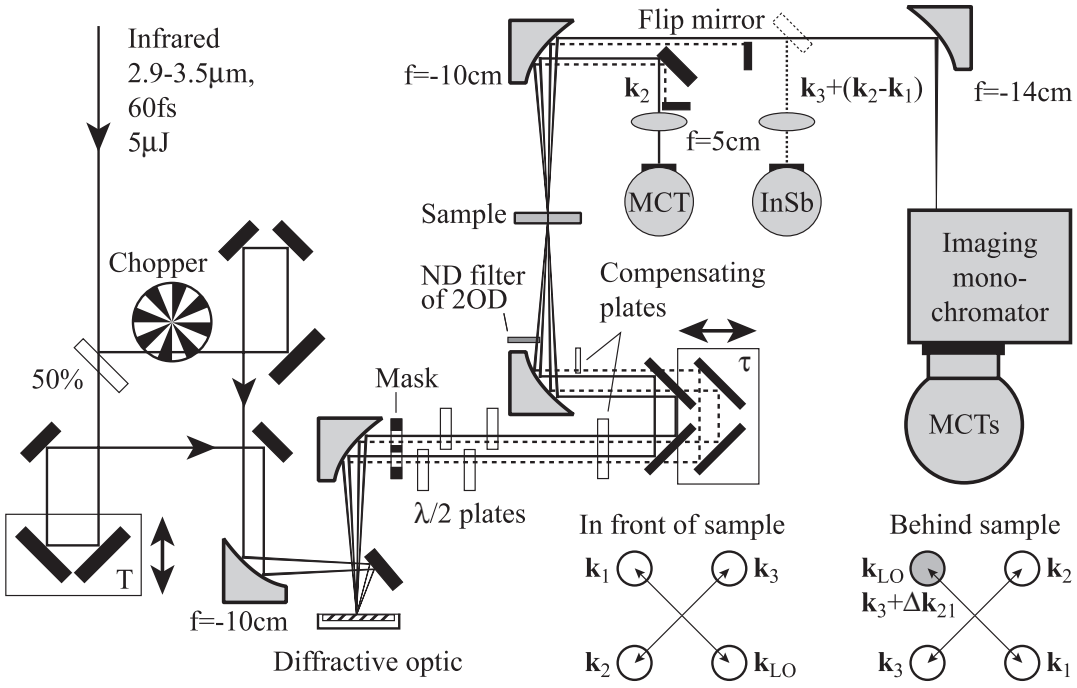

Figure 3.7: Heterodyne-detected photon echo experiment with passive phase-locking. Lower right: k-vector projections onto the focal plane with grating vector $\Delta\mathbf{k}_{21} = \mathbf{k}_2 - \mathbf{k}_1$.

0.5mm of CaF_2 are inserted into the path of $\mathbf{k}_3$ to advance the local oscillator pulse, $\mathbf{k}_{LO}$, by a delay t with respect to the point in time when the signal is generated, i.e. when $\mathbf{k}_3$ passes the sample. The attenuated local oscillator should pass the sample before all other pulses to avoid any interaction between the local oscillator and the excited sample volume which potentially introduces signal artifacts. This implies that the maximum scan range, given by $T + \tau$, sets a lower limit to t. The upper limit is set by the resolution of the detector array because t is the inverse of the fringe spacing of the spectral interferogram. Typically t was advanced by about 1.5ps in the experiments.

The two top pulses, $\mathbf{k}_1$ and $\mathbf{k}_3$, are reflected by a pair of fixed mirrors whereas the two bottom pulses, $\mathbf{k}_2$ and $\mathbf{k}_{LO}$, are reflected by an identical pair that is mounted on a second translation stage for control of the coherence time delay τ. The four pulses are focused into the sample by a 90° off-axis parabolic mirror and collimated by the same type of mirror. Pulses $\mathbf{k}_1$ and $\mathbf{k}_3$ are blocked whereas pulse $\mathbf{k}_2$ is used to monitor the pulse energy and exclude pulse sequences that are outside a predefined energy window. The signal and local oscillator are focused into the entrance slit of a monochromator with a parabolic mirror and the spectral interferogram is recorded by stepping the monochromator's grating through the entire pulse spectrum. Great care was taken in programming the monochromator control routine to precisely overlap the spectral parts of the spectra at detection time with overlap uncertainties of 10% of the resolution. For detection an array of 16 MCT detector elements is used with a spectral resolution of 6cm^{-1} at 4μm to 10cm^{-1} at 2.6μm. Pulses $\mathbf{k}_1$ and $\mathbf{k}_2$ are chopped at 500Hz as described in the other experiments. The spectrum of the local oscillator is then alternately recorded with and without third-order signal to compute

the difference on a two-shot basis and remove contributions from background scatter. Apart from the main advantage of passive phase-locking, the use of diffractive optics has the local oscillator automatically aligned with the signal as shown in the bottom right of Figure 3.7. For fine tuning, the ND filter can be moved to translate the local oscillator and maximize the interferogram contrast. For spectrally integrated photon echo measurements the local oscillator is blocked and a flipping mirror directs the third-order signal toward an InSb-detector. The excellent passive phase stability of the heterodyne-detected signal exceeds $\lambda/150$ at 3μm and produces reliable 2D data sets. For consecutive data acquisition, equally reliable motorised translation stages were employed to control temporal delays between the pulses. Inch worm stages (EXFO Burleigh Products Group Inc.) use two clamping piezo-electric crystals to hold the front or rear end of the translational piezo-electric crystal in place while it is expanding or contracting. The caterpillar-like motion is said to have virtually no backlash and an absolute position accuracy is specified with $\pm$100nm over the scan range of 25mm.

At last, the subtle difference in configuration between a two-pulse photon echo and a three-pulse photon echo at $T = 0$ should be mentioned. In the three-pulse photon echo, negative coherence time, $\tau < 0$, means that pulses $\mathbf{k}_1$ and $\mathbf{k}_2$ are interchanged whereas the waiting time is defined between the second and the third pulse, i.e $\mathbf{k}_1$ and $\mathbf{k}_3$. Hence, for negative coherence time, only the τ-delay is moved, for positive coherence time, delay T has to be moved to keep the relative temporal separation between $\mathbf{k}_2$ and $\mathbf{k}_3$ constant.

3.5 Characterisation of ultrashort pulses

Pulse characterisation is of vital importance in order to analyse the measured data properly. Usually, non-resonant signals from solvent molecules and sample cell window material contribute substantially during pulse overlap. These signals are typically caused by the induced nonlinear refractive index [50]. Though often unavoidable, these signals can be taken into consideration when simulating or fitting the acquired data. Signals that depend on the coherence properties of interfering light fields are called coherent artifacts although this term is not limited to coherent light sources [130]. Unfortunately, the shorter the pulses are the stronger the coherent artifact is in general which spoils some of the resolution increase by a larger ratio of coherent artifact to desired signal.

The pump-probe technique offers resonant and non-resonant ways to measure the pulse length. In this work, the cross-correlation of the pump and the probe pulse was determined by two-photon absorption in 70μm thin pieces of germanium and indium arsenide for wavelength in the three and six micron range, respectively. The pump pulse was attenuated by fine copper wire-grids to suppress the generation of long-lived free charge carriers. The pump-induced absorbance change as a function of pump-probe delay is the second-order intensity autocorrelation function

$$G_2(T) \;=\; \int_{-\infty}^{\infty} dt |E(t)E(t-T)|^2 \;=\; \int_{-\infty}^{\infty} dt I(t)I(t-T). \tag{3.5}$$

For Gaussian pulse shapes G_2 will also be of Gaussian shape with a width σ that is $\sqrt{2}$-times the one of $I(t)$. Such a measurement is shown in Figure 3.8 for an infrared pulse at

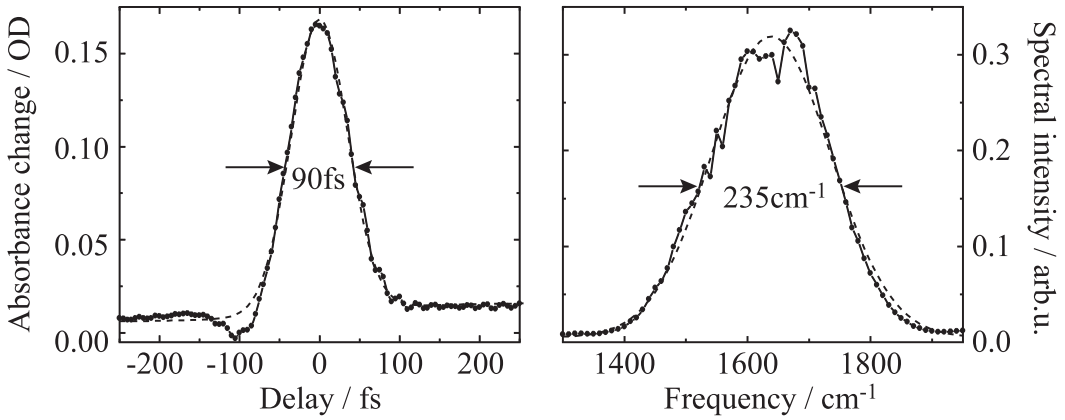

Figure 3.8: Two-photon absorption in 70μm of InAs as a function of pump-probe delay (left) and the corresponding pulse spectrum (right). The dashed lines are fits of Gaussians to the data. The pulse duration τ is about 65fs and the time-bandwidth-product $\tau\Delta\nu = 0.45$ is close to the Fourier-limit for Gaussian pulses of 0.44.

6μm generated in the three-stage BBO-OPA with a 0.75mm-thin $AgGaS_2$-crystal. To the left of the autocorrelation trace the corresponding spectrum is displayed from which we can infer that the pulse is essentially transform-limited.

In four-wave mixing setups, a non-resonant signal can easily be generated in common sample cell windows such as CaF_2. This type of signal generation is called optical gating because one pulse acts as a temporal gate for self-diffraction of a second pulse on the induced nonlinear refractive index grating. In the three-pulse photon echo configuration, measurement of the pulse width is accomplished by either scanning pulse $\mathbf{k}_1$ or pulse $\mathbf{k}_3$ with respect to the other two. The resulting third-order intensity autocorrelations,

$$\begin{aligned} G_3^{SD}(\tau) &= \int_{-\infty}^{\infty} dt |E(t)E(t)E^*(t-\tau)|^2 = \int_{-\infty}^{\infty} dt I^2(t) I(t-\tau), \\ G_3^{TG}(\tau) &= \int_{-\infty}^{\infty} dt |E(t)E(t-\tau)E^*(t-\tau)|^2 = \int_{-\infty}^{\infty} dt I(t) I^2(t-\tau), \end{aligned} \tag{3.6}$$

apply to self-diffraction (SD) and transient grating (TG) optical gating. The preservation of the Gaussian shape applies to these correlation functions, too. A short calculation with Gaussian-shaped pulses reveals that for an integrand of the form $I^m(t)I^n(t-\tau)$, the ratio of the temporal widths is given by

$$\frac{\sigma(G_{m+n})}{\sigma(I)} = \sqrt{\frac{m+n}{m \cdot n}}. \tag{3.7}$$

The autocorrelation trace and the corresponding spectrum of a pulse generated in the KTP-OPA is shown in Figure 3.9. The idler bandwidth is less than the infrared pulse generated in difference frequency mixing. Nonetheless is the pulse almost transform-limited.

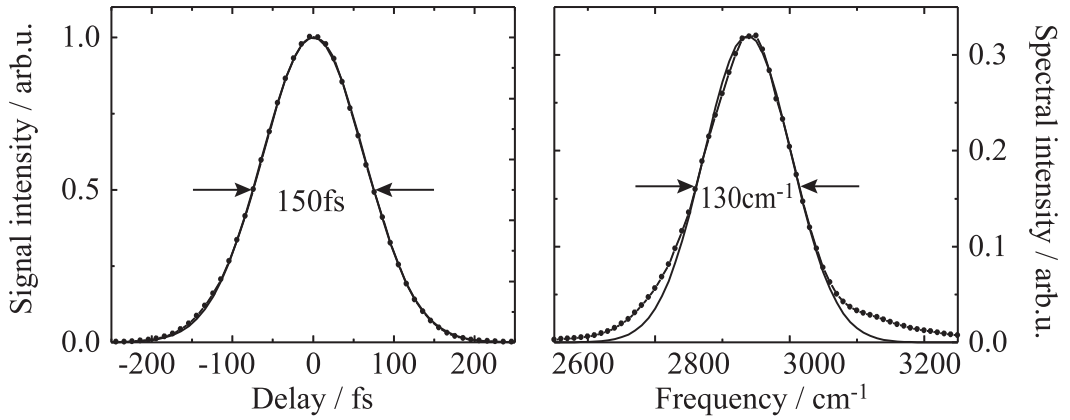

Figure 3.9: Self-diffraction signal in 2mm of CaF_2 as a function of coherence time (left) and the corresponding pulse spectrum (right). The dashed lines are fits of Gaussians to the data. The pulse duration τ is shorter than 125fs and the time-bandwidth-product $\tau\Delta\nu = 0.48$ is fairly close to the Fourier-limit for Gaussian pulses of 0.44.

If only the pulse duration is of interest and the time-bandwidth product is close to the Fourier-limit it suffices to measure the intensity autocorrelation. But no information of the phase of the electric field can be extracted. Frequency-resolved optical gating (FROG) supplies the additional information needed for complete reconstruction of the electric field function. The heterodyne-detected three-pulse photon echo setup is, at the same time, a FROG device by simply blocking the local oscillator and frequency-resolving the diffracted signal from a CaF_2 window. A FROG trace allows for the complete reconstruction of very short pulses of two optical cycles or less [120]. Two TG-FROG traces are plotted in Figure 3.10. The trace of a linearly chirped pulse can be seen on the left. The blue frequency components of the pulse are clearly advanced (Delay < 0) with respect to the red ones. But with the right material at hand the linear chirp can be compensated for [119]. Second-order signals can just as well be used for FROG but the signal will not be as intuitive as for third-order signals, e.g. linear chirp tilts the contours of such a FROG trace.

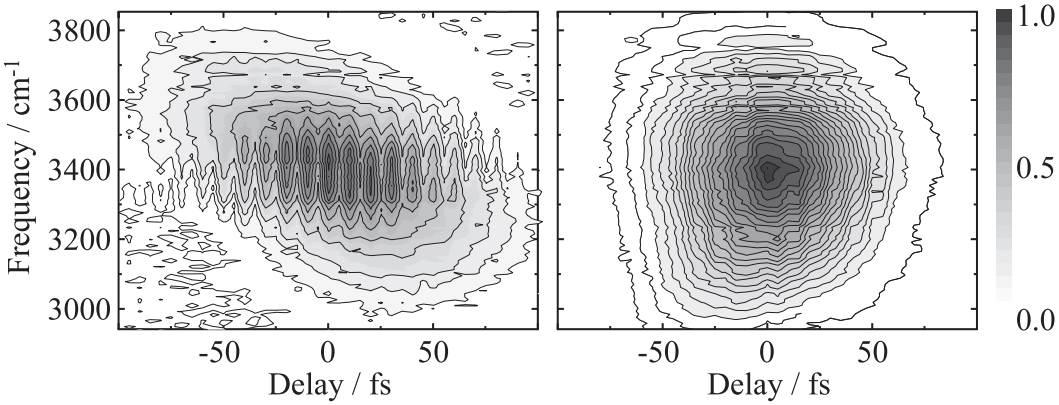

Figure 3.10: FROG trace of a chirped (left) and a chirp-compensated (right) infrared pulse. Scattered light caused the interference fringes along the time delay in the left FROG trace.

A recently proposed method to measure the group delay dispersion of the ultrashort pulse in a molecular solvent [131] also seems appropriate for infrared pump-probe experiments in the liquid phase were coherent Raman excitations of solvent modes are possible. Finally, the table below summarises the parameters of the three OPA variants used to perform the infrared pump-probe and photon echo experiments:

OPA type	Tuning range λ / μm	Pulse energy E_p / μJ	Pulse duration τ_p / fs	Bandwidth $\Delta\nu$ / cm^{-1}
1. KTP	3 – 4	≤ 8	≥ 120	≤ 130
2. BBO/Ag_2GaS	3 – 10	≤ 2	≥ 100	≤ 250
3. BBO·2/Ag_2GaS	3 – 10	≤ 9	≥ 60	≤ 350

Table 3.1: Summary of the infrared pulse parameters. The quantum yield of the 800nm/IR conversion is constant for most of the tuning range such that $E_p \propto \lambda^{-1}$. The bandwidth decreases less rapidly and approximately $\Delta\nu \propto \lambda^{-1/2}$. Compensation of GVD at the expense of pulse energy will shorten the pulses of the second OPA type.

4 Coupling mechanisms in cyclic acetic acid dimers

The symmetric cyclic dimer of carboxylic acids in gas phase and apolar liquids is of well-defined geometry and represents one limiting case of hydrogen-bonded molecular systems. Liquid water is quite the opposite; it constitutes a rapidly fluctuating hydrogen bond network that undergoes continuous hydrogen bond cleavage and reformation. This second limiting case will be discussed in the next chapter. In this chapter advances in understanding the nature of acetic acid dimers in apolar solvents will be presented. The extensive experimental investigations and new and more comprehensive quantum mechanical modelling have led to interesting insights into this seemingly simple though complex quantum system.

4.1 Carboxylic acids

Acetic acid belongs to the class of carboxylic acids such as formic, benzoic, and acetylsalicylic acid (aspirin) to name a few. These compounds are of major importance in modern industry. Acetic acid alone has a very wide range of applications including adhesives and artificial fibres, cleaning, fumigation, packaging, paints, and photography. From a more fundamental scientific point of view, carboxylic acids have received a lot of experimental and theoretical interest over more than a century. In the early 1880s molecular weight determination of solutes had become accessible through measurement of freezing point changes of the solvent. It was found that carboxylic acids in apolar solvents behaved as if their molecular weight had doubled [132, 133]. When Nernst proposed a modification of the law of mass action in 1891 to incorporate molecular aggregation he already stated that the tendency of acetic acid to form bimolecular aggregates was commonly known [134]. To elucidate the type of interaction that caused dimerisation, it took another 50 years.

As already mentioned in the introductory chapter, the hydrogen bond concept engendered from 1900 onward [9]. Latimer and Rodebush are considered the first to have formulated this concept [6]. They also expected the behaviour of dimer-forming compounds to be very different from that of water and alcohols. Linus Pauling was the first to gather experimental evidence of planar dimer formation in gaseous carboxylic acids from electron diffraction measurements [135]. Soon after, the relationship between infrared absorption of vibrations and the symmetric dimer structure in gas phase and apolar solvents had been found [35, 36]. Indeed, carboxylic acids tend to form C_2-symmetric dimers with two degenerate intermolecular hydrogen bonds in the gas phase and apolar solvents [42, 136–138]. In crystalline phase only the heavier group members form symmetric cyclic dimers, formic and acetic acid crystals consist of chains [139–141]. This is generally the case for

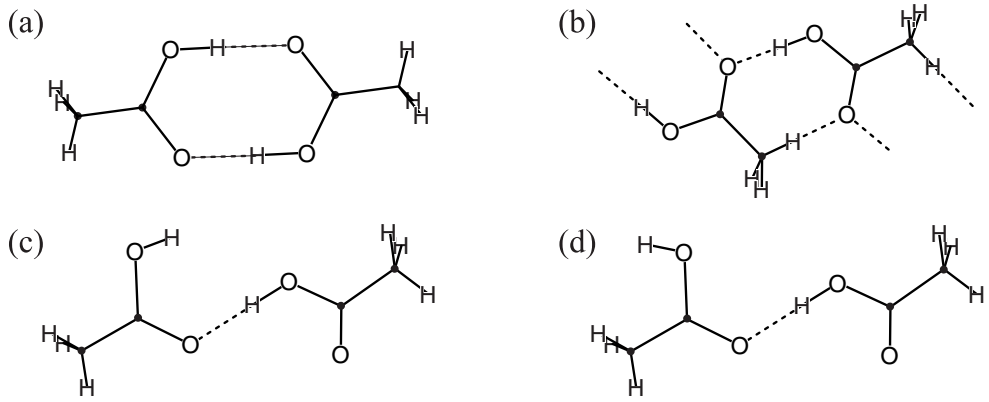

Figure 4.1: Dimer configurations reproduced from [143]: (a) symmetric cyclic dimer, (b) cyclic dimer of the crystalline unit cell, (c) cis-cis linear dimer, and (d) cis-trans linear dimer.

carboxylic acids in polar liquids including pure liquid carboxylic acids where chain-like structures of various sizes dominate [142, 143].

In Figure 4.1 the different dimer configurations of acetic acid are shown. The crystalline unit cell really consists of non-symmetric dimers which belong to the chain structure mentioned afore. The linear cis-cis and cis-trans configurations are found in less ordered chains and rings of liquid acetic acid. However, neutron and x-ray diffraction data shows a remarkable similarity of the hydrogen bond length when going from the crystal to the liquid structure and it was concluded that the liquid structure is similar to that of a disordered crystal [144–146]. The cyclic dimer features C_{2h} symmetry, i.e. it has a centre of inversion defined by its centre of mass and a symmetry axis normal to the dimer plane. It represents a valuable model system of coupled intermolecular hydrogen bonds. In terms of hydrogen bonding their structure resembles the base pairs of B-type DNA [2], in particular that of the adenine-thymine base pairs.

Although it was long known that acetic acid predominantly forms cyclic dimers in various environments, the dynamics and the underlying microscopic coupling mechanisms were still not clear for many decades. A proper quantum mechanical understanding should comprise all relevant intramolecular and intermolecular couplings. Most theoretical approaches to the problem have concentrated on modelling the optical response of the OH stretching vibration of the cyclic dimer [59, 61, 147–154] because its infrared absorption spectrum shows dramatic changes upon hydrogen-bonding. Figure 4.2 shows the absorption spectrum of the OH stretching vibration of acetic acid dissolved in carbon tetrachloride in a temperature range from close to the freezing point to just below the boiling point of the solution. The narrow band at 3538cm^{-1} represents the free OH group. Its rise reflects the increase in free OH groups with temperature as does the decrease of the broad band that belongs to the hydrogen-bonded OH groups of the symmetric cyclic dimer. The spectra show four remarkable consequences of hydrogen bond formation: (i) a strongly broadened absorption band, (ii) a red shift of the band centre, (iii) an enormous increase in total absorption cross-section, and (iv) a distinct substructure. It should be clear that linear absorption spectra do not deliver sufficient information on the various coupling mechanisms. Nonetheless, it is informative that there is little dependence of the shape of the

absorption spectrum on temperature, suggesting a minor influence of thermal populations of low-frequency modes. Rather, the band behaves more like an entity with respect to temperature in the investigated range.

The complicated lineshape has also been the object of many experimental investigations and the coupling of the OH stretching vibration to other degrees of freedom has been debated for more than half a century. There are three types of coupling mechanisms that are generally considered to be relevant: (i) anharmonic coupling to low-frequency modes, (ii) excitonic (Davydov) coupling of the two degenerate OH stretching oscillators, and (iii) anharmonic coupling to combination and overtones (Fermi resonances). All models that have been employed to describe these coupling mechanisms, justify the various coupling parameters by a more or less good agreement of the model with the OH stretching absorption in Figure 4.2. However, there is a large degree of freedom in the various model parameters and experimental verification would be desirable. Moreover, spectroscopic techniques that are capable of separating the different contributions to the absorption band, would be very beneficial to resolving this scientific dilemma.

The assignment of the low-frequency spectrum to the Raman and infrared-active vibrations was also controversial [146, 155–159]. However, the author is confident that the recent assignment [160] reflects the nature of cyclic dimer modes very well for there is unprecedented experimental and theoretical agreement that is to be discussed.

Despite the many experimental investigations of the hydrogen-bonded acetic acid dimer, only a few time-resolved spectroscopic studies of the vibrations such as pump-probe and photon echo measurements have been performed that have the potential to deliver information on ultrafast dynamics and the underlying coupling mechanisms. Hochstrasser and coworkers [161] investigated the stretching vibration of the hydrogen-bonded carbonyl group with 100fs time resolution and found a non-exponential population decay and sub-picosecond rotational diffusion. The OH stretching vibration of the same dimer was studied in picosecond pump-probe experiments [162] and an excited state lifetime of 4ps as

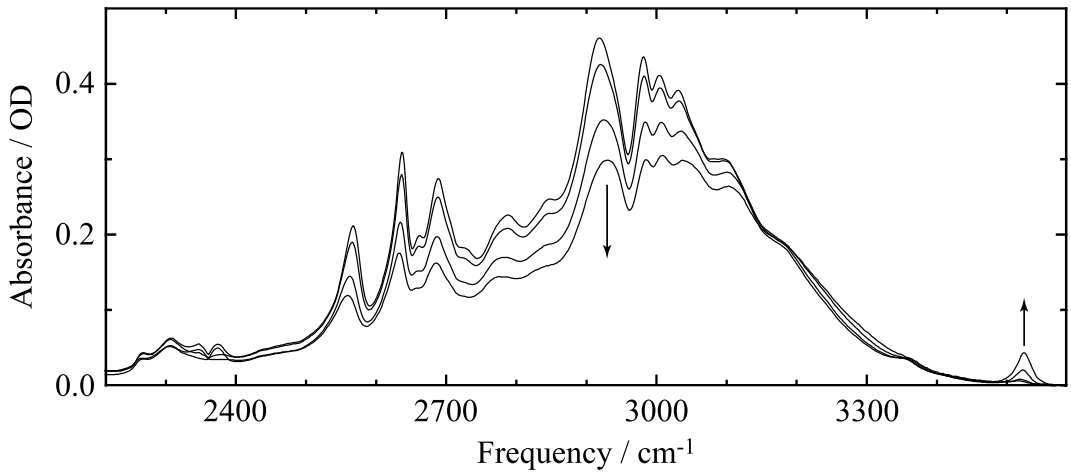

Figure 4.2: Linear absorption spectra of the 0→1 transition of the OH stretching mode for 0.5M acetic acid in CCl_4. The spectra were recorded at -25°C, -10°C, 30°C, and 70°C. The absorptive signature of the free OH group at 3538cm^{-1} increases with temperature whereas the absorption of the hydrogen-bonded OH group decrease.

well as a 15ps thermalisation component due to microscopic heat diffusion were deduced from the results. This experiment has missed relevant portions of the dynamics due to the picosecond time resolution.

In the following sections, results of experiments with 100fs time resolution are presented that reveal ultrafast coherent and incoherent dynamics of the cyclic acetic acid dimer in apolar liquid solvents. The main probe will be the OH stretching oscillator of acetic acid. The OH bending oscillator has also been probed to study the coupling between the two high-frequency vibrations of the OH group. In section 4.2, results on the coupling between the OH/OD stretching vibration and low-frequency modes of the hydrogen-bonded dimer are discussed along with excitonic (Davydov) coupling between two degenerate OH/OD stretching oscillators in symmetric dimers. In section 4.3, experiments on the coupling between the OH stretching and the OH bending mode will be presented in the context of energy relaxation pathways in acetic acid dimers. In section 4.4, coherent OH stretching excitations with photon echo spectroscopy are discussed along with a simple model for multilevel coherences in acetic acid dimers. In section 4.5, experimental and theoretical results of coherent multidimensional spectroscopy of acetic dimers are presented that elucidate the Fermi resonance coupling in the acetic acid dimer. The chapter concludes with a summary in section 4.6.

4.2 Coherent nuclear motions of hydrogen bond modes

Dynamics of hydrogen bond modes occur on ultrafast time scales. In the case of cyclic acetic acid dimers they are due to relative motions of the monomers along the hydrogen bond but involve to a smaller extent relative motion within each monomer. The two studies on acetic acid dimers that have been mentioned above [161, 162] do not reveal coupling related to dimer modes and it has been one of the objectives of this work to explore coherent nuclear motions related to hydrogen bonding [160, 163, 164].

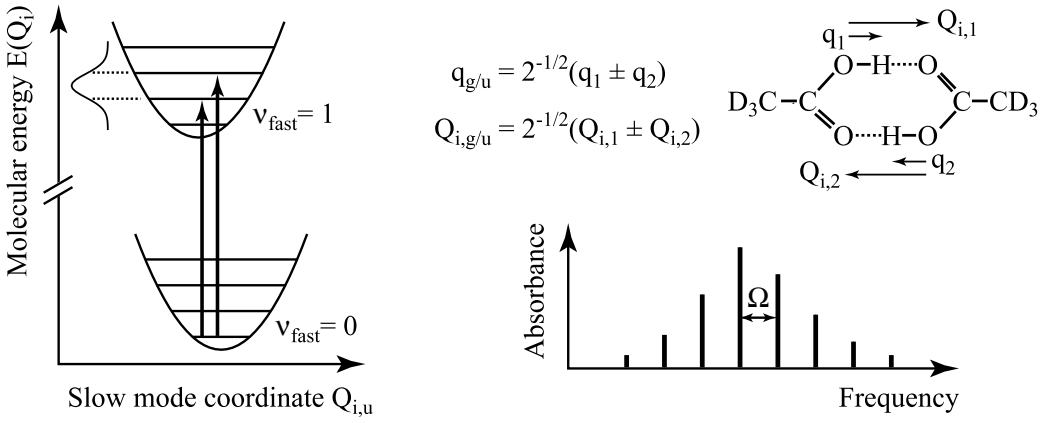

Figure 4.3: Schematic drawing of potential energy surfaces (left) and a Frank-Condon progression (bottom right). On the top right, cyclic coordinates of the $\nu_{\mathrm{OH/OD}}$ and the dimer modes for symmetric dimers are defined.

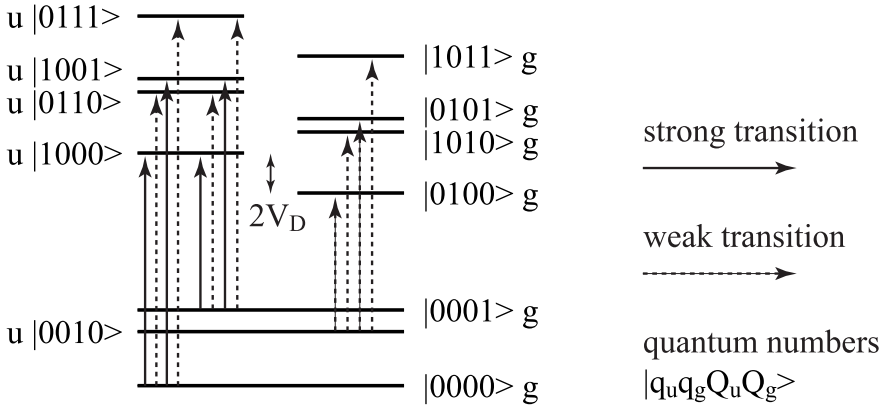

Figure 4.4: Selection rules for coupled C_{2h} symmetric oscillators with a gerade and an ungerade fast mode $q_{g/u}$ coupled to a gerade and an ungerade slow mode $Q_{g/u}$.

Strong coupling between the OH stretching vibration and modes that modulate the hydrogen bond length should be expected. The eigenfrequencies of such hydrogen bond modes are typically much smaller than those of the OH/OD stretching vibration and an adiabatic separation of time scales allows to treat the coupled modes in the Born-Oppenheimer approximation [54, 61, 165]. This description is in full analogy to electronic spectroscopy where potential energy surfaces for the electronic eigenstates are a function of the vibrational coordinates. Such a coupling mechanism will give rise to a series of transitions in the spectral domain – the well-known Frank-Condon progressions. The principle is illustrated schematically on the left of Figure 4.3. An infrared pulse causes a transition between states of the high-frequency oscillator. If the bandwidth of the pulse spans over at least one low-frequency transition, a coherent superposition of low-frequency quantum states results, i.e. a nuclear wave packet is created. After the interaction with the infrared pulse, the high-frequency mode can either be in the ground or first excited state. In the first case, a resonant Raman process has created a low-frequency wave packet in the ground state of the high-frequency oscillator that is often long-lived. If the coherent wave packet is created in the first excited state of the high-frequency oscillator, the coherence will usually not survive the population relaxation of the high-frequency oscillator. Generally, the more eigenstates participate in a coherent superposition of states, the more the resulting wave packet motion resembles classical motion.

The C_{2h} symmetry of dimers I and III allows for the introduction of nonlocal cyclic coordinates, $q_{g/u}$ and $Q_{i,g/u}$, which are termed gerade and ungerade. They are defined in Figure 4.3 and describe infrared and Raman active modes. The C_{2h} symmetry will cause a change in the Frank-Condon progression because it lifts the degeneracy between the symmetric (gerade) and the anti-symmetric (ungerade) modes as illustrated in Figure 4.4. There are two subsets of molecules, those that are thermally populated in the gerade modes and those that are populated in the ungerade modes. There will also be molecules with population in both modes, but for the relevant modes, this subset will comprise only very few molecules. Each subset will have a Frank-Condon progression that is shifted by twice the Davydov coupling V_D with respect to the progression of the other subset and

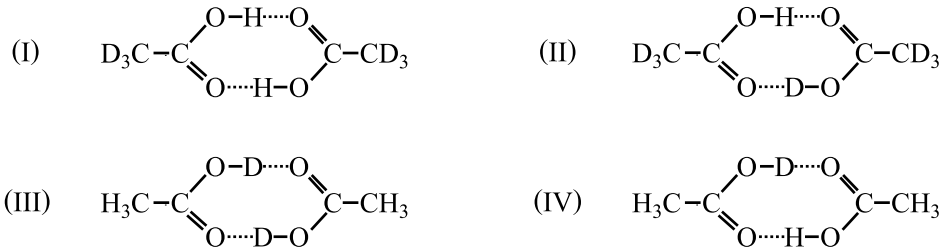

Figure 4.5: Isotopomers of cyclic acetic acid dimers: (I) methyl-deuterated OH dimer, (II) methyl-deuterated mixed OH/OD dimer, (III) carboxy-deuterated OH dimer, and (IV) mixed OH/OD dimer.

hence, shifted frequency components should appear in the linear and non-linear spectra. However, it is the nature of the heterodyne detection process to be insensitive to a beat that would correspond to $2V_D$ because the spectral components of the emitted electric fields are interfered with the much stronger probe field and the cross-term of two Davydov-shifted frequency components, $\Re\{E(\omega + V_D/\hbar)E^*(\omega - V_D/\hbar)\}$, will be of negligible intensity.

Experimental

Acetic acid with a deuterated carboxyl group (DAc-h3) and acetic acid with a deuterated methyl group (HAc-d3) were used in two-colour pump-probe experiments. The acetic acid was dissolved in carbon tetrachloride at concentrations between 0.5M and 0.8M to form cyclic dimers I and III shown on the left of Figure 4.5. To suppress excitonic coupling of the OH/OD stretching oscillators in some measurements mixtures of HAc-d3 and DAc-h3 with respective volume ratios of 1:6 and 6:1 were used for dimers II and IV, respectively. 100μm of solution were held a room temperature between two calcium fluoride windows of 2mm thickness. The sample transmission T_0 was adjusted for the optical density $A = -\log(T_0)$ to be less than 0.7. The corresponding linear absorption spectra are found in Figure 4.6.

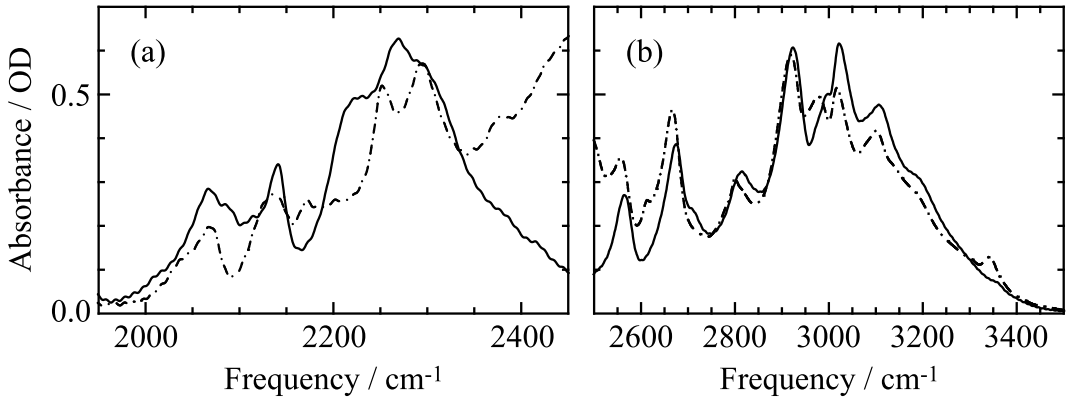

Figure 4.6: Linear absorption bands of the hydrogen-bonded OH group of dimers I and II (right, solid and dot-dashed) and the hydrogen-bonded OD group of dimers III and IV (left, solid and dot-dashed).

The OH/OD stretching vibration was monitored as a function of the probe pulse spectrum for different spectral positions of the pump-pulse. The pump and probe pulse were generated from two independently tunable optical parametric amplifiers described in section 3.1 with a pump pulse energy of 1 to 1.5μJ. The probe pulse had a factor of 20 less energy. The details of the experimental setup were already discussed in section 3.2. About 1% of the OH/OD oscillators were excited with the polarisation of the pump pulse being either parallel or perpendicular to the polarisation of the probe pulse. For the determination of population lifetimes, both signals, $\Delta A_{\parallel}$ and $\Delta A_{\perp}$, were added to retrieve the isotropic signal $\Delta A_{\circ} = (\Delta A_{\parallel} + 2\Delta A_{\perp})/3$.

Transient spectra

First, the incoherent dynamics will be discussed. Transient spectra have been recorded as a function of pump-probe delay and a section of these spectra is plotted in Figure 4.7. The transient spectra show a decrease of absorption in the central part of each spectrum between 2550cm^{-1} and 3150cm^{-1} for the OH band and between 2050cm^{-1} and 2300cm^{-1} for the OD band due to bleaching of the ground state v = 0 and stimulated emission from the first excited state v = 1. On the red side of the spectra induced absorption stems from the shifted excited state absorption of the v = 1 $\rightarrow$ 2 transition that reveals the anharmonic potential of the OH/OD stretching oscillator. The corresponding Feynman diagrams of these three contributions have been introduced in Figure 2.3. The induced absorption on the blue side of the spectra is commonly referred to as the hot ground state absorption, i.e. the v = 0' $\rightarrow$ 1' transition of the OH/OD oscillators that have relaxed to the ground state and have passed the excess energy to the immediate environment. This will be intramolecular modes of the monomer and dimer and solvent modes. The population of such accepting modes leads to an overall increase of the distance between the proton donor and acceptor groups which corresponds to a weakening of the hydrogen bond and a blue shift of the fundamental transition (cf. Figure 1.3). This relaxation pathway is

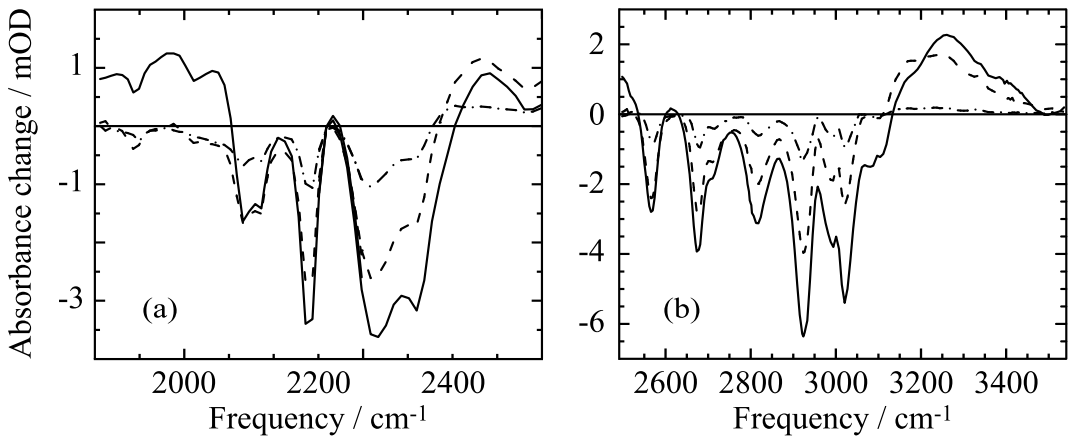

Figure 4.7: Differential absorption spectra of the OH stretching band of dimer I (a) and the OD stretching band of dimer III (b) of acetic acid for different time delays between the pump and the probe pulse (solid: 0.5ps, dashed: 2ps, dot-dashed: 16ps).

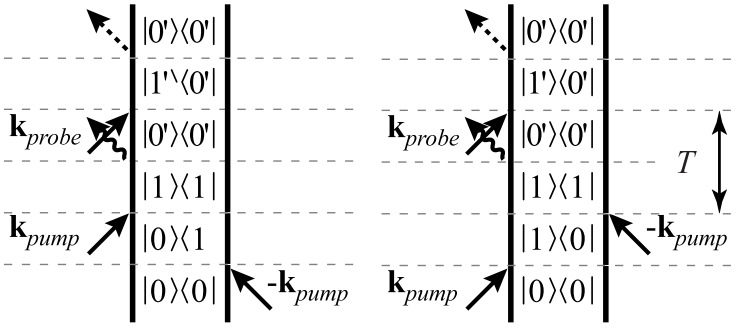

Figure 4.8: Feynman diagrams of 3^{rd} order processes with radiationless transitions (wiggled) to hot ground states.

described by the additional Feynman diagrams in Figure 4.8. Such a pathway incorporates population relaxation to the hot ground state of a molecule empirically. It should also be mentioned that no absorbance change was detected at the spectral position of the free OH/OD stretching vibration, which means that upon OH/OD stretching excitation no breaking of hydrogen bonds occurs.

The spectral holes and dips in the wings of the transient spectra coincide well with the peaks of the linear spectra. Their width and position seem to be constant up to the measured delays of 100ps. However, a more detailed analysis of the transient spectral hole centred at 2815cm^{-1} has been performed by fitting a Lorentzian and a baseline with variable slope and offset to the range of the spectral hole. Its width and centre position are plotted in Figure 4.9 as a function of time delay. The width of the spectral hole shows pronounced oscillations that will be discussed below in the context of coherent dynamics. The mean hole width changes by about ten percent within the first 3ps and reaches a final value of about 52cm^{-1}. In the same time range, the centre of the spectral hole shifts to the blue. Biexponentials have been fit to the data with time constants of 0.5ps and 3ps obtained from the kinetics of the hole centre. The short time constant is identical to and the slower very close to measured correlation times of the solvent carbon tetrachloride [166, 167]. Similar time constants have also been observed in the spectral evolution of C=O stretching excitations of the acetic acid dimer dissolved in the same solvent [161]. Thus, the spectral evolution of the holes is attributed to solvent dynamics. The difference of the measured data and the fits has been Fourier transformed and similar frequencies are found in the modulation of the width and the centre of the spectral hole. The origin of these oscillations will be discussed below in the subsection on coherent dynamics.

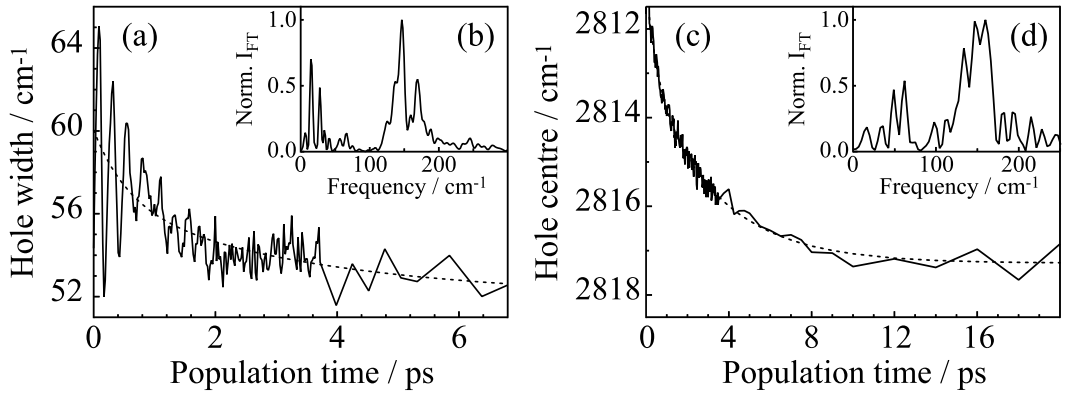

Figure 4.9: Width (a) and centre (c) of the spectral hole at 2815cm^{-1}. The dotted lines are biexponential fits with time constants of 0.5ps and 3ps. The inserts (b) and (d) show the power spectral density of the difference between measured data and fits.

The small change of width and centre frequency of the spectral holes indicates negligible spectral diffusion and suggest a predominantly homogeneous broadening of the absorption band. Thus, a Lorentzian lineshape model is apt for the analysis of the spectral hole. Echo peak shift measurements will also confirm this finding. Furthermore, the knowledge of the spectral width will be exploited in the context of polarisation decay analysis of the OH stretching vibration in section 4.4 because the maximum spectral width of the spectral features sets a lower boundary to the phase relaxation time constant (dephasing time). In structural terms, it means that the acetic acid dimer in a apolar solvent is of well defined geometry with very little inhomogeneity opposed to the other extreme case of water with a broad distribution of local structures.

Incoherent dynamics

Turning to the transient signals at certain spectral positions, time evolution of the absorbance difference after excitation of the OH stretching vibration will be discussed. The lifetime of the first excited state of the OH stretching vibration can be determined from the decay of the red-shifted excited state absorption in the spectral region where no ground state bleaching and stimulated emission is present. The pump pulse was tuned to 3000cm^{-1} in the centre of the linear absorption band and the probe pulse was set to monitor the region between 2000cm^{-1} and 2400cm^{-1}. The transient absorption for two probe pulse spectra centred at 2120cm^{-1} and 2270cm^{-1} (170cm^{-1} FWHM) was spectrally integrated and is plotted as a function of time delay in Figure 4.10. To correct for rotational diffusion, the isotropic signal $\Delta A_\circ$ was calculated and its decay analysed by fitting an instantaneous rise at zero delay and an exponential decay convoluted with the cross-correlation of pump and probe pulse to the transient in Figure 4.10c. The data is well reproduced with a time constant equivalent to the lifetime of the $v_{OH} = 1$ level of 200fs. Apart from the oscillatory behaviour, the induced absorption decay in Figure 4.10a is also reproduced with

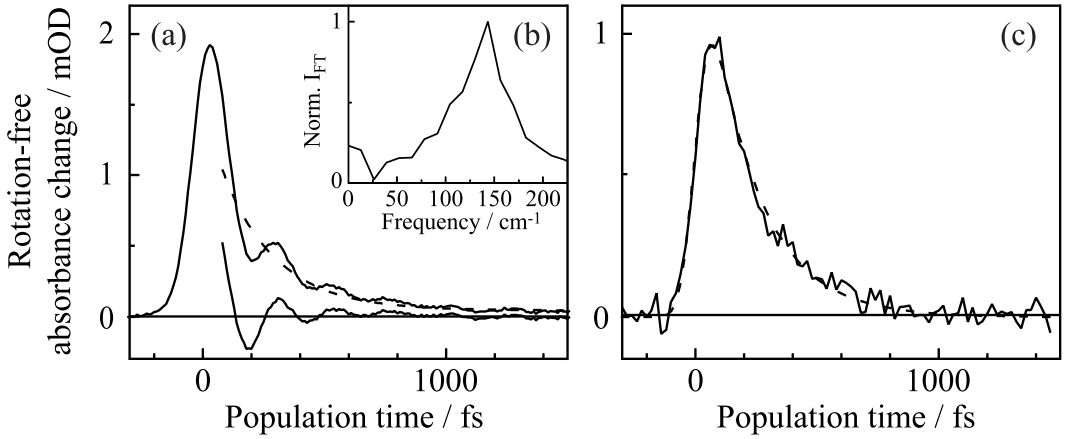

Figure 4.10: Pump-probe transients of dimer I excited at 3000cm^{-1}. (a) Spectrally integrated transient centred at 2120cm^{-1} (solid line), single exponential fit (dashed line), and oscillatory residue (dash-dotted line). (b) Normalised Fourier transform of the oscillatory component. (c) Spectrally integrated transient at 2270cm^{-1} (solid line) and numerical fit (dashed line).

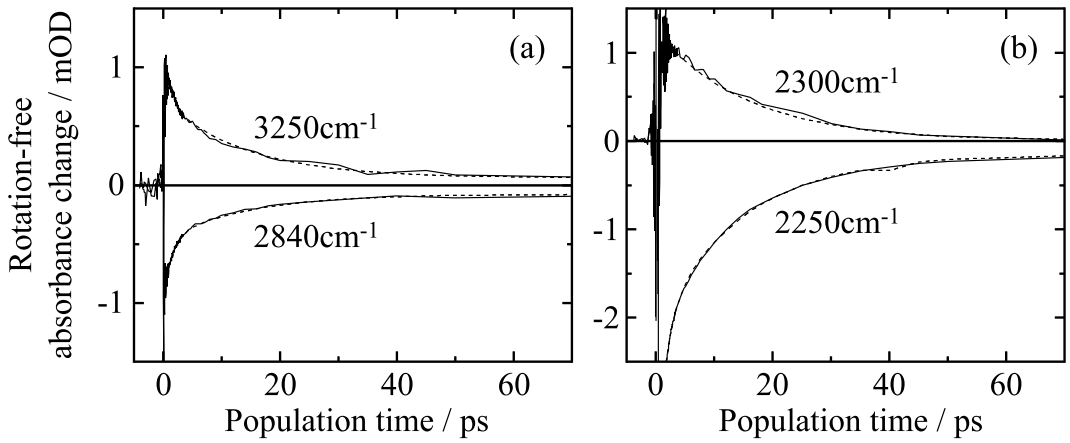

Figure 4.11: Pump-probe transients of dimers I and III. (a) Experimental data (solid) from dimer I excited at 3000cm^{-1} and triple-exponential fit (dashed) with 0.2ps, 1.3ps, and 15ps time constants. (b) Experimental data (solid) from dimer III excited at 2150cm^{-1} and triple-exponential fit (dashed) with a 0.3ps, 0.8ps, and 15ps time constants.

the same time constant. The oscillatory component will be discussed in detail in the next subsection. The lifetime of the OD stretching vibration has been extracted from global fits to the entire data set yielding 300fs for the first excited state $v_{OD} = 1$.

The incoherent dynamics in the centre and on the blue side of the transient spectra are more complex. Pump-probe transients of the OH and the OD stretching vibrations in this spectral region are plotted up to 70ps time delay in Figure 4.11. The sharp spike around zero delay is the so-called coherent artifact. It arises mainly from instantaneous contributions of the cell windows and the solvent but may also contain sample contributions from resonant quantum paths that only contribute during pulse overlap [50, 83]. Additionally, the perturbed free induction decay is present at negative delay times signalling a dephasing time longer than the time resolution of the experiment.

The response of the OH stretching vibration is best reproduced by fitting with triexponentials with time constants of 0.2ps, 1.3ps, and 15ps. For the OD stretching vibration similar time constants of 0.3ps, 0.8ps, and 15ps fit best. The short time constant is the lifetime of the first excited state, $v = 1$, with which the excited state absorption (red-shifted positive signal) and the stimulated emission (central negative signal) decay. The slower kinetics on picosecond time scales reflect intra- and intermolecular energy redistribution and cooling processes. They manifest in reduced absorption in the centre of the band due to ground state bleaching and the blue-shifted induced absorption due to hot ground state formation. The 15ps time constant for the thermally equilibrated ground state agrees very well with the largest time constant found by Seifert and coworkers [162]. A note should be made on the terms *hot* and *cool* since they usually imply some sort of temperature definition: after the stretching oscillator has relaxed to the ground state and other modes of the molecule have been populated the molecule might not be in thermodynamic equilibrium that allows to define a molecular temperature as has been shown in other systems [168–170]. As mentioned before, the hot ground state means that populated low-frequency modes (generally not being in thermal equilibrium for picoseconds) shift the $v = 0 \rightarrow 1$

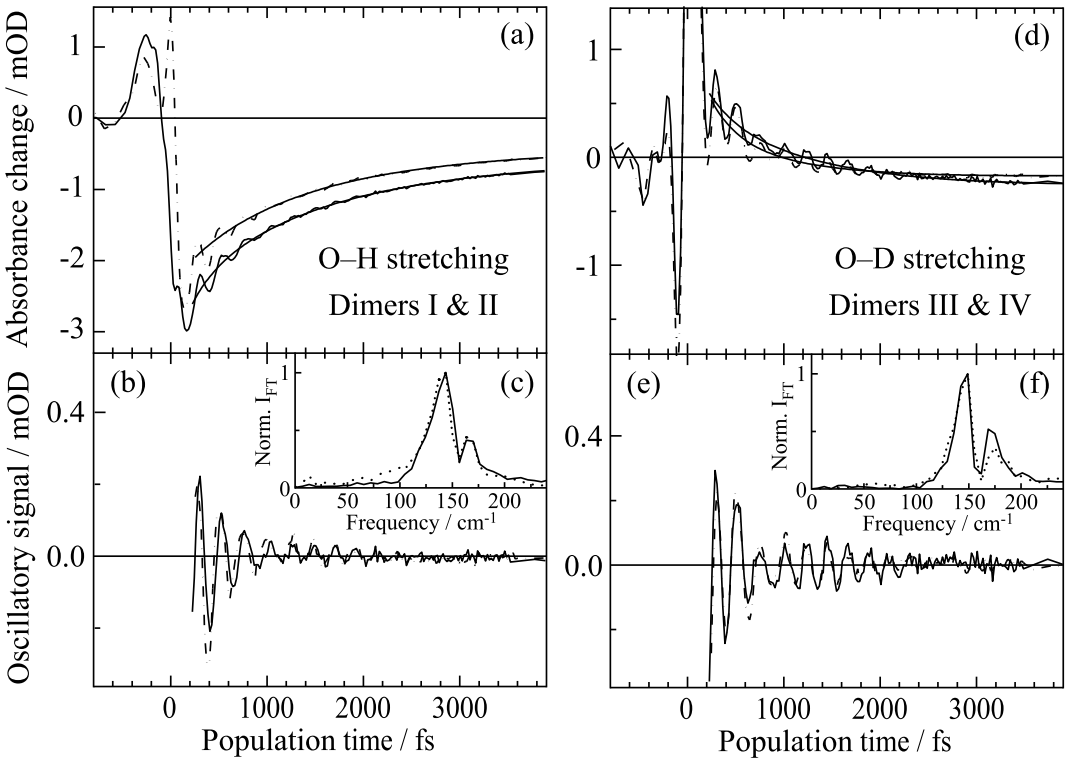

Figure 4.12: Comparison of pump-probe transients obtained from dimers I & III (solid lines) and II & IV (dash-dotted lines). Pump and probe pulses were centred at 2950cm^{-1} and 2880cm^{-1} (a–c) and at 2100cm^{-1} and 2020cm^{-1} (d–f). Triexponentials were fit to the transients with time constants of 0.2ps, 1.3ps, and 15ps (a) and 0.3ps, 0.8ps, and 15ps (d). Residual oscillations of dimers I & II (b) and of dimers III & IV (e). The corresponding normalised Fourier transforms are plotted in the inserts (c) and (f).

transition due to anharmonic coupling between the $\nu_{\mathrm{OH/OD}}$ mode and other modes of the dimer and the solvent.

So far, there was no mentioning of results from mixed dimers II and VI. In these dimers, excitonic (Davydov) coupling is absent and thus its contributions to the infrared optical response should become apparent from a comparison of the data of all four dimer isotopomers. Two transients for each pair of dimers, I & II and III & VI, are plotted in Figure 4.12 along with triexponential fits. Below the top graphs, the residual oscillations are plotted with their Fourier transforms displayed in the inserts. There is no significant difference within the uncertainty of the measurement, neither in the incoherent nor coherent dynamics. These systems behave much the same as the symmetric dimers I and III in pump-probe spectroscopy. The Davydov coupling therefore does not change the dimer dynamics significantly nor does it change the population and cooling dynamics. Lim and Hochstrasser [161] have published an investigation of the carbonyl stretching vibrations $\nu_{\mathrm{C{=}O}}$ that is in favour of a coupling constant $V_D = 56\mathrm{cm}^{-1}$ between the two $\nu_{\mathrm{C{=}O}}$ oscillators published earlier by Bertie and Michaelian [157]. The question arises whether the coupling constant for the OH/OD stretching vibration is much smaller. Since the OH stretching vibration has a 20 times smaller transition dipole moment as compared to the

$\nu_{C=O}$ vibration, the excitonic coupling should also be considerably smaller. And from the photon echo measurements on dimers I and II in section 4.4 it can be concluded that the Davydov coupling is of minor importance to the band shape; it must lie well below $56cm^{-1}$.

Coherent dynamics

All pump probe transients from the red to the blue side of the differential absorption spectra show pronounced oscillatory signals up to 3ps. These components have been isolated by subtracting multiexponential fits from the measured transients. The fits follow ordinary rate equation models and describe the incoherent dynamics. The residual signals were Fourier transformed to identify characteristic frequencies of the dimers and gain knowledge of the coupled vibrations. Transients of absorbance change are shown on the left of Figure 4.13 along with triexponential fits. The isolated oscillatory components are plotted on the right of the same figure. Weak damping and a clear beat note are evident from the residual transients alone. Fitting the sum of two exponentially damped sine functions to the residual oscillations allows for a more detailed analysis of the data. The result has been included as dashed lines in Figure 4.13. The dephasing time of these oscillations is about 700fs corresponding to a homogeneous width of $14cm^{-1}$ and the relative phase of the simulated sine waves for a given $\nu_{OH/OD}$ frequency is essentially zero.

The Fourier transforms of all oscillatory components are displayed in Figure 4.14 along with a Raman spectrum of pure liquid acetic acid. To obtain these transforms, the raw data has been sampled with 20fs delay steps up to 3.5ps. Since the oscillations have decayed by then, zero-padding has been used to exploit the fine sampling and slow decay*. Two peaks at about $145cm^{-1}$ and $165cm^{-1}$ are present in all Fourier transforms and coincide with the shoulders in the Raman spectrum. In fact, these two oscillatory components are found over the entire spectral range of the $v = 0 \rightarrow 1$ and the $v = 1 \rightarrow 2$ transition. A $45cm^{-1}$ component appears only in the centre of the OD stretching vibration where the two dominating oscillations are weak. The coupling between the $\nu_{OH/OD}$ mode and these low-frequency modes also modulates the width of the transient spectral holes in Figure 4.7 as can be inferred from comparison of the Fourier-transforms of Figures 4.9 and 4.14.

The Fourier transforms of the simulated damped sine waves match very well. Furthermore, excited state contributions have not been accounted for. In view of the short lifetime of the $v = 1$ state it is mainly the ground state wave packet, created through a resonance Raman process [80] that causes the oscillatory modulation. Interestingly, zero relative phase between the two oscillations at $145cm^{-1}$ and $165cm^{-1}$ yields the most pronounced dip at about $158cm^{-1}$ whereas a relative phase of π would not produce a dip.

The relative phase between wave packets on the blue and the red side of the $\nu_{OH/OD}$ band centre is precisely π. It reflects the oscillatory shift of the $v = 0 \rightarrow 1$ transition. In principle, inhomogeneous line broadening cannot be excluded, in particular for the broad $45cm^{-1}$ component. However, the small amplitude of this oscillatory component (or components) leaves the lineshape and exact position rather unclear. The reproducibility of the

*Interpolation of the residue data on to a constant frequency grid of 20fs step size up to maximum delay yields the same results but oversamples the Fourier transforms.

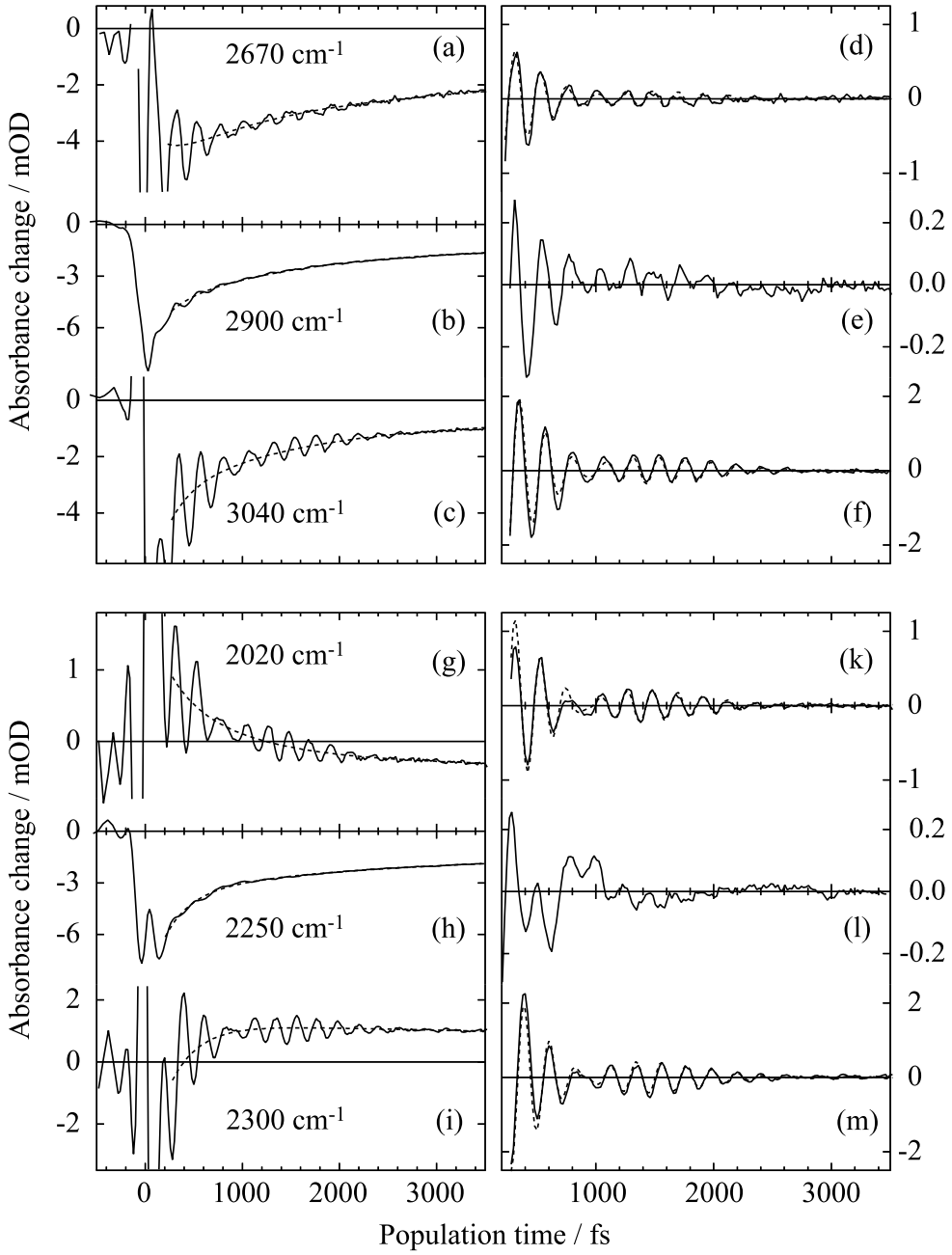

Figure 4.13: Pump-probe transients (solid lines) of dimers I (a–c) and III (g–i) and triexponential fits (dashed lines) with the time constants of Fig. 4.11. Residual oscillatory components are shown on the right (d–f) and (k–m). Two exponentially damped sine functions (T_2 = 0.7ps) have been plotted as dashed lines with frequencies of 144cm^{-1} and 163cm^{-1} and zero relative phase (d, f) and frequencies of 147cm^{-1} and 167cm^{-1} and a relative phase of 0.1π (k, m).

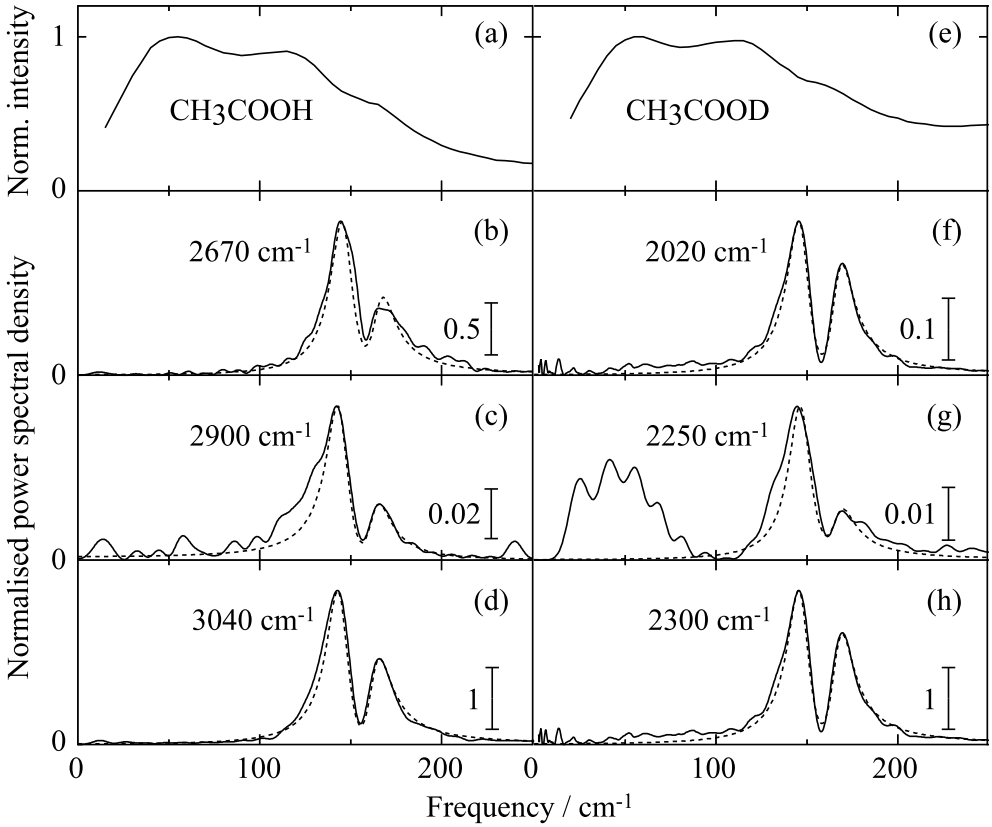

Figure 4.14: Raman spectra of liquid acetic acid taken from [158] (a and e) and Fourier transforms of the oscillatory residues of Figure 4.13 (b–d, f–h). The relative intensity of each transform is indicated by the scale bars in each graph. Fourier transforms of the damped sine fits have also been included (dashed).

lineshape of the 145cm^{-1} and 165cm^{-1} components by Lorentzian lineshapes throughout the entire spectral range and the fact that the OH stretching vibration shows negligible inhomogeneity (section 4.4) suggest homogeneous broadening of these oscillators, too.

These findings demonstrate a coupling of the OH/OD stretching vibration to several underdamped low-frequency vibrational modes with substantial modulation of the hydrogen bond length. Admittedly, it is quite remarkable that such clearly underdamped coherent vibrations persist for several picosecond in liquid phase. Since the eigenfrequencies of these modes are at least an order of magnitude smaller than those of the OH/OD stretching vibration, an adiabatic separation of time scales allows to treat the coupled modes in the Born-Oppenheimer approximation [54, 61, 165].

Theoretical modelling

It has been mentioned that several experimental and theoretical investigations have tried to elucidate the nature of the Raman band in the range of 0cm^{-1} to 250cm^{-1}. The approach outlined here [160] combines ultrafast nonlinear vibrational spectroscopy with density functional theory and a finite differences method. Harmonic normal mode infrared

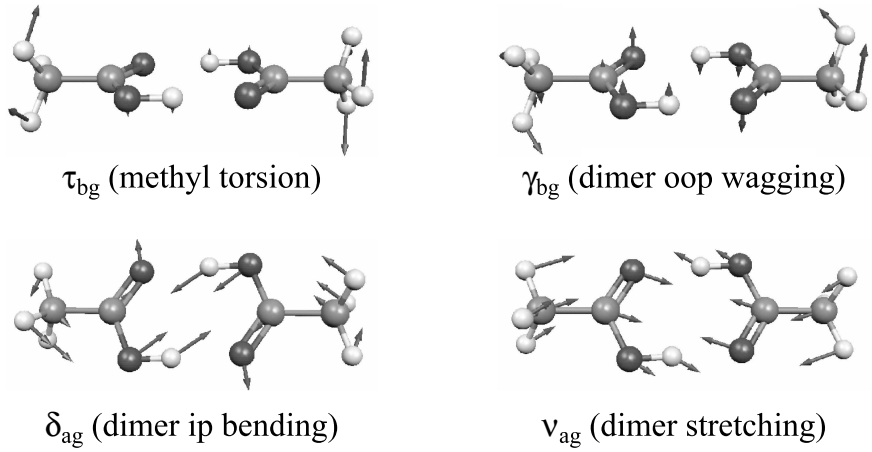

Figure 4.15: Illustration of the calculated Raman active (gerade) normal modes of the cyclic acetic dimer with eigenfrequencies of less than 200cm^{-1}.

and Raman spectra and anharmonic couplings between high- and low-frequency normal modes were calculated for isotopomers I and III of Figure 4.5 by J. Dreyer. Density functional theory (DFT) with the B3LYP functional [171–174] and the 6–311+G(d,p) basis set [175–177] as implemented in GAUSSIAN 98 [178] were used for geometry optimisation and normal mode calculations. The ultrafine grid option of GAUSSIAN 98 was used in numerical integrations with no further convergence for larger grids. The calculated geometry compares well with a recently published structure [154].

The normal mode analysis reveals four infrared and four Raman active modes with eigenfrequencies below 200cm^{-1}. All other eigenfrequencies are higher than 400cm^{-1} and the corresponding modes cannot be excited coherently by the experimentally feasible pulses. The symmetry of the dipole operator prohibits simultaneous excitation of two infrared active modes thus excluding the four infrared active low-frequency modes when exciting the infrared-active $\nu_{\mathrm{OH/OD}}$ mode. However, simultaneous excitation of the infrared-active $\nu_{\mathrm{OH/OD}}$ mode and a Raman-active low-frequency mode is allowed. The relevant Raman modes are illustrated in Figure 4.15. The arrows indicate the relative vibrational amplitude of the molecular parts in a classical picture. Three of these modes are not present in monomers but result from hydrogen bonding. The coupling between the fast OH/OD stretching mode and these normal modes was implemented by Taylor expansion of the potential energy V in the dimensionless coordinates of the normal modes. The expansion was performed with respect to the equilibrium geometry and was truncated after fourth order. The latter was restricted to semi-diagonal quartic force constants:

$$V = \frac{1}{2}\sum_{i}^{N}\Omega_i q_i^2 + \frac{1}{6}\sum_{i,j,k}^{N}\Phi_{ijk}q_i q_j q_k + \frac{1}{24}\sum_{i,j,k}^{N}\Phi_{ijkk}q_i q_j q_k^2\,, \qquad \Phi_{ijk\ldots} = \frac{\partial^n V}{\partial q_i \partial q_j \partial q_k \ldots}\,. \tag{4.1}$$

The harmonic frequencies Ω_i and the higher order force constants are the corresponding derivatives evaluated at the equilibrium point. The third and higher order force constants were calculated numerically by three-point finite differences as proposed by Schneider and Thiel [179] with a dimensionless displacement of 0.04. The cubic force constants constitute

	$(CH_3\text{-}COOH)_2$			$(CD_3\text{-}COOH)_2$			$(CH_3\text{-}COOD)_2$			$(CD_3\text{-}COOD)_2$		
j	Ω_j	ρ_j	ϕ_{i^2j}	Ω_j	ρ_j	ϕ_{i^2j}	Ω_j	ρ_j	ϕ_{i^2j}	Ω_j	ρ_j	ϕ_{i^2j}
τ_{bg}	44	0.75	2*	33	0.75	-2*	44	0.75	2*	33	0.75	-3*
γ_{bg}	118	0.75	0	111	0.75	0	118	0.75	0	111	0.75	0
δ_{ag}	159	0.65	151	155	0.67	148	156	0.67	111	153	0.67	109
ν_{ag}	174	0.07	-145	169	0.08	-143	174	0.09	-103	168	0.09	-102

Table 4.1: Theoretically calculated dimer modes of four symmetric isotopomers: harmonic frequencies Ω_j, depolarisation ratios ρ_j, and cubic force constants Φ_{i^2j} (for values with *, Φ_{ij^2} is given) with $i = \nu_{\mathrm{OH/OD}}(b_u)$ and low-frequency modes j (in cm^{-1}).

the main contribution to the off-diagonal anharmonic coupling parameters between the OH/OD stretching mode and the Raman modes. They are summarised along with the harmonic frequencies and depolarisation ratios in Table 4.1. For better comparison with experimental data, the calculated Raman spectra and cubic force constants are also plotted below the experimental Raman spectra by Nielsen and Lund in Figure 4.16 and may be compared with the spectra in Figure 4.14. The methyl torsion mode τ_{bg} is assigned to the lowest frequency of 44(33)cm^{-1} and shows the largest Raman activity and isotopic frequency shift (-11cm^{-1}) upon methyl group deuteration. It is only weakly coupled to the $\nu_{\mathrm{OH/OD}}$ mode. The out-of-plane wagging mode γ_{bg} shows similar Raman activity and an isotopic shift of -7cm^{-1} but does not couple to the $\nu_{\mathrm{OH/OD}}$ mode. As is to be expected from geometrical arguments, the stretching and in-plane bending modes influence most strongly the $\nu_{\mathrm{OH/OD}}$ mode and display the largest couplings of more than 100cm^{-1}. Raman activity follows the decreasing experimental spectrum. These results not only reproduce the main features of the Raman spectra but are in excellent agreement with the experimental findings of figure 4.14. Even the small negative isotopic shift of about 3cm^{-1} upon deuteration of the methyl groups is reproduced.

The above assignment differs from the work of Nielsen and Lund who measured fully depolarised components at 45cm^{-1} and 110cm^{-1} and a partially polarised component at around 165cm^{-1}. In the C_{2h} group, the B_g modes are fully depolarised ($\rho_j = 0.75$) whereas the A_g modes are at least partially polarised ($\rho_j < 0.75$). Nielsen and Lund took only the three dimer modes into consideration and concluded that the most polarised stretching vibration causes the peak at 165cm^{-1} and assigned the in-plane bending vibration δ_{ag} to be the 45cm^{-1} component. Table 4.1 shows that indeed the δ_{ag} mode is only weakly polarised. The out-of-plane wagging and methyl torsion mode are fully depolarised and it is most conclusive from the point of depolarisation measurements to assign both B_g modes to the lowest frequency maxima. Bertie and Michaelian [157] held a lattice mode of the liquid responsible for the 45cm^{-1} component. The excellent agreement with relative Raman activities and experimental frequency positions of the strongly coupled dimer modes strongly support our interpretation. Finally, the Hartree-Fock-based calculations of

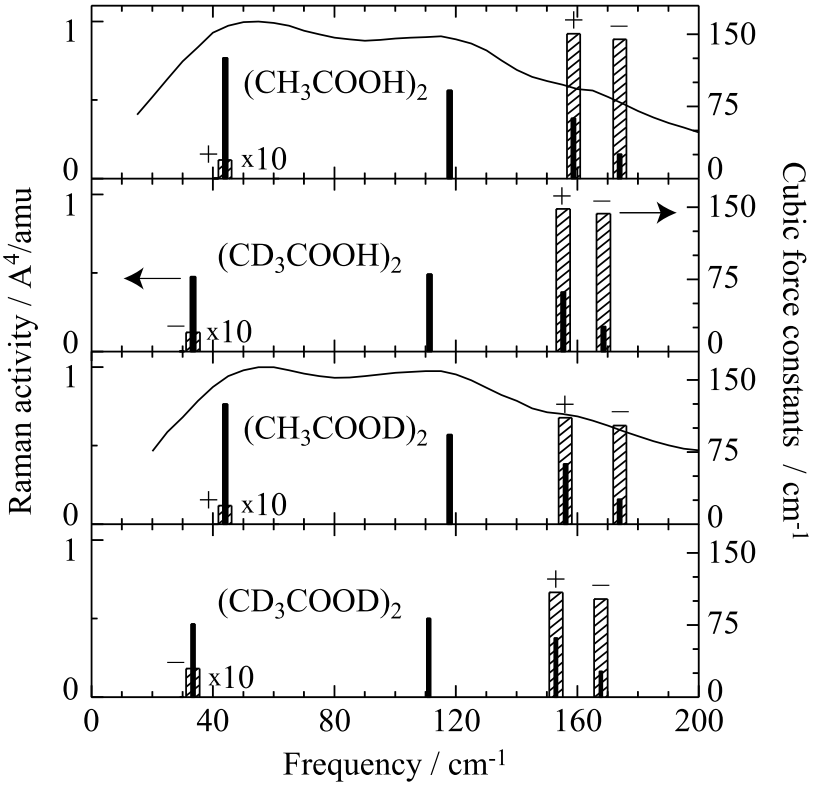

Figure 4.16: Measured [158] and calculated Raman spectra of low-frequency normal modes (solid bars, left ordinate) and cubic force constants Φ (hashed bars, right ordinate). + and − denote the sign of the force constants.

Nakabayashi and coworkers [146] give less good agreement in terms of frequency positions of the four Raman active modes but lead to the similar assignments with the methyl torsion modes as the lowest vibration and the dimer stretching mode as the one with highest eigenfrequency.

To this point, the anharmonic coupling to low-frequency modes as one of the three main coupling mechanisms between the OH/OD stretching mode and its environment has been identified and described quantitatively. But the resulting Frank-Condon progression cannot account for the extremely large absorption band of this mode for two reasons: (i) the maxima of the absorption band are irregularly spaced and do not match the two interleaved progressions and (ii) the temperature dependence of the hot bands of Frank-Condon progressions is not evident in Figure 4.2. Also, the spectrally resolved pump-probe technique is inherently insensitive to Davydov coupling in the time domain and the congested lineshapes of the linear spectra do not allow to identify the coupling parameter V_D. But the spectrally integrated photon echo experiments in section 4.4 will show the weak magnitude of this coupling type. The coupling via Fermi resonances has been suggested as the coupling mechanism that predominantly determines the lineshape [153, 154]. Indeed, it will become apparent in section 4.5 that ultrafast two-dimensional spectroscopy combined with high-level DFT calculations will confirm this view.

4.3 Vibrational coupling & relaxation of OH excitations

The results of the previous section have shown that the excited state decays rapidly but the ground state bleaching persists for tens of picoseconds while other modes that couple anharmonically to the OH stretching vibration are transiently populated. The multitude of coupling mechanisms raises the question which possible energy relaxation pathways exist that cause this behaviour. This issue has been mainly discussed in the context of the OH stretching vibration of isotopically substituted water HOD and opposing views either favour the relaxation of the ν_{OH} quantum into low-frequency hydrogen bond modes or consider the Fermi resonance with the first overtone of the OH bending vibration, δ_{OH}, to be the main relaxation channel. In acetic acid dimers, several vibrational modes have states that are believed to be in Fermi resonance with each other. With respect to the first excited state v = 1 of the OH stretching vibration, these states are overtones and combination tones of the OH bending vibration, the carbonyl ($\nu_{\mathrm{C=O}}$) and the C–O ($\nu_{\mathrm{C-O}}$) stretching vibrations, and the methyl group wagging mode ($\gamma_{\mathrm{CH_3}}$). The present section discusses two-colour pump-probe experiments that investigate the lifetime of the OH bending vibration and its anharmonic coupling to the OH stretching vibration [180].

Experimental

Methyl-deuterated acetic acid was dissolved in carbon tetrachloride at 0.3M. A 100μm thick layer of the solution was held between two barium fluoride windows of 1mm thickness at 294K. The relevant part of the linear infrared spectrum of the OH group is shown in Figure 4.17. The broad band of the OH stretching vibration centred at about 2900cm^{-1} is believed to contain several Fermi resonances. The absorption maximum at 2815cm^{-1} has been attributed to such a resonance between the first excited state of the stretching mode with a combination tone of the bending mode. This combination tone would contain one quantum of the infrared active and one quantum of the Raman active bending mode. To

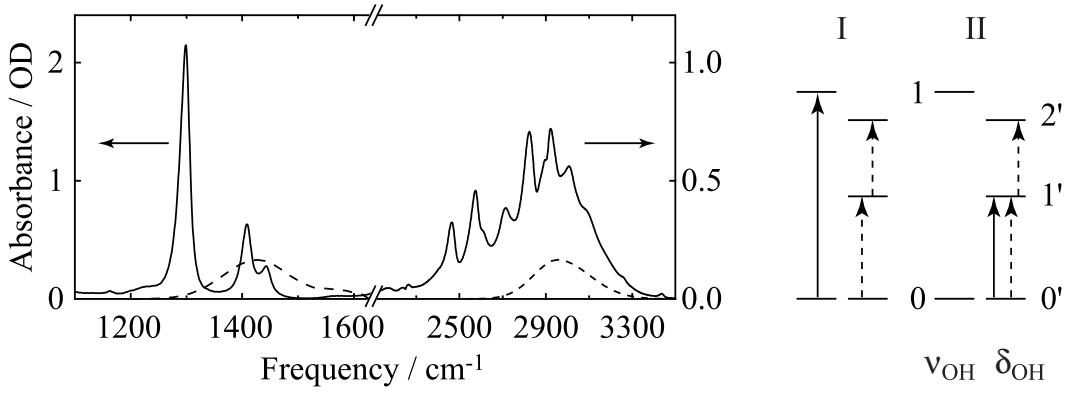

Figure 4.17: Linear absorption spectrum of $(CD_3COOH)_2$ in CCl_4, solvent contributions have been subtracted. Absorption bands of the C–O stretching, OH bending, and OH stretching modes are centred at about 1300cm^{-1}, 1410cm^{-1}, and 2900cm^{-1}, respectively. The dashed curves are the spectra of the pump pulses. In the level scheme of OH stretching and bending vibrations, the solid and dashed arrows represent the pump and probe pulse interactions, respectively.

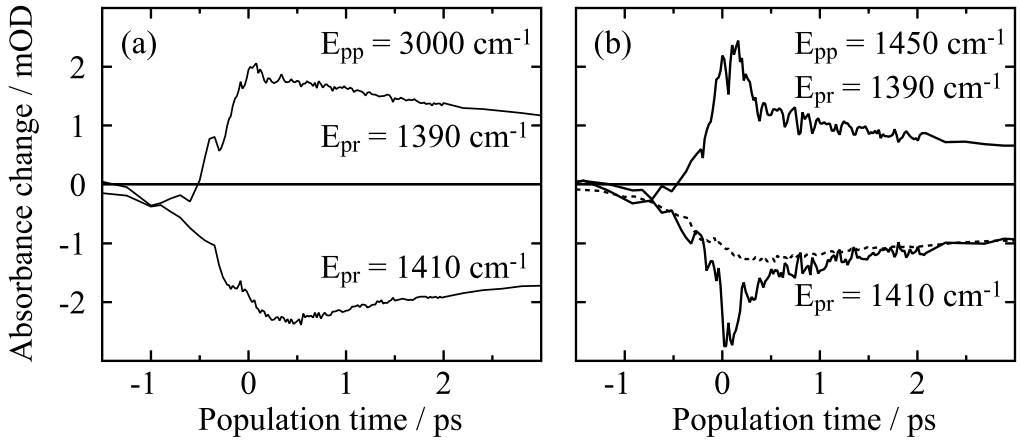

Figure 4.18: Pump-probe transients in the spectral region of the OH bending vibration. (a) transient absorbance change for excitation at 3000cm^{-1} and (b) transient absorbance change for excitation at 1450cm^{-1}. The dotted curve is the 1410cm^{-1} transient of panel (a) that has been rescaled by a factor of 0.55.

investigate the coupling between the OH stretching and bending vibrations, two infrared pulses from independently tunable optical parametric amplifiers were used. Details on these amplifiers are described in section 3.1 and on the experimental setup in section 3.2. The pump pulse of 1μJ energy and 100fs duration was tuned to 3000cm^{-1} in pump scheme I to induce the v = 0 $\rightarrow$ 1 transition of the stretching mode. For pump scheme II, it was tuned to 1450cm^{-1} to induce the v = 0' $\rightarrow$ 1' transition of the bending mode.

The probe pulse monitored the absorbance change of the v = 0' $\rightarrow$ 1' and 1' $\rightarrow$ 2' transitions in both schemes. The v = 2' $\rightarrow$ 3' transitions of the bending mode must also be considered in pump scheme I in which the v = 1 state of the stretching vibration is populated. If coupling between the two modes existed, the v = 2' $\rightarrow$ 3' transition would show as enhanced absorption on the red side of the fundamental transition because the v = 2' state would be populated along with the v = 1 state of the stretching vibration. This signal would rise within the time resolution of the experiment and drop with the lifetime of the v = 1 state. Subsequent population relaxation to the first excited state v = 1' of the bending mode would also induce a redshifted enhanced absorption of the probe pulse. A rise of induced excited state absorption on the v = 1' $\rightarrow$ 2' transition and a drop of absorption on the v = 0' $\rightarrow$ 1' transition due to bleaching of the ground state would display dynamics with time constants dictated by the 200fs lifetime of the v = 1 state. This dynamical behaviour can be compared with the OH bending mode transitions upon direct excitation of the v = 1' state as depicted in the pump scheme II.

Results and discussion

Transients of absorbance change in the spectral region of the bending vibration are shown in Figure 4.18. First, the transients in panel (a) are discussed that rise after excitation of the OH stretching vibration. At negative delay time, the probe precedes the pump pulse and a decrease in absorption with a time constant of 500fs is noticeable. The cross-

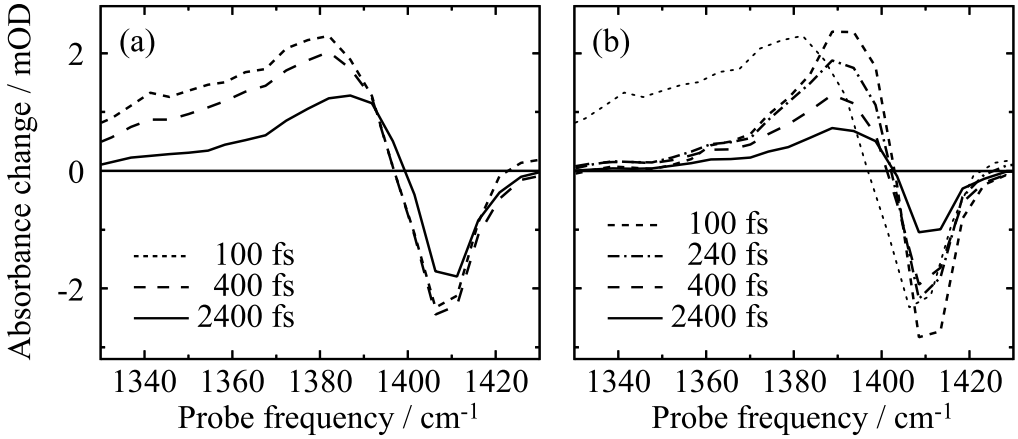

Figure 4.19: Transient absorption difference spectra of the OH bending vibration obtained with (a) the pump pulse centred at 3000cm^{-1} and (b) the pump pulse centred at 1450cm^{-1}. The 100fs transient spectrum of panel (a) has been plotted as a dotted line in panel (b) for better comparison.

correlation of pump and probe pulse is much shorter so that this signal can be attributed to the perturbed free induction decay that rises with the dephasing time T_2 of the $|0'\rangle\langle 1'|$ coherence. The dephasing time is related to the linewidth $\Gamma = (\pi c T_2)^{-1} = 21\text{cm}^{-1}$. This value agrees very well (within 1%) with the width of a Lorentzian fit to the OH bending peak at 1408cm^{-1} in Figure 4.17 and is strong evidence for homogeneous broadening of this transition. The fit itself matches within the noise level of the linear spectrum.

After the maximum absorbance change at zero delay has been reached, the enhanced absorption at 1390cm^{-1} and the reduced absorption at 1410cm^{-1} decays over a delay range of 60ps. There is no evidence of fast dynamics on the order of the v = 1 lifetime of the ν_{OH} mode. The transients in panel (b) of Figure 4.18 show the absorbance change for excitation pulses centred at 1450cm^{-1}. Clearly, a fast decay of the enhanced absorption at 1390cm^{-1} to about half the peak value and the analogous decay of decreased absorption at 1410cm^{-1} are visible for delay times below 1ps. For delay times longer than 1ps the dynamics are much the same in the transients whether excitation occurs at 3000cm^{-1} or at 1450cm^{-1}. A double-exponential fit to the transients that were obtained when exciting at 1450cm^{-1} yields a fast 250fs component and a slow 15ps component. The fast component is the lifetime of the first excited state of the OH bending vibration which is very similar to that of the OH stretching vibration. The long component describes the cooling dynamics that are essentially identical to those of the ν_{OH} ground state bleaching.

Transient spectra of the same data set are shown in Figure 4.19. There is also a marked difference between the spectra whether excitation takes place around 3000cm^{-1} or 1450cm^{-1}. A fast decay of induced absorption on the red side of the fundamental transition is noticeable in panel (b). This feature is absent in panel (a). For easier comparison the 100fs transient spectrum for excitation at 3000cm^{-1} has been plotted as a dotted line in panel (b). The induced absorption is shifted more to the red and also extends much further in the same direction. However, the two spectra at 2400fs resemble each other much more than the other spectral pairs do. The lack of fast dynamics and the simulta-

neous rise of enhanced and decreased absorption in Figure 4.18a suggest a red shift of the v = 0' → 1' transition that is due to anharmonic coupling of the δ_{OH} mode to the ν_{OH} mode. When the v = 1 state is depopulated with a lifetime of 200fs other modes (possibly low-frequency modes) are populated that are also coupled to the δ_{OH} mode. This coupling causes a similar red shift that more closely resembles the red shift that is observed when the v = 1' state has been directly excited and relaxed again. Such behaviour of the δ_{OH} mode is not so surprising since it has been observed in other system before [17, 181, 182].

To conclude this section, the dephasing time of the 0' → 1' transition of the OH bending vibration has been observed in accordance with the homogeneous lineshape. A lifetime of 250fs for the v = 1' state has been measured but no transient population of that state is detected upon OH stretching excitation in contrast to another system with an intramolecular hydrogen bond [183] that has been investigated recently. Rather, anharmonic coupling between the two states shifts the 0' → 1' transition to lower frequencies as does the population of low-frequency modes coupled to the OH bending vibration.

4.4 Multilevel quantum coherences of OH stretching excitations

The optical properties of solvents and solutions are closely related to fast structural dynamics on sub-picosecond time scales and in turn provide means to study these ultrafast dynamics. Many investigations on structural correlations in liquids have been performed in the visible spectral range [48, 87, 90] but ultrafast vibrational spectroscopy has engendered as a valuable tool because of the local character of many vibrational oscillators and their sensitivity to the microscopic surroundings [41, 184]. In particular, numerous investigations on liquid water have been published which will be reviewed in the next chapter. Concerning the dephasing dynamics of acetic acid dimers, not much has been explored apart from the work of Lim and Hochstrasser.

Lack of spectral diffusion in acetic acid dimers (Fig. 4.9) hints at homogeneously broadened transitions and indeed, the following photon echo experiments reveal the homogeneous nature of the OH stretching transition. However, the liquid environment with its fluctuating short- and long-range forces that govern the structural dynamics on a multitude of time scales may generate different environments for the dimer ensemble. Thus, it is not clear to what extent inhomogeneous broadening contributes to the vibrational transitions in the acetic acid dimer. Furthermore, vibrational dephasing processes have been described for coherent excitations on transitions of anharmonic oscillators that are subjected to fluctuating forces of the solvent [28, 185] but it is unknown how the dephasing is influenced by the complicated multi-level structure of the cyclic dimers and how the various coupling mechanisms manifest themselves.

The present section is dedicated to the dephasing of the fundamental transition of the OH stretching vibration of the two isotopomers shown on the right of Figure 4.20. The difference of interest between these two dimers is the absence of Davydov coupling in the mixed dimer. The absorption spectra of the OH stretching vibration on the left side of the same figure look much alike and the pump-probe experiments of previous sections

showed that the dimer modes are not influenced by this coupling mechanism between OH stretching oscillators. However, self-heterodyning in spectrally resolved pump-probe experiments renders this technique insensitive to interference of spectral components that could supply information on Davydov coupling.

Experimental

Pure liquid acetic acid (CH_3COOH) was dissolved in carbon tetrachloride to yield a solution of 0.2M with a peak absorbance of 0.4OD at 2925cm^{-1}. For mixed dimers the same volume of pure acetic acid and 2.57ml of fully deuterated acetic acid (CD_3COOD) were dissolved in 23.4ml carbon tetrachloride. This solution had a 20% higher peak absorbance mostly due to the background of the fully deuterated species. The spectra in Figure 4.20 have been rescaled for better comparison. The solution was pumped through a stainless steel flow cell with Teflon spacers that provide 0.2mm sample thickness. The flow speed was sufficient to exchange the excitation volume from pulse to pulse. The focus of the infrared light was slightly less than 0.1mm. The cell windows were made of 2mm calcium fluoride and provided sufficiently low group velocity dispersion at 3000cm^{-1} for pulses of 130cm^{-1} spectral width. The thinnest possible windows should be used to reduce non-resonant window contribution as far as possible. The sample thickness is limited by the maximum concentration of dimers that excludes non-negligible formation of aggregates. The lower acetic acid concentrations in the photon echo experiments compared to those in the pump-probe experiments are necessary because the photon echo signal is more sensitive to optical density if no heterodyne detection is used and the signal intensity rather than the signal amplitude is measured. Signal reduction is already substantial at 0.6OD.

Infrared pulses of about 120fs were generated in an optical parametric amplifier with a KTP crystal as the nonlinear optical medium. The pulse shape varies across the tuning range of the OPA. Of the three spectral positions used in the experiments it is shortest and closest to a Gaussian profile at 3120cm^{-1}. The pulse features an exponential-like decay on the trailing edge of the photon echo signal at 2830cm^{-1}. The same type of

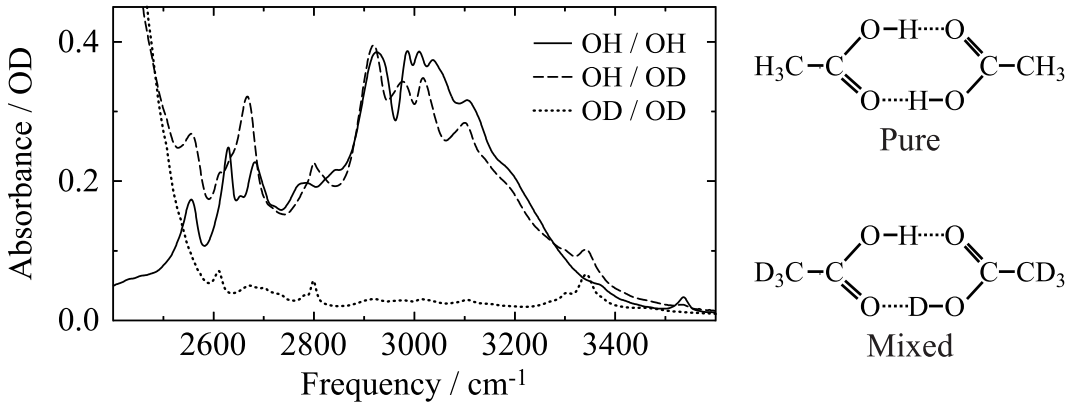

Figure 4.20: Linear absorption spectra of the OH stretching vibration of three isotopomers of cyclic acetic acid dimers. The solid line belongs to the pure dimer and the dashed-dotted line to the mixed one. The linear absorption of the fully deuterated dimer is shown as a dotted line.

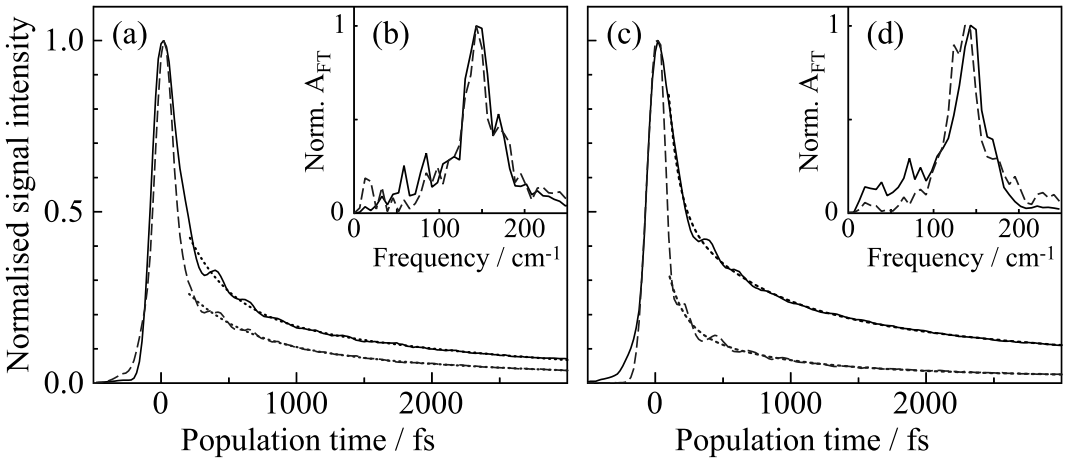

Figure 4.21: Transient grating scans. (a) Signals of pure (solid) and mixed dimers (dashed), and double-exponential fits (dotted) with time constants of 0.6ps and 6.5ps. Pulses were centred at 2940cm^{-1}. (b) Fourier transforms of residual oscillations with line encoding of (a). (c) Signal of the pure dimer with pulses centred at 2830cm^{-1} (solid) and 3120cm^{-1} (dashed). Fits are shown as dotted lines. (d) Fourier transforms of residual oscillations with line encoding of (c).

behaviour on the rising edge has been observed above 3300cm^{-1} [186]. It can probably be attributed to chirp due to group velocity dispersion of the KTP crystal. A detailed description of the optical parametric amplifier is found in section 3.1. The mid-infrared pulse was split in three replicas, two of which were passed over optical delay stages as shown in Figure 3.6. Parabolic mirrors with 142mm effective focal length were used to create focal spots below 100μm in the sample. In the photon echo experiments, the first pulse $(\mathbf{k}_1, \omega_1)$ was advanced with respect to the other two by the coherence time τ to measure the homogeneous dephasing of the coherent excitations. The transient grating scans were performed with the first two pulses fully overlapped and the third pulse $(\mathbf{k}_3, \omega_3)$ was delayed by the population time T. The signal was detected in the phase-matched directions $\mathbf{k}_3 \pm (\mathbf{k}_2 - \mathbf{k}_1)$. Further details of the experiment are described in section 3.3.

Transient grating dynamics

Transient grating scans give information on population dynamics, similar to pump-probe experiments. But the spectrally integrated transient grating signal contains contributions from the diffractive part of the optical response, resulting in additional signals contributions during pulse overlap. Therefore, early population dynamics are partially hidden.

Spectrally integrated transient grating scans are displayed in Figure 4.21. The initial rise reflects the time resolution and the main part of the signal has no distinct features. This signal contains non-resonant signals intensities from the calcium fluoride windows, the solvent, and the solute. After the cross-correlation time of 150fs (Figure 3.9) the signal stems solely from the acetic acid dimers. Weak oscillatory modulation of the signals is observable and double exponential fits allow to isolate those oscillations. Subsequent Fourier transformation reveals well-known low-frequency maxima at positions of the dimer

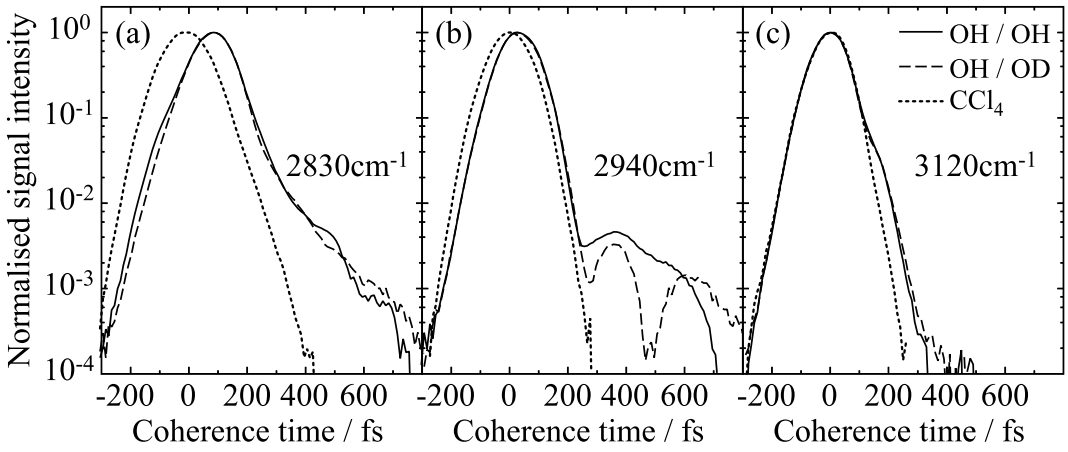

Figure 4.22: Photon echo scans of the solvent (dotted), the pure acetic acid dimer (solid), and the mixed acetic acid dimer (dashed) are shown for three spectral positions of the excitation pulses: (a) 2830cm^{-1}, (b) 2940cm^{-1}, (c) 3120cm^{-1}.

stretching and in-plane bending modes at about 145cm^{-1} and more weakly at 165cm^{-1}, thus retrieving the results of previous pump-probe measurements. The time constants of the double-exponentials correspond quite well to the 1.3 and 15ps used in fitting triple-exponentials to the pump-probe transients. Note that transient grating intensities rather than electric field amplitudes are measured. Hence, extracted decay constants correspond to half the lifetime determined in pump-probe experiments. In principle a fast component of 100fs can be fit to the transient gratings signals, albeit with less accuracy than the pump-probe data and a refined deconvolution is advisable. Nonetheless, the two techniques give consistent results for the population and low-frequency wave packet dynamics. The signal difference between the pure and the mixed dimer is caused by the optical density of the mixed sample which is already quite high; concentration-dependent photon echoes show signal saturation for optical densities approaching 0.4OD.

Photon echoes

Photon echo scans have been measured with a high signal-to-noise ratio of better than 10^4 for three spectral positions of the excitation pulses. The resulting time traces are displayed in Figure 4.22. An initial pulse-width limited decay over the first order of magnitude is common in all signals. An increasing peak shift is observed the more red-shifted the excitation pulse spectrum is. Weak oscillatory modulations are evident at 2830cm^{-1} and to a lesser extent at 3120cm^{-1} due to the extremely rapid coherence decay. At 2940cm^{-1}, a pulse width limited decay over more than two orders of magnitude is visible but in particular for the mixed dimer, clear recurrences of the signal are visible up to coherence times of more than 800fs.

The temporal separation of the photon echo signal recurrences agrees well with an average frequency of 150cm^{-1}. This finding suggests a modulation of the OH stretching coherence by the low-frequency wave packets of the dimer stretching and in-plane bending

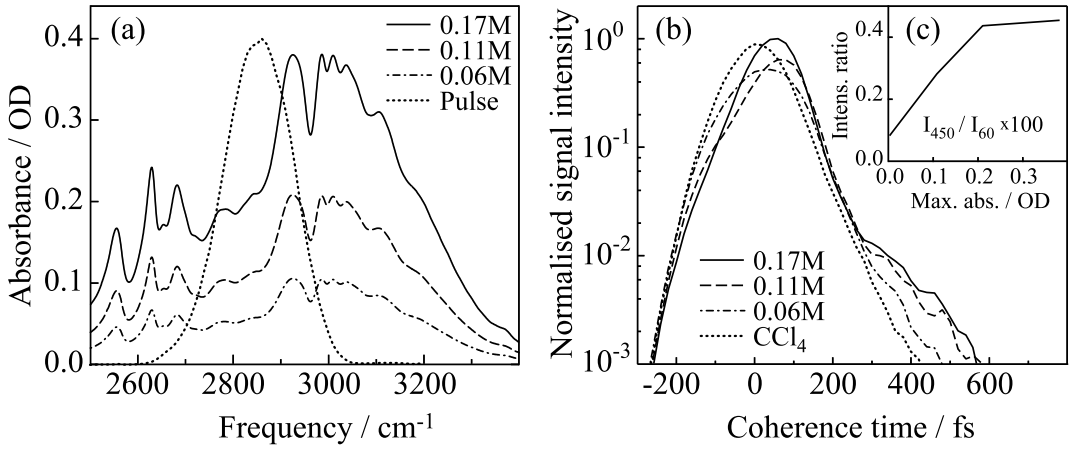

Figure 4.23: (a) Linear spectra of pure acetic acid (CH_3COOH) for three concentrations as indicated in the legend and the spectrum of the excitation pulses, (b) photon echo measurements for the three concentrations and the solvent response (dotted), and (c) intensity ratio of the echo signal for coherence times of 60fs and 450fs. Pulses were centred at 2830cm^{-1}.

modes. Such modulated coherences were already observed in visible photon echo spectroscopy [187, 188]. For such signal decays, the real dephasing time is difficult to extract without an estimate of the solvent and window contributions and a model that takes the recurrences into account. The peak shift is also inconclusive with respect to spectral inhomogeneity. It is evident from the data in Figure 4.22 that only little differences between the pure and the mixed dimer exist although no heterodyne detection was used. This clearly shows the minute influence of Davydov coupling on the spectroscopic data. Some theoretical models have proposed coupling constants on the order of 100cm^{-1} [61, 75] but a more realistic value is an order of magnitude smaller.

The solvent contribution to the four-wave mixing signal was investigated by comparing the photon echo scans of solutions with different acetic acid concentrations. The linear spectra for these mixtures are plotted in Figure 4.23 along with the pulse spectrum in panel (a). No higher concentrations than the standard one of about 0.2M were used. The coherence time scans of the solvent response and the three solutions are shown in panel (b) of the same figure. The solvent response and the data of the highest concentration reproduce the data in Figure 4.22a. The two intermediate concentrations show signals with rising edges shift from the solvent response to the high concentration signal. This measurement demonstrates that the solvent contribution does not dominate the first order of magnitude of the signal as might have been concluded from the measurements in Figure 4.22. In Figure 4.23c the ratio of the signal intensities at 60fs and 450fs coherence time, I_{450}/I_{60}, is displayed as a function of peak optical density. Saturation behaviour of intensity ratios for optical densities above 0.2OD is observed although the absolute intensity is still increasing. The absolute signal increase seems to be limited to maximum optical densities of 0.6OD, in contrast to pump-probe signals. It is surprising that the signal decreases so strongly when creating solutions of only 0.1OD peak absorption. The reason might be the extensive spatial filtering of the optical detection pathway to suppress scattered light from the sample windows, and other surfaces.

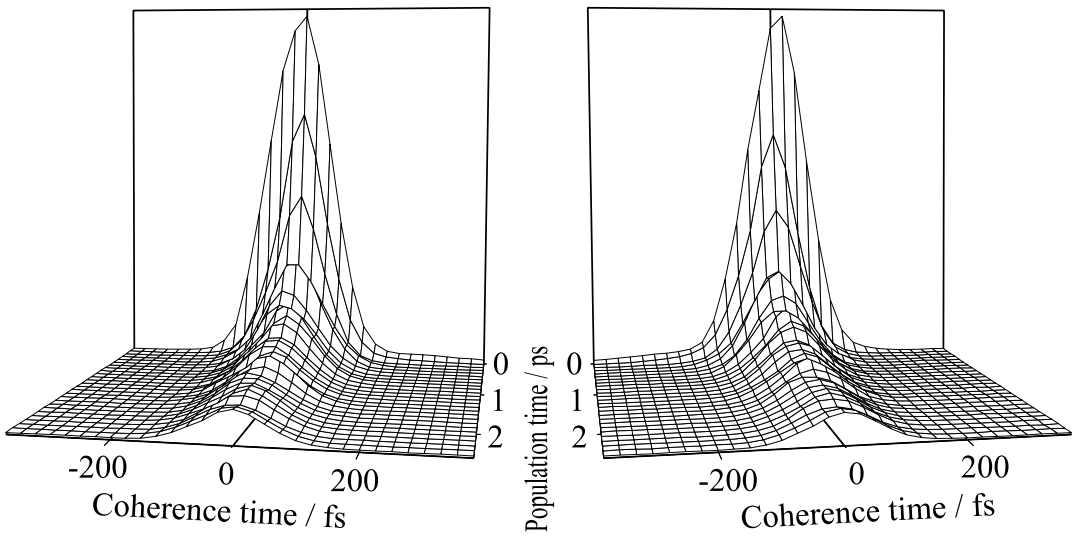

Figure 4.24: Real and virtual photon echo signals as a function of coherence and population time for excitation at 2940cm^{-1}. In both channels similar intensities have been recorded and normalised to unity. All axes have linear scales.

Peak shift measurements

The echo peak shift in four-wave mixing experiments has been theoretically introduced in section 2.3. For simple two-level systems the peak shift decay resembles the frequency fluctuation correlation function (FFCF) of the probed transition and can provide time constants for structural correlations of the fluctuating environment (hereafter called the bath). The dynamical behaviour of the FFCF controls the time characteristics of the coherences that are monitored by the experiment. In the static limit, the frequency fluctuations are very small compared to the inverse correlation time of the bath, τ_{Bath}, and the dephasing will have a Gaussian nature. In the fast modulation (motional narrowing) limit the frequency fluctuations are much greater than τ_{Bath} and an average transition frequency with a Lorentzian linewidth results.

Experimentally, an echo peak shift is recorded by scanning the coherence time τ as a function of the population time T. For $T = 0$ the peak shift of the photon echo signal is largest and in the static limit remains shifted from $\tau = 0$. It usually decays in a complex manner. A data set recorded for excitation at 2940cm^{-1} is shown in Figure 4.24. The data set on the right side is the recorded photon echo in the phase-matched direction $\mathbf{k}_3 + (\mathbf{k}_2 - \mathbf{k}_1)$. The mirror image on the left side is the data set of the second detection channel that records the so-called virtual photon echo, i.e. the signal of the non-rephasing quantum pathways in the direction $\mathbf{k}_3 - (\mathbf{k}_2 - \mathbf{k}_1)$. For negative delay, the virtual echo corresponds to the echo decay and thus, provides a mirror image of the real echo. The dual channel recording is commonly employed for a more accurate determination of zero coherence time. Each data set is fit with a series of Gaussian functions along the coherence time axis to determine the position of maximum signal intensity as a function of population time. The difference between the two maxima is twice the peak shift of the photon echo.

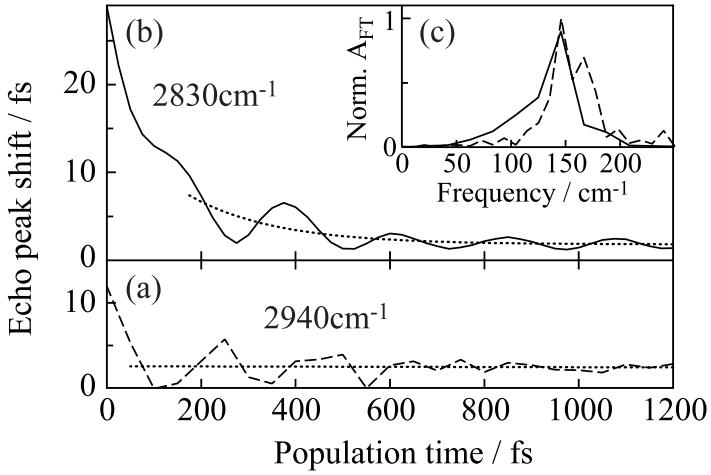

Figure 4.25: (a) Echo peak shift (dashed) of the data in Figure 4.24 and a linear regression (dotted) to isolate the oscillatory component (b) Echo peak shift as a function of population time (solid) for excitation at 2830cm^{-1} and an exponential fit (dotted) with a time constant of 180fs and an offset of 2fs. (c) Fourier transforms of the residual oscillations with the corresponding line coding of panels (a) and (b).

Such a scan is shown in Figure 4.24. The peak shift is hardly visible but becomes clearer after a quantitative analysis: the signal in the vicinity of the main peak along the coherence time axis behaves like a Gaussian function. Fitting allows to extract the peak position for every time delay T quite accurately. The result as displayed in Figure 4.25a (dashed) shows an initial value of 12fs that drops to only 2fs outside the temporal pulse overlap. A second peak shift measurement was done with excitation pulses centred at 2830cm^{-1} and the result is plotted as the solid graph in Figure 4.25b. The initial peak shift of about 30cm^{-1} is much larger but is less than half that value outside the temporal pulse overlap. The seemingly omnipresent oscillatory modulation is also present in both peak shift data. A linear regression (panel a) and an exponential fit with a constant offset (panel b) were used to isolate the oscillatory signals and determine the long-lived inhomogeneities that are beyond the recorded population time of 1.2 (solid) and 2.5ps (dashed). The Fourier transforms of the residual oscillations are displayed in Figure 4.25c and show peaks at 145cm^{-1} and 165cm^{-1}. The slower peak shift decay at 2830cm^{-1} can partly be ascribed to the longer pulses and the chirp that leads to an exponentially decaying pulse edge. There is also a correlation between increasing peak shift and decreasing excitation frequency.

Finally, the question arises what the remaining static component of the peak shift represents. It is likely to be within measurement error but may also be caused by the solvent relaxation: the afore-mentioned work [161] on the carbonyl stretching vibration revealed a two-component frequency fluctuation correlation with a fast sub-50fs and a slower 2ps component. The fast component decays during pulse overlap and was not assigned. The 2ps component has been attributed to the solvent's rotational correlation time that was determined from quadrupolar relaxation [166] of ^{35}Cl in CCl_4. The more recent work on solvent dynamics [168] also revealed a 0.5ps component that has also been found in the shift of the spectral holes of Figure 4.7.

In conclusion, the peak shift measurements reveal the predominantly homogeneous broadening of the $0 \rightarrow 1$ transition of the OH stretching vibration. The width of the transient spectral holes in Figure 4.9 is thus a good measure of the inverse dephasing time. The peak shift itself is negligible though clearly modulated by the dimer stretching and in-plane bending modes through anharmonic coupling.

Theoretical modelling

Equipped with information on the line broadening, the strong and weak anharmonic coupling to three low-frequency modes, and the solvent contribution to the four-wave mixing signal, the third-order response was modelled by use of a density matrix formalism [189]. A model Hamiltonian of the form (2.22) was used and the three Feynman diagrams that contribute to photon echo signal, $R_1^\dagger$, R_2, and R_3, where calculated in the form of (2.41). The lineshape function was approximated by an exponential function that corresponds to a homogeneous linewidth of 55cm^{-1}. Two low-frequency modes at 150cm^{-1} and 50cm^{-1} were assumed with a strong coupling of the first mode and a weak coupling of the second mode, i.e. the dimensionless displacements were chosen to be $|\mathbf{D}_{150}| = 0.7$ and $|\mathbf{D}_{50}| = 0.2$. For the calculation of the Frank-Condon factors equation 2.43 was employed. The level scheme consisted of $\mathrm{v}_{\mathrm{OH}} = 0, 1, 2$, $\mathrm{v}_{150} = 0, \ldots, 7$, and $\mathrm{v}_{50} = 0, \ldots, 20$ and all transitions within a bandwidth of $\pm 160\text{cm}^{-1}$ relative to the pulse spectrum centred at 2940cm^{-1} were taken into account. The temperature in the Boltzmann factor $P(a)$ that weighted the different quantum pathways was set to 294K. The contributions during pulse overlap, i.e. non-rephasing diagrams and small window and solvent contributions were empirically incorporated by adding an instantaneous component to the calculated signal with a relative amplitude ratio of 4 to 1 at coherence time zero. The pulse convolution was performed with 100fs pulses.

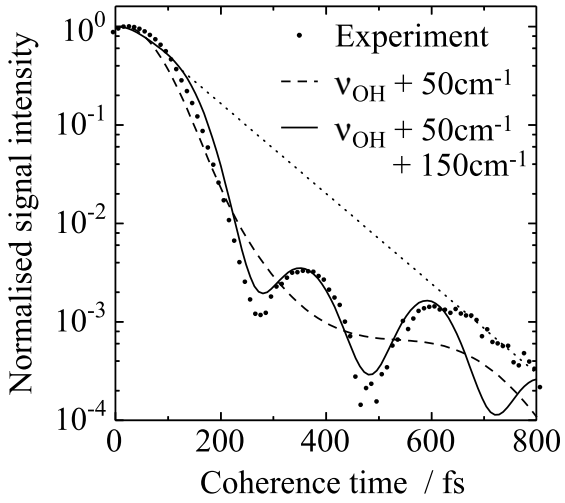

Figure 4.26: Comparison of measured and calculated four-wave mixing intensities. The scattered points are the experimental data from Figure 4.22b, the dashed line is a calculation with a weakly coupled 50cm^{-1} mode, the solid line is comprises a 50cm^{-1} and a 150cm^{-1} mode. The dotted line is a 100fs exponential decay.

The results are compared to the experimental data in Figure 4.26. The round symbols are the measured data, the solid line is the calculated photon echo with the two low-frequency modes. The 150cm^{-1} mode is phase-shifted by π with respect to the peak of the signal at 30fs coherence time. The calculation is in good agreement with the data and reproduces the initial fast non-exponential decay quite well. For a better comparison the dotted line is included in the figure that simulates a coherence decay of a two-level system with a dephasing time T_2 of 200fs. The recurrences originate from the coherent excitations of the 150cm^{-1} progression that underlies the broad OH stretching band centred at about 2950cm^{-1}. This simple model also suggests a slower modulation of the echo decay that arises from a coherent excitations of the 50cm^{-1} progression and the apparent fast decay of the coherence only partially reflects the loss of coherence. The actual decay of the coherence between the ground and first excited state of the OH stretching vibration occurs with a dephasing time T_2 of 200fs. If coupling to the low-frequency modes of the cyclic dimer was absent, the dephasing of coherent OH stretching excitations would result in a exponential decay as indicated by the dotted line in Figure 4.26. In conclusion, the multilevel character of the ν_{OH} vibration also manifests in the complex dephasing dynamics which displays pronounced quantum beats. Coherent excitations of this multilevel structure decay with a dephasing time of 200fs.

4.5 The role of Fermi resonances

The simple model reproduces the data surprisingly well but the role of Fermi-resonances has until now not been elucidated. The anharmonic coupling between the OH stretching and the infrared-active bending vibration has been demonstrated and the questions remains as to how these resonances contribute to the spectrum. Theoretical studies suggest that the Fermi resonances contribute substantially if not dominate the linear spectrum and the anharmonic coupling to dimer modes is of minor importance [75, 153, 154]. On the other hand, the fingerprint of these low-frequency vibrations seem omnipresent in all time-resolved data presented in the previous chapter. The results in this final section on two-dimensional spectroscopic experiments in conjunction with density functional theory will reconcile these two findings and identify the Fermi resonances as the coupling mechanism that mainly determines the shape of the linear spectrum [77, 78, 190].

Experimental

The sample preparation was identical to that of the previous section. The original light source for photon echo experiments was replaced by an extended BBO based optical parametric amplifier with three amplification passes through BBO crystals. The schematic drawing of the setup is shown in Figure 3.2. The reader is again referred to section 3.1 for details on the amplifier setup. The pulses were characterised by the solvent response as described in section 3.7 yielding pulse durations between 60fs and 80fs (FWHM). However, the bandwidth of the intensity spectrum usually exceeded 270cm^{-1}, the latter corresponding to almost 400cm^{-1} FWHM in amplitude. The chirp on the pulse had not been compensated at the time of the experiment. The pulses were spectrally tuned to the centre

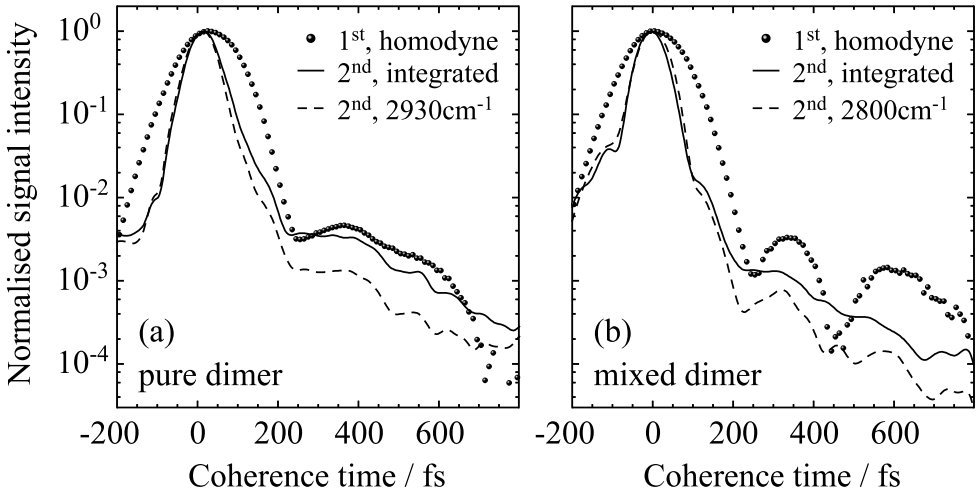

Figure 4.27: Comparison of spectrally integrated data of Figure 4.22b (symbols) and photon echo data recorded with spectral interferometry. The intensity of the spectrally resolved data is shown at a specific frequency (dashed) and as the numerical integral over the recorded spectral range (solid) for the pure (a) and the mixed (b) dimer.

of the OH stretching band. A pronounced shoulder on the red side of the pulse spectra aided recording 2D spectra over the broad spectral of the ν_{OH} absorption band without shifting the pulse spectra.

The setup for two-dimensional spectroscopy is shown in Figure 3.7 and has been introduced in section 3.1 of the previous chapter. The spectrally dispersed and heterodyne-detected signal was recorded over a spectral range of 800cm^{-1} for each coherence time and the 2D data was processed as described in section 2.3. If not indicated otherwise, it is always the real part of the emitted electric field that is plotted as a function of excitation and emission frequency. Signals were recorded for 300 laser shots before the grating or the stepper motor was moved. The 2D data sets were recorded in twice in consecutive scans over the spectral range (sampling 4.5points per spectral interference period) and the temporal range (sampling in 4fs steps for the 12fs period at the centre of the OH stretching absorption) for each population time delay. A power monitor was fed to the data acquisition programme and gated data acquisition within the set power window to minimise long-term laser drifts. Data analysis was carried by use of MathWorks' Matlab© that uses algorithms from the *Numerical Recipes* [191] and the FFTW project [192].

Results

First, the new data is compared to the spectrally integrated data of Figure 4.22b. The spectrally resolved photon echo intensity was extracted from the spectral interferograms as a function of coherence time according to the procedure described on page 24. For comparison the data was numerically integrated over the recorded spectral range between 2535cm^{-1} and 3325cm^{-1}. The result is plotted in Figure 4.27 indicating a very good agreement for coherence times larger than 200fs. The improved time resolution in the

newer experiments reveals an even faster dephasing and an oscillatory modulation on the rising and the falling edge of the signal for both the pure and the mixed dimer. The clear recurrences of the mixed dimer are less pronounced in the new integrated data but for individual frequency positions the oscillations are identical and follow the model calculations. In essence, old and new data sets are consistent.

The full information of the two-dimensional data sets is plotted in Figure 4.28b and c. Panel (b) shows the 2D spectrum for zero population time. A structure of four positive peaks is observable in the centre of the 2D spectrum, two of which are off-diagonal peaks that prove the coupling of the transitions that underlie the two diagonal peaks. Negative signals on the left half of the spectrum stem from excited state absorption and have essentially vanished in the 2D spectrum at 400fs population time in panel (c). This is consistent with the v = 1 lifetime of 200fs. In this spectrum, a similar structure in the centre is found and more ridges appear on the red side of the spectrum. In the top panel, the linear absorption spectrum is plotted (solid line) along with 2D cross-sections at 2920cm^{-1} excitation frequency. The cross-section at 0fs population time is negative below 2900cm^{-1} but reveals shoulders and peaks on top throughout the detected spectral range that precisely coincide with all peaks in the linear spectrum. The cross-section at 400fs shows the same finding: the entire linear absorption spectrum consists of strongly coupled transitions.

In Figure 4.29 the real and the imaginary part of the mixed dimer 2D spectrum are displayed. The real part in panel (b) is very similar to that of the pure dimer. The comparison between the cross-section at 2920cm^{-1} (dash-dotted red) and the linear spectrum yields a more quantitative picture. The excited state absorption is superimposed on peaks and shoulders that correspond to the linear spectrum. The imaginary part is dominated by the solvent and looks complicated because it is the sum of the solvent and the acetic acid contribution. As the manifestation of causality in the spectral domain, the real and the imaginary part are unambiguously connected by the Kramers-Kronig relations [97]. The imaginary part belongs to the dispersive part of the optical response that is essentially linked to the real part of the complex refractive index. In turn, the real part mainly belongs to the absorptive part of the optical response that is described by the imaginary part of the complex refractive index. The missing cross-peaks along the excitation frequency axis in panel (c) is surprising because the 2D spectrum should be symmetric with respect to its diagonal. If the excitation pulses were chirped in a certain manor, an effective bandwidth loss along the coherence time axis might lead to an effective bandwidth loss along the excitation frequency axis. The second dimension was directly measured in the frequency domain and the spectral bandwidth was fully exploited.

The 2D spectra are the first direct experimental proof of an entirely coupled OH stretching band. The Davydov coupling can be largely excluded as a coupling mechanism that is responsible for this finding. The anharmonic coupling between the ν_{OH} mode and the low-frequency modes is large but the temperature dependence of the fundamental absorption band of the ν_{OH} mode is very week for it to be dominated by Frank-Condon progressions. To identify the pronounced peaks as mixed states due to Fermi resonances, calculations analogous to those described in section 4.2 were performed. The results are published in great detail [77, 78] and only the main results are presented in the last section of this chapter.

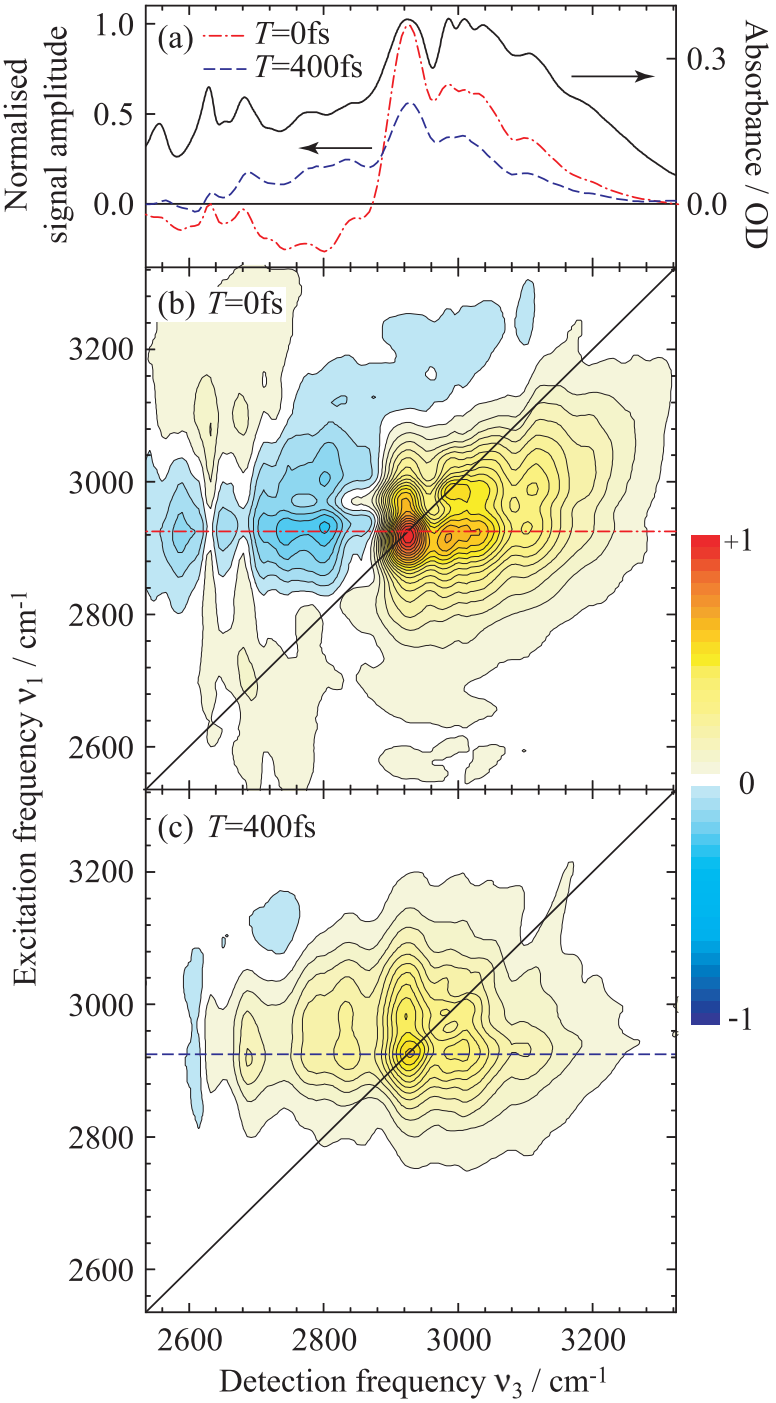

Figure 4.28: (a) Linear spectrum of pure acetic acid and cross-sections of the 2D spectra for 2910cm^{-1} excitation frequency. (b) Real part of the 2D spectrum for T=0fs. The weak solvent contribution has been subtracted. Negative signals are due to excited state absorption. (c) Real part of the 2D spectrum for T = 4000fs. No solvent contributions were observed. The excited state absorption has vanished.

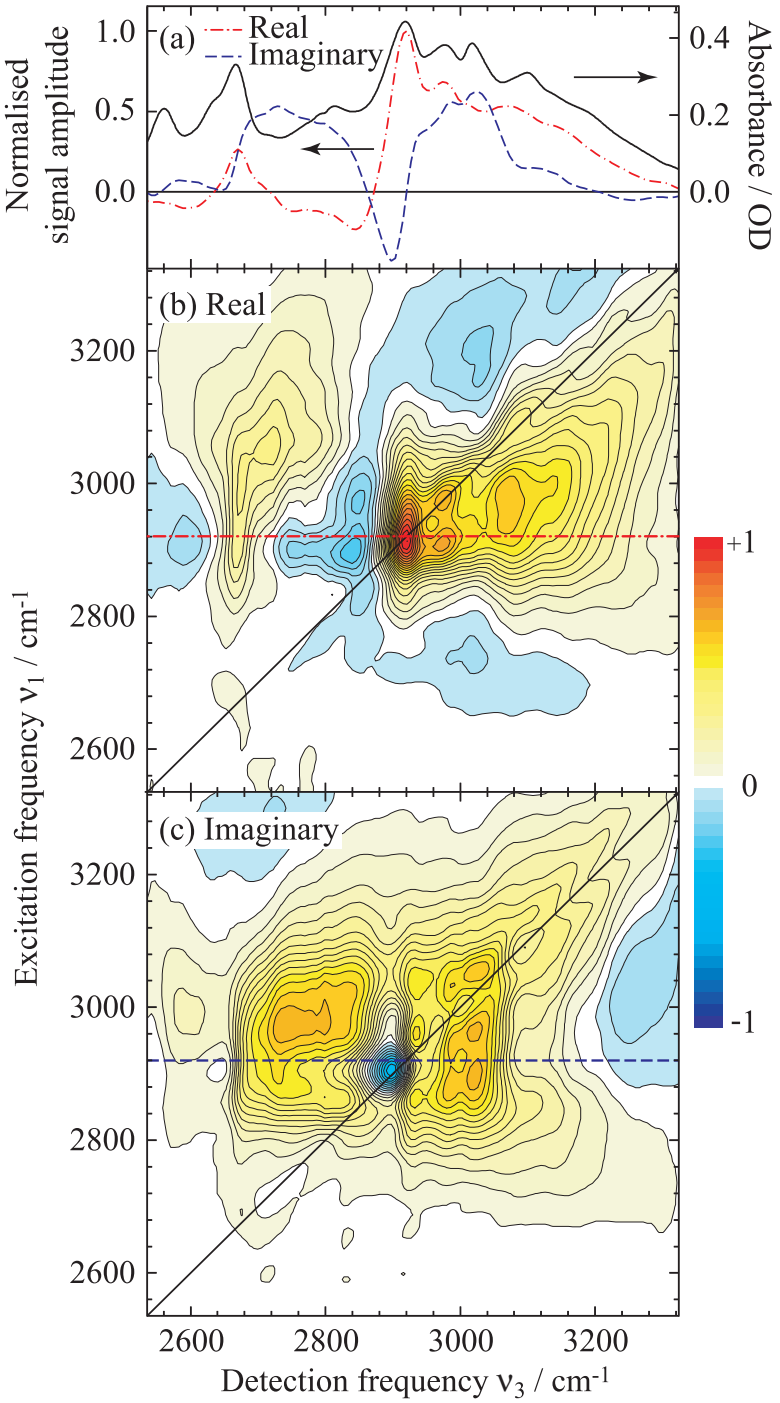

Figure 4.29: (a) Linear spectrum of mixed acetic acid (solid) and cross-sections of the 2D spectra for 2940cm^{-1} excitation frequency at T = 0fs (dash-dotted) and T = 400fs (dashed). (b) Real part of the 2D spectrum T = 0fs. The weak solvent contribution was not subtracted. Negative signals are due to excited state absorption. (c) Imaginary part of the 2D spectrum for T = 0fs. Gaussian-like solvent contributions overlap with signals from mixed dimers of acetic acid.

Modelling of the nonlinear response

Quantum-chemical calculations were performed by use of density functional theory as described on page 57. The anharmonic potential energy surfaces for the ν_{OH} mode and the ten normal modes displayed in Figure 4.30 were calculated by expansion of the potential energy V to sixth order with semi-diagonal quartic, quintic and sextic force constants:

$$\begin{aligned} V &= \sum_{i}^{N} \omega_i q_i^2 + \sum_{i,j,k}^{N} \Phi_{ijk}\, q_i q_j q_k + \sum_{i,j,k}^{N} \Phi_{ijkk}\, q_i q_j q_k q_k + \sum_{i,j,k}^{N} \Phi_{ijkkk}\, q_i q_j q_k q_k q_k \\ &\quad + \sum_{i,j,k}^{N} \Phi_{ijkkkk}\, q_i q_j q_k q_k q_k q_k\,, \qquad \Phi_{ijk\ldots} = \frac{\partial^n V}{\partial q_i \partial q_j \partial q_k \ldots}\,. \end{aligned} \tag{4.2}$$

The resulting eigenvalues of the total Hamiltonian were used to calculate the linear absorption spectrum and the third-order response of the pure dimer. The transition dipole moments were calculated by expanding the dipole moment operator to first order in the normal mode coordinates. For the calculation of nonlinear spectra, a sum over states approach was used as outlined on page 17. The temperature was 0K. Solvent interactions were empirically modelled by an exponential damping term that was deduced from the measured dephasing time of the fundamental ν_{OH} transition. This damping is equivalent to a homogeneous linewidth of $55\mathrm{cm}^{-1}$. The harmonic frequencies were shifted by a global constant in order to match the calculated linear spectrum to the experimental one. The results are shown in Figure 4.31. In the top panel the experimental linear spectrum (solid black) is compared to the homogeneously broadened calculated spectrum (dotted black). The stick spectrum underneath shows the series of calculated coupled transitions. The dashed blue and the dash-dotted red line are the cross-sections of the calculated 2D spectra in panels (b) and (c). In panel (b) the 2D spectrum is plotted as calculated from all three Feynman diagrams that contribute to an echo signal. The excited state absorption has negative contributions and is mainly found on the blue side of the spectrum. The 2D spectrum of the ground state diagram R_3 is plotted in panel (b) in which no excited state contribution from diagrams $R_1^{\dagger}$ and R_2 are present.

The excited state contributions do not agree with the experimental findings of a red-shifted overtone. It is not clear which couplings are not accounted for to cause the shift in opposite direction. However, comparison of the calculated linear and the ground state 2D spectra with the experimental counterparts show very good agreement with the experimental one in terms of structure. The calculated ground state 2D spectrum and the experimental spectrum recorded at $T = 400\mathrm{fs}$ show that the central structure and all ridges on the red side of the central transition are well reproduced. Since δ-like pulses were used in the calculations, a flat infinite pulse spectrum does not limit the detectable spectral range opposed to the experimental case. The differences in relative infrared intensities do not match so well but one has to keep in mind that the calculations do not comprise hot bands that arise for nonzero temperatures and lead to an increased signal on the high-frequency-side of the spectra. Furthermore, a gas-phase model is used that does not explicitly account for solute-solvent interactions. Instead, homogeneous broadening was introduced empirically. The agreement between theory and experimental gas-phase spectra [77, 78] is even better and shows the very good quality of the theoretical model.

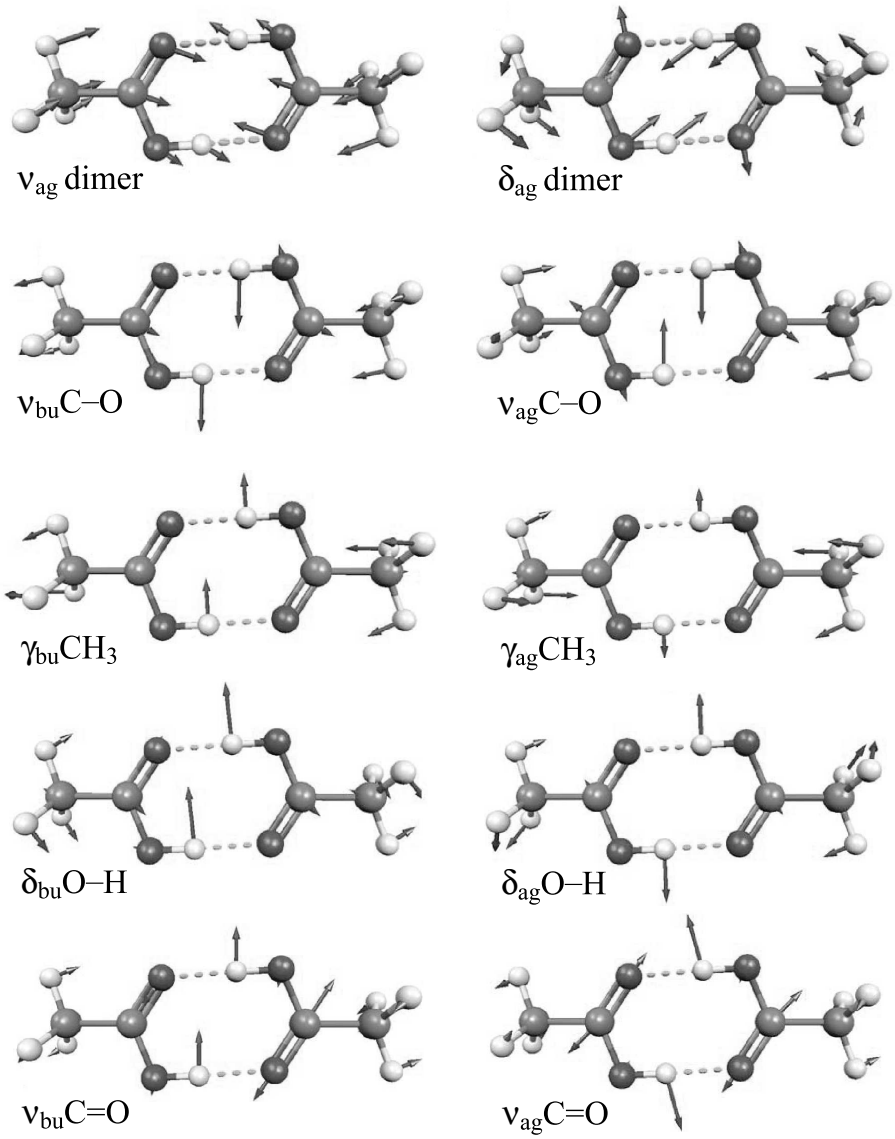

Figure 4.30: Normal modes with strong anharmonic coupling to the $\nu_{\mathrm{OH}}(b_u)$ mode and relevant contributions to the absorption band. The two modes on the top are the dimer stretching (left) and in-plane bending (right) modes. The remaining eight modes are the so-called fingerprint modes of the respective groups. Stretching vibrations are denoted by ν, bending vibrations by δ, and torsional vibrations by γ. The IR active high-frequency modes are placed on the left, the Raman active ones on the right. The arrows indicate the amplitude of displacement.

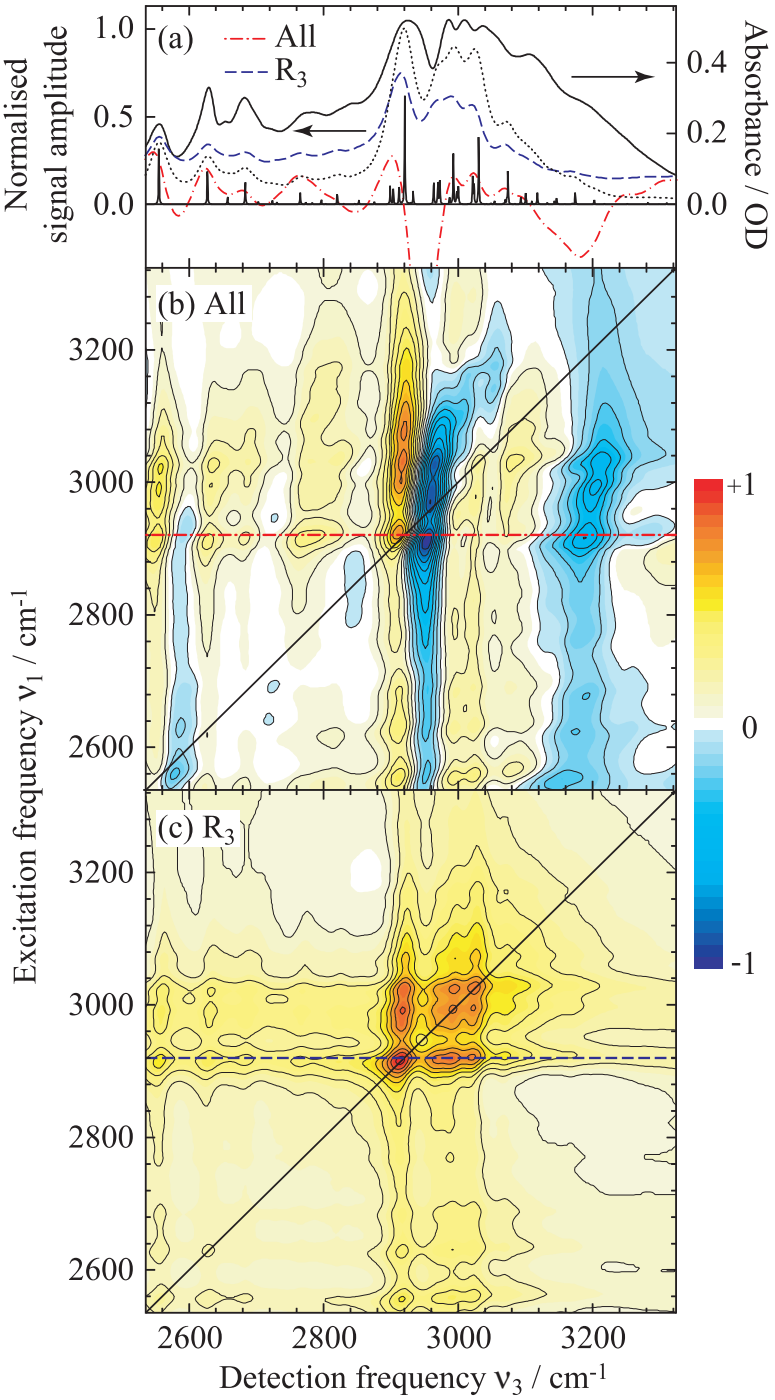

Figure 4.31: (a) Experimental (solid) and calculated (dotted) linear spectra of pure acetic acid and cross-sections of the calculated 2D spectra for $\nu_1 = 2915\text{cm}^{-1}$ and $T = 0\text{fs}$ including (dash-dotted) and excluding excited state diagrams (dashed). (b) Real part of the calculated 2D spectrum with all photon echo diagrams included. Negative signals are due to excited state absorption. (c) Real part of the calculated 2D spectrum without excited state transitions.

$j(a_g)$	γ_{OH}	ν_{C-O}	ν_{C-O}	ν_{C-O}	ν_{C-O}	γ_{CH_3}	γ_{CH_3}	γ_{CH_3}	γ_{CH_3}
$k(b_u)$	γ_{OH}	ν_{C-O}	γ_{CH_3}	δ_{OH}	$\nu_{C=O}$	ν_{C-O}	γ_{CH_3}	δ_{OH}	$\nu_{C=O}$
ϕ_{ijk}	-776	150	-118	-126	48	90	-64	-70	24
$j(a_g)$	δ_{OH}	δ_{OH}	δ_{OH}	δ_{OH}	$\nu_{C=O}$	$\nu_{C=O}$	$\nu_{C=O}$	$\nu_{C=O}$	
$k(b_u)$	ν_{C-O}	γ_{CH_3}	δ_{OH}	$\nu_{C=O}$	ν_{C-O}	γ_{CH_3}	δ_{OH}	$\nu_{C=O}$	
ϕ_{ijk}	-142	95	99	-31	-86	62	61	-21	

Table 4.2: Non-vanishing cubic coupling constants $\phi_{ijk}/\mathrm{cm}^{-1}$ of $(CH_3–COOH)_2$ in dimensionless normal mode coordinates for $i = \nu_{OH}(b_u)$ with an eigenfrequency of $2915\mathrm{cm}^{-1}$.

To facilitate comparison of the strength of the different coupling mechanisms, third-order coupling constants between the ν_{OH} mode and combinations tones of the eight fingerprint modes (cf. Figure 4.30) were calculated for a nine-dimensional Hamiltonian that did not include any low-frequency modes. The results are summarised in Table 4.2. The strongest coupling exists between the γ_{OH} and the ν_{OH} mode. This coupling does not contribute to the absorption spectrum because of the large detuning $\Delta = (2915 - 1840)\mathrm{cm}^{-1}$ between the combination tone $\gamma_{OH}(b_u)+\gamma_{OH}(a_g)$ and and the fundamental ν_{OH} transition.Two-colour pump-probe experiments have been performed which reveal a pronounced anharmonic shift of the γ_{OH}fundamental transition upon OH stretching excitation (data not published). However, no clear signature of transient v = 1 population of the γ_{OH} mode was observed.

The other fingerprint modes are coupled fairly strongly to the ν_{OH} mode as are the two dimer modes in Figure 4.30 with third-order coupling constants of up to $150\mathrm{cm}^{-1}$. This complicated case of two coupling mechanisms with similar magnitude precludes the perturbative approaches commonly used for a hierarchic introduction of coupling mechanisms, e.g. in spin-orbit coupling (Russel-Saunders vs. jj-coupling). However, the transitions in the linear and 2D spectra can still be assigned to the calculated Fermi resonances as illustrated in Figure 4.32. The arrows point to the calculated absorption lines of transitions with no change in the quantum number of the low-frequency modes. The remaining lines belong to Frank-Condon progressions that originate at the various Fermi resonance transitions. Hot transitions are absent at 0K.

4.6 Conclusions

A comprehensive study of the acetic acid dimer in an apolar solvent has been presented in this chapter. With the employed nonlinear spectroscopic techniques, it has been possible to dissect the various contributions to the third-order response. In this way, the underlying coupling mechanisms are elucidating that lead to the complicated lineshape of the OH stretching vibration which has been debated for many decades. Finally, the relative importance of the different coupling mechanisms can be identified:

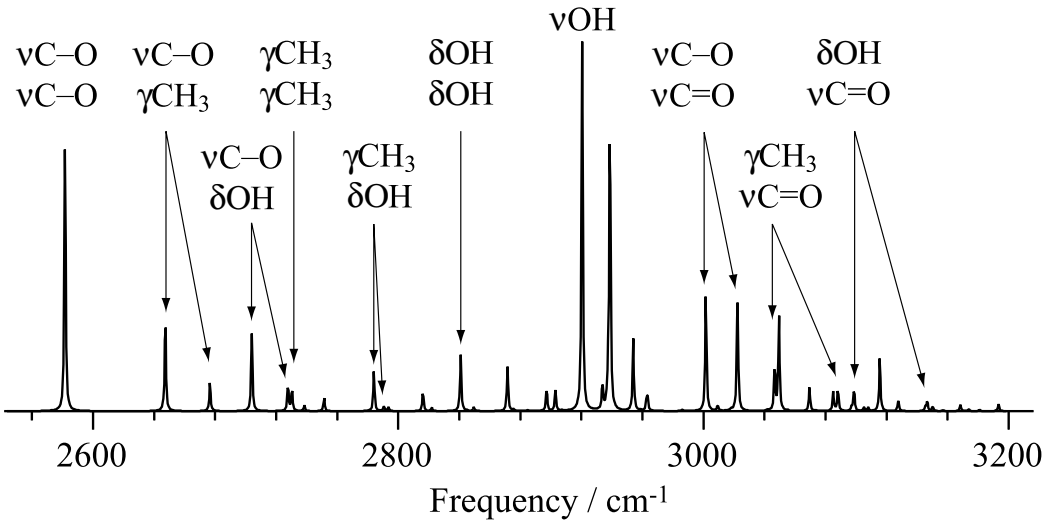

Figure 4.32: Calculated linear absorption spectrum with the main eigenvector contributions besides the $\nu_{\mathrm{OH}}(b_u)$ mode as indicated by arrows. Remaining lines are part of Frank-Condon progressions of low-frequency modes with origins at the various Fermi resonances. Combination tones consist of two different vibrational quanta, one in a Raman-active (a_g) and another in an infrared-active (b_u) mode.

(i) The Davydov coupling is not of significant magnitude being much smaller than 56cm^{-1}. This estimate is concluded from comparison of pump-probe data in Figure 4.12 and the similar decay of coherent OH stretching excitations in Figure 4.27.

(ii) The anharmonic coupling between the $\nu_{\mathrm{OH/OD}}$ mode and two low-frequency vibrations, namely the dimer stretching and in-plane wagging mode, is about 150cm^{-1} (Table 4.1). Coherent excitations of these modes upon $\nu_{\mathrm{OH/OD}}$ excitation lead to pronounced oscillations in the optical response with a dephasing time of 700fs (Figures 4.9, 4.13, 4.25).

(iii) The anharmonic coupling between the $\nu_{\mathrm{OH/OD}}$ mode and fingerprint vibrations is equally strong (Table 4.2) and manifests in Fermi resonances between the v = 1 level of the $\nu_{\mathrm{OH/OD}}$ mode and combination and overtones of fingerprint vibrations. The dephasing time of the OH stretching vibration is 200fs being more than three times shorter than the dephasing time of low-frequency wave packets in the $\nu_{\mathrm{OH/OD}}$ ground state. Furthermore, the decay of coherent excitations of the v = 0 → 1 transition and thus the coherent 2D spectra are dominated by signals stemming from coherent excitations of Fermi resonances (Figures 4.22, 4.28, 4.29, and 4.31).

The combination of nonlinear spectroscopy and high-level DFT calculations has yielded an unprecedented understanding of the complicated coupling mechanisms in acetic acid dimers in apolar environments on a molecular level. It serves as the model system for the family of carboxylic acids and similar systems, e.g. DNA base pairs in solution and to some extent in the native DNA in which stacking interactions between neighbouring base pairs are relevant [193]. Furthermore, the results of this chapter should be very useful in the study of more complicated hydrogen-bonded systems in solution and in a wider sense in their native environment such as carboxylic and similar side groups in proteins [194].

5 Structural dynamics of water

Water is the second system that is studied in this thesis. It is one of the few substances if not the only one that has attracted strong attention over thousands of years, owing to to the fact that essentially all life takes place in aqueous solution (apart from a few exceptions). Over the last centuries a scientific perspective developed and revealed many outstanding properties of water. Most of these properties are believed to be linked to hydrogen bond formation which takes place upon condensation of water steam. The spectroscopic advances in hydrogen bond research in the 1930s have rendered infrared vibrational spectroscopy an important tool to study liquid water. Modern laser development now allows for nonlinear vibrational spectroscopy of water on ultrafast timescales close to the oscillation periods of the main probe, the OH stretching vibration. This chapter presents some recent developments in spectroscopic techniques and new results on structural dynamics and energy redistribution and relaxation in pure liquid water.

5.1 Introduction

For thousands of years humans have wondered about water. Few accounts from Greece, China and the middle ages still exist in which water was conceived as elementary. This interest led to scientific literature on water that is so abundant, it would take several theses of their own for a more complete treatise on the historic developments and today's knowledge. Nonetheless, a short historic account is comprised in this introductory section to outline the relevance of water in nature.

A scientific notion was probably first developed during Italian renaissance. Leonardo da Vinci [195] treated the matter but it was not until the end of the eighteenth century that Cavendish and Lavoisier proved water to consist of oxygen and hydrogen [196, 197]. In the nineteenth century, scientific studies proved that water differed from other liquids in many physical properties. Apart from its high melting and boiling points, the low density, and a high dielectric constant, one of the earliest findings was the anomalous density behaviour of cold water which is densest at 4°C. If ice did not float, fresh water reservoirs would freeze from the bottom and no winter sanctuary in the cold bottom water would exist for marine life resulting in mainly primitive species in fresh water bodies in higher latitudes of the earth. The relatively high surface tension was already measured in 1847 by Brunner [198] and is closely related to capillary forces that allow for vertical plant growth of more than 100m [199]. In the 1850s to 1870s it was found that the compressibility of water decreased with temperature [200, 201], the thermal expansion coefficient rose with pressure [202], and the famous Wolfgang Conrad Röntgen found the viscosity to decrease with rising pressure*. Some groups have argued that several water anomalies can be explained by

*Röntgen started his water study in 1880 but did not have enough funding to finish it. The following year,

thermodynamic singularities that arise in simulated phase diagrams of H_2O [205–207].

Röntgen might have also been the first to propose a heuristic model that explained many water anomalies by two different kinds of molecules – ice molecules and water molecules [208]. In modern terms this would translate to an equilibrium of fully and partially coordinated water molecules. The crystal structure of ice was determined in 1921 and revealed a tetrahedral structure [209]. A decade later, x-ray data of water was recorded [210, 211] and along with Mulliken's quantum mechanical treatment of polyatomic molecules [212] an extensive publication appeared by Bernal and Fowler [213]. They computed the proton transfer rates from a simple quantum mechanical model and discussed possible structures comparing calculated and experimental radial distribution functions. Pauling has answered the important question whether or not the hydrogens in ice are unequally spaced between the oxygens [214] and deduced a crystal structure as shown in Figure 5.1. The debate over the nature of molecular association, as hydrogen bonding was originally termed, continued into the 1930s [215] but eventually, the special properties of water were attributed to this type of intermolecular coupling mechanism.

Vibrational spectroscopy has been an important tool in the investigation of hydrogen bonding from early on despite the strong absorption of the OH stretching vibration. Ångström, for instance, used reflective vibrational spectroscopy to study the effect of ions on the association of water molecules [216], thereby circumventing the very short absorption length of 800nm that water exhibits at 3μm wavelength. However, the concept of hydrogen bonds was not yet established nor was the dependence of the eigenfrequency of the OH stretching oscillator on the hydrogen bond length and angle.

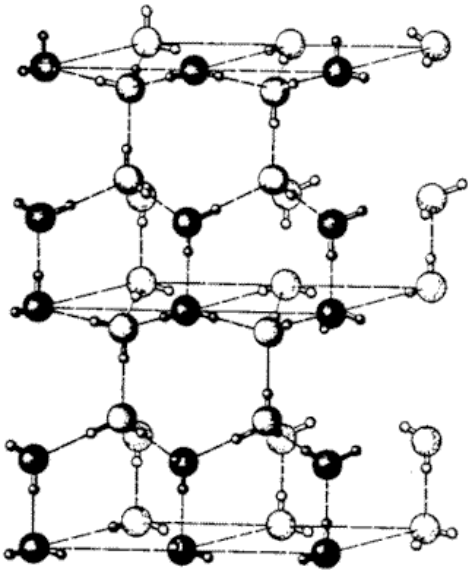

Figure 5.1: Hexagonal structure of ice.

Important aspects of the spectral properties of water have also been studied in the field of atmospheric research because of the key role that water vapour and droplets play in the world's climate [217]. Cloud formation contributes considerably to the earth's albedo, i.e. the total reflectivity with respect to the sun's spectral emission profile. The formation of a cold trap – the tropopause – at about 10km height generated the troposphere, the main climate zone between the earth's surface and the tropopause in which gaseous and droplet water is circulated. The reason why water is so important in global radiation and thermal energy budgets is partially contained in Figure 5.2 where the inverse absorption lengths of ice and water are plotted as a function of wavelength on a double logarithmic scale. The deep absorption minimum around 400nm fits the solar emission spectrum and allows sunlight to penetrate the atmosphere down to the earth's surface and into the

he communicated his findings to Warburg who reproduced Röntgen's results in an extended study with the help of his doctoral student Sachs in 1884. Before publishing, he suggested to Röntgen to publish his preliminary results in an article that preceded his own [203, 204].

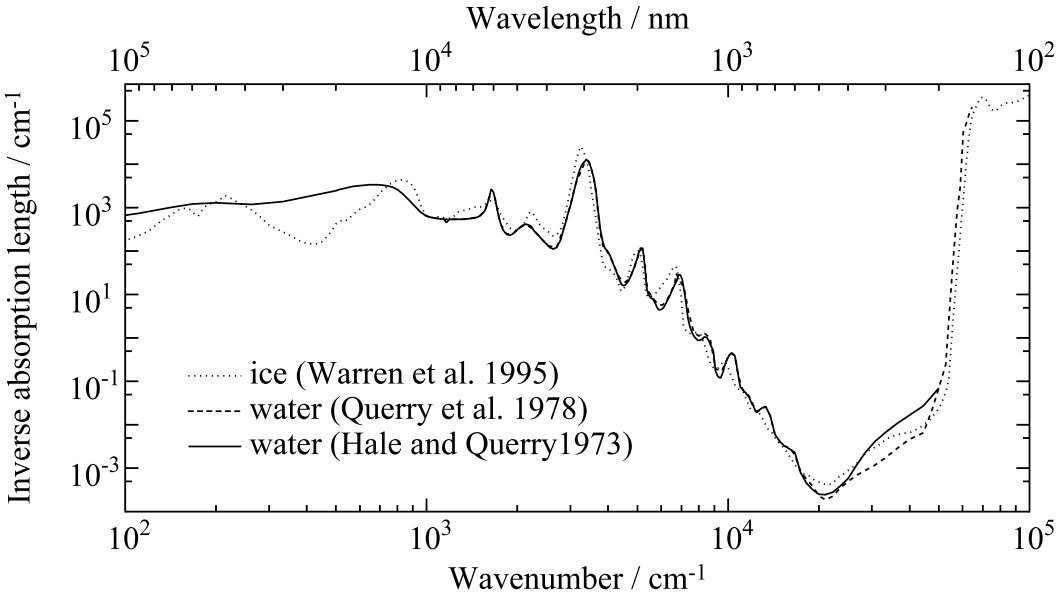

Figure 5.2: Inverse absorption length of ice Ih and pure water as a function of wavelength (top abscissa) and frequency (bottom abscissa) from the far infrared to the very ultraviolet spectral range on a double-logarithmic scale taken from the literature [220–222].

oceans. The resulting thermal equilibrium between the earth's surface and the atmosphere leads to an average surface temperature of 15°C which is mainly due the overlap of the surface emission spectrum and the infrared absorption spectrum of gaseous and liquid water [217–219]. This is the natural greenhouse effect of about 20°C. Without the troposphere, the earth would be much colder and might even look like the desert planet of mars because of photo-dissociation of water and subsequent loss of hydrogen to space. Today's enhanced greenhouse effect is due to an increase in the second most contributor to the thermal equilibrium, atmospheric carbon dioxide. The temperature rise is currently estimated to be of a few Kelvin [219].

More than a hundred years have passed since Röntgen's first conceptual ideas on the structure of water and there are still heavy debates over this structure and its dynamics, e.g a theoretical controversy over structural correlations [223–227] and an experimental one over coordination number [228–234]. This chapter will not engage in these controversies but will instead contribute to the understanding of ultrafast dynamical processes such as vibrational energy transfer and relaxation as well as loss of structural correlations. Nonetheless, disagreement also exist over the dynamics of energy relaxation and thermal equilibration [235–239].

The water molecule

An isolated water molecule contains an oxygen atom and two hydrogen atoms with bond lengths of 0.957Å and an H–OH angle of 104.5°. The dissociation energy of the intramolecular OH bond amounts to 5.4eV [240]. However, the lowest electronic transition from

the ground state is to an anti-bonding state that is centred at 7.5eV corresponding to an optical wavelength of about 165nm [241, 242]. This transition manifests in the steep rise of the absorption below 200nm in figure 5.2. In the ground electronic state, the second electronic shell of the oxygen is sp^3 hybridised in water molecules and mixes with the 1s orbitals of the two hydrogen atoms to form a tetrahedral structure with C_{2v} symmetry. This results in an electron density that is mainly centred on the oxygen atom, in particular due to the two lone-pair orbitals that show little to no participation in the covalent bonds. Consequently, a relatively large dipole moment of 1.855D (1Debye $\approx$ 0.2e/Å) exists [243] that leads to the polar nature of liquid water.

The lone-pair electrons form hydrogen bonds with the hydroxy groups of their neighbours, the distance of which is is usually defined by the O$\cdots$O spacing. This distance depends on the coordination number, i.e. the number of hydrogen bonds a water molecule forms with its neighbours. When the number of hydrogen bonds increases, the hydrogen bond distance decreases from 2.98Å in the gas phase dimer [244] to 2.85 for two such bonds, to 2.79Å for three hydrogen bonds formed, and down to 2.75Å for normal (Ih) ice [245]. This cooperative effect† also leads to an alteration of the electronic structure and a substantially higher molecular dipole in liquid water and ice. A first experimental estimate of 2.9D was extracted from x-ray diffraction measurements of the structure factor of water [248]. Theoretically predicted values range from 2.6 to 3.1D [249–251] but disagreement exists over the microscopic mechanism.

Theoretical studies on the hydrogen bond character of the gas-phase dimer suggest negligible covalent character [252, 253]. A theoretical study of Saykally's group found polarisation effects of the surrounding charge distribution to be the cause for an enhanced dipole moment in clusters of six water molecules [249]. This group also challenged the results of the highly debated work on the low coordination number of liquid water [230, 231]. A substantial covalent character of the hydrogen bond in water had been deduced from x-ray emission spectroscopy [254] and the authors emphasise the significant difference between gas-phase and liquid-phase dimers. Among other techniques, the hydrogen bond character in ice has been investigated with Compton x-ray scattering and a substantially covalent character was inferred but shortly after challenged as well [253, 255].

Over all these disputes it seems as though the character is manifold with opposing trends for polarisation and covalent character when moving from the gas-phase dimer to the ice Ih structure. In any case, the relation between water structure and its properties is still not clear today and a comprehensive theoretical model that could explain the many experimental observations is lacking.

Recent spectroscopic developments

Vibrational spectroscopy has used the OH stretching vibration as the main probe for hydrogen bond dynamics in liquid water. However, liquid H_2O(neat water) has a very short short absorption length of 800nm at the centre of the corresponding vibrational band

†Such cooperative changes in interaction are not restricted to hydrogen bonds but occur in different chemical contexts. One of the most famous concerns the oxygen binding affinity of hemoglobin [246] and investigations of such effects led to the Nobel price in physiology [247]

at 3400cm^{-1} (Figure 5.2). To circumvent the high absorption, H_2O and D_2O can be mixed. Because of rapid proton and deuteron exchange [256] such solutions will consist of isolated HOD molecules surrounded by D_2O or H_2O. Typical H_2O:D_2O mixture were used with a volume ratio of 1:100 yielding 1M solutions of HOD in D_2O. There are several differences between pure water and HOD in D_2O, e.g. lack of resonant energy transfer in isotopically diluted mixtures, a much weaker Fermi resonance between the OH stretching fundamental and the first OH bending overtone due to the large detuning between the two states, a spectral density of intermolecular modes in D_2O that is generally shifted to smaller frequencies in the spectral range above 200cm^{-1}, different dipole moments of H_2O and HOD, and the absence of a symmetric and an asymmetric stretching mode in HOD. These differences are manifested in the linear absorption spectrum of the ν_{OH} mode shown in Figure 5.3. Some of the consequences such as shorter OH stretching and bending lifetimes and resonant energy transfer between excited of OH stretching oscillators will become apparent in the following sections.

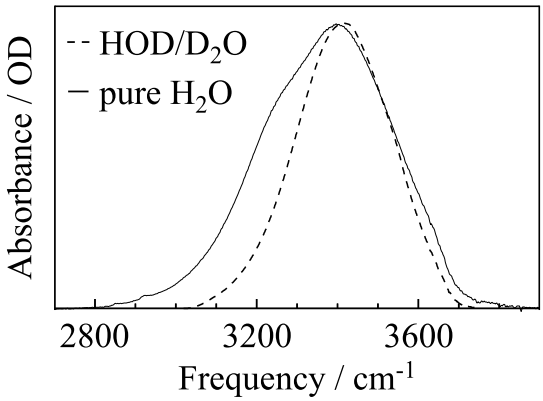

Figure 5.3: Linear absorption spectrum of liquid H_2O and HOD in D_2O with an OH group concentration of 0.3M.

The first group to study ultrafast dynamics of HOD in D_2O by vibrational pump-probe spectroscopy of the OH stretching vibration was the one of Laubereau [257]. The observed dynamics were attributed to coexisting static water configurations. Bratos [258] proposed a different type of structural model with a continuum of hydrogen bond lengths. The main controversy still concerns these two conceptions: several distinct structural components versus a continuous distribution of structures. Ultrafast experiments were published by several groups [259–269] but disagreement over the exact lifetime of the $\nu_{OH} = 1$ state of the OH stretching vibration and rotational and spectral diffusion time constants exists. Depending on the model and the pulse length, lifetimes of 740fs, 1ps, and 1.3ps have been reported. The unpublished data in Figure 5.7 is in good agreement with measurements of Tokmakoff's group [270, 271] which reported a lifetime of 700fs. Spectral diffusion constants seemed to decrease with time and are now ranging between 500fs and 1ps. An inertial fast component of 170fs has been attributed to a local reorganisation of only one or a few water molecules [266] because of a similarly fast component in the dielectric response of water [272–274]. An empirical OH potential also suggested delocalisation of the hydrogen atom in the O—H$\cdots$O structure when transferred to the second excited state [275].

Several groups have developed visible echo spectroscopy, pioneered by those of Shank and Wiersma [276, 277], to study solvent and solvation dynamics by use of chromophore responses in liquids. Sufficiently strong and short infrared pulses have triggered numerous photon echo studies that can probe liquid dynamics without the use of chromophores through vibrational oscillators. The first two-pulse photon echo studies on water, i.e. on the OH stretching vibration of HDO in D_2O revealed a very fast pure dephasing time of 90fs which was ascribed to the large anharmonicity of the OH stretching potential in

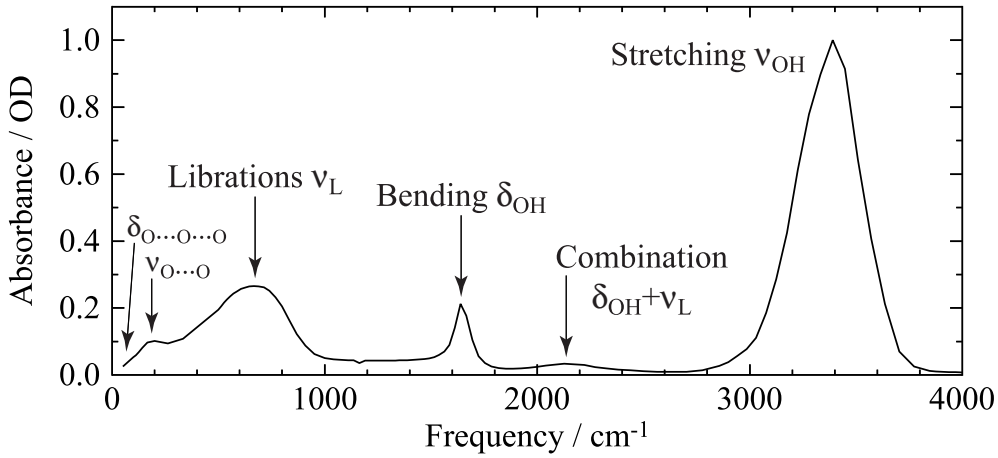

Figure 5.4: Linear vibrational absorption spectrum of pure water, taken from [220]. Three intramolecular modes are preserved in liquid water, the bending vibration and the overlapped symmetric and asymmetric stretching vibrations. Peaks at 200cm^{-1} and 60cm^{-1} have been assigned to the O$\cdots$O stretching and O$\cdots$O$\cdots$O bending vibrations, respectively. The combination tone was already assigned in the 1930s [292].

water [186]. Echo peak shift and heterodyne-detected photon echo measurements [278–280] showed that spectral diffusion within the OH stretching absorption band happens on many time scales. The fastest dynamics have been attributed to anharmonic coupling between the OH and the underdamped O$\cdots$O stretching mode as proposed by Lawrence and Skinner as well as Rey and Hynes [281, 282]. The reported fast and intermediate components of about 150fs and 1ps agree quite well with spectral diffusion found in pump-probe experiments. The longest component reported [278] ranges between 5ps and 15ps and coincides with the dominant dielectric relaxation time of 9.5ps [283–285]. Fairly recently, Fayer's group investigated the OD stretching vibration of HOD in H_2O with pump-probe and photon echo correlation spectroscopy. This oscillator has a comparably long lifetime of about 1.5ps to 1.8ps [268, 286, 287] and is subjected to fluctuations with the spectral density of neat water. The hydrogen bond network dynamics of H_2O rather than D_2O were discussed in collaboration with Lawrence, Skinner, and coworkers [288–291]. The frequency correlation extracted from the two-dimensional spectra yielded time constants of sub-50fs, 400fs, and 1.4ps. Thus, similar hydrogen bond dynamics on multiple time scales in H_2O and D_2O have been reported.

Generally, the time ranges of spectral diffusion can also be found in the various low-frequency spectral responses of the heterodyne-detected Raman-induced optical Kerr-effect [293, 294], Raman and depolarised Raman scattering [294, 295], reflection THz time domain spectroscopy [272], and far-infrared absorption [296]. The infrared spectrum of some of the modes of the hydrogen-bonded water network along with the three intramolecular modes of the water molecule is shown in Figure 5.4. Although the fluctuating structure and dynamics of water are more complicated than in acetic acid dimers surrounded by a apolar solvent, the structural dynamics of the intermolecular modes should also govern the frequency correlations of the intramolecular modes. An article was published by Agmon

[297] on the interpretation of the hydrogen bond network's spectral density. According to Agmon, tetrahedral displacement manifests itself in the dielectric relaxation time of about 9ps whereas molecular rotation is necessary for hydrogen bond breaking and reformation. The theoretical work of Geissler and Chandler [298] leads to a similar view: proton transfer occurs along some sort of 'nanowire' that is defined by a hydrogen bond network fraction and proton transfer involves the breakage of hydrogen bonds. The same view is shared by Bratos and coworkers which recently published a combined experimental and theoretical work [299]. In an earlier work [223, 224], Luzar and Chandler not only suggest uncorrelated hydrogen bond formation and breakage for correlation times greater than several hundreds of femtoseconds but state that the most important motions that lead to hydrogen bond reformation are librations on the timescale of less than 0.1ps, and inter-oxygen vibrations on the timescale of 0.1ps to 0.2ps. These vibrations constitute the fastest parts of the hydrogen bond network dynamics and will govern structural correlations on ultrashort timescales. With this in mind, correlation spectra will be discussed in the next section.

Despite the large interest for liquid water in the spectroscopic community, only very few investigations of neat water with nonlinear vibrational techniques have been published. Such studies have been hampered by the enormous absorption of the main probe oscillator. It is even more critical for coherent multidimensional spectroscopy than for pump-probe spectroscopy because the optical transmission should be higher than 50% in order to avoid artefacts through pulse and signal distortion. Bakker's group has published pump-probe data on pure water [261, 300] with a time resolution that cannot resolve the fastest dynamics. Dlott's group has also studied pure water with infrared pump-Raman probe spectroscopy [269, 301–303] pump and probe pulses of 700fs.

5.2 Dynamics of the OH stretching vibration

The introductory section has outlined a small fraction of the numerous efforts in water research. The main target in vibrational spectroscopy has been the OH stretching vibration because of its sensitivity to hydrogen bonding. In this section, recent results on pure and isotopically diluted water are discussed that will shed new light on long-standing questions. Several leading theoretical groups have spent decades on the subject and the absence of a comprehensive water theory shows how formidable a task such an undertaking represents. For this reason, little theoretical modelling will be presented and it will be limited to extraction of relevant time constants of dynamical processes and reasonable arguments for possible causes of the spectroscopic behaviour of water.

Experimental

The infrared source of the ultrashort infrared pulses has been described in chapter 3 and is displayed in Figure 3.2. Two BBO crystals were used to convert the 800nm pulses of the amplified Ti:Sapphire laser system into signal and idler in the near infrared which were mixed in a 0.75mm thick $AgGaS_2$ crystal. The power spectral density of the infrared pulses covered the spectral region from 2800cm^{-1} to 3600cm^{-1} as shown in Figure 5.8a by the

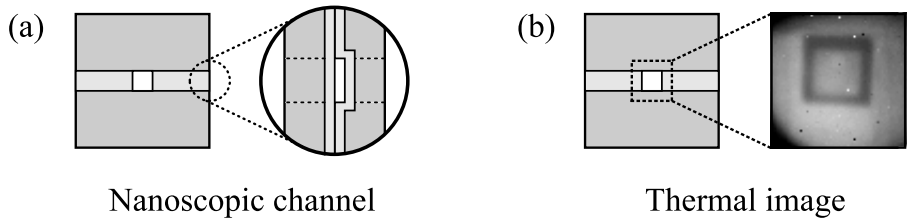

Figure 5.5: Nanofluidic cell with low-stress silicon nitride (light grey) on silicon substrates (dark grey). (a) schematic front view and zoom of assembled cell side with the nanofluidic channel (centre white) and (b) thermal image of window section.

solid line at the bottom. The broad bandwidth allowed for the recording of the entire signal at positions of the fundamental absorption band and the excited state absorption. The pulses had a temporal FWHM below 70fs after simple chirp compensation was performed by insertion of 8mm CaF_2. This measure reduced second order chirp but introduced higher order GVD. The bandwidth allows for much shorter pulses and lately, pulses as short as 50fs were recorded.

The newly developed heterodyne-detected three-pulse photon echo experiment has been described in section 3.4. The difference to other setups is the excellent passive phase stability of the spectrally resolved signal. It exceeds $\lambda/150$ at 3μm wavelength and produces reliable 2D data sets [125]. Signals were recorded for 300 laser shots before the grating or the stepper motor was moved. The 2D data sets were recorded twice in consecutive scans over the spectral and temporal range[‡] for each population time delay to check consistency and long term phase stability. A power monitor was fed to the data acquisition programme to gate data acquisition within the set power window and minimise long-term laser drifts. Data analysis was carried out with MathWorks' Matlab© using algorithms from the *Numerical Recipes* [191] and the FFTW project [192].

Most of the experimental groups in the field have studied isotopically diluted water to circumvent the enormous absorption of the probe oscillator. But energy transfer processes, energy relaxation and subsequent redistribution, and thermal equilibration could not be studied in the oscillator structures of water with a fully resonant environment. Optically polished calcium fluoride, sapphire, or diamond windows can easily be assembled in a metal holder with a water film in between them of less than 0.3OD that is stable for more than a day. But first experiments revealed dynamics that are hardly resolvable with 60fs pulses. Window contributions render signal analysis impossible for these fast water dynamics. Hence, the main challenge has been the invention of a sample cell with negligible window contribution and sub-micron water layers.

Low-stress silicon nitride[§] membranes of sub-micron thickness were used to construct a nanofluidic cell with a 500nm thin channel sketched in Figure 5.5. Such structures are commonly used in electron and x-ray spectroscopy and diffraction of liquids [228] but are well suited in the infrared to wavelength up to 10μm similar to barium fluoride although

‡Spectral sampling was done with 4.5 points per spectral interference period; the time domain was sampled with 3fs steps for the 10.3fs period at the centre of the OH stretching absorption.
§Low-stress silicon nitride, SiN_X, does not have the regular stoichiometric composition of Si_3N_4 [304]

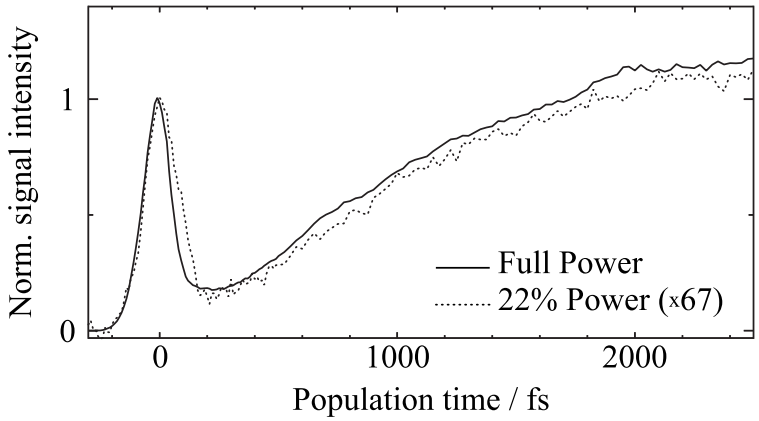

Figure 5.6: Spectrally integrated transient grating signal of H_2O between CaF_2 windows. The signals were obtained with pulses of 0.5μJ (solid) and 0.11μJ (dotted).

the latter is transparent in the UV whereas silicon nitride is not (as can be deduced from its yellow colour). To deal with the hydrophobicity of silicon nitride, the surface was coated with 5nm of silicon dioxide to produce adhesive forces between the cell and the water molecules. The cell is shown in Figure 5.5a. It consists of two separate 0.5mm thick silicon substrates on which a layer of silicon nitride of 800nm thickness had been deposited. Square holes of 2mm side length had been etched into the silicon. A 2mm wide well of 1.3μm depth had also been etched into one of the substrates before silicon nitride deposition. Both cell walls were held together with minimum force to avoid stress that would result in cell deformation. Water was introduced on one side of the channel and capillary forces drew the water into the channel without major inclusion of air. Sealing of the cell sides kept the water inside for eight hours and more. Absolutely no diffracted signal of single silicon nitride windows was detectable.

One major concern was the temperature rise in the excitation volume. Diamond is an ideal heat conductor for optical experiments but in first experiments calcium fluoride was used to test the power dependence of the transients grating signals. A water film with 50% transmission at 3400cm^{-1} was held between 0.5mm thick calcium fluoride windows and population time scans with three pulses were recorded with pulse energies of 0.5 and 0.11μJ at the sample¶. The results are shown in Figure 5.6. The peak at zero delay contains about 35% contributions from the calcium fluoride windows as can be inferred from the signal intensities at zero delay in Figure 5.6 and the insert of Figure 5.7a. The plateau-like signal at long delays of both data sets has been scaled to the same value such that the peak without window contributions is unity. The power dependence is calculated to 2.8 rather than 3. But the uncertainty of the power meter for 100nJ pulses at 3μm is so large that an exponent of 3 easily lies within the measurement error. The main check was thermal imaging of the silicon nitride water cell with a fast infrared camera in the frequency range of 2 to 5μm wavelength. Fastest sampling rates of 850Hz were obtained

¶The focal beam waist was 0.2mm and the sample thickness 0.6μm. 0.75μJ were absorbed in $2{\cdot}10^{-8}$cm^3 which amounts to a temperature rise of 9K per shot. For pulses centred at 2.95μm, less than 2% of the molecules are excited neglecting spectral pulse and absorption profiles.

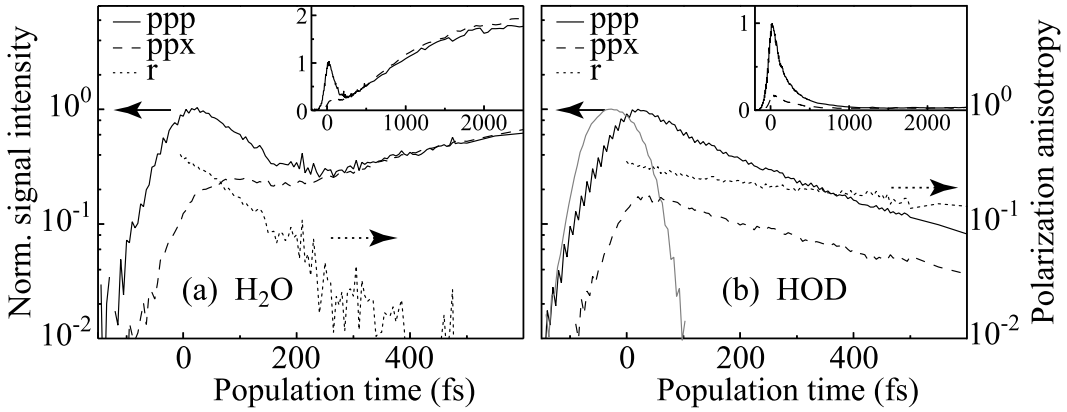

Figure 5.7: Spectrally integrated transient grating signal of pure and isotopically diluted water. (a) Signals of H_2O for parallel (solid) and perpendicular (dashed) polarisation of the third pulse and the corresponding polarisation anisotropy (dotted). (b) Same signals as on the left for HOD in D_2O with an OH concentration of 13.6M. The inserts show the signals for picosecond delays on a linear scale.

when an area of 16×32 MCT pixels was used on which the centre of the sample cell had been imaged as shown in Figure 5.5b. Maximum temperature rises turned out to be less than 10K so that heat accumulation effects can be regarded as negligible.

Energy transfer and population relaxation

To study the energy transfer and relaxation dynamics in water and HOD in D_2O, spectrally integrated transients grating scans were recorded with the polarisation of the third pulse parallel and perpendicular to the polarisations of the other two pulses. The polarisation anisotropy has been calculated from the square roots of the signals according to:

$$r(T) = \frac{\sqrt{I_{\parallel}(T)} - \sqrt{I_{\perp}(T)}}{\sqrt{I_{\parallel}(T)} + 2\sqrt{I_{\perp}(T)}} \,. \tag{5.1}$$

In electronic spectroscopy, the intensity signals contain electronic, vibrational, and rotational excitations [305]. The rotational contributions to the anisotropy decay are often much slower than the electronic and vibrational ones and can be neglected on the time scale of a few hundred femtoseconds for water. This is not true for the electronic contributions. Thus, equation 5.1 has to be used with caution and its validity depends on the coupling between electronic and vibrational degrees of freedom. In vibrational spectroscopy, the electronic polarisation anisotropy is of course not an issue.

Results on the transient grating dynamics are shown in Figure 5.7. On the left, the signal from the thin water film is plotted. The signal around zero delay is now free of window contributions and both polarisation conditions exhibit a fast exponential decay with a 95fs time constant that is followed by a rise with a 1.3ps time constant when fitted with a convolution of the Gaussian pulse width and exponential functions. The fast time

constant is attributed to population relaxation and yields a lifetime of the first excited state of 190fs. This lifetime is much shorter than in HOD in D_2O. The most likely reason is a Fermi resonance between the ν_{OH} =1 state of the stretching vibration and the δ_{OH} = 2 of the bending vibration [269].

The slower time constant is attributed to thermalisation of the excited sample volume. Strong evidence is given by the fact that the signal remains unchanged after 3ps up to the maximum time delay range of 50ps. Thermal equilibration after relaxation of the excited OH stretching vibration gives rise to a spatial thermal grating defined by the interference pattern of the first two excitation pulses. The dependence of the refractive index on temperature results in a very effective refractive index grating from which energy is diffracted of the third pulse into the detected optical path. Thermal diffusion on microsecond timescales leads to a decay of this grating which cannot be recorded with the short delay stages of the experimental setup. The insert of Figure 5.7a shows the large thermal grating signal in pure water whereas the insert in Figure 5.7b shows only a minute plateau of 0.03 for long delays due to a feeble thermal grating that results from the large volume of the D_2O heat bath. When the optical density at 3400cm^{-1} is kept constant for H_2O/D_2O mixtures, the D_2O volume increases linearly with H_2O dilution but the thermal grating signal vanishes nonlinearly, e.g the ratio of OH concentrations in panels (a) and (b) of Figure 5.7 is 7.4 but the signals at maximum delay have a ratio of 67 yielding a quadratic OH concentration dependence. This difference in thermalisation behaviour has its cause in different energy equilibration pathways in the hydrogen bond network of water and HOD in D_2O but there is also a volumetric effect because the thin H_2O film is excited from the front to the rear window and thermal diffusion is mainly in the transverse directions.

The thermalisation time of water is much faster than it is in other liquids. It is therefore possible to increase local temperatures in aqueous solution within 2ps. Temperature jump experiments with temperature changes of more than 100K are thus possible within picoseconds when using strong infrared lasers allowing for many interesting applications.

Turning now to the subject of resonant energy transfer, the calculated polarisation anisotropy is analysed. This quantity quickly decays with a time constant of 80fs as shown in Figure 5.7a. Rotational diffusion is much slower in water which leaves but the resonant energy transfer between neighbouring OH stretching oscillators[‖]. This fast energy transfer has already been suggested [261] and can now be quantified due to the short pulse duration of the experiment and the unique sample cell. Recent theoretical studies that have treated a small number of water molecules quantum mechanically [306–308] indicate a very fast energy transfer probability in the observed time range of less than 100fs.

In contrast to this fast energy transfer, the mixture of HOD in D_2O with 25% HOD molecules shows much slower dynamics. The calculated rotation-free signal was fit with an exponential decay and a rise of the form $A(1-e^{t/\tau})$. Time constants of 250fs, and τ=800fs were extracted. This yields a lifetime of 500fs which is faster than usually reported because of the substantial OH concentration of one fourth of all OH and OD groups. The decay of the polarisation anisotropy has also been analysed according to [261]. The model includes

‖Despite the comparably weak transition dipole of the ν_{OH} mode, the transition dipole density of this mode is comparable or higher than those found in semiconductors with high doping concentrations. This fact results in a peculiar spectroscopic behaviour including, maybe, radiative coupling effects.

a Förster radius parameter to account for resonant energy transfer. However, the fit results for an OH stretching lifetime of 700fs depend sensibly on the fitting range. When fixing the Förster radius at 2.1Å [261], the data is fit with a rotational diffusion time τ_r of 1250fs. If the Förster radius is not fixed, it converges to 1.44Å – about half the average hydrogen bond length of 2.85Å. The rotational diffusion time τ_r converges towards 860fs, a value that is fairly close to the value of 700fs obtained from an exponential model suggeesting a small contribution of resonant energy transfer to the decay of the polarisation anisotropy at these OH concentrations.

Spectral diffusion and structural dynamics

To extend the study, heterodyne-detected transient grating signals were recorded by spectral interferometry and the real and imaginary parts were extracted according to the procedure described in section 2.3. The result for the real part is displayed in Figure 5.8a. The sign convention in this plot is opposite of the one used to display the experimental pump-probe data; here, the excited state transition signal is negative and plotted in blue. It is due to a π phase shift introduced in Equation 2.12 which applies to the relevant Feynman diagrams $R_1^\dagger$ and $R_2^\dagger$ of Figure 2.5. The black graph at the bottom is the spectrum of the infrared pulses. The most remarkable behaviour is the fast signal loss at the edges of the spectral range. To emphasise this behaviour, integrals over the spectral wings and the centre of the transient grating were calculated. The arrows on the top of the Figure mark the integration limits. The results are displayed in panel (b). The central part behaves much like the integrated transient grating scans. The rise of the thermal grating signal is centred at 3200cm^{-1} and grows in with a picosecond time constant. The edges vanish within the duration of the excitation pulses. The delayed dynamics on the blue side might attributed to remaining pulse chirp. Also, the symmetric stretching vibration showed faster energy relaxation in simulations [306, 307] which might explain the spectral centre of the thermal grating that engenders after a few hundreds of femtoseconds.

The decay of the excited state transition signal is generally used to quantify the lifetime of the first excited state. But the results displayed in Figure 5.7 yielded a lifetime of 190fs. Furthermore, there is no indication of coupling constants between the OH stretching vibration and other accepting modes that is large enough to cause such a fast energy relaxation. A possible reason is fast spectral diffusion toward the centre of the spectral range similar to solvation effects in electronic spectroscopy of chromophores in aqueous solutions: upon excitation of the OH stretching vibration, the change in the dipole of the excited water molecule causes the surrounding water molecules to adjust very quickly thereby lowering the energy of the $\nu_{\mathrm{OH}} = 1$ state. This causes a red shift of the fundamental transition and a blue shift of the excited state transition observed in Figure 5.8.

Spectral diffusion will also give rise to changes in the lineshape of two-dimensional spectra. Coherent 2D spectra of neat water have been recorded for several population times, T, and are plotted in Figure 5.9. The negative signal between 2800cm^{-1} and 3100cm^{-1} is due to the strongly red-shifted excited state transition. It has essentially vanished after 50fs in accordance with the data in Figure 5.8.

More interesting in these spectra is the 2D lineshape along the diagonal that stems from the fundamental transition of the OH stretching oscillators. For $T = 0$, i.e. zero delay

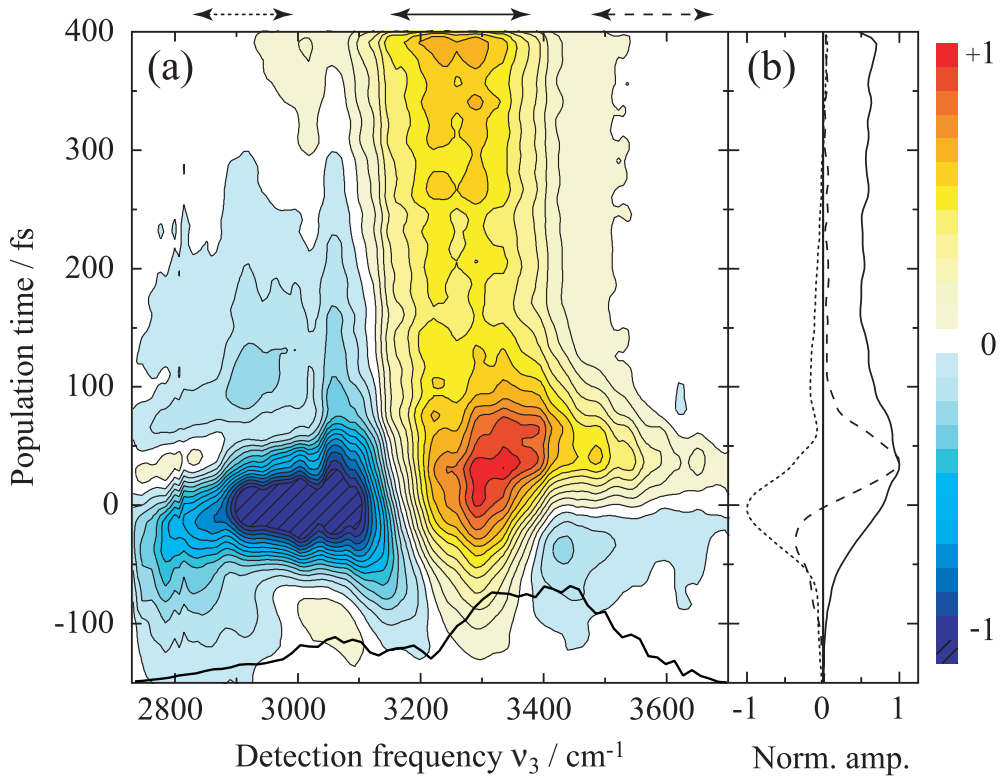

Figure 5.8: (a) Real part of the heterodyne-detected transient grating signal. The phase between the signal and the local oscillator was determined by a global fit to pump-probe signals at 5 evenly spaced delays between 0fs and 400fs. The black graph along the ν_3-axis indicates the spectrum of the excitation pulses (b) Normalised integrals over the spectral intervals that are indicated by the double arrows on top of the figure: the red side (dotted) is the excited state absorption, the central part (solid) and blue side (dashed) represent ground state bleaching and stimulated emission.

between the second and the third excitation pulse, an elongated lineshape extends along the diagonal reflecting a large inhomogeneous distribution of transition frequencies of the ensemble of OH stretching oscillators. Upon delay of the third pulse by 50fs, the ellipticity of the diagonal peak has almost disappeared showing that spectral diffusion occurs on this timescale. It means that the transition frequencies of the ensemble of excited oscillators has changed within the linewidth in only 50fs, and this to an extent were hardly any frequency correlations persist. The decay of such correlations is sometimes called memory loss since the FFCF can be viewed as the systems memory for its past spatial frequency distribution. It is worth noting, that the fast dynamics are consistent with the decay of the spectral edges of the transient grating signal. Also, no significant recurrence of the lineshape ellipticity is observed at longer population times in agreement with similar measurements on the OD stretching vibration in H_2O[288].

The microscopic mechanism behind these observations are ultrafast molecular rearrangements within the hydrogen bond network. Hydrogen bond geometries with various O$\cdots$O distances and O$\cdots$O$\cdots$O angles determine the local molecular transition frequencies. A

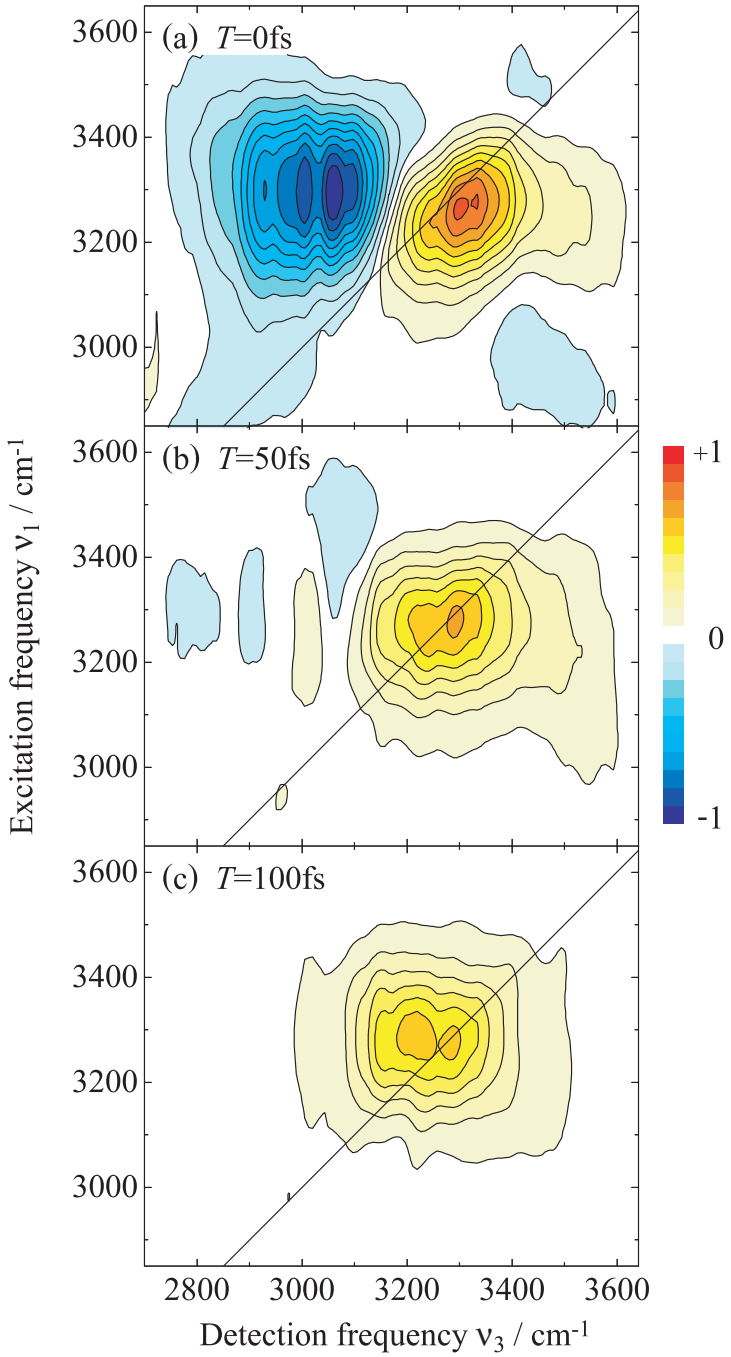

Figure 5.9: Real part of the 2D spectrum of pure water for population times of 0fs, 50fs, and 100fs. Ground state bleaching and stimulated emission are chosen to be positive whereas the excited state contribution is of opposite sign. The colour scale applies to all panels and is linear.

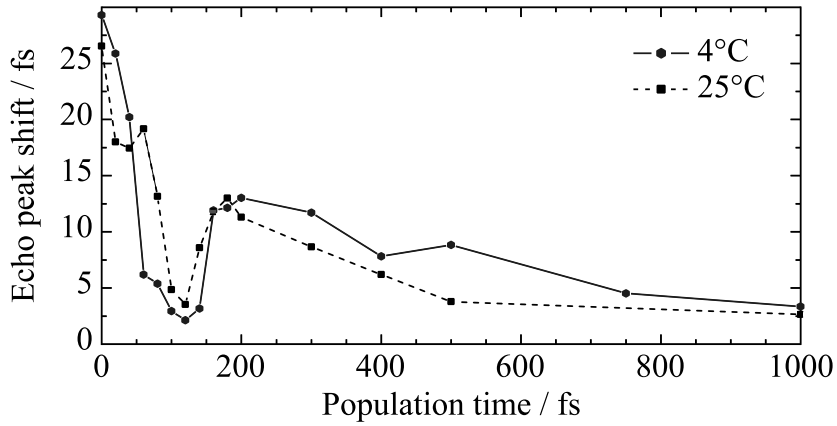

Figure 5.10: Echo peak shift measurement of water as a function of the population time for two different temperatures. There is uncertainty in the baseline of about 5fs.

change in local hydrogen bond geometry causes a change in local transition frequencies thereby providing a link between structural and frequency correlations. However, the structure-to-frequency function is disjunct which means that there is no unambiguous relation between a hydrogen bonded structure and the OH stretching frequencies of the water molecules that constitute it.

The timescale of the ellipticity change provides some clue about the underlying structural changes since only nuclear motions that occur within the time range of 50fs may result in the observed loss of frequency correlations. Theoretical studies of HOD in D_2O have predicted an underdamped motion of the O$\cdots$O stretching mode [282, 309] and Tokmakoff's group published echo peak shift measurements of HOD in D_2O [280] that indicate a very fast initial decay of the frequency fluctuation correlation function (FFCF). A recurrence of the peak shift at 170fs was observed and further analysis hinted at the predicted underdamped motion of the O$\cdots$O stretching mode as the cause, similar to acetic acid but with much stronger damping (Figure 4.25). Echo peak shift measurements of neat water have yielded very similar experimental results as shown in Figure 5.10. A very fast initial decay of the peak shift is followed by a recurring peak shift that decays more slowly. The question arises, how this recurrence can be reconciled with the coherent 2D spectra in which no recurrence of lineshape ellipticity is observed. It should be noted that FFCFs derived from the echo peak shift rely on spectrally integrated signals which contain excited state absorption signals as well. Series of 2D spectra at different population times directly measure the time evolution of spectral inhomogeneity from which the frequency fluctuation correlation function can be deduced [288].

Hindered rotations, generally referred to as librations, have much higher eigenfrequencies than the O$\cdots$O stretching mode as seen from Figure 5.4. Their oscillation periods are as short as 30fs and a librational response upon OH stretching excitation is likely to be the cause for the fast loss of inhomogeneity. Luzar and Chandler's MD simulations [223, 224] suggest that librations play an important role in structural rearrangements that lead hydrogen bond reformation. Their measure of hydrogen-bonding involves a correlation function that relates to the frequency correlation of the OH stretching vibration. In view

of the short timescale on which the spectral diffusion takes place, librational motions with oscillation periods as fast as 30fs are most likely the cause of the very fast initial spectral diffusion and decay of the inhomogeneity. This does not preclude contributions from the O$\cdots$O stretching mode, in particular after the first tens of femtoseconds. However, the vibrational period is about 200fs much longer than the initial decay. Either way, such fast responses of the local environment are truly astonishing and show the extraordinary difference between water and other liquids.

The fast disappearance of the excited state transition signal and the inhomogeneity loss have been explained by a lowering of the first excited state due to ultrafast librational motion. The similarity to solvation dynamics hints at an important aspect, i.e. the excited OH group constitutes a solute in a solvent environment. Theoretical correlation functions have been calculated for equilibrated water structures whereas the excited water and its local environment do not constitute an equilibrated structure. Publications by Roy and Bagchi [310] as well as Geissler and Chandler [311] compare the equilibrium correlation function to a non-equilibrium response. The latter shows a much faster initial decay which qualitatively describes the observed inhomogeneity decay more appropriately than the correlation function does. Hence, it might well be that non-equilibrium processes contribute significantly.

In conclusion of this section, we have studied pure water to determine the microscopic processes that lead to energy redistribution between resonant OH stretching oscillators embedded in a rapidly fluctuating hydrogen bond network. The fluctuation correlation time of this network exhibits a fast component below 50fs that is mainly attributed to a fast librational response of the local environment. Additionally, energy transfer between resonant OH stretching oscillators occurs that is faster than in any other liquid and takes place on sub-100fs timescales. Energy relaxation of local excitations is similarly fast as in acetic acid dimers with a lifetime of the $\nu_{\mathrm{OH}} = 1$ state of 200fs. The local thermalisation of non-equilibrium conditions seems to be reached within a few picoseconds and is presumably faster than in any other liquid.

5.3 The OH bending vibration & high-frequency librations

A large quantity of spectroscopic data has been published on the OH stretching vibration of water. Theoretical models have tried to describe this oscillator and its interaction with the environment. Among the different phenomena, the de-excitation mechanism of the OH stretching vibration, ν_{OH} has been discussed which involve intermolecular modes such as high-frequency librations of the Hydrogen bond network but also the OH bending vibration, δ_{OH} [301, 312, 313]. The second overtone of the OH bending vibration is situated at about 3200cm^{-1} and overlaps with the broad OH stretching band. It is assumed that anharmonic coupling to the OH oscillators exist that results in a Fermi resonance between $\nu_{\mathrm{OH}} = 1$ level and the $\delta_{\mathrm{OH}} = 2$ level. Such a coupling mechanism opens a possible energy relaxation pathway via the bending vibration comparable to the de-excitation scheme in a recent publication [183]. Little is known about the OH bending vibration, the energet-

ically lowest intramolecular mode of water. Its population relaxation can only occur via intermolecular modes of the hydrogen bond network which makes it particularly interesting. For these reasons, the first ultrafast pump-probe study of the bending vibration of neat water was undertaken.

Experimental

Spectrally resolved pump-probe measurements were performed on the OH bending vibration δ_{OH} and the high-frequency librations. The light source is the same as in the previous water experiment and the experimental setup has been described in detail in section 3.2. The infrared pulses were tuned to the spectral region of the OH bending vibration and the pump-probe cross-correlation was measured by two-photon absorption in 70μm thick InAs with a wire-grid attenuated pump pulse. The pulse spectra are displayed in Figure 5.11. The two-photon signal had a full width at half maximum of 80fs for pulses centred at 1650cm^{-1}, 100fs for pulses centred at 1480cm^{-1}, and 130fs for pulses centred at 1350cm^{-1}. The latter pulse width was longer because of increased group velocity dispersion near the three-phonon line of the difference frequency generating crystal at about 1200cm^{-1}. The two-photon signal has been included in Figures 5.12a and 5.14b.

Samples were identical to the ones used in the photon echo experiments but a small water droplet was placed on one sample window before the second one was placed on top. The assembled cell was enclosed in a cell holder that exerted some pressure on the two windows resulting in slight window deformation. Both measures led to a six-fold increase in water film thickness so that the optical density was about 0.45. For measurements in isotopically diluted water, an HOD concentration of 5M was used to reduce resonant interactions between OH oscillators and still maintain a substantial bending absorption compared to the broad overtone background of pure D_2O that is situated at the same spectral position. The thickness of the H_2O/D_2O film was set by a 13μm Teflon spacer resulting in a net optical density of the bending mode of just below 0.3OD.

Results and discussion

First, ultrafast dynamics of the OH bending vibration of HOD in D_2O are discussed. Transient absorption spectra were obtained from spectrally resolved pump-probe experiments and the results are displayed in Figure 5.12a. For zero delay, the induced absorbance change has the typical signature of an anharmonic oscillator: ground state bleaching and stimulated emission result in a decrease of absorption at 1480cm^{-1} and excited state absorption is red-shifted by about 60cm^{-1}. At long delays a broad background absorption is observed that is indicated by a dotted line. Superimposed on this background is an increased absorption at 1450cm^{-1} and decreased absorption at 1490cm^{-1}, both of which are caused by a red shift of the OH bending transition with increased temperature. The temperature effect has been observed in linear absorption spectra of the OH bending mode of pure water between 3 and 95°C [314]. When the temperature increases, the lineshape shifts to the red and becomes narrower although the integrated intensity is constant [315]. The transient red shift decays by heat diffusion on the timescale of microseconds. The

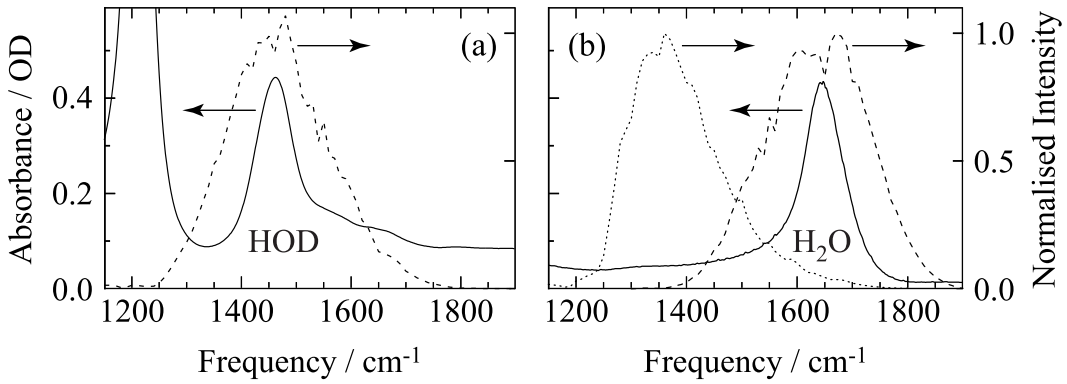

Figure 5.11: Absorption spectrum in the region of the OH bending vibration of (a) HOD in D_2O and (b) pure water (solid lines). In the left panel, the absorption of the D_2O bending vibration is situated at 1200cm^{-1} and the broad combination tone of D_2O overlaps with the bending mode of HOD. Spectra of the excitation pulses are included as dotted and dashed lines. In the right panel, the background absorption extends to 1700cm^{-1} and is attributed to high-frequency librations.

broad absorption background stems from absorption changes in the solvent which also has a temperature dependent absorption.

Kinetics have been analysed by fitting exponential functions to the data. Two transients at 1420cm^{-1} and 1480cm^{-1} and corresponding exponential fits with time constants of 400fs are plotted in Figure 5.12b. The decay of the initial signals is followed by an induced absorption that grows in at the same rate as excited state absorption and ground state bleaching/stimulated emission decay. The induced absorption does not change up to the measured delay of 100ps. The population of the first excited state of the OH bending vibration hence decays with a lifetime of 400fs and the energy transfer into the solvent results in a thermalisation of the excitation volume within a few picoseconds. All results are in very good agreement with recent publications that appeared during the course of the measurements [316, 317]. Very similar values have been predicted from theoretical calculations [313]. Also, experiments of isolated H_2O molecules in organic solvents produced much longer lifetimes in the picosecond range [318] which is probably due to fewer accepting modes and weaker solvent-solute coupling.

Experiments on the high-frequency librations and the OH bending vibration of pure water show a different behaviour. Transient spectra of pump-induced absorbance changes are plotted in Figure 5.13. In the left panel, a very flat positive librational response is found in the entire spectral range of the excitation pulse between 1200cm^{-1} and 1600cm^{-1}. This response extends into the region of the excited state absorption of the OH bending mode at about 1550cm^{-1} in the right panel. The excited state absorption of the OH bending vibration cannot be distinguished from the librational response in the transient spectra but can be identified by the different relaxation times in the time transients. Ground state bleaching and stimulated emission appear at the fundamental transition of 1650cm^{-1} at early pump-probe delays. With larger pump-probe delay, increased absorption grows in at 1640cm^{-1}. Decreased absorption at 1670cm^{-1} for long delays is not obvious because of a broad background absorption that stems from the librations and has been indicated

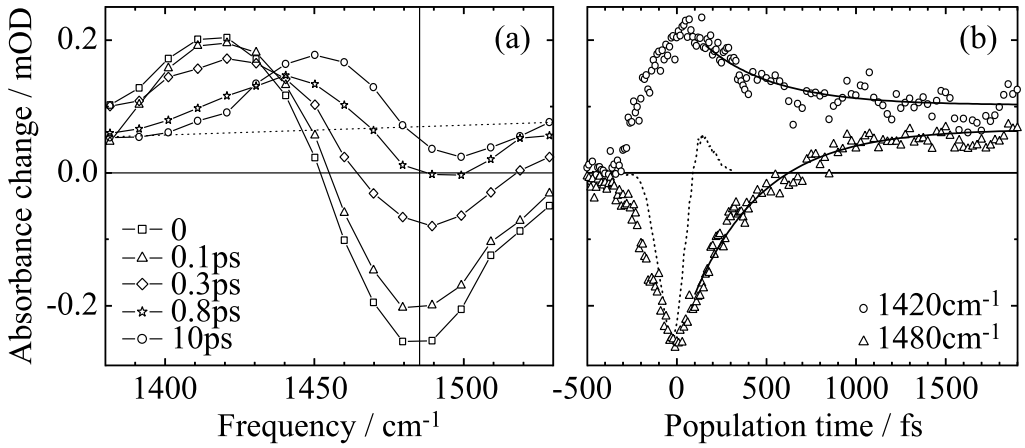

Figure 5.12: Pump-probe data of the OH bending vibration of HOD in D_2O. (a) Transient absorption spectra as a function of probe frequency. (b) Spectral transients as a function of pump-probe delay (symbols) and exponential fits $A_1 e^{-t/t_0} + A_2(1 - e^{-t/t_0})$ with t_0=400fs. The dotted graph is the two-photon absorption in 70μm thin InAs.

by a dotted line in Figure 5.13b. The cause for the picosecond absorbance changes is the temperature effect that was already mentioned [314]. When temperature increases, the OH bending mode of H_2O also shifts to the red and the absorptive lineshape becomes narrower.

The time scales of energy relaxation and thermalisation are contained in Figure 5.14. Transients are plotted in the spectral region of the librations (left) and the OH bending mode of H_2O (right). The librational response is very fast and cannot be resolved. One is tempted to attribute this response to the dispersive part of the electric susceptibility or to cross-phase modulation between the pump and the probe pulse. However, cross-phase modulation looks quite different from the entirely flat spectral response of the librations. Figure 5.4 shows the broad extent of the librational band between 1000 and 1600cm^{-1} that belongs to delocalised excitations with a very short lifetime. The fast librational response actually reflects population relaxation. The fast response is followed by decreased absorption that grows in exponentially with a time constant of (430±50)fs and persists for maximum pump-probe delay of 100ps.

The transient signals of the excited state absorption and the ground state bleaching/stimulated emission of the bending vibrations are displayed in the right panel of Figure 5.14. The rise of both transients is much slower than the two-photon absorption signal that is shown as a dotted negative peak. It is due to the perturbed free induction decay and rises with the dephasing time of the transition. The linewidth of the OH bending vibration is about 80cm^{-1} which sets a lower limit of 133fs to the pure dephasing time. But some inhomogeneous broadening of the OH bending lineshape can be expected in view of the large distribution of hydrogen bond geometries. Furthermore, the rise is of the perturbed free induction decay is not exponential in shape, suggesting inhomogeneous broadening to some extent. Walrafen et al. used two Gaussian lineshapes to fit temperature dependent Raman spectra of the OH bending vibration, implicitly assuming a strong inhomogeneous

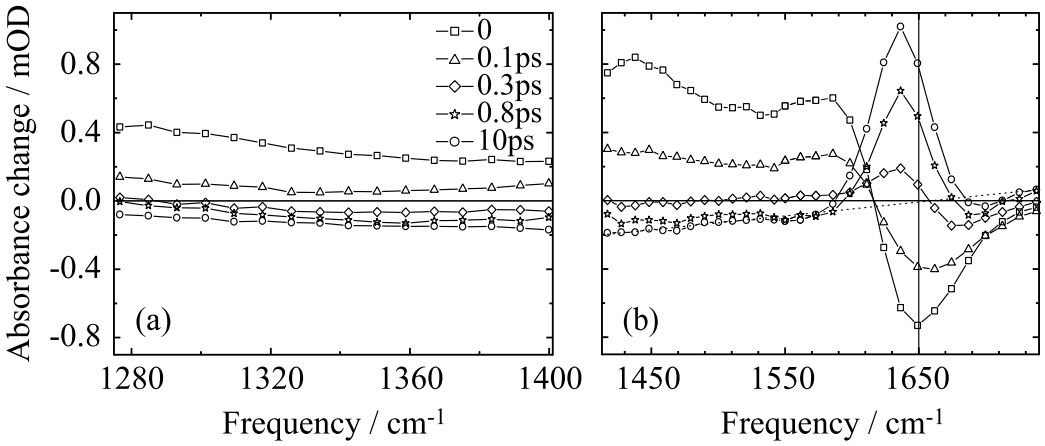

Figure 5.13: Transient absorption spectra as a function of probe frequency in the region of the high-frequency librations (a) and the OH bending vibration of pure water (b).

broadening [314]. Their decomposition shows a narrow component (FWHM$\approx$100cm^{-1}) at about 1650cm^{-1} and a broad component (FWHM$\leq$300cm^{-1}) that is red-shifted by about 40cm^{-1}. In view of the complicated water structure, a lineshape model with a continuous distribution of water geometries might be more apt than a two component model. Eventually, photon echo spectroscopy of the OH bending mode will advance the knowledge on this subject.

The excitation of the δ_{OH} mode always includes simultaneous excitation of the librations because of the spectral overlap. To account for the underlying librational response, the transient at 1560cm^{-1} has been fit with an exponential decay to which the fixed librational fits have been added during variation. The resulting decay time was (170$\pm$)30fs. To confirm this short time constant, the same procedure has been used in the fit of the transient at 1650cm^{-1}. A fast decay constant of 170 was retrieved along with a slow rise time of (770$\pm$150)fs. The fast decay time corresponds to the lifetime unless significant energy transfer among OH bending oscillators occurs. Then, the decay of the isotropic absorbance difference contains the lifetime. A Förster energy transfer rate between neighbouring oscillators scales with the product of the oscillators' dipoles. To estimate the time constant for resonant energy transfer between neighbouring OH bending oscillators, the ratio of maximum absorption cross-section of the OH bending and stretching oscillators can be used. This ratio is about 4.5 [220, 221]. Thus, the Förster transfer time between OH bending oscillators should be about 20 times longer than for OH stretching oscillators, i.e. several picoseconds. The rotation correlation time of water is 700fs or longer as calculated on page 93. Therefore, the decay of the parallel pump-probe signal must reflect the population decay, free of delocalisation of energy and molecular re-orientation.

The polarisation anisotropy has been calculated from a pump-probe measurement with crossed polarisations of the two pulses and seems to decay with 170fs. A fast decay of the polarisation anisotropy would indicate a rapid delocalisation of vibrational energy over a large number of water molecules. However, the data quality is not so good as to extract reliable time constants, especially because the transient signals change sign at about 300fs.

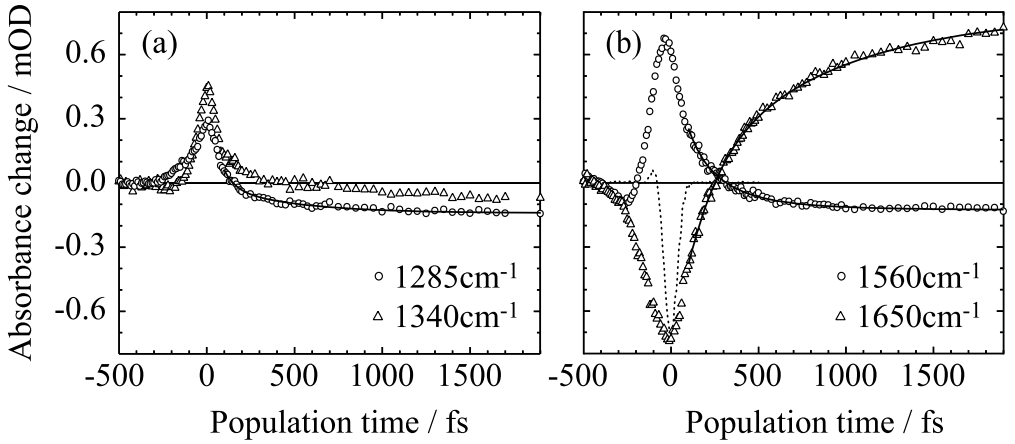

Figure 5.14: Pump-probe transients of pure water in the region of the high-frequency librations (a) and the OH bending vibration (b). The measured pump-probe transients (symbols) are displayed along with fits (lines) $A_1 e^{-t/t_1} + A_2(1 - e^{-t/t_2})$: t_1=60fs and t_2=430fs for the high-frequency librations and t_1=170fs and t_2=770fs for water. The dotted lines is the two-photon absorption in 70μm thin InAs.

A comparison of the OH bending lifetimes of H_2O in H_2O, H_2O in D_2O, and HOD in D_2O suggests that the spectral density of the solvent is the main cause for the different lifetimes. In D_2O, the δ_{OH} mode relaxes directly to the ground state and populates the low-frequency solvent modes. The lifetime of 400fs is very similar to the thermalisation time in H_2O after excitation of the high-frequency librations. In pure water, the first excited state of the OH bending mode relaxes more than twice as fast and thermalisation takes twice as long. Maybe, an intermediate state is populated, possibly via Fermi-resonances between librational combination and overtones and the first excited state of the OH bending mode. Surely, the decisive difference between OH modes in H_2O and D_2O that determines energy relaxation and equilibration is the spectral density of intermolecular modes of the solvent. It would be interesting to study pure D_2O to see whether similar behaviour between pure H_2O and pure D_2O exists.

Pakoulev et al. [301] have reported a lifetime of 1.4ps for the bending mode's first excited state. They assumed relaxation of the excited OH stretching modes within 0.6ps via a Fermi resonance with the second overtone of the bending mode. Although this relaxation pathway is quite probable in regard of the shorter lifetime of the OH stretching mode in H_2O compared to HOD in D_2O, the lifetimes derived in this work are many times shorter. The reason probably lies in the high excitation energies of up to 50μJ in IR pump-Raman probe experiments of Pakoulev et al. causing a temperature jump as high as 60K within the pump pulse duration of 1ps. It has been shown that the lifetimes of OH oscillators increase with temperature [235]. As local temperatures rise by tens of degrees, thermal breaking of hydrogen bonds becomes more frequent resulting in weakly bound or isolated OH oscillators that will exhibit much longer lifetimes than at room temperature. This might explain why systematically longer time constants have been reported by Pakoulev et al. compared with all other groups that have recently investigated liquid water.

5.4 Conclusions

Concluding the chapter, neat and isotopically diluted water has been investigated with ultrafast infrared spectroscopy. First, the OH stretching vibration has been investigated with photon echo spectroscopy. Its first excited state has a lifetime of 200fs. Upon local OH stretching excitation, spectral diffusion toward the centre of the OH stretching band occurs within 50fs. Underlying this spectral behaviour are ultrafast structural rearrangements of the surrounding hydrogen bond network that have been attributed to hindered rotations (librations) of the neighbouring water molecules. Furthermore, fast energy transfer between adjacent OH stretching oscillators very efficiently delocalises the energy with a time constant of 80fs. The excess energy is very effectively redistributed upon de-excitation of the OH stretching vibration such that the excitation volume equilibrates thermally with a time constant of about 1ps.

Next, the OH bending vibration and the high-frequency librations in neat water have been investigated with pump-probe spectroscopy. The lifetime of the bending mode's first excited state is even shorter than that of the stretching modes, i.e. 170fs. The energy relaxes into intermolecular modes of the hydrogen bond network that are delocalised such that the polarisation anisotropy vanishes upon de-excitation of the OH bending vibration. Absorbance changes that can be attributed to thermal equilibration of the excitation volume rise with a time constant of 0.8ps. The librational optical response is extremely short-lived, such that it cannot be resolved. Again, the fast librational response is followed by fast thermalisation processes with a time constant of 0.4ps.

Water remains a fascinating liquid that needs further efforts and explorations in many disciplines. The ultrafast spectroscopic experiments of this chapter have contributed, using new sample cells and new experimental setups, to elucidate microscopic dynamics of the complicated hydrogen bond network. It has been shown that energy transfer, relaxation, and equilibration processes are extremely fast in water – faster than in any other liquid. It will be interesting to investigate the biological relevance to the observed water behaviour. Rapid energy delocalisation may be advantageous for the protection of native molecular structures that are coupled to the hydrogen bond network of water, in particular weakly bound configurations such as proteins but also base pairs in DNA strands. The interaction between water and such solution constituents has been debated for a long time and I am convinced that nonlinear vibrational spectroscopy will be one of the more preferential tools in future investigation.

Summary

Hydrogen bonds are weak interactions compared to ionic or covalent bonds, nonetheless, they have a great influence on the structure and the dynamical behaviour of molecular systems. They are of fundamental importance in nature, e.g. they play a key role in the genome of all living organisms, in the structure and function of proteins, and the peculiarities of water. The research on hydrogen-bonded systems has its origins in the nineteenth century and the hydrogen bond concept emerged at the beginning of the twentieth century. Since then, infrared spectroscopy is one of the main scientific methods for the investigation of this interaction.

The motivation for this thesis has been a deeper understanding of intermolecular hydrogen bonds in liquids and molecular complexes in liquid environments. Famous scientist such as Wilhelm Conrad Röntgen, Walther Nernst, Anders Jonas Ångström, and Linus Pauling have investigated hydrogen-bonded systems, among them the acetic acid dimer and water. These systems form O–H$\cdots$O bonds in which the OH stretching vibration constitutes a very sensitive probe of structural dynamics and underlying couplings between the molecular constituents. Acetic acid dimers in apolar solvents form intermediately strong hydrogen bonds and are of well-defined geometry. In contrast, water molecules are held together by weak hydrogen bonds and form a rapidly fluctuating network with a multitude of hydrogen bond lengths and angles.

With the advent of pulsed laser technology, it has become possible to follow molecular processes in real time, ultimately reaching ultrafast resolution that allowed to follow nuclear motions. Time-resolved infrared spectroscopy has become an important experimental method because of its chemical specificity and the confinement of information to small parts of the molecule. The development of optical analogues of multidimensional nuclear magnetic resonance spectroscopy has proved to be particularly suited for ultrafast infrared spectroscopy. Parts of this thesis were dedicated to the advancement of these techniques, producing the first passively phase-locked experiment for coherent multidimensional infrared spectroscopy.

Acetic acid forms symmetric dimers in apolar liquids and serves as a model system of coupled intermolecular hydrogen bonds. A quantum mechanical description of this system based on experimental results has been lacking but its development would contribute substantially to the understanding of similar more complex systems such as DNA base pairs. The OH stretching vibration in these dimers displays a very complex absorption band, the origin of which is being debated for more than half a century. Three coupling mechanisms are mainly held responsible for this absorptive behaviour: (i) excitonic (Davydov) coupling between the degenerate OH stretching modes, (ii) anharmonic coupling between the OH stretching modes and low-frequency hydrogen bond modes, and (iii) Fermi resonances

between the first excited state of the OH stretching modes and combination and overtones of other intramolecular vibrational modes.

Experimental results of ultrafast infrared pump-probe and photon echo spectroscopy were combined with high-level quantum chemical calculations to dissect the various contributions to the lineshape under discussion. The Davydov coupling between the OH stretching modes turns out to be of minor importance and is estimated to be less than 10cm^{-1}. Strong anharmonic coupling with cubic force constants of more than 150cm^{-1}exists between the OH stretching modes and the low-frequency dimer stretching and in-plane wagging modes. The latter ones have eigenfrequencies of 145cm^{-1} and 165cm^{-1}. Clearly underdamped coherent nuclear motions of the monomers, i.e. wave packets in hydrogen bond modes, can be created upon excitation of the OH stretching modes in liquid phase. These coherences have a dephasing time of 0.7ps. Coherent polarisations of the OH stretching modes decay with a dephasing time of 200fs and show pronounced beating due to quantum interference caused by the simultaneous excitation of coherences in the hydrogen bond modes. Fermi resonances between the first excited state of the OH stretching modes and combination and overtones of the OH bending, C=O and C–O stretching, and the methyl torsion modes, are due to equally strong anharmonic coupling with cubic force constants of 150cm^{-1}. Faster dephasing of these transitions disguise their nature in the time domain whereas the more slowly dephasing wave packets of the dimer modes manifest on longer time scales. However, the linear and the coherent two dimensional spectra are dominated by these Fermi resonances. Lifetime measurements of the OH stretching and bending modes yield values of 200fs and 250fs, respectively. A dominant decay channel of the OH stretching modes does not seem to exist. In summary, the first comprehensive quantum mechanical model based on experimental results and quantum chemical calculations has been developed that describes the acetic acid dimer in the gas phase and apolar solvents with high fidelity and answers several long-standing questions.

One of the key questions in water research concerns the structure of this rapidly fluctuating hydrogen bond network and its dynamical behaviour. Characteristic timescales of these dynamics span over a wide range. Equivalently, the spectral density of water shows many pronounced features from a few Gigahertz to frequencies of hard x-rays. Hydrogen-bonding between water molecules is largely responsible for this behaviour and many ultrafast spectroscopic experiments in the infrared have been published in the last 15 years. However, only a few of these studies have investigated neat water (liquid H_2O) because the main probe, the OH stretching vibration (ν_{OH}), has too high an absorption cross-section to perform transmission experiments with water films thicker than 1μm. A newly developed sample cell with negligible window contributions during pulse overlap containing a stable 500nm thick water film allows for investigations of neat water with vibrational pump-probe and photon echo spectroscopy with the highest currently available time-resolution.

The OH stretching vibration has been investigated with coherent multidimensional infrared spectroscopy. Most striking is the fast spectral diffusion of ν_{OH} transition frequencies within 50fs. It is dominantly caused by hindered rotations in the hydrogen bond network, called librations, which respond to the vibrationally excited water molecule. The distribution of ν_{OH} transition frequencies is randomised so quickly that the transition frequency correlation vanishes within 50fs. In other words, an excited water molecule 'loses its mem-

ory' of the transition frequency it has been excited by within 50fs. Also observable is a fast decay of the polarisation anisotropy with a time constant of 80fs upon OH stretching excitation. It is attributed to resonant energy transfer between neighbouring water molecules. The average lifetime of the first excited state of the OH stretching mode is 200fs, shorter than anticipated from experiments on isotopically diluted water. The thermalisation of the excitation volume happens in only a few picoseconds. This means that temperature jumps of more than 100K within 2ps are feasible which is remarkably fast as well.

Finally, the OH bending vibration and high-frequency librations were investigated with ultrafast vibrational pump-probe spectroscopy. The OH bending mode is the intramolecular mode with the lowest eigenfrequency and, thus, can only be de-excited by coupling to modes of the hydrogen bond network. Despite this interesting direct coupling, little is known about the dynamical behaviour of this vibration. It turns out that the lifetime of the OH bending mode is only 170fs and the librational response is faster than the 70fs time resolution. After femtosecond excitation of these modes, population relaxation distributes the excess energy into low-frequency modes and the excitation volume reaches thermal equilibrium even more rapidly than it does after excitation of the OH stretching mode. The corresponding time constants of this thermalisation due to bending and librational excitation are 800fs and 430fs, respectively.

A comprehensive water model is still not at hand that correctly describes the results of various experimental techniques, e.g. neutron and x-ray diffraction, near edge fine structure x-ray absorption spectroscopy, and vibrational spectroscopy. Therefore, it would be desirable to combine the different techniques to get complimentary time-resolved information. Also, interactions between water and proteins and water and DNA are highly relevant in many biological systems and many questions on the molecular coupling mechanisms in these systems remain that might be answered with vibrational spectroscopy.

Publications

[1] N. Huse, B. D. Bruner, M. L. Cowan, J. Dreyer, E. T. J. Nibbering, R. J. D. Miller, and T. Elsaesser, "Anharmonic couplings underlying ultrafast vibrational dynamics of hydrogen bonds in liquids," Phys. Rev. Lett. **95,** 147402 (2005).

[2] N. Huse, J. Dreyer, E. T. J. Nibbering, T. Elsaesser, B. D. Brunner, M. L. Cowan, and R. J. D. Miller, "Heterodyne 2D-IR Photon Echo Spectroscopy of Multi-Level O–H stretching Coherences in Hydrogen Bonds," In *Ultrafast Phenomena XIV*, T. Kobayashi, T. Okada, T. Kobayashi, K. A. Nelson, and S. De Silvestri, eds., Springer Ser. Chem. Phys. pp. 407–409 (Springer-Verlag, Berlin Heidelberg, 2005).

[3] M. L. Cowan*, B. D. Brunner*, N. Huse*, J. Dwyer, B. Chugh, E. T. J. Nibbering, T. Elsaesser, and R. J. D. Miller, "Ultrafast memory loss and energy redistribution in the hydrogen bond network of liquid H_2O," Nature **434,** 199 (2005).

[4] N. Huse, S. Ashihara, E. T. J. Nibbering, and T. Elsaesser, "Ultrafast vibrational relaxation of O–H bending and librational excitations in liquid H_2O," Chem. Phys. Lett. **404,** 389 (2005).

[5] K. Heyne, N. Huse, J. Dreyer, E. T. J. Nibbering, T. Elsaesser, and S. Mukamel, "Coherent low-frequency motions of hydrogen bonded acetic acid dimers in the liquid phase," J. Chem. Phys. **121,** 902 (2004).

[6] N. Huse, K. Heyne, J. Dreyer, E. T. J. Nibbering, and T. Elsaesser, "Vibrational Multilevel Quantum Coherence due to Anharmonic Couplings in Intermolecular Hydrogen Bonds," Phys. Rev. Lett. **91,** 197401 (2003).

[7] K. Heyne, N. Huse, E. T. J. Nibbering, and T. Elsaesser, "Ultrafast relaxation and anharmonic coupling of O–H stretching and bending excitations in cyclic acetic acid dimers," Chem. Phys. Lett. **382,** 19 (2003).

[8] K. Heyne, N. Huse, E. T. J. Nibbering, and T. Elsaesser, "Ultrafast coherent nuclear motions of hydrogen bonded carboxylic acid dimers," Chem. Phys. Lett. **369,** 591 (2003).

[9] K. Heyne, N. Huse, E. T. J. Nibbering, and T. Elsaesser, "Coherent vibrational dynamics of intermolecular hydrogen bonds in acetic acid dimers studied by ultrafast mid-infrared spectroscopy," J. Phys.: Condens. Mat. **15,** 129 (2003).

Other publications

[1] E. Engel, N. Huse, T. A. Klar, and S. W. Hell, "Creating $\lambda/3$ focal holes with a Mach-Zehnder interferometer," Appl. Phys. B **77,** 11 (2003).

[2] N. Huse, A. Schönle, and S. W. Hell, "Z-polarized confocal microscopy," J. Biomed. Opt. **6,** 273 (2001).

Bibliography

[1] S. Bratos, J.-C. Leicknam, G. Gallot, and H. Ratajczak, "Infra-red spectra of hydrogen bonded systems: Theory and experiment," in *Ultrafast hydrogen bonding dynamics and proton transfer processes in the condensed phase*, Vol. 23 of *Understanding chemical reactivity*, T. Elsaesser and H. J. Bakker, eds., (Kluwer Academic Publishers, Dordrecht, The Netherlands, 2002), p. 5.

[2] J. D. Watson and F. H. C. Crick, "Molecular Structure of Nucleic Acids – A Structure for Deoxyribose Nucleic Acid," Nature **171,** 737 (1953).

[3] I. Rayment, H. M. Holden, M. Whittaker, C. B. Yohn, M. Lorenz, K. C. Holmes, and M. R. A., "Structure of the Actin-Myosin Complex and its Implications for Muscle-Contraction," Science **261,** 58 (1993).

[4] J. H. Taylor, P. S. Woods, and W. L. Hughes, "The Organization and Duplication of Chromosomes as Revealed by Autiradiographic Studies using Tritium-Labeled Thymidine," Proc. Natl. Acad. Sci. USA **43,** 122 (1957).

[5] G. Wald, "Molecular Basis of Visual Excitation," in *Nobel Lectures, Physiology or Medicine 1963-1970* (Elsevier Publishing Company, Amsterdam, 1972), p. 292.

[6] W. M. Latimer and W. H. Rodebush, "Polarity and Ionization from the Standpoint of the Lewis Theory of Valence," J. Am. Chem. Soc. **42,** 1419 (1920).

[7] L. Pauling, "The Shared-Electron Chemical Bond," Proc. Natl. Acad. Sci. USA **14,** 359 (1928).

[8] T. S. Moore and T. F. Winmill, "The State of Amines in Aqueous Solution," J. Chem. Soc., Trans. **101,** 1635 (1912).

[9] A. Werner, "Ueber Haupt- und Nebenvalenzen und die Constitution der Ammoniumverbinungen," Liebigs Ann. d. Chemie **322,** 261 (1902).

[10] P. Pfeiffer, "Zur Theorie der Farblacke II," Liebigs Ann. d. Chemie **398,** 137 (1913).

[11] L. Pauling, *The Nature of the Chemical Bond and the Structure of Molecules and Crystals: An Introduction to Modern Structural Chemistry* (Cornell University Press, Ithaca, U.S.A., 1939).

[12] L. Pauling, R. Corey, and H. Branson, "The Structure of Proteins: Two Hydrogen-Bonded Helical Configurations of the Polypeptide Chain," Proc. Natl. Acad. Sci. USA **37,** 205 (1951).

[13] C. C. F. Blake, G. A. Koenig, G. A. Mair, A. C. T. North, D. C. Phillips, and V. R. Sarma, "Structure of Hen Egg-White Lysozyme," Nature **206,** 757 (1965).

[14] W. K. Alderton, C. E. Cooper, and R. G. Knowles, "Nitric oxide synthases: structure, function and inhibition," Biochem. J. **357,** 593 (2001).

[15] I. Antes, D. Chandler, H. Wang, and G. Oster, "The Unbinding of ATP from F_1-ATPase," Biophys. J. **85,** 695 (2003).

[16] T. Elsaesser and W. Kaiser, "Visible and infrared spectroscopy of intramolecular proton transfer using picosecond laser pulses," Chem. Phys. Lett. **128,** 231 (1986).

[17] M. Rini, J. Dreyer, E. T. J. Nibbering, and T. Elsaesser, "Ultrafast vibrational relaxation processes induced by intramolecular excited state hydrogen transfer," Chem. Phys. Lett. **374,** 13 (2003).

[18] M. Rini, B. Z. Magnes, E. Pines, and E. T. J. Nibbering, "Real-time observation of bimodal proton transfer in acid-base pairs in water," Science **301,** 349 (2003).

[19] K. Chen, J. Hirst, R. Camba, C. A. Bonagura, C. D. Stout, B. K. Burgess, and F. A. Armstrong, "Atomically defined mechanism for proton transfer to a buried redox centre in a protein," Nature **405,** 814 (2000).

[20] *The Hydrogen Bond: Recent developments in theory and experiments*, P. Schuster, G. Zundel, and C. Sandorfy, eds., (North Holland, Amsterdam, The Netherlands, 1976).

[21] *Ultrafast hydrogen bonding dynamics and proton transfer processes in the condensed phase*, Vol. 23 of *Understanding chemical reactivity*, T. Elsaesser and H. J. Bakker, eds., (Kluwer Academic Publishers, Dordrecht, The Netherlands, 2002).

[22] *Hydrogen-Transfer Reactions*, R. L. Schowen, J. P. Klinman, J. T. Hynes, and H.-H. Limbach, eds., (Wiley-VCH, Weinheim, Germany, 2006), Vol. 1: Physical and Chemical Aspects, in press.

[23] C. Rischel, A. Rousse, I. Uschmann, P. A. Albouy, J. P. Geindre, P. Audebert, J. C. Gauthier, E. Förster, J. L. Martin, and A. Antonetti, "Femtosecond time-resolved X-ray diffraction from laser-heated organic films," Nature **390,** 490 (1997).

[24] C. W. Siders, A. Cavalleri, K. Sokolowski-Tinten, C. Tóth, T. Guo, M. Kammler, M. H. v. Hoegen, K. R. Wilson, D. v. d. Linde, and C. P. J. Barty, "Detection of Nonthermal Melting by Ultrafast X-ray Diffraction," Science **286,** 1340 (1999).

[25] H. Ihee, V. A. Lobastov, U. M. Gomez, B. M. Goodson, R. Srinivasan, C.-Y. Ruan, and A. H. Zewail, "Direct Imaging of Transient Molecular Structures with Ultrafast Diffraction," Science **291,** 458 (2001).

[26] B. J. Siwick, J. R. Dwyer, R. E. Jordan, and R. J. D. Miller, "An Atomic-Level View of Melting Using Femtosecond Electron Diffraction," Science **302,** 1382 (2003).

[27] M. Bargheer, N. Zhavoronkov, Y. Gritsai, J. C. Woo, D. S. Kim, M. Woerner, and T. Elsaesser, "Coherent Atomic Motions in a Nanostructure Studied by Femtosecond X-ray Diffraction," Science **306,** 1771 (2004).

[28] D. W. Oxtoby, "Dephasing of molecular vibrations in liquids," in *Advances in Chemical Physics*, I. Prigogine and R. S. A., eds., (J. Wiley, New York, U.S.A., 1979), Vol. 40, p. 1.

[29] A. Novak, "Hydrogen bonding in solids. Correlation of spectroscopic and crystallographic data," Structure & Bonding **18,** 177 (1974).

[30] G. E. Hilbert, O. R. Wulf, S. B. Hendricks, and U. Liddel, "The Hydrogen Bond between Oxygen Atoms in Some Organic Compunds," J. Am. Chem. Soc. **58,** 548 (1936).

[31] R. H. Gillete and F. Daniels, "The Effect of Association on the Infra-red Absorption Spectrum of Acetic Acid," J. Am. Chem. Soc. **58,** 1139 (1936).

[32] J. Errera and P. Mollet, "Intermolecular forces and O-H absorption bands in alcohols at 3μ," Nature **139,** 882 (1936).

[33] E. L. Kinsey and J. W. Ellis, "Infrared Absorption Spectra of the Alcohols, Two Acids, and Their Solutions in Carbon Tetrachloride," J. Chem. Phys. **5,** 399 (1937).

[34] R. M. Badger and Bauer, "Spectroscopic Studies of the Hydrogen Bond II. The Shift of the O–H Vibrational Frequency in the Formation of the Hydrogen Bond," J. Chem. Phys. **5,** 839 (1937).

[35] A. M. Buswell, W. H. Rodebush, and M. F. Roy, "Infrared Absorption Studies. V. Association in the Carboxylic Acids," J. Am. Chem. Soc. **60,** 2239 (1938).

[36] M. M. Davies and G. B. B. M. Sutherland, "The Infra-Red Absorption of Carboxylic Acids in Solution. I. Qualitative Features," J. Chem. Phys. **6,** 755 (1938).

[37] R. E. Rundle and M. Parasol, "O–H stretching Frequencies in Very Short and Possibly Symmetrical Hydrogen Bonds," J. Chem. Phys. **20,** 1487 (1952).

[38] J. Donohue, "The Hydrogen Bond in Organic Crystals," J. Phys. Chem. **56,** 502 (1952).

[39] N. Fuson, M.-L. Josien, R. L. Powell, and E. Utterback, "The NH Stretching Vibration and NH–N Hydrogen Bonding in Several Aromatic Compunds," J. Chem. Phys. **20,** 145 (1952).

[40] K. Nakamoto, M. Margoshed, and R. E. Rundle, "Stretching Frequencies as a Function of Distances in Hydrogen Bonds," J. Am. Chem. Soc. **77,** 6480 (1955).

[41] E. T. J. Nibbering and T. Elsaesser, "Ultrafast Vibrational Dynamics of Hydrogen Bonds in the Condensed Phase," Chem. Rev. **104,** 1887 (2004).

[42] J. L. Derissen, "A reinvestigation of the molecular structure of acetic acid monomer and dimer by gas electron diffraction," J. Mol. Struct. **7,** 67 (1971).

[43] G. A. Jeffrey, *Introduction to Hydrogen Bonding* (Oxford University Press, New York, 1997).

[44] T. Steiner, "The hydrogen bond in the solid state," Angew. Chem. **41,** 48 (2002).

[45] J. Ireta, J. Neugebauer, and M. Scheffler, "On the Accuracy of DFT for Describing Hydrogen Bonds: Dependence on the Bond Directionality," J. Phys. Chem. A **108,** 5692 (2004).

[46] J. A. Belot, J. Clark, J. A. Cowan, G. S. Harbison, A. I. Kolesnikov, Y.-S. Kye, A. J. Schultz, C. Silvernail, and X. Zhao, "The Shortest Symmetrical O-H$\cdots$O Hydrogen Bond Has a Low-Barrier Double-Well Potential," J. Phys. Chem. B **108,** 6922 (2004).

[47] S. Mukamel, *Principles of Nonlinear Optical Spectrsocopy* (Oxford University Press, New York, U.S.A., 1995), chapter 8.

[48] E. T. J. Nibbering, *Femtosecond Optical Dynamics in Liquids*, Ph.D. thesis, Rijksuniversiteit Groningen, The Netherlands, 1993.

[49] P. Hamm, "Principles of Nonlinear Spectroscopy,", 2001, lecture at the Max-Born-Institut, Berlin, Germany.

[50] R. W. Boyd, *Nonlinear Optics* (Academic Press, London, U.K., 1993), pp. 274–280.

[51] C. W. Luo, K. Reimann, M. Woerner, T. Elsaesser, R. Hey, and K. H. Ploog, "Phase-Resolved Nonlinear Response of a Two-Dimensional Electron Gas under Femtosecond Intersubband Excitation," Phys. Rev. Lett. **92,** 047402 (2004).

[52] J. J. Sakurai, *Modern Quantum Mechanics*, 2 ed. (Addison Wesley, Boston, U.S.A., 1994).

[53] R. Zwanzig, "Ensemble Method in the Theory of Irreversibility," J. Chem. Phys. **33,** 1338 (1960).

[54] M. Born and J. R. Oppenheimer, "Zur Quantentheorie der Molekeln," Ann. d. Physik **389,** 457 (1927).

[55] W. Magnus, "On the Exponential Solution of Differential Equations for a Linear Operator," Commun. Pure Appl. Math. **7,** 649 (1954).

[56] R. Kubo and K. Tomita, "A General Theory of Magnetic Resonance Absorption," J. Phys. Soc. Jap. **9,** 888 (1954).

[57] R. Kubo, "Statistical-Mechanical Theory of Irreversible Processes," J. Phys. Soc. Jap. **12,** 570 (1957).

[58] M. Tokuyama and H. Mori, "Statistical Mechanical Theory of Random Frequency Modulations and Generalized Brownian Motions," Prog. Theor. Phys. **55,** 411 (1976).

[59] S. Bratos, "Inrared Spectra of Molecules with Hydrogen Bonds," J. Chem. Phys. **27,** 991 (1957).

[60] R. L. Fulton and M. Gouterman, "Vibronic Coupling. II. Spectra of Dimers," J. Chem. Phys. **41,** 2280 (1964).

[61] Y. Maréchal and A. Witkowski, "Infrared Spectra of H-Bondod Systems," J. Chem. Phys. **48,** 3697 (1968).

[62] S. Bratos, "Profiles of Hydrogen Stretching IR Bands of Molecules with Hydrogen Bonds: A Stochastic Theory. I. Weak ad Medium Strength Hydrogen Bonds," J. Chem. Phys. **63,** 3499 (1975).

[63] G. R. Robertson and J. Yarwood, "Vibrational Relaxation of Hydrogen-Bonded Species in Solution. I. Theory," Chem. Phys. **32,** 267 (1978).

[64] P. Ruggiero and M. Zannetti, "Microscopic derivationof the stochastic process for the quantum Brownian oscillator," Phys. Rev. A **28,** 987 (1983).

[65] Y. J. Yan and S. Mukamel, "Electronic dephasing, vibrational relaxation, and solvent friction in molecular nonlinear optical line shapes," J. Chem. Phys. **89,** 5160 (1988).

[66] S. A. Passino, Y. Nagasawa, and G. R. Fleming, "Three pulse stimulated photon echo experiments as a probe of polar solvation dynamics: Utility of harmonic bath models," J. Chem. Phys. **107,** 6094 (1997).

[67] W. P. de Boeij, M. S. Pshenichnikov, and D. A. Wiersma, "Ultrafast Solvation Dynamics Explored by Femtosecond Photon Echo Spectroscopies," Ann. Rev. Phys. Chem. **49,** 99 (1998).

[68] F. Bloch, "Nuclear Induction," Phys. Rev. **70,** 460 (1946).

[69] J.-L. Leviel and Y. Maréchal, "Infrared Spectra of H-Bondod Systems: Anharmonicity of the H-Bond Vibrations in Cyclic Dimers," J. Chem. Phys. **54,** 1104 (1971).

[70] N. Rösch and M. A. Ratner, "Model for the effects of a condensed phase on the infrared spectra of hydrogen-bonded systems," J. Chem. Phys. **61,** 3344 (1974).

[71] S. Mühle, K.-E. Süsse, and D.-G. Welsch, "The Influence of Intramolecular Interactions on the Broadening of the IR Absorption of Hydrogen-Bonded Species," Phys. Lett. A **66,** 25 (1978).

[72] Y. Maréchal, "Dynamique des hydrogènes dans les liaisons hydrogène des dimères de l'acide acétique," J. Phys. B **6,** L188 (1973).

[73] A. Witkowski and M. Wójcik, "Infrared spectra of hydrogen bond a general theoretical model," Chem. Phys. **1,** 9 (1973).

[74] D. Chamma and O. Henri-Rousseau, "IR theory of weak H-bonds: Davydov coupling, Fermi resonances and direct relaxations. I. Basis equations within the linear response theory," Chem. Phys. **248,** 53 (1999).

[75] D. Chamma and O. Henri-Rousseau, "IR theory of weak H-bonds: Davydov coupling, Fermi resonances and direct relaxations. II. General trends, from numerical experiments," Chem. Phys. **248,** 71 (1999).

[76] A. M. Moran, J. Dreyer, and S. Mukamel., "Ab initio simulation of the two-dimensional vibrational spectrum of RDC," J. Chem. Phys. **118,** 1347 (2003).

[77] J. Dreyer, "Hydrogen-bonded acetic acid dimers: Anharmonic coupling and linear infrared spectra studied with density functional theory," J. Chem. Phys. **122,** 184306 (2005).

[78] J. Dreyer, "Density functional theory simulations of two-dimensional infrared spectra for hydrogen-bonded acetic acid dimers," Int. J. Quant. Chem. **104,** 782 (2005).

[79] R. L. Fulton and M. Gouterman, "Vibronic Coupling. I. Mathematical Treatment for Two Electronic States," J. Chem. Phys. **35,** 1059 (1961).

[80] W. T. Pollard, S.-Y. Lee, and R. A. Mathies, "Wave packet theroy of dynamic absorption spectra in femtosecond pump-probe experiments," J. Chem. Phys. **92,** 4012 (1990).

[81] H. Hamaguchi and T. L. Gustafson, "Ultrafast Time-Resolved Spontaneous and Coherent Raman Spectroscopy: The Structure and Dynamics of Photogenerated Transient Species," Ann. Rev. Phys. Chem. **45,** 593 (1994).

[82] C. Sandorfy, "Anharmonicity and hydrogen bonding," in *The Hydrogen Bond: Recent developments in theory and experiments*, G. Z. P. Schuster and C. Sandorfy, eds., (North Holland, Amsterdam, the Netherlands, 1976), Vol. II. Structure and Spectroscopy, p. 613.

[83] C. H. B. Cruz, J. P. Gordon, P. C. Becker, R. L. Fork, and C. V. Shank, "Dynamics of Spectral Hole Burning," IEEE J. Quantum Electron. **24,** 261 (1988).

[84] P. Hamm, "Coherent effects in femtosecond infrared spectroscopy," Chem. Phys. **200,** 415 (1995).

[85] G. R. Fleming, *Chemical applications of ultrafast spectroscopy* (Oxford University Press, New York, U.S.A., 1986), chapter 6.

[86] N. A. Kurnit, I. D. Abella, and S. R. Hartmann, "Observation of a Photon Echo," Phys. Rev. Lett. **13,** 567 (1964).

[87] W. P. de Boeij, M. S. Pshenichnikov, and D. A. Wiersma, "On the relation between the echo-peak shift and Brownian-oscillator correlation function," Chem. Phys. Lett. **253,** 53 (1996).

[88] W. P. de Boeij, M. S. Pshenichnikov, and D. A. Wiersma, "System-Bath Correlation Function Probed by Conventional and Time-Gated Stimulated Photon Echo," J. Phys. Chem. **100,** 11806 (1996).

[89] T. Joo, Y. Jia, J.-Y. Yu, M. J. Lang, and G. R. Fleming, "Third-order nonlinear time domain probes of solvation dynamic," J. Chem. Phys. **104,** 6089 (1996).

[90] M. Cho, J.-Y. Yu, T. Joo, Y. Nagasawa, S. A. Passino, and G. R. Fleming, "The Integrated Photon Echo and Solvation Dynamics," J. Phys. Chem. **100,** 11944 (1996).

[91] D. M. Jonas, "Two-Dimensional Femtosecond Spectroscopy," Ann. Rev. Phys. Chem. **54,** 425 (2003).

[92] J. Jeener, B. H. Meier, P. Bachmann, and R. R. Ernst, "Inverstigation of exchange processes by two-dimensional NMR spectroscopy," J. Chem. Phys. **71,** 4546 (1979).

[93] R. R. Ernst, G. Bodenhausen, and A. Wokaun, *Principles of nuclear magnetic resonance in one and two dimensions* (Clarendon Press, Oxford, U.K., 1987).

[94] J. Jeener, 1971, lecture at the Ampère International Summer School, Basko Polje, Yugoslavia.

[95] V. Cervetto, J. Helbing, J. Bredenbeck, and P. Hamm, "Double-resonance versus pulsed Fourier transform two-dimensional infrared spectroscopy: An experimental and theoretical comparison," J. Chem. Phys. **121,** 5935 (2004).

[96] Q. Wu and X.-C. Zhang, "Free-space electro-optics sampling of mid-infrared pulses," Appl. Phys. Lett. **71,** 1285 (1997).

[97] L. Lepetit, G. Chériaux, and M. Joffre, "Linear techniques of phase measurement by femtosecond spectral interferometry for applications in spectroscopy," J. Opt. Soc. Am. B **12,** 2467 (1995).

[98] A. Einstein, "Zur Quantentheorie der Strahlung," Physik. Z. **18,** 121 (1917).

[99] J. P. Gordon, H. J. Zeiger, and C. H. Townes, "Molecular Microwave Oscillator and New Hyperfine Structure in the Microwave Spectrum of NH_3," Phys. Rev. **95,** 282 (1954).

[100] T. H. Maiman, "Stimulated optical Radiation in Ruby," Nature **187,** 493 (1960).

[101] R. J. Collins, D. F. Nelson, A. L. Schawlow, W. Bond, C. G. B. Garrett, and W. Kaiser, "Coherence, Narrowing, Directionality, and Relaxation Oscillations in the Light Emission from Ruby," Phys. Rev. Lett. **5,** 303 (1960).

[102] F. J. McClung and R. W. Hellwarth, "Giant Optical Pulsations from Ruby," J. Appl. Phys. **33,** 828 (1962).

[103] J. A. Armstrong, "Measurement of Picosecond Laser Pulse Width," Appl. Phys. Lett. **10,** 16 (1967).

[104] E. P. Ippen and C. V. Shank, "Dynamic spectroscopy and subpicosecond pulse compression," Appl. Phys. Lett. **27,** 488 (1975).

[105] J.-C. Diels, E. V. Stryland, and G. Benedict, "Generation and measurement of 200 femtosecond optical pulses," Opt. Comm. **25,** 93 (1978).

[106] R. L. Fork, B. I. Greene, and C. V. Shank, "Generation of optical pulses shorter than 0.1 psec by colliding pulse mode locking," Appl. Phys. Lett. **38,** 671 (1981).

[107] A. Baltuska *et al.*, "Attosecond control of electronic processes by intense light fields," Nature **421,** 611 (2003).

[108] D. Strickland and G. Mourou, "Compression of amplified chirped optical pulses," Opt. Comm. **56,** 219 (1985).

[109] P. F. Moulton, "Spectroscopic and laser characteristics of Ti:Al_20_3," J. Opt. Soc. Am. B **3,** 125 (1986).

[110] P. Albers, E. Stark, and G. Huber, "Continuous-wave laser operation and quantum efficiency of titanium-doped sapphire," J. Opt. Soc. Am. B **3,** 134 (1986).

[111] P. Di Trapani, A. Andreoni, G. P. Banfi, C. Solcia, R. Danielius, A. Piskarskas, P. Foggi, M. Monguzzi, and C. Sozzi, "Group-velocity self-matching of femtosecond pulses in noncollinear parametric generation," Phys. Rev. A **51,** 3164 (1995).

[112] T. Wilhelm, J. Piel, and E. Riedle, "Sub-20-fs pulses tunable across the visible from a blue-pumped single-pass noncollinear parametric converter," Opt. Lett. **22,** 1494 (1997).

[113] R. A. Kaindl, M. Wurm, K. Reimann, P. Hamm, A. M. Weiner, and M. Woerner, "Generation, shaping, and characterization of intense femtosecond pulses tunable from 3 to 20 μm," J. Opt. Soc. Am. B **17,** 2086 (2000).

[114] I. Z. Kozma, P. Baum, S. Lochbrunner, and E. Riedle, "Widely tunable sub-30 fs ultraviolet pulses by chirped sum frequency mixing," Opt. Express **11,** 3110 (2003).

[115] D. E. Spence, P. N. Kean, and W. Sibbet, "60-fsec pulse generation from a self-mode-locked Ti:sapphire laser," Opt. Lett. **16,** 42 (1991).

[116] B. Proctor, E. Westwig, and F. Wise, "Characterization of a Kerr-lens mode-locked Ti:sapphire laser with positive group-velocity dispersion," Opt. Lett. **18,** 1654 (1993).

[117] V. G. Dmitriev, G. G. Gurzadyan, and D. N. Nikogosyan, *Handbook of Nonlinear Optical Crystals*, 2 ed. (Springer-Verlag, Berlin & Heidelberg, Germany, 1997).

[118] R. R. Alfano and S. L. Shapiro, "Observation of Self-Phase Modulation and Small-Scale Filaments in Crystals and Glasses," Phys. Rev. Lett. **24,** 592 (1970).

[119] N. Demirdöven, M. Khalil, O. Golonzka, , and A. Tokmakoff, "Dispersion compensation with optical materials for compression of intense sub-100-fs mid-infrared pulses," Opt. Lett. **27,** 433 (2002).

[120] R. Trebino, *Frequency-resolved optical gating: the measurement of ultrashort pulses* (Kluwer Academic Publishers, Norwell, U.S.A., 2000).

[121] P. Hamm, R. A. Kaindl, and J. Stenger, "Noise suppression in femtosecond mid-infrared light sources," Opt. Lett. **25,** 1798 (2000).

[122] L. Müller, A. Kumar, and R. R. Ernst, "Two-dimensional carbon-13 NMR spectroscopy," J. Chem. Phys. **63,** 5490 (1975).

[123] M. C. Asplund, M. T. Zanni, and R. M. Hochstrasser, "Two-dimensional infrared spectroscopy of peptides by phase-controlled femtosecond vibrational photon echoes," Proc. Natl. Acad. Sci. USA **97,** 8219 (2000).

[124] C. Dorrer, N. Belabas, J.-P. Likforman, and M. Joffre, "Spectral resolution and sampling issues in Fourier-transform spectral interferometry," J. Opt. Soc. Am. B **17,** 1795 (2000).

[125] V. Volkov, R. Schanz, and P. Hamm, "Active phase stabilization in Fourier-transform two-dimensional infrared spectroscopy," Opt. Lett. **30,** 2010 (2005).

[126] M. L. Cowan, J. P. Ogilvie, and R. J. D. Miller, "Two-dimensional spectroscopy using diffractive optics based phased-locked photon echoes," Chem. Phys. Lett. **386,** 184 (2004).

[127] T. Brixner, I. V. Stiopkin, and G. R. Fleming, "Tunable two-dimensional femtosecond spectroscopy," Opt. Lett. **29,** 884 (2004).

[128] J. P. Ogilvie, M. L. Cowan, M. Armstrong, A. Nagy, and R. J. D. Miller, "Diffractive optics-based heterodyne detected three-pulse photon echo," In *Ultrafast Phenomena XIII*, R. J. D. Miller, M. M. Murmane, N. F. Scherer, and A. M. Weiner, eds., Springer Ser. Chem. Phys. p. 571 (Springer-Verlag, Berlin & Heidelberg, Germany, 2003).

[129] N. Belabas and M. Joffre, "Visible-infrared two-dimensional Fourier-transform spectroscopy," Opt. Lett. **27,** 2043 (2002).

[130] H. A. Ferweda, J. Terpstra, and D. A. Wiersma, "Discussion of the "coherent artifact"in four-wave mixing experiments," J. Chem. Phys. **91,** 3296 (1989).

[131] P. J. Rizo and T. Kobayashi, "Chirp characterization of ultrashort pulses utilizing molecular vibrations," Appl. Phys. Lett. **85,** 28 (2004).

[132] M. F.-M. Raoult, "Loi Générale de Congélation des Dissolvants," Ann. Chim. et Phys. VI. Série, **2,** 66 (1884).

[133] E. Beckmann, "Über die Methode der Molekulargewichtsbestimmung durch Gefrierpunktserniedrigung," Z. phys. Chemie **2,** 715 (1888).

[134] W. Nernst, "Verteilung eines Stoffes zwischen zwei Lösungsmitteln und zwischen Lösungsmittel und Dampfraum," Z. phys. Chemie **8,** 110 (1891).

[135] L. Pauling and L. O. Brockway, "The Structure of the Carboxyl Group. I. The Investigation of Formic Acid by the Diffraction of Electrons," Proc. Natl. Acad. Sci. USA **20,** 336 (1934).

[136] L. Pauling and L. O. Brockway, "The Structure of the Carboxyl Group. II. The Crystal Structure of Basic Beryllium Acetate by the Diffraction of Electrons," Proc. Natl. Acad. Sci. USA **20,** 340 (1934).

[137] J. Karle and L. O. Brockway, "An Electron Diffraction Investigation of the Monomers and Dimers of Formic, Acetic and Trifluoroacetic Acids and the Dimer of Deuterium Acetate," J. Am. Chem. Soc. **66,** 574 (1944).

[138] Y. Fujii, H. Yamada, and M. Mizuta, "Self-Association of Acetic Acid in Some Organic Solvents," J. Phys. Chem. **92,** 6768 (1988).

[139] F. Holtzberg, B. Post, and I. Fankuchen, "The Crystal Structure of Formic Acid," Acta Cryst. **6,** 127 (1953).

[140] R. E. Jones and D. H. Templeton, "The Crystal Structure of Acetic Acid," Acta Cryst. **11,** 484 (1958).

[141] I. Nahringbauer, "Hydrogen-Bond Studies .39. Reinvestigation of Crystal Structure of Acetic Acid (at +5°C and -190°C)," Acta Chem. Scand. **24,** 453 (1970).

[142] I. Bakó, G. Schubert, T. Megyes, G. Pálinkás, G. I. Swan, J. Dore, and M.-C. Bellisent-Funel, "Structural investigation of liquid formic acid by neutron diffraction. II: Isotopic substitution for DCOO[H/D]," Chem. Phys. **306,** 241 (2004).

[143] K. Kosugi, T. Nakabayashi, and N. Nishi, "Low-frequency Raman spectra of crystalline and liquid acetic acid and its mixtures with water. Is the liquid dominated by hydrogen-bonded cyclic dimers?," Chem. Phys. Lett. **291,** 253 (1998).

[144] H. Bertagnolli and H. G. Hertz, "Preservation and Loss of Structural Features of Solid Acetic Acid during Melting Process," Phys. Status Solidi A **49,** 463 (1978).

[145] H. Bertagnolli and H. G. Hertz, "The structure of liquid acetic acid – an interpretation of neutron diffraction results by geometrical models," Chem. Phys. Lett. **93,** 287 (1982).

[146] T. Nakabayashi, K. Kosugi, and N. Nishi, "Liquid structure of acetic acid studied by raman spectroscopy and ab initio molecular orbital calculations," J. Phys. Chem. A **103,** 8595 (1999).

[147] N. Sheppard, "Infrared Spectroscopy and Hydrogen Bonding – Band-Widths and Frequency Shifts," in *Hydrogen Bonding*, D. Hadži, ed., (Pergamon Press, London, 1959), p. 85.

[148] M. Haurie and A. Novak, "Gas phase spectra of acetic acid," J. Chim. Phys. **62,** 146 (1965).

[149] Y. Greenie, J.-C. Cornut, and J.-C. Lassegues, "Infrared spectra of matrix isolated acetic acid dimers," J. Chem. Phys. **55,** 5844 (1971).

[150] R. L. Redington and K. C. Lin, "On the OH stretching and the low-frequency vibrations of carboxylic acid cyclic dimers," J. Chem. Phys. **54,** 4111 (1971).

[151] M. J. Wojcik, A. Y. Hirakwara, and M. Tsuboi, "Ab-Initio Calculation of Cubic Force Constants in Formamide Monomer, Formamide Dimer, Formic Acid dimer and their D, D2, and D4 Derivatives - an Estimation of Fermi Resonance and Intra-Intermolecular Coupling," Int. J. Quantum Chem., Quantum Biol. Symp. **13,** 133 (1986).

[152] Y. Maréchal, "IR spectra of carboxylic acids in the gas phase: A quantitative reinvestigation," J. Chem. Phys. **87,** 6344 (1987).

[153] G. M. Florio, T. S. Zwier, E. M. Myshakin, K. D. Jordana, and E. L. Sibert, "Theoretical modeling of the OH stretch infrared spectrum of carboxylic acid dimers based on first-principles anharmonic couplings," J. Chem. Phys. **118,** 1735 (2003).

[154] C. Emmeluth, M. A. Suhm, and D. Luckhaus, "A monomers-in-dimers model for carboxylic acid dimers," J. Chem. Phys. **118,** 2242 (2003).

[155] P. Waldstein and L. A. Blatz, "Low-Frequency Raman Spectra and Molecular Association in Liquid Formic and Acetic Acids," J. Phys. Chem. **71,** 2271 (1967).

[156] J. E. Bertie and R. W. Wilton, "Acetic Acid under pressure: The formation below 0°C, x-ray powder diffraction pattern, and far-infrared absorption spectrum of phase II," J. Chem. Phys. **75,** 1639 (1981).

[157] J. E. Bertie and K. H. Michaelian, "The Raman spectrum of gaseous acetic acid at 21°C," J. Chem. Phys. **77,** 5267 (1982).

[158] O. F. Nielsen and P.-A. Lund, "Intermolecular Raman active vibrations of hydrogen bonded acetic acid dimers in the liquid state," J. Chem. Phys. **78,** 652 (1983).

[159] H. R. Zelsmann, Z. Mielke, and Y. Marechal, "Far IR spectra of acetic acids in the gas phase. A reinvestigation of the intermonomer vibrations," J. Mol. Struct. **237,** 273 (1990).

[160] K. Heyne, N. Huse, J. Dreyer, E. T. J. Nibbering, T. Elsaesser, and S. Mukamel, "Coherent low-frequency motions of hydrogen bonded acetic acid dimers in the liquid phase," J. Chem. Phys. **121,** 902 (2004).

[161] M. Lim and R. M. Hochstrasser, "Unusual vibrational dynamics of the acetic acid dimer," J. Chem. Phys. **115,** 7629 (2001).

[162] G. Seifert, T. Patzlaff, and H. Graener, "Ultrafast vibrational dynamics of doubly hydrogen bonded acetic acid dimers in liquid solution," Chem. Phys. Lett. **333,** 248 (2001).

[163] K. Heyne, N. Huse, E. T. J. Nibbering, and T. Elsaesser, "Ultrafast coherent nuclear motions of hydrogen bonded carboxylic acid dimers," Chem. Phys. Lett. **369,** 591 (2003).

[164] K. Heyne, N. Huse, E. T. J. Nibbering, and T. Elsaesser, "Coherent vibrational dynamics of intermolecular hydrogen bonds in acetic acid dimers studied by ultrafast mid-infrared spectroscopy," J. Phys.: Condens. Mat. **15,** S129 (2003).

[165] P. Blaise and O. Henri-Rousseau, "Linear response theory and IR spectral density of direct damped weak H-bonds: validity of adiabatic approximation," Chem. Phys. **243,** 229 (1999).

[166] D. E. O'Reilly and G. E. Schacher, "Rotational Correlation Times for Quadrupolar Relaxation in Liquids," J. Chem. Phys. **39,** 1768 (1963).

[167] D. S. Larsen, K. Ohta, and G. R. Fleming, "Three pulse photon echo studies of nondipolar solvation: Comparison with a viscoelastic model," J. Chem. Phys. **111,** 8970 (1999).

[168] A. P. Shreve and R. A. Mathies, "Thermal Effects in Resonance Raman Scattering: Analysis of the Raman Intensities of Rhodopsin and of the Time-Resolved Raman Scattering of Bacteriorhodopsin," J. Phys. Chem. **99,** 7285 (1995).

[169] V. Kozich, W. Werncke, and J. Dreyer, "Vibrational Excitation after Ultrafast Intramolecular Proton Transfer of TINUVIN: a Time-Resolved Resonance Raman Study," Chem. Phys. Lett. **399,** 484 (2004).

[170] V. Kozich and W. Werncke, "Influence of vibrational cooling on the time-dependence of stokes and anti-stokes resonance raman scattering," J. Mol. Struct. **735,** 145 (2005).

[171] C. Lee and R. G. Yang, W. Parr, "Development of the Colle-Salvetti correlation-energy formula into a functional of the electron density," Phys. Rev. B **37,** 785 (1988).

[172] B. Miehlich, A. Savin, H. Stoll, and H. Preuss, "Results obtained with the correlation energy density functionals of becke and Lee, Yang and Parr," Chem. Phys. Lett. **157,** 200 (1989).

[173] A. D. Becke, "Density-functioanl thermochemistry. III. The exact role of exchange," J. Chem. Phys. **98,** 5648 (1993).

[174] R. H. Hertwig and W. Koch, "On the parameterization of the local correlation functional. What is Becke-3-LYP?," Chem. Phys. Lett. **268,** 345 (1997).

[175] R. Krishnan, J. S. Binkley, and R. Seeger, "Self-consistent molecular orbital methods. XX. A basis set for correlated wave functions," J. Chem. Phys. **72,** 650 (1980).

[176] A. D. McLean and G. S. Chandler, "Contracted Gaussian basis sets for molecular calculations. I. Second row atoms, Z=11–18," J. Chem. Phys. **72,** 5639 (1980).

[177] T. Clark, J. Chandrasekhar, G. W. Spitznagel, and P. v. R. Schleyer, "Efficient Diffuse Function-Augmented Basis-Sets for Anion Calculations .3. the 3-21+G Basis Set for 1st-Row Elements, LI–F," J. Comp. Chem. **4,** 294 (1983).

[178] M. J. Frisch *et al.*, *Gaussian 98 (Revision A.9)*, Gaussian, Inc., Pittsburgh PA, 1998.

[179] W. Schneider and W. Thiel, "Anharmonic force fields from analytic second order derivatives: Method and application to methyl bromide," Chem. Phys. Lett. **157,** 367 (1989).

[180] K. Heyne, N. Huse, E. T. J. Nibbering, and T. Elsaesser, "Ultrafast relaxation and anharmonic coupling of O–H stretching and bending excitations in cyclic acetic acid dimers," Chem. Phys. Lett. **382,** 19 (2003).

[181] P. Hamm, S. M. Ohline, and W. Zinth, "Vibrational cooling after ultrafast photoisomerization of azobenzene measured by femtosecond infrared spectroscopy," J. Chem. Phys. **106,** 519 (1997).

[182] I. V. Rubtsov, J. Wang, and R. M. Hochstrasser, "Dual frequency 2D-IR of peptide amide-A and amide-I modes," J. Chem. Phys. **118,** 7733 (2003).

[183] K. Heyne, E. T. J. Nibbering, T. Elsaesser, M. Petković, and O. Kühn, "Cascaded Energy Redistribution upon O–H Stretching Excitation in an Intramolecular Hydrogen Bond," J. Phys. Chem. A **108,** 6083 (2004).

[184] P. Hamm, M. Lim, and R. M. Hochstrasser, "Non-Markovian dynamics of the vibrations of ions in water from femtosecond infrared three-pulse photon echoes," Phys. Rev. Lett. **81,** 5326 (1998).

[185] R. Rey and J. T. Hynes, "Vibrational phase and energy relaxation of CN- in water," J. Chem. Phys. **108,** 142 (1998).

[186] J. Stenger, D. Madsen, P. Hamm, E. T. J. Nibbering, and T. Elsaesser, "Ultrafast vibrational dephasing of liquid water," Phys. Rev. Lett. **87,** 027401 (2001).

[187] C. J. Bardeen and C. V. Shank, "Femtosecond electronic dephasing in large molecules in solution using mode suppression," Chem. Phys. Lett. **203,** 535 (1993).

[188] W. P. de Boeij, M. S. Pshenichnikov, , and D. A. Wiersma, "Mode suppression in the non-Markovian limit by time-gated stimulated photon echo," J. Chem. Phys. **105,** 2953 (1996).

[189] N. Huse, K. Heyne, J. Dreyer, E. T. J. Nibbering, and T. Elsaesser, "Vibrational Multilevel Quantum Coherence due to Anharmonic Couplings in Intermolecular Hydrogen Bonds," Phys. Rev. Lett. **91,** 197401 (2003).

[190] N. Huse, B. D. Bruner, M. L. Cowan, J. Dreyer, E. T. J. Nibbering, R. J. D. Miller, and T. Elsaesser, "Anharmonic couplings underlying ultrafast vibrational dynamics of hydrogen bonds in liquids," Phys. Rev. Lett. **95,** 147402 (2005).

[191] W. H. Press, S. A. Teukolsky, W. T. Vetterling, and B. P. Flannery, *Numerical Recipes in C. The Art of Scientific Compunting*, 2 ed. (Cambridge Univ. Press, Cambridge, UK, 1993).

[192] M. Frigo and S. Johnson, "The design and implementation of FFTW3," Proc. IEEE **93,** 216 (2005).

[193] J. Sponer, J. Leszczynski, and P. Hobza, "Hydrogen bonding and stacking of DNA bases: A review of quantum-chemical ab initio studies," J. Biomol. Struct. & Dynamics **14,** 117 (1996).

[194] T. E. Creighton, *Proteins. Structures and Molecular Properties*, 2 ed. (W. H. Freeman and Company, New York, USA, 1993).

[195] L. da Vinci, *Delle Acque* (Sellerio di Giorgianni, Palermo, Italia, 2001).

[196] H. Cavendish, "Experiments on Air," Philosophical Transactions of the Royal Society of London **74,** 119 (1784), archival records support that Cavendish already made his observations in 1781.

[197] A. L. Lavoisier, "Mémoire dans lequel on a pour but de prouver que l'eau n'est point une substance simple, un élément proprement dit, mais qu'elle est susceptible de décomposition et de recomposition," Observations sur la Physique, sur l'Histoire Naturelle et sur les Arts **23,** 452 (1783), see also Mémoires de l'Académie des Sciences, 468 (1781), published in 1784.

[198] C. Brunner, "Untersuchung über die Cohäsion der Flüssigkeiten," Poggend. Ann. d. Phys. u. Chem. **146,** 481 (1847), band LXX der damaligen Folge.

[199] G. W. Koch, S. C. Sillett, G. Jennings, and S. D. Davis, "The limits to tree height," Nature **428,** 851 (2004).

[200] M. Grassi, "Sur la compressibilité des liquides," Ann. Chim. et Phys. III. Série, **31,** 437 (1851).

[201] M. Grassi, in *Lehrbuch der Experimentalphysik*, 3 ed., A. Wüllner, ed., (Teubner Verlag, Leipzig, 1874), Vol. 1, p. 230.

[202] M. E.-H. Amagat, "Mémoire sur la Compressibilité des Liquides," Ann. Chim. et Phys. V. Série, **11,** 520 (1877).

[203] W. C. Röntgen, "Ueber den Einfluss des Druckes auf die Viscosität der Flüssigkeiten, speciell des Wassers," Wied. Ann. **258,** 510 (1884).

[204] E. Warburg and J. Sachs, "Ueber den Einfluss der Dichtigkeit auf die Viscosität tropfbarer Flüssigkeiten," Wied. Ann. **258,** 518 (1884).

[205] R. J. Speedy and C. A. Angell, "Isothermal compressibility of supercooled water and evidencefor a thermodynamic singularity at -45°C," J. Chem. Phys. **65,** 851 (1976).

[206] C. A. Angell, "Supercooled Water," Ann. Rev. Phys. Chem. **34,** 593 (1983).

[207] I. Ohmine and H. Tanaka, "Fluctuation, relaxations, and hydration in liquid water. Hydrogen-bond rearrangement dynamics," Chem. Rev. **93,** 2545 (1993).

[208] W. C. Röntgen, "Ueber die Constitution des flüssigen Wassers," Wied. Ann. **281,** 91 (1892).

[209] D. M. Dennison, "The Crystal Structure of Ice," Phys. Rev. **17,** 20 (1921).

[210] H. H. Meyer, "Der Einfluss der Temperatur und gelöster Elektrolyte auf das monochromatische Debye-Scherrer-Diagramm des Wassers," Ann. d. Physik **397,** 701 (1930).

[211] G. W. Stewart, "X-Ray Diffraction in Water: The Nature of Molecular Association," Phys. Rev. **37,** 9 (1931).

[212] R. S. Mulliken, "Electronic Structures of Polyatomic Molecules and Valence II. Quantum Theory of the Double Bond," Phys. Rev. **41,** 751 (1932).

[213] J. D. Bernal and R. H. Fowler, "A Theory of Water and Ionic Solution, with Particular Reference to Hydrogen and Hydroxyl Ions," J. Chem. Phys. **1,** 515 (1933).

[214] L. Pauling, "The Structure and Entropy of Ice and of Other Crystals with Some Randomness of Atomic Arrangement," J. Am. Chem. Soc. **57,** 2680 (1935).

[215] J. W. Ellis, "Polymers and New Infrared Absorption bands of Water," Phys. Rev. **38,** 693 (1931).

[216] A. K. Ångström, "Some Observations on the Selective Reflection from Solutions in the Infra-Red," Phys. Rev. **3,** 47 (1914).

[217] N. Wells, *The atmosphere and ocean: a physical introduction* (Taylor & Francis Ltd., London, U.K., 1986).

[218] S. N. Mikhailenko, V. G. Tyuterev, K. A. Keppler, B. P. Winnewisser, Winnewisser, G. Mellau, S. Klee, and K. N. Rao, "The $2\nu_2$ Band of Water: Analysis of New FTS Measurements and High-K_a Transitions and Energy Levels," J. Mol. Spec. **184,** 330 (1997).

[219] J. Houghton, "Global Warming," Rep. Prog. Phys. **68,** 1343 (2005).

[220] G. M. Hale and M. R. Querry, "Optical constants of water in the 200-nm to 200-micrometer wavelength region," Federation Proc. **12,** 555 (1973).

[221] M. R. Querry, P. G. Cary, and R. C. Waring, "Split-pulse laser method for measuring attenuation coefficients of transparent liquids: application to deionized filtered water in the visible region," Appl. Opt. **17,** 3587 (1978).

[222] S. G. Warren, "Optical constants of ice from the ultraviolet to the microwave," Appl. Opt. **23,** 1206 (1984).

[223] A. Luzar and D. Chandler, "Hydrogen-bond kinetics in liquid water," Nature **379,** 55 (1996).

[224] A. Luzar and D. Chandler, "Effect of Environment on Hydrogen Bond Dynamics in Liquid Water," Phys. Rev. Lett. **76,** 928 (1996).

[225] I. Ohmine and S. Saito, "Water dynamics: Fluctuation, relaxation, and chemical reactions in hydrogen bond network rearrangement," Acc. Chem. Res. **32,** 741 (1999).

[226] G. Reddy, C. P. Lawrence, J. L. Skinner, and A. Yethiraj, "Liquid state theories for the structure of water," J. Chem. Phys. **119,** 13012 (2003).

[227] D. Xenides, B. R. Randolf, , and B. M. Rode, "Structure and ultrafast dynamics of liquid water: A quantum mechanics/molecular mechanics molecular dynamics simulations study," J. Chem. Phys. **122,** 174506 (2005).

[228] J.-H. Guo, Y. Luo, A. Augustsson, J.-E. Rubensson, C. Såthe, H. Ågren, H. Siegbahn, and J. Nordgren, "X-Ray Emission Spectroscopy of Hydrogen Bonding and Electronic Structure of Liquid Water," Phys. Rev. Lett. **89,** 137402 (2002).

[229] R. Torre, P. Bartolini, and R. Righini, "Structural relaxation in supercooled water by time-resolved spectroscopy," Nature **428,** 296 (2004).

[230] P. Wernet *et al.*, "The Structure of the First Coordination Shell in Liquid Water," Science **304,** 995 (2004).

[231] J. D. Smith, C. D. Cappa, K. R. Wilson, B. M. Messer, R. C. Cohen, and R. J. Saykally, "Energetics of Hydrogen Bond Network Rearrangements in Liquid Water," Science **306,** 851 (2004).

[232] A. Nilsson *et al.*, "Comment on *Energetics of Hydrogen Bond Network Rearrangements in Liquid Water*," Science **308,** 793 (2005).

[233] L. Åke Näslund, D. C. Edwards, , P. Wernet, U. Bergmann, H. Ogasawara, L. G. M. Pettersson, S. Myneni, and A. Nilsson, "X-ray Absorption Spectroscopy Study of the Hydrogen Bond Network in the Bulk Water of Aqueous Solutions," J. Phys. Chem. A **109,** 5995 (2005).

[234] L. . Näslund, J. Lüning, Y. Ufuktepe, H. Ogasawara, P. Wernet, U. Bergmann, L. G. M. Pettersson, and A. Nilsson, "X-ray Absorption Spectroscopy Measurements of Liquid Water," J. Phys. Chem. B **109,** 13835 (2005).

[235] A. J. Lock and H. J. Bakker, "Temperature dependence of vibrational relaxation in liquid H2O," J. Chem. Phys. **117,** 1708 (2002).

[236] A. Pakoulev, Z. Wang, and D. D. Dlott, "Vibrational relaxation and spectral evolution following ultrafast OH stretch excitation of water," Chem. Phys. Lett. **371,** 594 (2003).

[237] H. J. Bakker, A. J. Lock, and D. Madsen, "Strong feedback in the vibrational relaxation of liquid water," Chem. Phys. Lett. **384,** 236 (2004).

[238] H. J. Bakker, A. J. Lock, and D. Madsen, "Comment on 'Vibrational relaxation and spectral evolution following ultrafast OH stretch excitation of water' by A. Pakoulev, Z. Wang, D.D. Dlott," Chem. Phys. Lett. **385,** 329 (2004).

[239] A. Pakoulev, Z. H. Wang, Y. S. Pang, and D. D. Dlott, "Reply to: Comment on 'Vibrational relaxation and spectral diffusion following ultrafast OH stretch excitation of water', by H.J. Bakker, A.J. Lock, D. Madsen," Chem. Phys. Lett. **385,** 332 (2004).

[240] U. C. Singh and P. A. Kollman, "A water dimer potential based on ab initio calculations using Morokuma component analyses," J. Chem. Phys. **83,** 4033 (1985).

[241] K. Wanatabe and M. Zelikoff, "Absorption Coefficients in the Vacuum Ultraviolet," J. Opt. Soc. Am. **43,** 753 (1953).

[242] V. Engel, V. Staemmler, R. L. V. Wal, F. F. Crim, R. J. Sension, B. Hudson, P. Andresen, S. Hennig, K. Weide, and R. Schinke, "Photodissociation of water in the first absorption band: a prototype for dissociation on a repulsive potential energy surface," J. Phys. Chem. **96,** 3201 (1992).

[243] S. A. Clough, Y. Beers, G. P. Klein, and L. S. Rothman, "Dipole moment of water from Stark measurements of H_2O, HDO, and D_2O," J. Chem. Phys. **59,** 2254 (1973).

[244] T. R. Dyke, K. M. Mack, , and J. S. Muenter, "The structure of water dimer from molecular beam electric resonance spectroscopy," J. Chem. Phys. **66,** 498 (1977).

[245] W. F. Kuhs and M. S. Lehmann, "The structure of the ice Ih by neutron diffraction," J. Phys. Chem. **87,** 4312 (1983).

[246] J. Monod, J. Wyman, and J. P. Changeux, "On the Nature of Allosteric Transitions – a Plausible Model," J. Mol. Biol. **12,** 88 (1965).

[247] J. Monod, "From Enzymatic Adaption to Allosteric Transitions," in *Nobel Lectures, Physiology or Medicine 1963-1970* (Elsevier Publishing Company, Amsterdam, 1972), p. 188.

[248] Y. S. Badyal, M.-L. Saboungi, D. L. Price, S. D. Shastri, D. R. Haeffner, and A. K. Soper, "Electron distribution in water," J. Chem. Phys. **112,** 9206 (2000).

[249] J. K. Gregory, D. C. Clary, K. Liu, M. G. Brown, and R. J. Saykally, "The Water Dipole Moment in Water Clusters," Science **275,** 814 (1997).

[250] L. X. Dang, "Importance of Polarization Effects in Modeling the Hydrogen Bond in Water Using Classical Molecular Dynamics Techniques," J. Phys. Chem. B **102,** 620 (1998).

[251] P. L. Silvestrelli and M. Parrinello, "Water Molecule Dipole in the Gas and in the Liquid Phase," Phys. Rev. Lett. **82,** 3308 (1999).

[252] J. Korchowiec and T. Uchimaru, "New energy partitioning scheme based on the self-consistent charge and configuration method for subsystems: Application to water dimer system," J. Chem. Phys. **112,** 1623 (2000).

[253] T. K. Ghanty, V. N. Staroverov, P. R. Koren, and E. R. Davidson, "Is the Hydrogen Bond in Water Dimer and Ice Covalent?," J. Am. Chem. Soc. **122,** 1210 (2000).

[254] S. Kashtanov, A. Augustsson, Y. Luo, J.-H. Guo, C. Såthe, J.-E. Rubensson, H. Siegbahn, J. Nordgren, and H. Ågren, "Local structures of liquid water studied by x-ray emission spectroscopy," Phys. Rev. B **69,** 024201 (2004).

[255] E. D. Isaacs, A. S. P. M. Platzman, D. R. Hamann, B. Barbiellini, and C. A. Tulk, "Covalency of the Hydrogen Bond in Ice: A Direct X-Ray Measurement," Phys. Rev. Lett. **82,** 600 (1999).

[256] S. Meiboom, "Nuclear Magnetic Resonance Study of the Proton Transfer in Water," J. Chem. Phys. **34,** 375 (1961).

[257] H. Graener, G. Seifert, and A. Laubereau, "New Spectroscopy of water using tunable picosecond pulses in the infrared," Phys. Rev. Lett. **66,** 2092 (1991).

[258] S. Bratos and J.-C. Leicknam, "Ultrafast infrared pump-probe spectroscopy of water: A theoretical description," J. Chem. Phys. **101,** 4536 (1994).

[259] S. Woutersen, U. Emmerichs, and H. J. Bakker, "Femtosecond Mir-IR Pump-Probe Spectroscopy of Liquid Water: Evidence for a Two-Component Structure," Science **278,** 658 (1997).

[260] S. Woutersen, U. Emmerichs, H.-K. Nienhuys, and H. J. Bakker, "Anomalous Temperature Dependence of Vibrational Lifetimes in Water and Ice," Phys. Rev. Lett. **81,** 1106 (1998).

[261] S. Woutersen and H. J. Bakker, "Resonant intermolecular transfer of vibrational energy in liquid water," Nature **402,** 507 (1999).

[262] S. Woutersen and H. J. Bakker, "Hydrogen bond in liquid water as a Brownian oscillator," Phys. Rev. Lett. **83,** 2077 (1999).

[263] G. M. Gale, F. H. G. Gallot, N. Lascoux, S. Bratos, and J.-C. Leicknam, "Femtosecond Dynamics of Hydrogen Bonds in Liquid Water: A Real Time Study," Phys. Rev. Lett. **82,** 1068 (1999).

[264] S. Bratos, G. M. Gale, G. Gallot, F. Hache, N. Lascoux, and J.-C. Leicknam, "Motion of hydrogen bonds in diluted HDO/D_2O solutions: Direct probing with 150 fs resolution," Phys. Rev. E **61,** 5211 (2000).

[265] G. Gallot, N. Lascoux, G. M. Gale, S. Bratos, J.-C. Leicknam, and S. Pommeret, "Non-monotonic decay of transient infrared absorption in dilute HOD/D_2O solutions," Chem. Phys. Lett. **341,** 535 (2001).

[266] H. J. Bakker, H.-K. Nienhuys, G. Gallot, N. Lascoux, G. M. Gale, J.-C. Leicknam, and S. Bratos, "Transient absorption of vibrationally excited water," J. Chem. Phys. **116,** 2592 (2002).

[267] R. Laenen, C. Rauscher, and A. Laubereau, "Dynamics of Local Substructures in Water Observed by Ultrafast Infrared Hole Burning," Phys. Rev. Lett. **80,** 2622 (1998).

[268] R. Laenen, K. Simeonidis, and A. Laubereau, "Subpicosecond Spectroscopy of Liquid Water in the Infrared: Effect of Deuteration on the Structural and Vibrational Dynamics," J. Phys. Chem. B **106,** 408 (2002).

[269] J. C. Deák, S. T. Rhea, L. K. Iwaki, and D. D. Dlott, "Vibrational Energy Relaxation and Spectral Diffusion in Water and Deuterated Water," J. Phys. Chem. A **104,** 4866 (2000).

[270] D. Cringus, S. Yeremenko, M. S. Pshenichnikov, and D. A. Wiersma, "Hydrogen Bonding and Vibrational Energy Relaxation in Water-Acetonitrile Mixtures," J. Phys. Chem. B **108,** 10376 (2004).

[271] C. J. Fecko, J. J. Loparo, S. T. Roberts, and A. Tokmakoff, "Local hydrogen bonding dynamics and collective reorganization in water: Ultrafast infrared spectroscopy of HOD/D_2O," J. Chem. Phys. **122,** 054506 (2005).

[272] C. Rønne, L. Thranea, P.-O. Åstrand, A. Wallqvist, K. V. Mikkelsen, and S. R. Keiding, "Investigation of the temperature dependence of dielectric relaxation in liquid water by THz reflection spectroscopy and molecular dynamics simulation," J. Chem. Phys. **107,** 5319 (1997).

[273] C. Rønne, P.-O. Åstrand, and S. R. Keiding, "THz Spectroscopy of Liquid H_2O and D_2O," Phys. Rev. Lett. **82,** 2888 (1999).

[274] C. Rønne and S. R. Keiding, "Low fequency spectroscopy of liquid water using THz-time domain spectroscopy," J. Mol. Liquids **101,** 199 (2002).

[275] H. J. Bakker and H.-K. Nienhuys, "Delocalization of Protons in Liquid Water," Science **297,** 587 (2002).

[276] P. C. Becker, H. L. Fragnito, J. Y. Bigot, C. H. Brito Cruz, R. L. Fork, and C. V. Shank, "Femtosecond photon echoes from molecules in solution," Phys. Rev. Lett. **63,** 505 (1989).

[277] E. T. J. Nibbering, D. A. Wiersma, and K. Duppen, "Femtosecond non-Markovian optical dynamics in solution," Phys. Rev. Lett. **66,** 2464 (1991).

[278] J. Stenger, D. Madsen, P. Hamm, E. T. J. Nibbering, and T. Elsaesser, "A Photon Echo Peak Shift Study of Liquid Water," J. Phys. Chem. A **106,** 2341 (2002).

[279] S. Yeremenko, M. S. Pshenichnikov, and D. A. Wiersma, "Hydrogen-bond dynamics in water explored by heterodyne-detected photon echo," Chem. Phys. Lett. **369,** 107 (2003).

[280] C. J. Fecko, J. D. Eaves, J. J. Loparo, A. Tokmakoff, and P. L. Geissler, "Ultrafast hydrogen-bond dynamics in the infrared spectroscopy of water," Science **301,** 1698 (2003).

[281] C. P. Lawrence and J. L. Skinner, "Vibrational spectroscopy of HOD in liquid D2O. II. Infrared line shapes and vibrational Stokes shift," J. Chem. Phys. **117,** 8847 (2003).

[282] R. Rey, K. B. Møller, and J. T. Hynes, "Hydrogen Bond Dynamics in Water and Ultrafast Infrared Spectroscopy," J. Phys. Chem. A **106,** 11993 (2002).

[283] R. J. Clayton, J. E. Houldin, H. R. L. Lamont, and W. F. Willshaw, J. Inst. Elec. Eng. **93,** 97 (1946).

[284] U. Kaatze, "The dielectric Spectrum of Water in the Microwave and Near-Millimeter Wavelength Region," Chem. Phys. Lett. **132,** 291 (1986).

[285] R. Buchner, J. Barthel, and J. Stauber, "The dielectric relaxation of water between 0°C and 35°C," Chem. Phys. Lett. **306,** 57 (1999).

[286] J. B. Asbury, T. Steinel, C. Stromberg, S. A. C. C. P. Lawrence, J. L. Skinner, and M. D. Fayer, "Water Dynamics: Vibrational Echo Correlation Spectroscopy and Comparison to Molecular Dynamics Simulations," J. Phys. Chem. A **108,** 1107 (2004).

[287] M. F. Kropman, H.-K. Nienhuys, S. Woutersen, and H. J. Bakker, "Vibrational Relaxation and Hydrogen-Bond Dynamics of HDO:H_2O," J. Phys. Chem. A **105,** 4622 (2001).

[288] J. B. Asbury, T. Steinel, K. Kwak, S. A. C. C. P. Lawrence, J. L. Skinner, and M. D. Fayer, "Dynamics of water probed with vibrational echo correlation spectroscopy," J. Chem. Phys. **121,** 12431 (2004).

[289] S. A. Corcelli, C. P. Lawrence, and J. L. Skinner, "Combined electronic structure/molecular dynamics approach for ultrafast infrared spectroscopy of dilute HOD in liquid H_2O and D_2O," J. Chem. Phys. **120,** 8107 (2004).

[290] S. A. Corcelli, C. P. Lawrence, J. B. Asbury, T. Steinel, M. D. Fayer, and J. L. Skinner, "Spectral diffusion in a fluctuating charge model of water," J. Chem. Phys. **121,** 8897 (2004).

[291] T. Steinel, J. Asbury, J. Zheng, and M. Fayer, "Watching Hydrogen Bonds Break: A Transient Absorption Study of Water," J. Phys. Chem. A **108,** 10957 (2004).

[292] P. C. Cross, J. Burnham, and P. A. Leighton, "The Raman Spectrum and the Structure of Water," J. Am. Chem. Soc. **59,** 1134 (1937).

[293] S. Palese, L. Schilling, R. J. D. Miller, P. R. Staver, and W. T. Lotshaw, "Femtosecond Optical Kerr Effect Studies of Water," J. Phys. Chem. **98,** 6308 (1994).

[294] E. W. Castner, Jr., Y. J. Chang, Y. C. Chu, and G. E. Walrafen, "The intermolecular dynamics of liquid water," J. Chem. Phys. **102,** 653 (1995).

[295] Y. Tominaga, A. Fujiwara, and Y. Amo, "Dynamical structure of water by Raman spectroscopy," Fluid Phase Equilibria **144,** 323 (1997).

[296] H. R. Zelsmann, "Temperature dependence of the optical constants for liquid H_20 and D_20 in the far IR region," J. Mol. Struct. **350,** 95 (1995).

[297] N. Agmon, "Tetrahedral Displacement: The Molecular Mechanism behind the Debye Relaxation in Water," J. Phys. Chem. **100,** 1072 (1996).

[298] P. L. Geissler, C. Dellago, D. Chandler, J. Hutter, and M. Parrinello, "Autoionization in Liquid Water," Science **291,** 2121 (2001).

[299] S. Bratos, J.-C. Leicknam, S. Pommeret, and G. Gallot, "Laser spectroscopic visualization of hydrogen bond motions in liquid water," J. Mol. Struct. **708,** 197 (2004).

[300] A. J. Lock, S. Woutersen, and H. J. Bakker, "Ultrafast energy equilibration in hydrogen-bonded liquids," J. Phys. Chem. A **105,** 1238 (2001).

[301] A. Pakoulev, Z. Wang, Y. Pang, and D. D. Dlott, "Vibrational energy relaxation pathways of water," Chem. Phys. Lett. **380,** 404 (2003).

[302] Z. Wang, A. Pakoulev, Y. Pang, and D. D. Dlott, "Vibrational substructure in the OH stretching band of water," Chem. Phys. Lett. **378,** 281 (2003).

[303] Z. Wang, A. Pakoulev, Y. Pang, and D. D. Dlott, "Vibrational Substructure in the OH Stretching Transition of Water and HOD," J. Phys. Chem. A **108,** 9054 (2004).

[304] C. Oliveri, F. Baroetto, and C. Magro, "Study of the chemical composition of silicon nitride films obtained by chemical vapour deposition and plasma-enhanced chemical vapour deposition," Surface and Coatings Technology **45,** 137 (1991).

[305] W. Qian and D. M. Jonas, "Role of cyclic sets of transition dipoles in the pump-probe polarization anisotropy: Application to square symmetric molecules and perpendicular chromophore pairs," J. Chem. Phys. **119,** 1611 (2003).

[306] J. A. Poulsen, G. Nyman, and S. Nordholm, "Wave Packet Study of Ultrafast Relaxation in Ice Ih and Liquid Water. Resonant Intermolecular Vibrational Energy Transfer," J. Phys. Chem. A **107,** 8420 (2003).

[307] C. Bäcktorp, J. A. Poulsen, and G. Nyman, "Direct Dynamics Study of Ultrafast Vibrational Energy Relaxation in Ice Ih," J. Phys. Chem. A **109,** 3105 (2005).

[308] L. Hernández de la Peña, M. S. Gulam Razul, and P. G. Kusalik, "Impacts of Quantization on the Properties of Liquid Water," J. Phys. Chem. A **109,** 7236 (2005).

[309] C. P. Lawrence and J. L. Skinner, "Vibrational spectroscopy of HOD in liquid D2O. III. Spectral diffusion, and hydrogen-bonding and rotational dynamics," J. Chem. Phys. **118,** 264 (2003).

[310] S. Roy and B. Bagchi, "Solvation dynamics in liquid water. A novel interplay between librational and diffusive modes," J. Chem. Phys. **99,** 9938 (1993).

[311] P. L. Geissler and D. Chandler, "Importance sampling and theory of nonequilibrium solvation dynamics in water," J. Chem. Phys. **113,** 9759 (2000).

[312] R. Rey and J. T. Hynes, "Vibrational energy relaxation of HOD in liquid D_2O," J. Chem. Phys. **104,** 2356 (1996).

[313] C. P. Lawrence and J. L. Skinner, "Vibrational spectroscopy of HOD in liquid D2O. VI. Intramolecular and intermolecular vibrational energy flow," J. Chem. Phys. **119,** 1623 (2003).

[314] G. E. Walrafen, M. S. Hokmabadi, and W.-H. Yang, "Raman Investigation of the Temperature Dependence of the Bending ν_2 and Combination $\nu_2 + \nu_L$ Bands from Liquid Water," J. Phys. Chem. **92,** 2433 (1988).

[315] G. E. Walrafen, "Raman Spectral Studies of the Effects of Temperature on Water Structure," J. Phys. Chem. **41,** 114 (1967).

[316] O. F. A. Larsen and S. Woutersen, "Vibrational relaxation of the H_2O bending mode in liquid water," J. Chem. Phys. **121,** 12143 (2004).

[317] P. Bodis, O. F. A. Larsen, and S. Woutersen, "Vibrational Relaxation of the Bending Mode of HDO in Liquid D_2O," J. Phys. Chem. A **109,** 5303 (2005).

[318] G. Seifert, T. Patzlaff, and H. Graener, "Pure intermolecular vibrational relaxation of the OH bending mode of water molecules," J. Chem. Phys. **120,** 8866 (2004).

Erklärungen

Hiermit erkläre ich, die Dissertation selbständig und nur unter Verwendung der angegebenen Hilfen und Hilfsmittel angefertigt zu haben.

Ich habe mich anderwärts nicht um einen Doktorgrad beworben und besitze einen entsprechenden Doktorgrad nicht.

Ich habe die dem Verfahren zugrunde liegenden Promotionsordnung der Mathematisch-Naturwissenschaftlichen Fakultät I der Humboldt-Universität zu Berlin zur Kenntnis genommen.

Berlin, den 7. Dezember 2005 Nils Huse

Danksagung / Acknowledgement

Die Forschung, die dieser Doktorarbeit zugrunde liegt, geht auf viele Beteiligte zurück, die mit mir zusammengearbeitet und mich unterstützt haben. Diesen Leuten möchte ich deshalb ausdrücklich danken.

Allen voran danke ich Dr. Thomas Elsässer, der mich bereitwillig als seinen Doktoranden aufgenommen und betreut hat, und der mir durch seine physikalische Intuition, seinen Scharfsinn und seine Effektivität vieles beigebracht hat.

Meinem Co-Betreuer Dr. Erik Nibbering danke ich für seinen Einsatz im Projekt, die große Unterstüzung und die tolle Zusammenarbeit. Ich hoffe auf noch mehr Erlebnisse am kulturellen und kulinarischen Menü Berlins.

Meiner Freundin Dagmar möchte ich für ihre Unterstützung, Rücksichtnahme, Geduld und Liebe danken, $^{\infty}$DW.

Im Rahmen des Essigsäure-Projektes danke ich Dr. Karsten Heyne und Dr. Jens Dreyer für die freundschaftliche und sehr erfolgreiche enge Zusammenarbeit.

Many thanks to the Canadian connection for the successfull multidimensional collaboration, the days and nights of fellowship in the lab, the kitchen excercises, and the good vibes (in order of appearance): R. J. Dwayne Miller*, Barry D. Brunner*, Michael D. Cowan*, Jason R. Dwyer*, Darren Kraemer, and Alex Paarmann.

Auch bedanke ich mich für die Zusammenarbeit, die anregenden Diskussionen, die erfahrene Unterstützung und die Freundschaft bei (alphabetisch): Christoph Lienau*, Claus Ropers, Corneliu-Catalin Neacsu, Felix Eickemeyer*, Fritz Weik*, Gero Stibenz, Günter Steinmeyer*, Jens Stenger*, Katrin Adamczyk, Klaus Reimann*, Manfred Fiebig*, Markus Raschke*, Mathias Mönster, Matias Bargheer*, Matteo Rini**, Michael Wörner*, Omar Farghaly Mohammed Abdelsaboor, Pancho Tzankov*, Rüdiger Grunwald*, Satoshi Ashihara*, Thomas Schultz*, Tobias Günther* und Uwe Griebner*,

Den C1-ern sei hier für die soziale Gemeinschaft, die Hilfe, Bowling, Wasserwerk und Kuchen gedankt (alphabetisch): Regina Goleschny, Valeri Kozich*, Regina Lendt, Hans-Gerd Ludewig, Peter Scholze, Brigitte Steinert, Helmut Walz und Wolfgang Werncke*

Natürlich bedarf es auch vielerlei technischer Unterstützung, um Experimente aufzubauen und zu verändern, Proben herzustellen, Softwareprobleme zu lösen, Bestellungen zu machen, sich mit dem Zoll zu arrangieren und vieles mehr. So sei weiteren Mitarbeitern gedankt (alphabetisch): Wolfgang Goleschny, Kathleen Krüger, Bernd Kinski, Thomas-Martin Kruel*, Margret Lehmann, Renate Steinsdörfer, Peter Stolz und Monika Tischer

∗Dr. oder PhD.